A study on the effective elastic properties of random porous materials : 3D Printing, Experiments and Numerics.

Othmane Zerhouni

INSTITUT POLYTECHNIQUE DE PARIS

NNT : 2019IPPAX008

Thèse de doctorat

Étude des propriétés élastiques effectives de matériaux avec microstructure: Impression 3D, caractérisation expérimentale et numérique.

Thèse de doctorat de l'Institut Polytechnique de Paris
préparée à l'École polytechnique

École doctorale n°626, École Doctorale de l'Institut Polytechnique de Paris
Spécialité de doctorat : Ingénierie, mécanique et énergétique

Thèse présentée et soutenue à Palaiseau, le 22 novembre 2019, par

OTHMANE ZERHOUNI

Composition du Jury :

Yves-Marie LEROY Expert Géomécanique, TOTAL (CSTJF)	Président
Justin DIRRENBERGER Associate Professor, Conservatoire National des Arts et Métiers (PIMM)	Rapporteur
François WILLOT Charge de Recherche, Mines ParisTech (C.M.M.)	Rapporteur
Renald BRENNER Directeur de Recherche CNRS, Institut Jean le Rond d'Alembert (MISES)	Examinateur
Julie DIANI Directrice de Recherche CNRS, Ecole Polytechnique (LMS)	Examinatrice
Sébastien BRISARD Chargé de Recherche, Ecole des Ponts ParisTech (Laboratoire Navier)	Co-directeur de thèse
Konstantinos DANAS Charge de Recherche CNRS, Ecole Polytechnique (LMS)	Directeur de thèse
Emmanuelle POLI Chef de projet R&D Carbonate, TOTAL (CSTJF)	Invitée

Thèse présentée pour l'obtention du titre de

DOCTEUR DE L'INSTITUT POLYTECHNIQUE DE PARIS

Spécialité : Mécanique et Sciences de matériaux

Étude des propriétés élastiques effectives de matériaux avec microstructure : Impression 3D, caractérisation expérimentale et numérique.

A study on the effective elastic properties of materials with microstructure : 3D Printing, Experiments and Numerics.

Laboratoire de Mécanique des Solides
Ecole Polytechnique, Palaiseau

PhD Student :
Othmane Zerhouni

PhD advisor :
Konstantinos Danas

PhD co-advisor :
Sébastien Brisard

À Lalla Jouhara,
À mes grands-parents...

Remerciements

En intégrant le mastère de recherche MAGIS pour finaliser mon diplôme d'ingénieur Arts et Métiers, je n'imaginais à aucun moment que cela me mènerait jusqu'à entreprendre une thèse, aventure tant professionnelle qu'humaine. Ce cap, entrepris après mon stage, n'aurait pas eu lieu sans la rencontre de mon directeur de thèse Kostas, qui a su, lors de nos différents entretiens pour mon stage de mastère, me partager sa vision de l'avenir de l'industrie et de l'importance d'entreprendre une thèse. Mes premiers remerciements lui sont adressés pour m'avoir accordé sa confiance et m'avoir encadré et formé au monde de la recherche.

J'aimerais, de même, exprimer toute ma gratitude envers Sébastien Brisard, qui a accepté de m'encadrer au cours de cette thèse. Je le remercie pour sa patience à mon égard au moment où je devais mener en parallèle les études sur la fabrication de matériaux architecturés et la génération de champs gaussiens. Au cours des différents échanges que nous avons pu avoir, il m'a partagé son goût pour la rigueur et la précision des travaux entrepris. J'espère que les publications qui suivront ce travail seront à l'image de ce que j'ai pu apprendre de nos réunions.

Je souhaiterais de même remercier les membres de mon jury d'avoir accepté d'examiner mes travaux. Je commence ainsi par faire part de ma gratitude à Messieurs Justin Dirrenberger et François Willot, pour avoir accepté d'être rapporteurs de mon mémoire de thèse et avoir rigoureusement mené cette tâche dans des délais pour le moins serrés. Leurs commentaires et corrections m'ont permis de prendre davantage de recul sur mes travaux et m'ont ouvert de nouvelles perspectives sur mes travaux de recherche. Je les remercie ainsi que les professeurs Renard Brenner, Julie Diani et Monsieur Yves-Marie Leroy de l'attention porté à ma présentation et la discussion qui s'en est suivi.

Ce travail n'aurait pu voir le jour sans le financement du groupe TOTAL. Je remercie les différents membres du Centre Scientifique et Technique Jean Féger de Pau, pour l'environnement de travail et les échanges scientifiques que l'on a pu avoir, afin de mieux comprendre les besoins du projet et en adapter les outils développés. La majeure partie de la thèse a été menée au sein du laboratoire de mécanique des solides (LMS), et je remercie le directeur Pr. Patrick Le Tallec d'avoir su en faire un lieu chaleureux et propice au développement personnel et scientifique. Je remercie également les membres de l'administration du laboratoire, Alexandra, Anna, Christiane, Elizabeth et Mme Valérie Jamet pour la bonne humeur quotidienne et la réactivité avec laquelle elles ont répondu à tous mes besoins. Merci à Vincent, Alexandre, Simon, ainsi que toute l'équipe d'ingénieurs et techniciens pour leur grand apport technique lors de la préparations des tests expérimentaux et l'analyse des matériaux imprimés par microscopie optique et MEB. Plusieurs résultats n'auraient pas vu le jour sans leur aide.

Je remercie également tous les doctorants et post-doctorants que j'ai croisé durant mon stage

et doctorat au LMS. En particulier, je remercie Gabriella de m'avoir accompagné et soutenu dans ce projet de thèse et pour son étroite collaboration sur les matériaux imprimés. Merci à Matthias pour, entre autres, son aide afin faire fonctionner le cluster et y installer le code Janus. Merci à Camille pour sa bonne humeur et son volontarisme pour reprendre tous les postes vacants, jusqu'à assumer la relève comme capitaine de football. Merci à mon acolyte Yanis pour sa présence avec moi pendant les week-ends de travail, les ambitions partagées pour le monde du conseil, les craintes et les doutes qui nous font avancer et les tactiques de football pour limiter la casse. Merci à Pierre, Vincent, Gautier, Alexandre J., Audrey, Cheng, Grigor, Erwann, Laurant, Florent, Alexandre El., Anchal, Erato, Siva, Federica, Alexis, Jean-Pierre, Blandine, Arthur, Anthony, Thomas, Foucault, François, Jérémie, Nikolai, Nicolas H, Ludo, Clément, Lucas, Michele, Matteo, Filippo, Nicole, Chloé, Cécile, Marco, Nicolas D., Martin, Svetlana, Sofia, Louis, Charles, Alexandre B., Anthony, Kubra, Julius et tout ceux avec qui j'ai apprécié les pauses repas pour discuter de la société en long, en large et en travers, les sessions du journal club pour discuter des sujets de chacun et bien sûr ; les matchs de football pour se dépenser un peu.

Pour finir, je remercie chaleureusement mes proches pour leur soutien infaillible. Merci à mes amis Simon, Mélanie et Antoine T, aux amis d'enfance et leurs compagnes, Mohammed Amine A. et Samia, Mohammed Amine C. et Hajjar pour les soirées organisées et leur indulgence face aux absences répétées aux évènements importants. Merci à mon cousin El Ghali d'avoir été de bonne compagnie et d'une grande aide tout au long de la thèse sur le campus de l'X. Un grand merci à mes parents qui m'ont toujours soutenu et m'ont permis d'aller au bout de ce que j'ai entrepris. *And last but not least*, merci à ma tendre Claire, rien de cela n'aurait pu se réaliser sans sa patience, son soutien et son réconfort au quotidien face aux hauts et bas de mes études et de ce projet.

Abstract: A study on the effective elastic properties of random porous materials: 3D Printing, Experiments and Numerics.

This thesis deals with the 3D-printing, numerical simulation and experimental testing of porous materials with random isotropic microstructures. In particular, we attempt to assess by means of well-chosen examples the effect of partial statistical descriptors (i.e., porous volume fraction or porosity, two-point correlation functions and chord-length distribution) upon the linear effective elastic response of random porous materials and propose (nearly) optimal microstructures by direct comparison with available theoretical mathematical bounds. To achieve this, in the first part of this work, we design ab initio porous materials comprising single-size (i.e. monodisperse) and multiple-size (polydisperse) spherical and ellipsoidal non-overlapping voids. The microstructures are generated using a random sequential adsorption (RSA) algorithm that allows to reach very high porosities (e.g. greater than 80%). The created microstructures are then numerically simulated using finite element (FE) and Fast Fourier Tranform (FFT) methods to obtain representative isotropic volume elements in terms of both periodic and kinematic boundary conditions. This then allows for the 3D-printing of the porous microstructures in appropriately designed dog-bone specimens. An experimental setup for uniaxial tension loading conditions is then developed and the 3D-printed porous specimens are tested to retrieve their purely linear elastic properties. This process allows, for the first time experimentally, to show that such polydisperse (multiscale) microstructures can lead to nearly optimal effective elastic properties when compared with the theoretical Hashin-Shtrikman upper bounds for a very large range of porosities spanning values between 0-82%. To understand further the underlying mechanisms that lead to such a nearly optimal response, we assess the influence of several statistical descriptors (such as the one- and two-point correlation functions, the chord-length distribution function) of the microstructure upon the effective elastic properties of the porous material. We first investigate the ability of the two-point correlation function to predict accurately the effective response of random porous materials by choosing two different types of microstructures, which have exactly the same first (i.e., porosity) and second-order statistics. The first type consists of non-overlapping spherical and ellipsoidal pores generated by the RSA process. The second type, which uses the thresholded Gaussian Random Field (GRF) method, is directly reconstructed by matching the one- and two-point correlation functions from the corresponding RSA microstructure. The FFT-simulated effective elastic properties of these two microstructures reveal very significant differences that are in the order of 100% in the computed bulk and shear moduli. This analysis by example directly implies that the two-point statistics can be highly insufficient to predict the effective elastic properties of random porous materials. We rationalize further this observation by introducing controlled connectivity in the original non-overlapping RSA microstructures. The computed effective elastic properties of all three microstructures show that the pore connectivity does not change neither the two-point correlation functions nor the chord-length distribution but leads to a significant decrease in the effective elastic properties. In order to quantify further these differences, we analyze the link between a geometrical measure of the microstructure and the corresponding computed elastic fields by computing the first (average) and second moments of the elastic strain fluctuations. This last analysis suggests that

partial statistical information of the microstructure (without any input from the corresponding elasticity problem) might be highly insufficient even for the qualitative analysis of a porous material and by extension of any random composite material.

Keywords: Linear elasticity, Porous materials, Effective properties, 3D printed microstructures, Statistical modeling, Porous network.

Résumé: Étude des propriétés élastiques effectives de matériaux poreux à microstructure aléatoire: caractérisation numérique, expérimentale et impression 3D.

Le travail présenté dans cette thèse porte sur l'impression 3D, la caractérisation numérique et expérimentale des matériaux poreux à microstructure aléatoire. Plus spécifiquement, ce travail a pour objectif d'évaluer, à partir de modèles spécifiques de microstructures poreuses aléatoires, la pertinence de descripteurs statistiques tels que la fraction volumique des pores, la fonction de corrélation et la distribution de tailles de cordes sur la détermination des propriétés élastiques effectives. De plus, ce travail met en évidence des microstructures aléatoires poreuses isotropes dont les propriétés élastiques sont proches des résultats optimaux définis par les bornes supérieures de Hashin-Shtrikman. Pour cela, nous concevons dans la première partie de cette thèse des matériaux poreux aléatoires qui se composent de pores sphériques ou ellipsoïdaux ayant soit la même taille (monodisperse) soit plusieurs tailles différentes (polydisperse). Ces microstructures sont générées à partir d'un procédé d'ajout séquentiel et aléatoire, appelé RSA, et qui permet d'atteindre de large fractions volumiques (allant au-delà de 80%). Les propriétés élastiques effectives de ces microstructures virtuelles sont ensuite calculés par des simulations numériques par la méthode des éléments finis ou par des méthodes utilisant la transformée de Fourier rapide (dite FFT). Ces méthodes sont utilisées pour déterminer la taille du volume élémentaire représentatif (VER) pour des conditions aux limites périodiques et des conditions aux limites homogènes en déformations. Ce VER permet ainsi de fabriquer par impression 3D des échantillons standards de matériaux poreux qui sont ensuite testés expérimentalement afin d'obtenir leurs propriétés linéaires élastiques effectives. Les résultats de cette procédure mettent pour la première fois en évidence que ces microstructures isotropes aléatoires et polydisperses (multi-échelles) peuvent expérimentalement donner des propriétés élastiques effectives proches des bornes supérieures de Hashin-Shtrikman pour une gamme de porosité allant de 0 à 82%. Afin de mieux comprendre les paramètres morphologiques qui permettent d'atteindre ces propriétés optimales, nous évaluons dans la seconde partie de la thèse, l'influence de descripteurs statistiques de la microstructure tels que la fraction volumique de pores, la fonction de corrélation à deux points et la distribution de tailles de cordes sur la détermination des propriétés élastiques effectives des matériaux poreux. Pour cela, nous commençons tout d'abord par tester la pertinence des fonctions de corrélation à deux points en considérant deux modèles de microstructures poreuses qui ont la même porosité et la même fonction de corrélation. La première microstructure, générée par le code RSA, se compose de différentes tailles de pores sphériques ou ellipsoïdaux. La deuxième microstructure est, quant à elle, obtenue par seuillage d'un champ gaussien généré à partir de la fonctions de corrélation et la porosité mesurées sur la première. Les propriétés élastiques effectives obtenues par la méthode FFT pour ces deux types de microstructures montrent d'importantes différences qui peuvent atteindre des écarts de 100% pour les modules effectives de compressibilité et de cisaillement. Ces résultats montrent que la fonction de corrélation est insuffisante pour prédire les propriétés effectives de matériaux poreux aléatoires. Afin de mieux comprendre les paramètres qui peuvent expliquer les différences entre ces deux familles de microstructures, nous proposons d'évaluer l'influence de la connectivité

sur les propriétés élastiques en introduisant de la connectivité entre les pores ellipsoïdaux dans les microstructures générées par le RSA. Les propriétés effectives de ces microstructures montrent que la connectivité entre les pores ne génère des écarts significatifs ni entre les fonctions de corrélation ni entre les distributions de tailles de cordes des trois microstructures. Elle peut néanmoins engendrer d'importantes différences dans les modules élastiques des microstructures. Pour mieux quantifier les différences, une analyse du lien entre la géométrie locale dans l'espace poreux et les champs élastiques du matériaux est proposée en étudiant la moyenne et l'écart type des fluctuations de la composante hydrostatique et de cisaillement du champ de déformation. avec les modules de compressibilité effectifs obtenus. Compte tenu de cette analyse, il semble qu'une description statistique partielle de la microstructure sans information sur les champs élastiques locaux est insuffisante pour prédire les propriétés effectives d'un matériau poreux aléatoire, et plus généralement celles de tout matériau composite aléatoire.

Mots clés: Elasticité linéaire, Matériaux poreux aléatoires, propriétés effectives, Microstructures imprimées, Modélisation statistique, Réseaux poreux.

Contents

CHAPTER

INTRODUCTION

This thesis is concerned with the estimation of the effective linear elastic properties of random porous materials. Such materials are largely abundant in nature (e.g. geomaterials, wood or biological tissues) and in man-made engineering industry (e.g. metals, foams and architectured materials). Their effective physical properties depend not only on the properties of the solid phase material but also on the distribution of the porosity in the matrix phase (Dean and Lopez, 1983; Fryxell and Chandler, 1964; Phani and Niyogi, 1987; Chen et al., 2015). For that reason, they constitute a challenging subject both for oil and gas exploration interest as well as for new 3D printed materials. This thesis has two major parts which both relate to the question of whether there exist a simple enough geometrical description of the microstructure that enables to predict the effective elastic properties. In other words, the two parts of the thesis investigate simple statistical descriptors of the porous phase in order to assess if they have a significant influence on the elastic properties of material.

In the first part of this thesis, we investigate numerically and experimentally random porous microstructures with spherical voids in order to produce isotropic porous materials with high relative stiffness properties and low densities. To that aim, a methodology combining numerical computations, 3D photopolymer printing and an experimental testing procedure has been developped to enable a rigorous comparison between the elastic properties obtained from virtual microstructures and those actually achieved by the 3D printed materials. Section I.1 presents a brief state-of-the-art of the 3D printing of new materials in order to build high-stiffness low-density material and then details the scope and objectives of this first part.

In the second part of this thesis, we investigate the ability of low-order statistics and simple geometrical measures extracted from random porous microstructures to distinguish the elastic properties of the microstructures. The objective of this part is to find a reduced geometrical description of a porous material to model the elastic properties of multi-scale porous microstructures of carbonate rocks. We thus study the influence of the aspet ratio of pores, the two-point correlation, the connectivity in order to quantitatively assess the pertinence of these parameters in the prediction of the effective

elastic properties.

I.1 The quest for high-stiffness porous materials

One major interest for porous materials lies in the ability of architecturing their internal microstructures in order to generate new materials that can extend the range of functional properties achieved by their different constituents. For example, porous materials can be created to fill the gaps of the Ashby's material performance map shown in Fig.I.1 for high-stiffness and low density materials. In the literature, one can recognize two categories among porous materials; materials with closed-cell porosity, i.e. non-interconnecting voids, and open-cell porosity, which comprises most lattice and foam materials. In particular, this latter class of composites has been extensively studied in an effort to adapt the physical properties of their microstructure or micro-architecture (Fleck et al., 2010) by controlling morphological features of the internal geometry (Gibson and Ashby, 1997; Deshpande and Fleck, 2000). Such open-cell porous materials find applications in high-stiffness lightweight structures (Zok et al., 2004; Berger et al., 2017), acoustic and vibration dampers (Göransson, 2006; Banhart et al., 1996; Ma et al., 2013), impact energy absorbers (Davies and Zhen, 1983), high electric capacitors (Wang et al., 2008) and filtration (Alderson et al., 2000) and spans fields from electro-magnetism (Schurig, 2006)(Landy et al., 2008) and optics (Smith et al., 2004) to acoustics (Chen and Chan, 2007), mechanics (Lee et al., 2012), (Zadpoor, 2016) and, more recently, mechanobiology (Ahmadi et al., 2018).

Over the past two decades, porous materials were extensively produced using the replication processing (Conde et al., 2006), a method developed in the late 90s. In recent years, however, these materials have attracted far lesser attention than cellular solids with a periodic architecture (mainly lattices). The reason for this is two-fold. First, periodic cellular materials exhibit higher strength and stiffness than stochastic foams of the same density because of the higher strain-energy stored during deformation. The latter is governed by cell wall stretching rather than bending (Deshpande et al., 2001). Second, lattices are also naturally amenable to optimization and thus offer unparalleled flexibility in achieving topology-optimized architectures depending, for instance, on the design objective, constituent material and manufacturing method. Noteworthy is the octet truss lattice by Deshpande et al (Deshpande et al., 2001). By virtue of its ideal nearly linear scaling of mechanical properties with density, such cellular systems have paved the way to novel lattice architectures with maximized strength and stiffness per unit weight. Examples, shown in Fig.I.2, comprise the ultra-low density lattices of high-strength metals and ceramics, whereby the cells are composed of either hollow trusses (Bauer et al., 2014)(Meza et al., 2014)(Zheng et al., 2014)(Jang et al., 2013)(Schaedler et al., 2011), and continuous thin shells (Han et al., 2015) ("shellular") with dimensions extending from nanometers to microns. These systems, efficiently combine the structural advantages of their stretch-dominated cellular geometry with the strengthening size effects of their nano- or microscale features, and are today the lightest, stiffest and strongest metamaterials achieved.

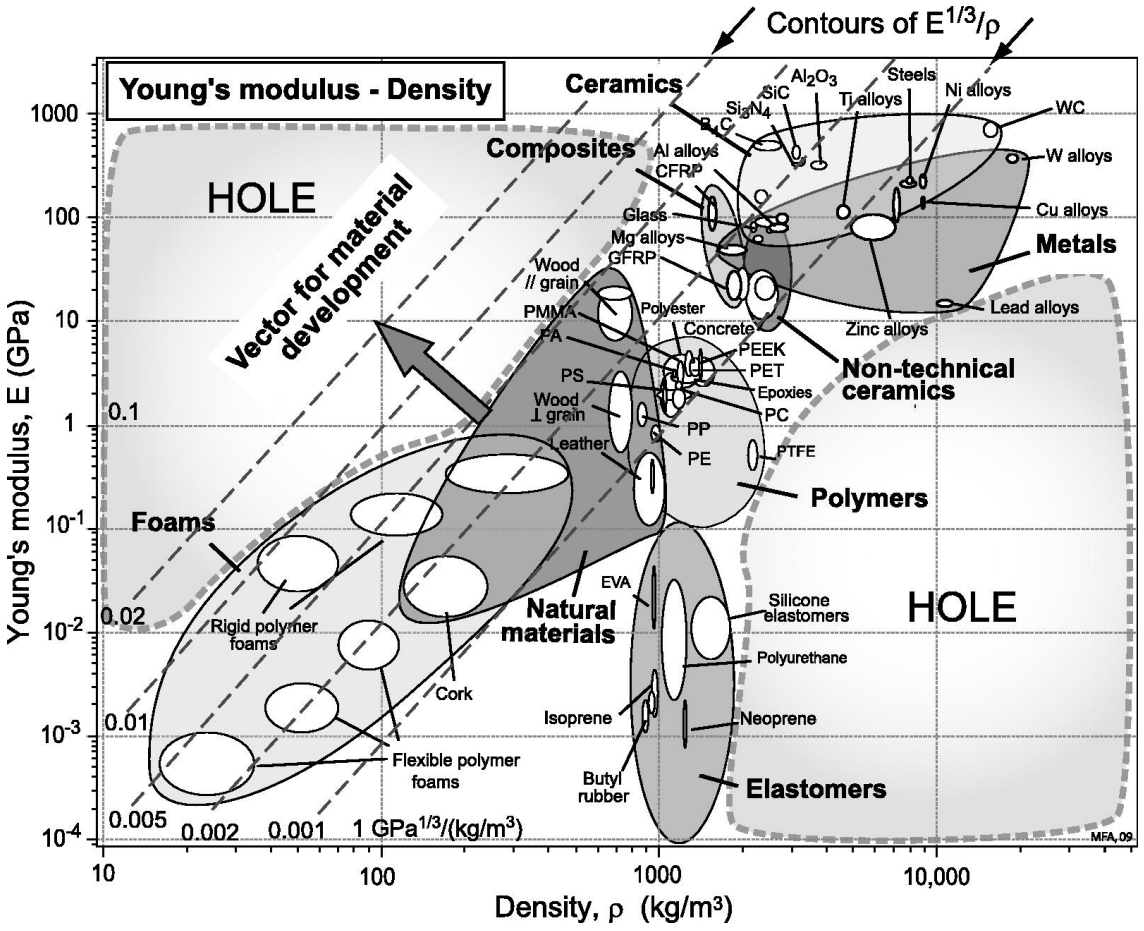

Figure I.1 – Ashby's material map for the Young's modulus-density space.(Ashby, 2013)

However, the poor scalability and highly anisotropic response largely limit the use of such cellular materials for macroscale engineering applications.

In contrast to conventional techniques, recent additive manufacturing (AM) technologies allow for the construction of microstructures layer-by-layer and thus, enable to incorporate complex architectures into a material system. Coupled with the robustness of modern computational methods, the various types of AM processes such as powder bed fusion (Heinl et al., 2007; Cansizoglu et al., 2008; Gorny et al., 2011), stereolithography (Hengsbach and Lantada, 2014), 3D laser lithography (Schaedler et al., 2011) and photon lithography Meza et al. (2014) have enabled extending the portfolio of materials now available to scientists and engineers to scales from nanometer to meter (Gosselin et al., 2016). The development of these new manufacturing processes has also led to the development of new methods for generating complex microstructures that can be 3D printed. One such popular approach is based on topology optimization methods among which is the ground approach (Bendsoe et al., 1994) that consists of finding the optimal structure using a discrete nodal description of the volume and minimizing a cost function of the boundary problem with a finite set of structural elements, usually taken as beams or voxels. Such materials are therefore optimal in

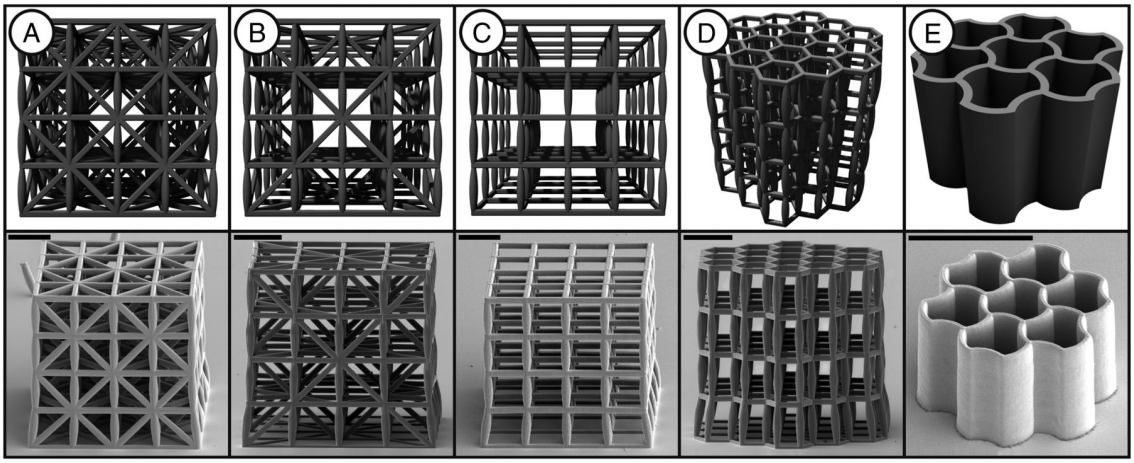

Figure I.2 – Examples of cellular microarchitectured systems fabricated using laser laser lithography.(Bauer et al., 2014)

a subset of microstructures resulting from that chosen element and the solution is dependent on the boundary conditions. Nevertheless, when using this methodology to create elastically-isotropic microstructures that can achieve extremal elastic properties and approach known bounds, for instance the Hashin-Shtrikman ones, such a task becomes less trivial. In particular, Sigmund (2000) has obtained such three-dimensional microstructures when assembling polyhedral regions connected by transversely isotropic three-rank laminates. The proposed microstructures, however, involve large scale variations and are therefore impossible to produce by current additive manufacturing techniques that only allow microstructures with similar length-scale orders.

Another approach, which is also popular in the literature, uses bio-inspired microstructures such as wood-inspired fiber-reinforced honeycombs (Compton and Lewis, 2014), the two-phase co-continuous solids that mimic biological exoskeletons and block copolymers (Wang et al., 2011) and lattice network topologies obtained by connecting closest neighbors of crystallographic-like structures such as the Face-Centered-Cubic (FCC) Berger et al. (2017). Such microstructures, similarly to other lattice microstructures, have been shown so far to deliver rather optimal mechanical properties in some specific directions but the anisotropic behavior related to their microstructural symmetries limits their engineering application to specific loading conditions(Dirrenberger et al., 2013). In an attempt to extend such microstructures to reach isotropic elastic behavior, Messner (2016), Meza et al. (2017) and Tancogne-Dejean and Mohr (2017) have recently designed nearly-isotropic elastic microstructures by imposing a group of constraints on lattice truss networks. The resulting lattices were shown to lead to a fixed overall Poisson's ratio and a fixed relative effective Young's Modulus for a given porosity which is found in many cases to be relatively far from the upper Hashin-Shtrikman bounds. Furthermore, the specific combination of the crystallographic-based microstructures proposed in order to fulfill the structural requirements have been numerically found by some of these authors to give an increasing deviation from the elastic-isotropy with increase of the relative density (i.e.

decrease of porosity).

An alternative approach, that is in the heart of the first part of this thesis, focuses on transferring theoretical and virtual microstructures that are very close to the Hashin-Shtrikman bounds numerically to fabrication and experimental testing. Contrary to the aforementioned lattice materials, most of the theoretical bounds account for closed-cell porous materials. Such work make use of minimization of energy principles which lead to rigorous theoretical bounds. Briefly, Hill (1952) derived the forst bounds based on Voigt (1889) and Reuss (1929) estimates that respectively consider the strain and stress constant in the material. By introducing a reference linear elastic homogeneous material and uniform stress polarization in the microscopic equilibrium equations of linear elasticity, Hashin and Shtrikman (1963a) and later Willis (1977) obtained rigorous bounds and estimates for the effective linear elastic behaviour for two- and N-phase isotropic and anisotropic materials, respectively. Such bounds are known to be optimal for isotropic two-phase microstructures as the effective bulk modulus is attained by the Hashin (1962) model of composite sphere assemblage (CSA) as shown Fig.I.3a). In turn, both effective shear and bulk moduli can be attained by the theoretical high-rank (6th rank) laminates (Francfort and Murat, 1986) and the dilated Poisson hyperplanes proposed by Jeulin (2001). As depicted by Fig.I.3, these microstructures lead to uniform elastic fields in each phase but inherently involves a large range (infinite in some cases) of length scales in order to attain statistical isotropy or to reach relatively high volume fraction. Motivated by these results, we propose in the first part to realize isotropic multi-scale closed-cell porous materials containing random distribution of non-overlapping spherical inclusions/voids (Lopez-Pamies et al., 2013a). The goal of the first part of this thesis is to introduce a methodology that allows to combine 3D printing, experimental testing, numerical and analytical modeling to create random closed-cell porous materials with statistically controlled and "isotropic" overall elastic properties that are extremely close to the Hashin-Shtrikman bounds. As a direct illustration of the framework, we examine the elastic response of porous-like solids consisting of non-overlapping, finite polydisperse (i.e. multiple size) spherical inclusions that are randomly dispersed into a homogeneous matrix. Those inclusions are made of a very soft support material, which has a Young's and bulk modulus that is one thousand times smaller than that of the matrix phase but of similar density. This result allows treating such materials as "porous-like" composites in terms of their quasi-static mechanical response given the very high inclusion/matrix contrast, but not as cellular solids in terms of relative density since the support material has (almost) the same density as that of the matrix. Henceforth, the term "porosity", denoted with c, refers to the volume fraction of the pore-like inclusions such that $1-c$ denotes the remaining volume fraction of the matrix phase (and not the relative density like for cellular solids and foams). More particularly, we exploit the polydispersity of the spherical voids to generate random porous architectures that provide an experimentally feasible approximation of the Hashin CSA model-microstructure (Hashin, 1962). This theoretical model is known to achieve the theoretical limit of isotropic elastic compressibility but inherently involves an "infinite" range of length scales, which makes the manufacturing of such composites practically impossible to achieve. To overcome this issue, we develop a numerical protocol that enables generating RVEs of multi-inclusion material

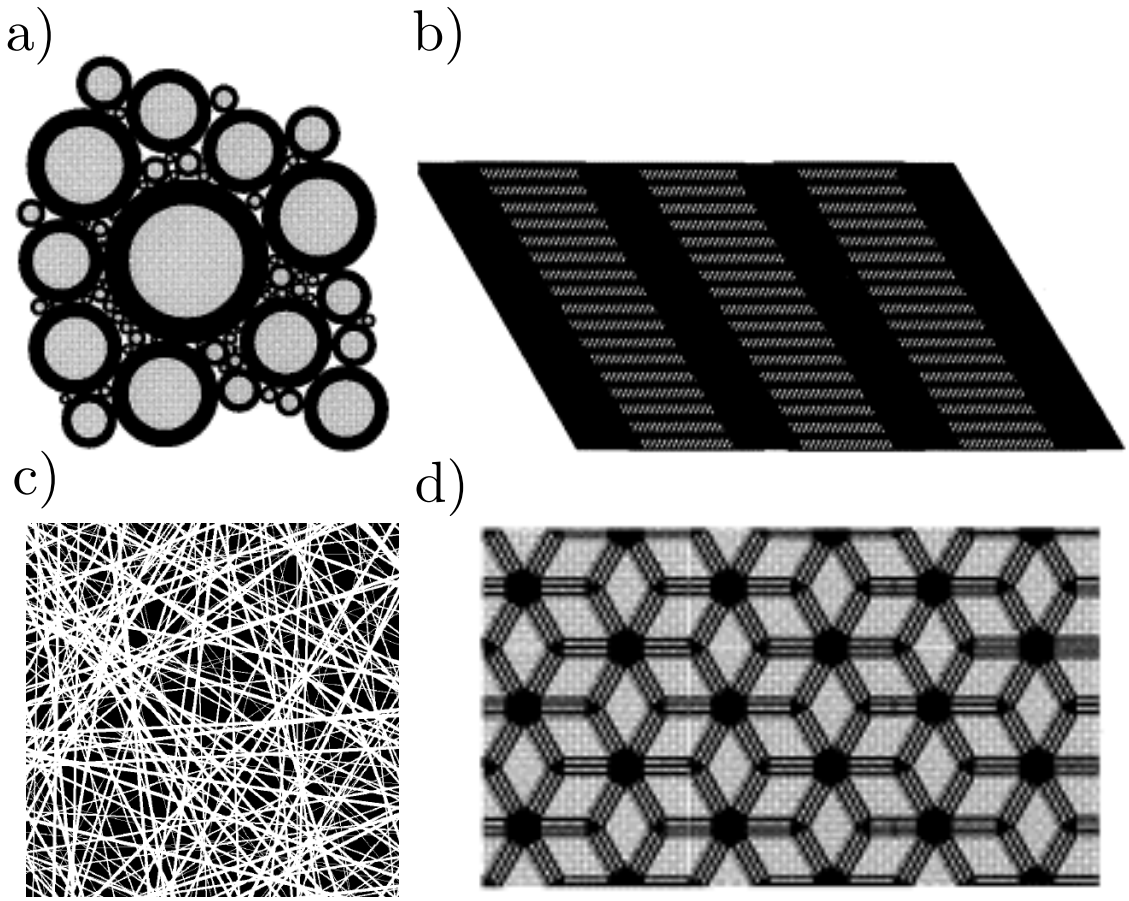

Figure I.3 – Illustrations of optimal microstructures for the effective elastic properties. (a) 2D slice of a coated sphere assemblage (Hashin, 1962) that reaches the effective bulk moduli for isotropic materials. (b) Illustration of a three-rank laminate (Francfort and Murat, 1986) which corresponds to the minimum number of scales needed to achieve isotropic extremal elastic properties in 2D. (c) 2D slice of a Poisson hyperplanes (Jeulin, 2001). (d) Example of an optimal 2D microstructure obtained by topological optimization design(Sigmund, 2000).

systems, whereby high volume fractions of spherical voided inclusions are obtained by employing inclusions with very different diameter. The virtual realizations of such heterogeneous materials are then transformed into physical microstructures via the use of a 3D polymer printer. Using relatively large computational resources, we are able to explore experimentally and numerically a very large range of porosities that spans values from $c = 0$ to 82%. In particular, we show that our 3D-printed random porous architectures are almost isotropic (both experimentally and numerically) and yield values of the effective elastic moduli that lie near the corresponding Hashin-Shtrikman upper bounds. Chapter II is devoted to the results obtained in the generation and fabrication of porous materials that are close to the optimal effective properties for isotropic microstructures using 3D printing polymeric technology and which have been published in two articles (Zerhouni et al., 2019; Tarantino et al., 2019). Firstly, Section II.1 describes the Random Sequential Adsorption (RSA) algorithm (Rintoul

and Torquato, 1997; Segurado and Llorca, 2002; Böhm et al., 2002; Lopez-Pamies et al., 2013a) used for generating virtual periodic microstructures. in Section II.2, we introduce the numerical homogenization approach used to determine a representative volume element (RVE) allowing for rigorous comparison between analytical, numerical and corresponding experimental results independently of the applied boundary conditions (i.e. periodic or affine etc). The second part of this chapter is devoted to the 3D printing process characterization and the framework to go from virtual to experimental materials. Section II.3 describes the process for assembling uniaxial tension specimens out of cubic porous RVEs and assesses the accuracy of printing with the aid of microscopy observations. Subsequently, an experimental setup is proposed to measure the linear elastic properties of the porous specimens by a multi-step relaxation procedure (Hossain et al., 2012). This procedure is used to examine the isotropy of the printing process for the pure matrix materials and analyze the measurement sensitivity and effect of the support material used during the 3D printing to obtain the spherical voids. Afterwards, in Section II.4, the effective experimental elastic properties of the porous materials are shown and probed by finite element (FE) numerical estimates and the analytical Hashin-Shtrikman bounds. A contour analysis of the local stress and strain fields is used to interpret the influence of the microstructural features on the effective elastic properties. One of the important outcomes of this study is that the 3D printed porous material specimens are found to be very close to the theoretical Hashin-Shtrikman upper bounds.

I.2 The porous structure of sedimentary rocks

The second part of this projet was devoted to understanding the influence of stastitical descriptors of the porous space description on the effective elastic properties of porous materials in the perspective of application on carbonate rocks which represent a large potential reservoirs for off-shore oil and gas production. Such sedimentary rocks are formed by successive deposits combined with diagenetic phenomena and fracture processing wich confere to the rock a complex and heterogeneous spatial distribution of porosity that spreads over multiple scales as depicted by Figure I.4. This multiscale porosity is composed of pores of different shapes and sizes and is difficult to capture with imaging techniques due to the limitations in sample scales that can be observed. Another difficulty related to the heterogeneous porous phase of such rocks lies in the fact that laboratory analysis of real materials, such as core flooding, porosimetry measurement and experimental testing, involves destructive testing which prevents from re-using rom the same sample for multiple characterization and induces an important cost. In turn, numerical simulations offers a faster and non-destructive way to compute the elastic properties of the material using direct computational methods on 2D or 3D images (Garboczi and Day, 1995; Moulinec and Suquet, 1998). However, the accurate characterization depends on the careful selection of the representative volume to overcome boundary conditions dependency and the comparison between the experimental and computational effective properties is usually limited by the resolution of the imaged sample in comparison with the scale of the experimentally tested specimen.

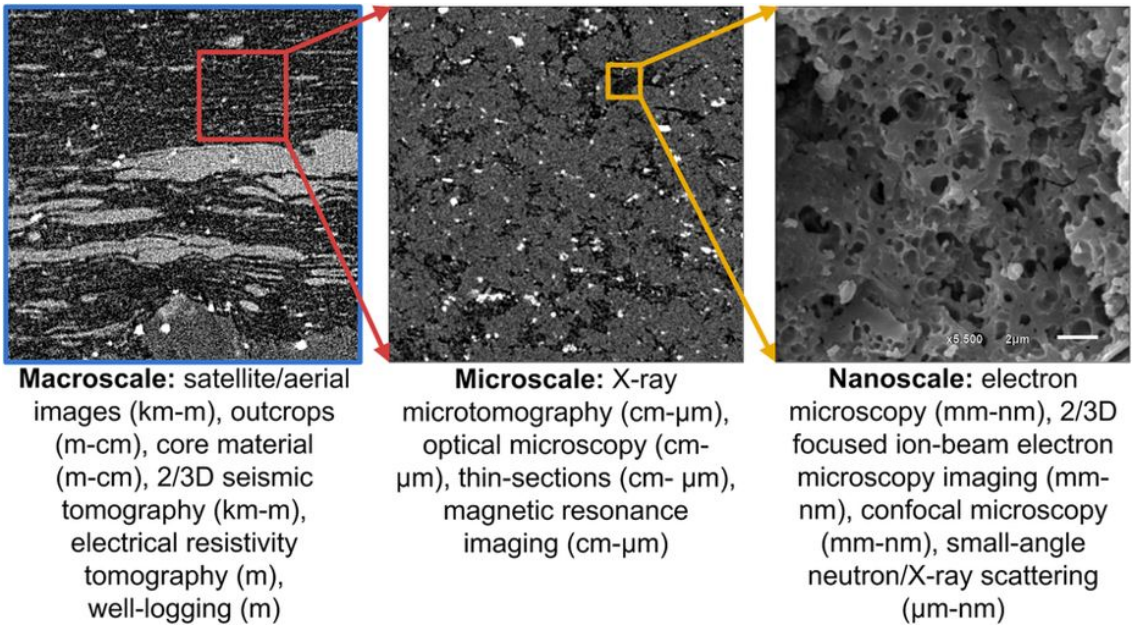

Figure I.4 – Three images of shale structure representing macro, micro and nanoscale (from left to right). Below each image are reported some common methods to obtain spatial information at each scale. The typical size of sample and resolution for each method are given in parentheses.(Gerke et al., 2015)

In this context, developping upscaling models with high predictive capacity for the effective properties of the microstructure is an important challenge which relies on both qualitative and quantitative understanding of how the pore characteristics such as pore shape, size and connectivity impacts the elastic properties of the rock is crucial for improving reservoir predictions. To that aim, a classical approach relies on the assumption that scales are well separated in order to use homogenization theory to construct (semi-)analytical models. Another popular approach have focussed on studying particular morphologies and developping models based on numerical or experimental available data (Gibson and Ashby, 1988; Roberts and Garboczi, 2001). Boosted by the recent advances in additive manufacturing technology, a similar approach consists in conducting a parametric study of the morphological features of the porous space in order to link the properties to the microstructure. Such process has been used to derive the influence of the processes in sedimentary rock on their experimental properties (Ishutov et al., 2017; Head and Vanorio, 2016). Their approach is based on image manipulation of the porous network of real rocks in order to highlight the microstructure resulting from a specific process such as compaction or dissolution. The resulting images are then printed and tested in order to compare between experiments on printed samples and numerical simulations on images. The preliminary results show good quantitative agreement for permeability related to the calculated porosity which shows the potential of additive manufacturing in developping methods to characterize the porous network influence on rock's properties and compare the experimental tests and the numerical simulation with the same samples. Another potential use of 3D printing consists of manufacturing the mathematical models of fractured rocks and porous

network in order to validate the theoretical studies and the numerical methods (Suzuki et al., 2014). By controlling the fracture and pore geometry in the mathematical models which is subsequently transferred into the experimental samples by 3D printing, this approach provide quantitative results of the influence of several aspects of the geometry such as the aperture of the interconnected porosity and the size of fractures on the flow properties. This approach enables to validate hypothesis for theoretical models and to build heuristic models for more complex microstructural parameters.

In this second part of the presented work, we propose a parametric study of the influence of pore characteristics such as shape, size and connectivity on the effective elastic properties by gradually complexifying the description of the porous space using measurable statistical and microstructural descriptors. The objective is to quantitatively measure the errors related to the statistical description of the material and investigate the question about which morphological parameters are sufficient to discriminate porous microstructures in term of their effective properties. To that aim, we first study the influence of second-order random field models by reconstructing level-cut Gaussian Random Fields from the correlation function of RSA microstructures consisting of different sizes of isolated ellipsoidal inclusions randomly distributed in the material at different volume fractions c and for different aspect ratios of ellipsoids ω. The second-order statistical reconstruction is a very popular approach for predictive modeling of heterogeneous materials and has been extensively developped and analyzed in the study of effective transport properties of materials (Teubner, 1991; Roberts and Teubner, 1995; Levitz, 1998; Roberts, 1997; Roberts and Garboczi, 2001; Øren and Bakke, 2002; Roubin et al., 2015). However, studies of the uncertainties related to predicting the effective elastic properties using the second-order models are missing. The results of this work, which will be further detailed in the Sec.III.3, highlight the significant influence of the shape of pores on the elastic properties and the lack of information about the connectivity and the pore shape of the GRF models which leads to high differences in the effective properties of materials. Subsequently, in order to study and analyze the effect of connectivity on microstructure properties, we generate porous network models by connecting the inclusions in the RSA microstructures using cylindrical channel of different radiuses and compute their effective properties for two ranges of porosities $c = 15\%$ and 25%. Such connected porous microstructures are popular in the study of the influence of the porous phase on the permeability of rocks. The parameters defining the pore geometry can be directly extracted from the image analysis of the porous space. The connected porous microstructures constitute a third microstructure type along with the isolated inclusions microstructure (RSA microstructures) and the thresholded GRF microstructures. The elastic properties of these three microstructures are compared for similar volume fraction $c = 15\%$ and $c = 25\%$ and analysis of the two-point correlation functions and the chord-length distributions is proposed for interpreting the differences. The results show that the differences in the effective elastic properties are unrelated to the similarities in neither the chord-distribution nor the correlation function. In order to analyze the influence of the local geometry of the porous space on the local elastic field, we link the Euclidean distance transform of the microstructure to the fluctuations of the hydrostatic and shear components of the strain field

measured at a given distance. The results presented in Sec.IV.2.3 show good qualitative agreement between the two measures.
The two parts of this work provide complementary approaches to the understanding of the porous space influence on the effective properties of porous materials and how to trigger the characteristic parameters of the pore space in order to create new light materials with controlled effective properties.

List of publications resulting from this thesis

- Zerhouni, O., Tarantino, M. G., Danas, K. (2019). Numerically-aided 3D printed random isotropic porous materials approaching the Hashin-Shtrikman bounds. Composites Part B: Engineering, 156, 344–354. https://doi.org/10.1016/j.compositesb.2018.08.032
- Zerhouni, O., Tarantino, M. G., Danas, K., Hong, F. (2019). Influence of the internal geometry on the elastic properties of materials using 3D-printing of computer-generated random microstructures. In 2018 SEG International Exposition and Annual Meeting, SEG 2018 (pp. 3713–3718). Society of Exploration Geophysicists.
- Tarantino, M. G., Zerhouni, O., Danas, K. (2019). Random 3D-printed isotropic composites with high volume fraction of pore-like polydisperse inclusions and near-optimal elastic stiffness. Acta Materialia, 175, 331–340. https://doi.org/10.1016/j.actamat.2019.06.020
- Hong, F., Bastide, F., Zerhouni, O., Planteblat, C. (2019). Factors influencing elastic properties on carbonate rocks, lessons learnt from two case studies and from simulation results. In International Petroleum Technology Conference 2019, IPTC 2019. International Petroleum Technology Conference (IPTC).
- Zerhouni, O., Brisard, S., Danas, K. (2020). Critical assessment of the influence of second-order statistics of the random porous microstructures on their effective elastic properties. (In preparation)

CHAPTER II

3D PRINTED MICROSTRUCTURES WITH NEARLY OPTIMAL EFFECTIVE ELASTIC PROPERTIES

Summary of this chapter: In this chapter, we introduce a methodology that allows to combine 3D printing, experimental testing, numerical and analytical modeling to create random closed-cell porous materials with statistically controlled and 'isotropic' effective elastic properties that lie near the optimal Hashin-Shtrikman bounds. In the first section II.1, we present the two procedures of the Random Sequential Adsorption (RSA) algorithm used to generate periodic microstructure consisting of isolated inclusions of ellipsoidal shape and randomly distributed in the unit cell. The first procedure was proposed by Anoukou et al. (2018) and consists of full input of the morphological descriptors of the different ellipsoidal inclusions inside the microstructure. The second procedure has been developped for this thesis in order to reach high volume fraction of pores with a minimum input parameters. Subsequently, Section II.2 presents the numerical procedure used in order to determine the Representative Volume Element that is suitable for the comparison between numerical and experimental characterization of porous microstructures. In Section II.3, we combines the results of the RVE determination with the 3D printer characterization in order to propose an experimental procedure to obtain the macroscopic elastic properties of the 3D printed samples. The 3D printing procedure of virtually generated materials. The last section II.4 presents the effective experimental elastic properties of the porous materials along with the finite elament (FE) numerical estimates and the analytical bounds. Contour plots of the local stress and strain fields obtained by the numerical computation are used to interpret the results and discuss the influence of some microstructural features on the effective elastic properties. The details of the 3D printing characterization and application of the methodology to monodisperse spherical inclusions at low volume fractions has been published in Zerhouni et al. (2019). The extension of this methodology to polydisperse in size spherical pores and high volume fractions using the modified RSA algorithm has been published in Tarantino et al. (2019).

II.1 Randomly distributed non-overlapping ellipsoidal inclusions

This section details the important parts that build the code used for the generation of isolated pores inside a homogeneous matrix. The random heterogeneous materials generated in this part are based on the random sequential addition (or adsorption) (RSA) process of ellipsoidal inclusions (Rintoul and Torquato, 1997). It consists in placing randomly, irreversibly, and sequentially non-overlapping objects into a volume (or onto a surface). In the recent investigations, for instance the works of (Segurado and Llorca, 2002), (Fritzen et al., 2012), (Lopez-Pamies et al., 2013a), the RSA algorithm is clearly explained and used in the context of linear and non-linear computational homogenization of composites or porous materials containing spherical shaped inclusions or voids. Two types of geometric constraints are generally imposed:

- The non-overlapping condition which specified that the distance between each pair of objects (center-to-center distance) has to exceed a minimum value noted s_1.
- The distance between the spherical object and the surfaces of the cuboidal cell must take a minimum value s_2.

Assuming periodicity of the spherical object distribution, the first condition has to be checked also between the object to be added and the periodic images of any previously accepted object which cuts any of the cuboidal cell surfaces. For more details on these geometric constraints, the reader is referred to the paper of (Segurado and Llorca, 2002).
In the recent work of Anoukou et al. (2018), the RSA algorithm has been used to generate non-overlapping randomly oriented or aligned inclusions of ellipsoidal shape uniformly distributed in the unit cell. The sequential addition of the spherical objects is constrained by some geometric conditions for adequate finite element discretization.. In this general case, the distance between non-spherical objects is more complicated to determine than using the center-to-center distance between the two objects. In the work of Pierard et al. (2007) on elasto-plastic composite materials reinforced with aligned (unidirectional orientation) elastic ellipsoidal inclusions, an algorithm proposed by (Lin and Han, 2002) is used to determined iteratively the minimum distance between two ellipsoids with a slight modified version of the iterative process for finding the minimum distance between two ellipsoids.
In this first part of the thesis, the main contribution related to the RSA algorithm corresponds to the proposed automatic generation of polydisperse in size ellipsoidal pores in order to achieve large volume fractions with non-overlapping ellipsoidal inclusions. This new algorithm is based on the minimum distance between two randomly oriented ellipsoids and the minimum distance between an ellipsoid and the boundary surface of the cubic unit cell developed in the work of Anoukou et al. (2018) which are detailed in the Appendix II.B. Section II.1.1 introduces the descriptors of the isolated pore microstructures generated with RSA algorithms. Subsequently, section II.1.2 details the two procedures for the generation of RSA microstructures; either the full input of morphological descriptiors of the different families of inclusions where the definition of a family of inclusions presented in the work of Anoukou et al. (2018) or th automatic generation of polydisperse in size

inclusions to reach high porosities with a small number of descriptors.

II.1.1 The Random Sequential Adsorption (RSA) method

II.1.1.a Characteristics of an ellipsoidal inclusion

An arbitrary oriented ellipsoid $\mathcal{E}_i(\mathbf{v}_i, \mathbb{Z}_i)$ is defined by all space points $\mathbf{x}$ solution of the quadric equation:

$$Q_i(\mathbf{x}) = \big(\mathbf{x} - \mathbf{v}_i\big)^T \mathbb{Z}_i \big(\mathbf{x} - \mathbf{v}_i\big) - 1 \leq 0 \tag{1}$$

where $\mathbf{v}_i$ denotes the center position of the ellipsoid and $\mathbb{Z}_i$ is the characteristic matrix of the ellipsoid expressed as :

$$\mathbb{Z}_i = \frac{1}{a_{i,3}^2}\big(\omega_{i,1}^2 \mathbf{n}_{i,1} \otimes \mathbf{n}_{i,1} + \omega_{i,2}^2 \mathbf{n}_{i,2} \otimes \mathbf{n}_{i,2} + \mathbf{n}_{i,3} \otimes \mathbf{n}_{i,3}\big) \tag{2}$$

where $\mathbf{n}_{i,1}, \mathbf{n}_{i,2}, \mathbf{n}_{i,3}$ are the principal vectors of the $\mathbb{Z}_i$ matrix related to the orientation of the ellipsoid which can be expressed using Euler angles ϕ, θ and ψ such that:

$$\mathbf{n}_{i,1} = \mathbb{R}_i \mathbf{e}_1 \quad , \quad \mathbf{n}_{i,2} = \mathbb{R}_i \mathbf{e}_2 \quad , \quad \mathbf{n}_{i,3} = \mathbb{R}_i \mathbf{e}_3 \tag{3}$$

with

$$\mathbb{R} = \begin{pmatrix} \cos(\phi)\cos(\psi) - \cos(\theta)\sin(\phi)\sin(\phi) & -\cos(\psi)\sin(\phi) - \cos(\phi)\cos(\theta)\sin(\psi) & \sin(\theta)\sin(\psi) \\ \cos(\theta)\cos(\psi)\sin(\phi) + \cos(\phi)\sin(\psi) & \cos(\phi)\cos(\theta)\cos(\psi) - \sin(\phi)\sin(\psi) & -\cos(\psi)\sin(\theta) \\ \sin(\phi)\sin(\theta) & \cos(\phi)\sin(\theta) & \cos(\theta) \end{pmatrix} \tag{4}$$

In order to build randomly oriented ellipsoid, the Euler angles have to be build such that ϕ and ψ are generated randomly $[-\pi, \pi]$ while the angle θ is generated by randomly picking $\cos(\theta) \in [-1, 1]$ and then setting $\theta = \cos^{-1}(\cos(\theta))$.

II.1.1.b The morphological descriptors of the microstructure

An RVE microstructure generated by the RSA algorithm consists of a cubic cell of size L made of n families of ellipsoidal pores each occupying a volume fraction c_i, $i = 1, ..., N$ embedded in a homogeneous matrix phase. In the case of a monodisperse microstructure (size, shape and eventually orientation), $n = 1$ and the RVE is composed of two phases. For the case of polydipserse microstructures, phases refer to sub-domains in the RVE which are different in size and/or shape and even in orientation and distribution.

In addition to the previous definition of polydispersion, particulate microstructures can be polydisperse regarding to the physical properties of phases. Simply says, in general, a phase is defined as a family of pores or particles that have the same size, shape, orientation and physical properties.

There are many possible ways for the creation of polydisperse microstructures. The following procedure is adopted:

- Creation of a fictitious reference microstructure of the RVE containing N_p^{ref} monodisperse (N=1) ellipsoids inclusions with volume fraction $c^{ref} = c$, where c is the total volume fraction of inclusions and N_p^{ref} is a characteristic number related to the characteristic size a_3^{ref} (Lopez-Pamies et al., 2013a) by:

$$a_3^{ref} = \left(\frac{3c\omega_1^{ref}\omega_2^{ref}}{4\pi N_p^{ref}}\right)\frac{1}{3} \tag{5}$$

For the construction of the polydisperse microstructure, morphological information such as size and shape of inclusion in each phase are calculated using the fictitious RVE microstructure. More precisely, the characteristic length $a_{r,3}$ of the r family of inclusions is proportional to the characteristic length a_3^{ref} following a size coefficient defined by the input of size distribution S_{size} such that:

$$S_{size} = \left\{\chi_1, \chi_2, ..., \chi_n\right\} \tag{6}$$

with $a_{r,3} = \chi_r a_3^{ref}$ with $r = 1..n$
and the other semi-axis lengths $a_{r,1}, a_{r,2}$ are retrieved from the set of aspect ratios S_{shape}, representing the shape of the polydisperse families of inclusions defined as:

$$S_{shape} = \left(\omega_{1,1}, \omega_{1,2}, \omega_{2,1}, \omega_{2,2}, ..., \omega_{n,1}, \omega_{n,2}\right) \tag{7}$$

such that $\omega_{r,1} = \dfrac{a_{r,3}}{a_{r,1}}, \omega_{r,2} = \dfrac{a_{r,3}}{a_{r,2}}$ for $r = 1..n$
In turn, the volume fraction c_r of each phase r is given by the set S_c which is expressed by the set of contributions δ_r to the total volume fraction c:

$$S_c = \delta_1, \delta_2, ..., \delta_n \tag{8}$$

such that $c_r = \delta_r c$ for $r = 1..n$ and $\sum_{r=1}^{n} \delta_r = 1$.
Thus, the general RSA algorithm in this study takes as input:

- The number N_p^{ref} of monodipserse pores (or particles) in the fictitious reference cuboidal cell.
- The total volume fraction c
- The number n of families of inclusions.
- The sets of microstructural descriptors S_{size}, S_{shape}, S_c
- Two offset parameter tol_1, tol_2 for the determination of distances s_1 and s_2.

It is worth mentionning that for the implementation of the iterative generation process, the microstructural descriptors have been sorted in a decreasing order of the characteristic size $a_{r,3}$ of the phases. Thus, the generation of inclusions inside the cubic cell is chosen to start from the pores with the biggest $a_{r,3}$ and regardless of the shape of inclusions.

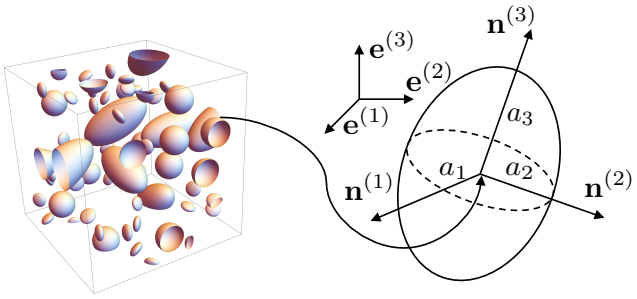

Figure II.1 – representation of an RSA unit-cell with the characteristic elements of an arbitrarly oriented ellipsoidal inclusion.

II.1.2 The RSA algorithm

II.1.2.a Controlled morphological descriptors

Accounting for the full description of the families of inclusions such that it is given in Sec.II.1.1.b, the RSA algorithm outcome consists of the centers of the different ellipsoids $\mathbf{v}_i$ and their characteristic parameters, namely the orientation parameters consisting of the Euler angles $(\phi_i, \theta_i, \psi_i)$ and the size and shape characteristics represented that the semi-axes lengths $(a_{i,1}, a_{i,2}, a_{i,3})$. The iterative RSA algorithm stores the current value of the total volume fraction in a variable called the apparent volume fraction c^t which is initiated to 0 and the addition process of inclusion can be decomposed to the following steps:

- **step 1:** Generate the center position $\mathbf{v}_i = (x_i, y_i, z_i) \in [0, L]^3$ of the i^{th} ellipsoid and its orientation by generating of randomly oriented ellipsoids using its Euler angles ϕ_i, θ_i, ψ_i following the procedure explained in the introduction to Sec.II.B.
- **step 2:** Check for which family of inclusions the ellipsoid is to be added following the total volume fraction c^t generated at that stage. For example, if $c_{r-1} \leq c^t < c_r$ for $r \in \{1, ..., n\}$ then the characteristic semi-lengths $a_{i,1}, a_{i,2}, a_{i,3}$ of the ellipsoid are computed in order to match the input parameter of the phase r given in Sec.II.1.1.b.
- **step 3:** Compute the minimum distance Δ_1 between the current inclusion i and any previously accepted inclusion $j = 1, ..., i-1$ and its 26 periodic images defined by the translation of the center $\mathbf{v}_j$ by a vector $\mathbf{h} = \big(h_1, h_2, h_3\big)$ with $h_1, h_2, h_3 \in \{0, -L_i, L_i\}$. The process for determination of the minimum distance between two randomly oriented ellipsoids is described in Sec.II.B.1 following the published work by (Anoukou et al., 2018). This distance is compared to the minimum value s_1 defined according to the input parameter tol_1 such that :

$$s_1 = \Big(\max(a_{i,1} + a_{i,2} + a_{i,3}) + \max(a_{j,1} + a_{j,2} + a_{j,3})\Big) tol_1 \tag{9}$$

  If $\Delta_1 < s_1$ for any of the $j, \mathbf{h}$ configurations, the process is reset to **step 1**. Otherwise, the process continue to **step 4**.
- **step 4:** Compute the minimum distance Δ_2 between the ellipsoid i and the six boundary planes of the cubic cell implemented following the results in Sec.II.B.2. In turn, this distance is

subjected to a comparison with the minimum value s_2 defined according to the input parameter tol_2 such that:

$$s_1 = \Big(\max(a_{i,1} + a_{i,2} + a_{i,3})\Big) tol_2 \tag{10}$$

Similarly to **step 3**, the current inclusion i passes this step if the distance $\Delta_2 < s_2$, otherwise the generation is reset to **step 1**.

- **step 5:** Once the inclusion verifies the minimum distance requirements, it is irreversibly added to the list of all accepted inclusions by storing its microstructural information as well as those of its 26 periodic images. The current volume fraction c is then incremented by the volume of the new inclusion such that:

$$c = c + \frac{4\pi a_{i,1} a_{i,2} a_{i,3}}{3L^3} \tag{11}$$

This implemented volume fraction represents the exact value of the current volume fraction of inclusion in the cell because the different subsets of the ellipsoid i that lie outside the volume V are included through the periodic images of the ellipsoid.

II.1.2.b Extension of the RSA algorithm to automatic polydispersion in size

The procedure defined in the previous section II.1.2.a offers the advantage to have full control over the morphology of the different phases and to mixing ellipsoidal inclusions with different aspect ratios. However, a heterogeneous microstructure with volume fraction c consisting of isolated ellipsoidal inclusions, of the same aspect ratios ω_1 and ω_2, can be defined in different ways by triggering the distribution of sizes and partition of volume fraction. Such versatility comes with the cost over simplistic description when a relatively high volume fraction of inclusions is targeted. Finding the suitable set of parameters as defined in Sec.II.1.1.b to create the microstructure with the desired c can be a long and difficult task to handle manually.

In order to ensure the achievement of a large range of volume fractions with a minimum of descriptors of each family of inclusions in the RSA generated microstructure, the algorithm shown in Sec.II.1.2.a has been modified for the specific case of microstructures with polydispersed-in-size inclusions having the same aspect ratios. This extension was also made to create a standard and uniform workflow for the study of 3D printed RSA generated microstructures indistinctively of the dispersion in size of isolated inclusions embedded inside the volume.

In the modified algorithm, the morphological descriptors consist of:

- The total volume fraction targeted c,
- The biggest characteristic size a_3^{max} among the families of inclusions.
- The aspect ratios $\omega_1 = a_3^{max}/a_1^{max}$ and $\omega_2 = a_3^{max}/a_2^{max}$ that is applied to all generated inclusions.
- The minimum distance criterion s_1 replacing the parameters tol_1 and tol_2 concerning the distance between two ellipsoids and the distance between an ellipsoid and a boundary surface of the microstructure.

- The minimum size criterion D_{lim} which is a stopping criterion for the generation of the process.

Before describing the generation procedure in the modified RSA algorithm, some remarks worth to be emphasized concerning the morphological parameter of control. Firstly, using a_3^{max} as a direct input parameter together with c requires that $a_3^{max} \leq a_{lim}$ such that the microstructures can contain at least one inclusion such that :

$$a_{lim} = \left(\frac{3\omega_1\omega_2}{4\pi c} \right)^{\frac{1}{3}} \tag{12}$$

Thus, the algorithm starts by checking the following condition before any generation and set the value of $a_3^{max} = a_{lim}$ otherwise. Secondly, the minimum size criterion D_{lim}, which has been based on fabrication limitations, forces the algorithm to stop the generation once the characteristic semi-axis lengths of the generated inclusion i verify that $\min(a_{i,3},a_{i,2},a_{i,1}) \leq D_{lim}$. In that case, the c may not be reached and the algorithm returns the periodic microstructure composed by the previously accepted inclusions and the corresponding volume fraction. However, since this parameter is put as a microstructural descriptors, it is possible to leave as null and thus allowing the generation of very small inclusions and large size ratios to the cost of long time of generation.
Taking into account these latter remarks, the modified RSA process starts by setting morphological parameters of the current inclusion with characteristic semi-lengths $a_3^{max}, a_2^{max} = \omega_2/a_3^{max}$ and $a_1^{max} = \omega_1/a_3^{max}$ and the apparent volume fraction is initiated to $c = 0$. The iterative procedure of generation of the inclusions can be described by four main step including an iteration tracker that is initiated to 0:

- **Step 1:** The algorithm generates the center position $\mathbf{v}_i = (x_i, y_i, z_i) \in [0, L]^3$ of the i^{th} ellipsoid and its Euler angles ϕ_i, θ_i, ψ_i following the same procedure described in SecII.1.2.a.
- **Step2:** Compute the minimum distance Δ_1 between the current inclusion i and any previously accepted inclusion $j = 1, ..., i-1$ and its 26 periodic images. This distance is compared to the global parameter s_1 which can be seen as the minimum thickness of a ligament of the matrix phase that is accepted. We highlight again that this change in the definition of s_1 make a switch in the strategy of the RSA algorithm by creating process based criterion instead of an easy-mesh criterion related to FE computations. If $\Delta_1 < s_1$ for any of the 27 configurations, the process is reset to **step 1**. Otherwise, the process continue to **step 3**.
- **Step3:** Compute the minimum distance Δ_2 between the ellipsoid i and the six boundary planes of the cubic cell implemented following the procedure in Sec.II.B.2 and add the inclusion i and its periodic images to the set of generated inclusions if the distance verifies $\Delta_2 \leq s_1$. The tracker of iterations is thus reset to 0 and the current volume fraction is then incremented by the volume of the new inclusion and such that:

  $$c^t = c^{t-1} + \frac{4\pi a_{i,1}a_{i,2}a_{i,3}}{3L^3} \tag{13}$$

  Otherwise the generation is reset to **step 1** and the iteration tracker is incremented by 1.

- **step 4:** Unless the iteration tracker reaches the cut-off value of iterations, the algorithm keep generating inclusions with the same morphological descriptors. In the current work, this cut-off value is set to 3000 consecutive rejected center positions to fastly reach an end of the process. Once the 3000 successive rejections are reached, the algorithm automatically reduces the characteristic sizes of the new generated inclusion $a_{i,3}$ by 1% such that:

$$a_{i,3} = 0.99 a_{i-1,3} \quad , \quad a_{i,1} = \frac{a_{i,3}}{\omega_1} \quad , \quad a_{i,2} = \frac{a_{i,3}}{\omega_2} \quad (\textbf{for } i \geq 1, a_{0,3} = a_3^{max}) \tag{14}$$

This procedure continues until the desired porosity c or the minimum size D_{lim} criterion is reached. The algorithm returns the previously accepted inclusions and their periodic images in a microstructure with total volume fraction $c = c^t$.
Using these two procedures, the following section details the parameters used to generate porous microstructures used in the 3D printing process.

II.1.3 Fabrication of the 3D printed microstructures

II.1.3.a Monodisperse RSA microstructures for moderate porosities

For relatively low volume fraction ($c \leq 30\%$), microstructures consisting of a randomly distributed spherical inclusions were constructed using the RSA algorithm in Sec.II.1.2.a. The porous phase is filled with single sized inclusions of diameter D and offset parameters for minimum distances criterions set to $tol_1 = 0.02$ and $tol_2 = 0.05$ in order to obtain easy-to-mesh realizations. Figure II.2 shows three such RVEs comprising monodisperse spherical voids of increasing porosity $c = \{10\%, 20\%, 30\%\}$ with the number of pores N used for their generation.

II.1.3.b Polydisperse RSA microstructures for moderate to very high porosities

For volume fraction $c > 30\%$ the virtual realizations of the porous microstructures are obtained using the modified random sequential addition (RSA) procedure and thus contain a finite number of polydisperse spherical voids. The generated cubic unit cells are periodic, and contain a finite number of families of identical spheres (here pores) randomly dispersed in the cell volume. In Fig. II.3, a few representative RSA-generated cubic cells containing a volume fraction of spherical pores are shown for illustration. it can be observed that for relatively low and moderate volume fractions, the generated microstructures contain pores of very similar size while the range of pore sizes in relatively high porous microstructures extends significantly and can reach more than 45:1 as discussed later. The fact that microstructures generated by the automatic procedure (see section II.1.2.b) for porosities below 30% gives a monodisperse in size microstructure, the polydispersed microstructure obtained for higher volume fraction can be seen as a possible extension to the monodisperse microstructures in the previous section.

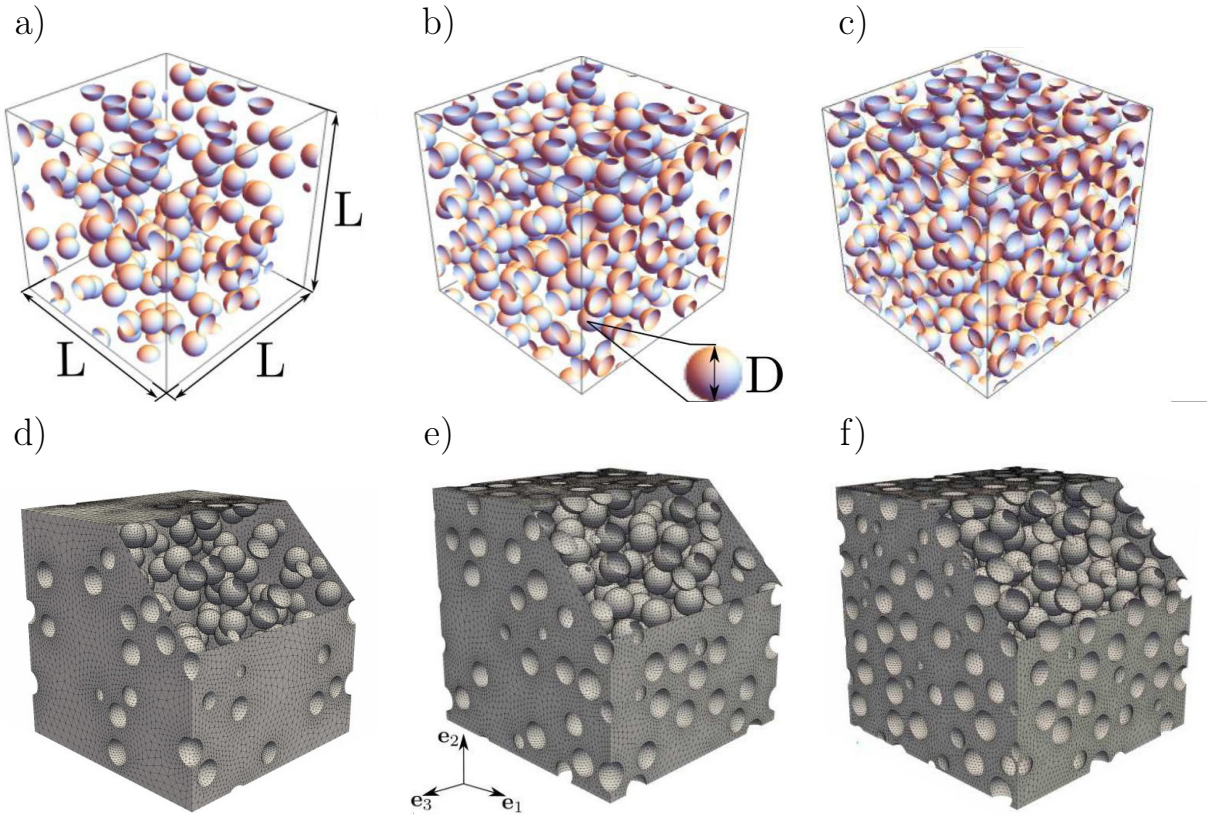

Figure II.2 – RVEs of unit volume L^3 with N randomly distributed spherical particles of monodisperse sizes for a total porosity (a) $c = 10\%$ and $N = 160$, (b) $c = 20\%$ and $N = 275$, (c) $c = 30\%$ and $N = 400$. (d-f) Representative meshes corresponding to the undeformed configuration of the representative cubic cells.

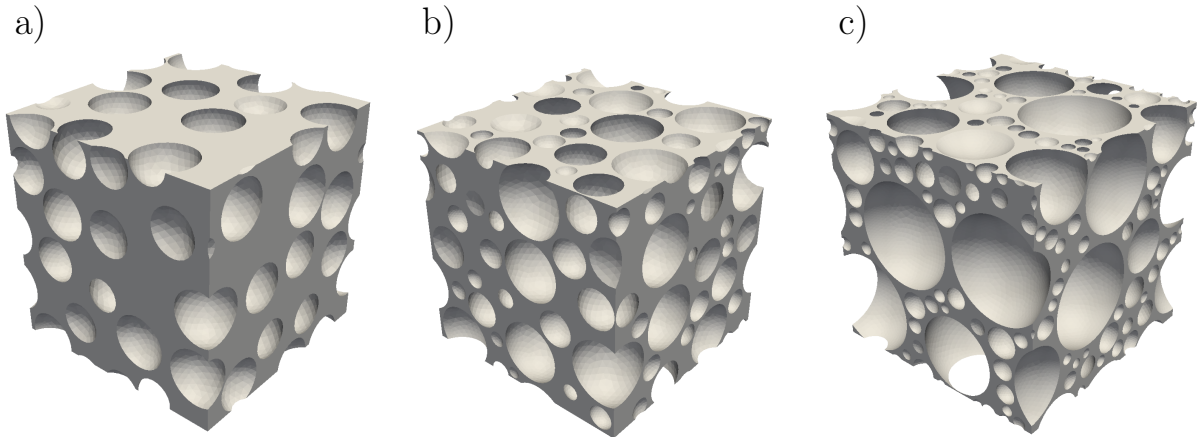

Figure II.3 – RVEs of unit volume L^3 with N randomly distributed spherical particles of polydisperse sizes obtained by the automatic RSA algorithm for a total porosity (a) $c = 40\%$ and $N = 160$, (b) $c = 60\%$ and $N = 275$, (c) $c = 75\%$ and $N = 400$.

II.2 Determination of the RVE for experimental testing

The physical dimension of the cubic cell or equivalently the RVE size is directly related to the applied conditions. Numerical studies (Suquet, 1987; Kanit et al., 2003) on periodic unit-cells have shown that the effective elastic properties of random particulate materials can be obtained with relatively small RVEs, i.e., for large values D/L where D the characteristic size of the smallest heterogeneities and L is the characteristic size of the cell under study. However, In the case of uniaxial experiments, we applied mixed boundary conditions, i.e., part of the specimen is subjected to displacement control and another is stress-free. The fabrication of porous material with accurate control of their effective properties requires the determination the RVE size that withdraws effects related to the applied boundary conditions.

To adress this question, we define the RVE by studying numerically two sets of boundary conditions, the periodic (PBC) and the uniform strain (KUBC) ones. The periodic boundary conditions are defined such that the dispacement field in the whole volume is decomposed into a displacement related the macroscopic strain tensor $\overline{\boldsymbol{\varepsilon}}$ and a L-periodic fluctuation field $\mathbf{u}^*$ such that (Suquet, 1987)

$$\mathbf{u}(\mathbf{x}) = \mathbf{E}\cdot\mathbf{x} + \mathbf{u}^*(\mathbf{x}) \qquad \forall \mathbf{x} \in V \tag{15}$$

Here, $\overline{\boldsymbol{\varepsilon}}$ denotes the average strain in the RVE and $\mathbf{u}^*$ has a zero volume average and accounts for the fluctuations of the field due to the voids. Imposing periodic fluctuations of the displacement field on a microstructure implies that the microstructure is periodic of the same period with that of the fluctuating displacement field and that for the equilibrium of the internal forces the traction vector fulfills anti-periodic condition such that for two homologous points $\mathbf{x}^+$ and $\mathbf{x}^-$ on ∂V:

$$\mathbf{u}^*(\mathbf{x}^+) = \mathbf{u}^*(\mathbf{x}^-) \tag{16}$$

$$\boldsymbol{\sigma}(\mathbf{x}^+)\cdot\mathbf{n} = -\boldsymbol{\sigma}(\mathbf{x}^-)\cdot\mathbf{n} \tag{17}$$

For a technical discussion on how to apply such periodic boundary conditions, the reader is referred to Mbiakop et al. (2015) and Appendix B of Danas (2017).

Contrary to the PBC, for which the homogenized elastic properties rapidly converge to the effective properties, the Kinematic Uniform Boundary Conditions (KUBC) are known to be an upper bound for the apparent elastic properties of voided materials (Huet, 1990). Their deviation from the effective elastic properties is of the same order as the one obtained by using the Static uniform boundary condition in which a traction vector $\mathbf{t}$ is prescribed at any point of the boundary. The KUBC consists in imposing a displacement at any material point $\mathbf{x}$ on the boundary ∂V prescribed through a uniform strain $\overline{\boldsymbol{\varepsilon}}$ such that

$$\mathbf{u}(\mathbf{x}) = \overline{\boldsymbol{\varepsilon}}\cdot\mathbf{x} \qquad \forall \mathbf{x} \in \partial V \tag{18}$$

the RVE problem can be formulated in terms of the parameters of the RSA microstructure by the problem of finding the ratio D/L for which we reach the convergence of the overall elastic properties obtained by numerical simulations for the two sets of boundary conditions, the periodic (PBC) and the uniform strain (KUBC) ones. Since the exact convergence can only be ensured for $D << L$, the

targeted convergence for finding an experimental RVE is considered when (a) the effective properties obtained by the application of the KUBC reach an asymptotic value that is less than 2% from those corresponding to the PBC and (b) further increase of the number of pores does not affect the KUBC result by more than 0.1 %.

II.2.1 Numerical procedure to determine the RVE size

For this purpose, a number of periodic cubic cells with gradually decreasing size D of inclusion, i.e. increasing number of voids, are generated using a fixed porosity c. In order to address the statistical deviation of the RSA process, four different realizations for each pair c and N (or D) have been simulated.

Subsequently, the microstructures are discretized by use of ten-node tetrahedral quadratic elements (C3D10 in ABAQUS Version 6.11 (2011) software) using the automatic mesh generator NETGEN (Schöberl, 1997), which is also capable of creating identical surface meshes at opposite faces of the cell. This, in turn, allows for a direct implementation of the periodic boundary conditions by elimination techniques (e.g., use the `*Equation` command in ABAQUS). For information, the converged RVEs comprise approximately 1.2M degrees of freedom (d.o.f) for low porosity ($0 \leq c \leq 30\%$), 5M d.o.f for the moderate ones ($30\% \leq c \leq 50\%$) and up to 18M d.o.f for the highest porosity ($c = 82\%$).

Numerical estimates of homogenized elastic moduli are obtained by linear elastic FE analysis where the matrix phase is modeled by an isotropic linear elastic constitutive behavior with Young's Modulus $E = 1.4$ GPa and Poisson's ratio $\nu = 0.42$ corresponding to those of the virgin matrix phase used during the printing while the inclusions are considered as voids. (More details on the 3D printing procedure and the properties of the matrix phase and the inclusion phase are given in Section II.3.2.)

The homogenized stiffness tensor is computed from the average stress and strain fields using the overall constitutive equation (Hill, 1963)

$$\overline{\boldsymbol{\sigma}}(\mathbf{x}) = \widetilde{\mathbb{C}} : \overline{\boldsymbol{\varepsilon}}(\mathbf{x}) \tag{19}$$

In practice, adopting Voigt notation, each column of the stiffness tensor $\widetilde{\mathbb{C}}$ is computed by imposing a strain field in a particular direction. For example, imposing the overall strain field $\overline{\boldsymbol{\varepsilon}} \equiv (\overline{\varepsilon}_{11}, 0, 0, 0, 0, 0)$, we obtain six linear relations: $\widetilde{C}_{kl11} = \overline{\sigma}_{kl}/\overline{\varepsilon}_{11}$ with $kl = 11, 22, 33, 12, 23, 31$. The computation of all six columns of $\tilde{\mathbb{C}}$ is done by applying all six independent average strains, $\overline{\boldsymbol{\varepsilon}}$, as described in Kanit et al. (2003). If the heterogeneous material is isotropic, the overall elastic properties can be described by its overall bulk modulus $\widetilde{\kappa}$ and its shear modulus $\widetilde{\mu}$ such that the isotropic stiffness tensor, denoted $\tilde{\mathbb{C}}^{iso}$, is introduced as a projection of $\tilde{\mathbb{C}}$ along the fourth-order deviatoric and hydrostatic tensors, i.e.,

$$\widetilde{\mathbb{C}}^{iso} = 3\tilde{\kappa}\,\mathbb{J} + 2\tilde{\mu}\,\mathbb{K} \qquad \text{with} \qquad \tilde{\kappa} = \frac{\widetilde{\mathbb{C}} :: \mathbb{J}}{3} = \frac{\widetilde{C}_{iijj}}{9}, \quad \tilde{\mu} = \frac{\widetilde{\mathbb{C}} :: \mathbb{K}}{10} = \frac{3\widetilde{C}_{ijij} - 9\tilde{\kappa}}{30}. \tag{20}$$

where, $\widetilde{\kappa}$ and $\widetilde{\mu}$ denote the isotropized bulk and shear moduli, and $\mathbb{J}$ ($J_{ijkl} = (1/3)\delta_{ij}\delta_{kl}$) and $\mathbb{K} = \mathbb{I} - \mathbb{J}$ are the isotropic projection tensors, with $\mathbb{I}$ such that $I_{ijkl} = (1/2)(\delta_{ik}\delta_{jl} + \delta_{il}\delta_{jk})$, the identity tensor in the space of symmetric fourth-order tensors, and δ_{ij} (with $i, j = 1, 2, 3$) the identity second-order

rank tensor. Note that $\mathbb{J}$ and $\mathbb{K}$ satisfy the relations $\mathbb{J}:\mathbb{J}=\mathbb{J}$, $\mathbb{K}:\mathbb{K}=\mathbb{K}$, and $\mathbb{J}:\mathbb{K}=\mathbb{K}:\mathbb{J}=\mathbb{O}$. In many cases, isotropy of the heterogeneous material is an assumption that needs to be verified using quantitative measure of the deviation of the overall stiffness tensor and the isotropic one. There are two possible approaches for a quantitative measure of the deviation from isotropy; the *geometrical approach* which consists in evaluating the deviation from isotropy of the RVE in a geometrical sense (geometrical isotropy), and the *mechanical approach*, consisting in assessing the gap from isotropy of the mechanical response (mechanical isotropy), e.g. the effective stiffness tensor in the linear elastic context. In this study, we use the notion of mechanical isotropy since the goal is the evaluation of the effective elastic properties, and a deviation in geometric anisotropy (which is inherently present in our unit-cells) cannot be translated directly to deviation in mechanical isotropy.

Several authors (see for instance Zener and Siegel (1949), Spoor et al. (1995), Bucataru and Slawinski (2008), Moussaddy et al. (2013), Ghossein and Lévesque (2014)) have proposed methods which can be used to estimate the deviation from mechanical isotropy. They differ from each other by the measure of the amplitude of the stiffness tensor (represented in matrix form adopting Voigt notation), as well as the number of the coefficients used in that measure. The well-known measure of Zener's anisotropy ratio defined via $\delta_z = 2\widetilde{C}_{44}/(\widetilde{C}_{11}-\widetilde{C}_{12})$ (using Voigt notation) takes only in consideration particular components of the stiffness tensor that correspond to cubic symmetry. Since our materials are random, we adopt the Frobenius norm as a measure of the amplitude of the stiffness matrix, which uses all components of $\widetilde{\mathbb{C}}$. The deviation from isotropy of $\widetilde{\mathbb{C}}$, denoted by δ_{iso}, is then evaluated as a ratio of the Frobenius elastic distance function (Moakher and Norris, 2006)

$$\delta_{iso} = \frac{\|\widetilde{\mathbb{C}} - \widetilde{\mathbb{C}}^{iso}\|_F}{\|\widetilde{\mathbb{C}}\|_F}, \tag{21}$$

where $\|\mathbb{A}\|_F = \sqrt{\mathrm{Tr}\,(\mathbb{A}\cdot\mathbb{A}^T)}$, is the Frobenius norm of the tensor $\mathbb{A}$. The value of $\delta_{iso}=0$ corresponds to exact isotropy.

The RSA algorithm is known to lead to very small deviations from isotropy when spherical inclusions are used (but see corresponding results for ellipsoidal inclusions in Anoukou et al. (2018)). In the present study, the maximum error is found to be $\delta_{iso} < 0.006$ and the deviation from $\delta_z = 1$ which corresponds to the isotropic case is less than 0.01. Therefore, the proposed RVEs can be considered isotropic.

II.2.2 Converged RVEs for monodisperse spherical pores

For spherical single sized voids in cubic cells, the ratio between the size of the pores and the size of the cubic unit cell D/L is related to the number of voids N and their volume fraction c such that:

$$c = \frac{N\pi}{6}\left(\frac{D}{L}\right)^3, \qquad \text{or} \qquad \frac{D}{L} = \sqrt[3]{\frac{6c}{N\pi}} \tag{22}$$

Using the above definitions and boundary conditions, we carry out calculations to estimate the number of pores required for convergence in the effective elastic properties or equivalently the size of the RVE which is defined by the ratio D/L in equation $(22)_2$. It is noted here that in addition to

the converged RVE, a number of technical constraints related to the 3D printing accuracy and the experimental equipment have to be taken into account. Those constraints are discussed in detail in the following section. We recall that convergence towards an experimental RVE is considered when (a) the effective bulk and shear moduli obtained by the application of the KUBC reach an asymptotic value that is less than 2% from those corresponding to the PBC and (b) further increase of the number of pores does not affect the KUBC result by more than 0.1 %.

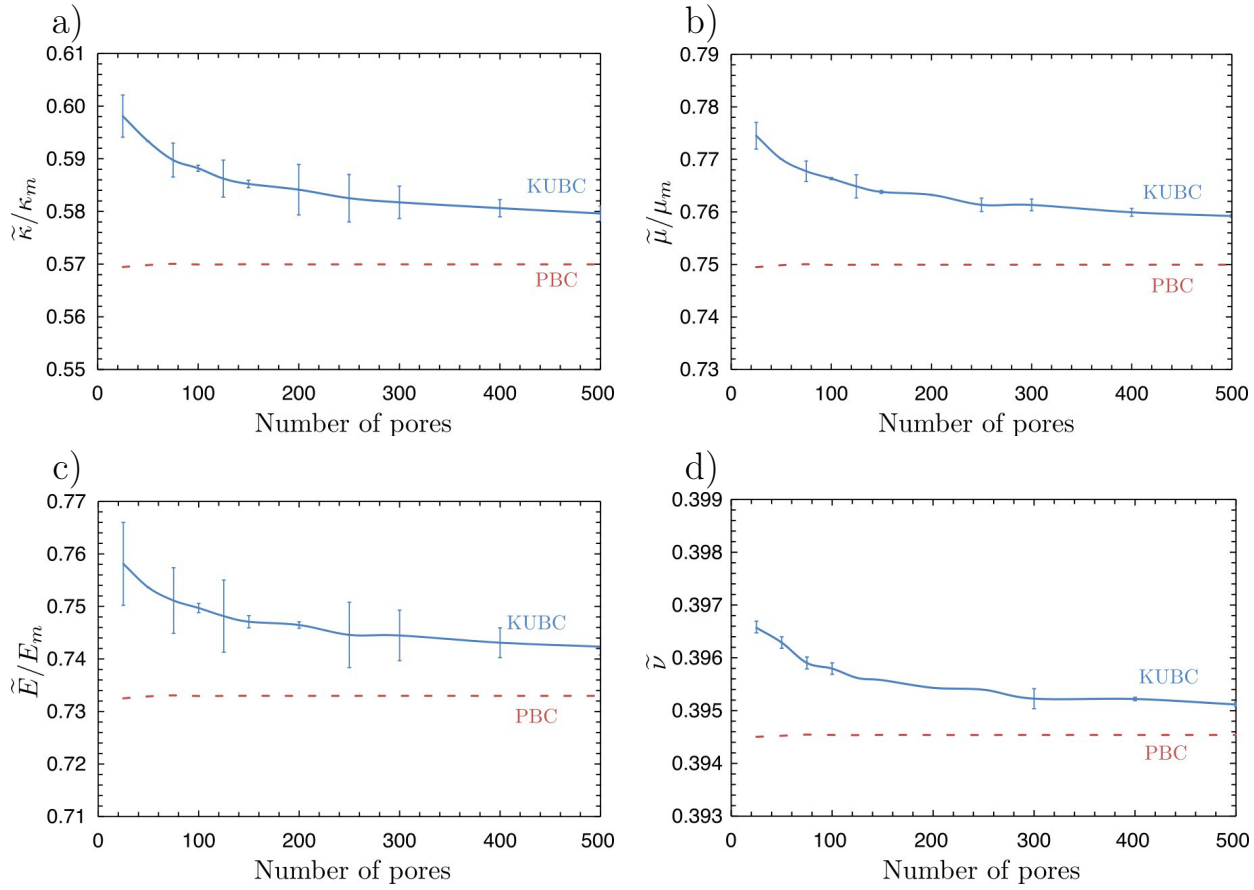

Figure II.4 – Numerical results to determine the number of monodisperse spherical pores that lead to convergence for the different boundary conditions PBC and KUBC. Normalized effective elastic moduli: (a) normalized bulk modulus $\widetilde{\kappa}/\kappa_m$, (b) normalized shear modulus $\widetilde{\mu}/\mu_m$, (c) normalized Young's modulus $\widetilde{E}/E_m$ and (d) Poisson's ratio $\widetilde{\nu}$ for $c = 15\%$. The matrix bulk, shear and Young's moduli are κ_m, μ_m and E_m, respectively.

Specifically, Fig. II.4 shows the evolution of the normalized effective moduli, defined as the ratio of the effective moduli of the RVE over the moduli of the matrix, for a porosity of $c = 15\%$ as a function of the number of pores N. The periodic boundary conditions (PBC) converge rapidly (i.e., for $N \sim 30$) to the effective elastic properties of the given microstructure and show no substantial dispersion among the various realizations. By contrast, the kinematically uniform boundary conditions (KUBC) require a much larger number of voids for convergence, in the order of $N = 225$. This, in turn,

leads to a size ratio $D/L \sim 0.103$, i.e. a side length of the cube that is approximately ten times the diameter of the void. Moreover, we observe that the KUBC loading leads to more dispersion among the different realizations.

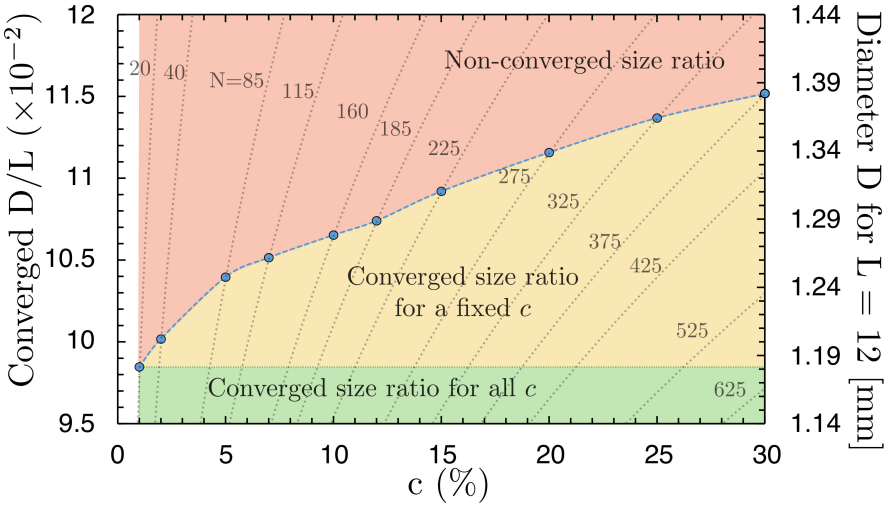

Figure II.5 – (Left axis) Converged in terms of elastic properties pore diameter-to-cube size ratio D/L and (right axis) pore diameter (in mm) for a cube side length $L = 12$mm as a function of the porosity c. Colored regions depict in red the non-converged D/L ratio, in yellow the converged D/L ratio for given porosity and in green the maximum pore size, i.e., D/L that can be used to obtain converged RVEs. Contours of equation $(22)_2$ for different number of pores N are shown as dotted lines.

Similar calculations, as those discussed in the context of Fig. II.4 for porosity $c = 15\%$, are carried out for the entire range of porosities analyzed in this study allowing us to get a converged size ratio D/L as a function of c, as shown in Fig. II.5. We observe that D/L increases with c and is of the order $D/L \sim 0.1$. Overall a ratio $D/L \sim 9.85 \cdot 10^{-2}$ is sufficient for a converged RVE (green area in Fig. II.5). This implies that the diameter of the voids should be less than $D \sim 1.18$mm for a cubic RVE of side length $L = 12$mm in order to get converged effective elastic properties for any porosity c (see right axis of Fig. II.5). Instead, one can use larger void diameters at larger porosities c, as shown by the yellow area in Fig. II.5 but it has to be taken case-by-case. The red regime, on the other hand, indicates non-converged D/L ratios. Note at last that the converged ratios D/L are also a function of the number of voids N in the RVE, which are shown in the same figure as contours of equation $(22)_2$ (dotted lines).

II.2.3 Extension to polydisperse RVEs

Following the procedure introduced in Sec.II.2.2, the size of the RVE can be defined by a single geometrical parameter D/L relating the unique heterogeneity size D which spherical void diameter and the characteristic size of the cell L. In the case of polydisperse systems, a similar approached was possible thanks to the automatic process of generation of polydisperse inclusions which for spherical inclusions can be related to only the diameter of the biggest inclusion D_{max} for any given volume

fraction c. Thus, the procedure for such microstructures consists in decreasing progressively the diameter D_{max} for fixed porosity c and measuring the overall elastic properties for the two sets of boundary conditions as described in Sec.II.2 until convergence of the elastic properties is reached. In Figs.II.6 a-d), the extended RVE procedure is described for a representative porosity $c = 60\%$. Fig II.6a represent different cubic cells with decreasing diameter D_{max} while the results of normalized effective elastic moduli obtained from the FE computations are plotted in Fig.II.6 b-d). In these figures, the diameter of the smallest voids D_{min} is used as secondary horizontal axis. For illustration purposes, we report in the inset of Figure II.6b the evolution of the ratio D_{max}/D_{min} as a function of D_{max}. To ensure statistical representativeness, each data point is the average of five simulations onto different realizations. It is observed that the normalized bulk and shear moduli of the porous microstructures computed using KUBC converge quite fast toward the PBC results and that decreasing D_{max} leads to an important increase in the total number of inclusions in the cell and thus increases the size of calculations.

Collecting the converge RVE size obtained for both studies, we plot the evolution of both D_{max}/D_{min} and D_{min} as a function of the volume fraction, i.e. c. At small porosities, i.e. $0 \leq c \leq 35\%$, the ratio D_{max}/D_{min} remains constant and equal to $D_{max}/D_{min} = 1$ with RVE size obtained for $D_{min} = 1.2$mm (for a unit cell of characteristic size $L = 12$mm) showing that RVEs for such volume fractions can be obtained with a single size of voids. It is worth noting that this result confirms earlier studies (Lopez-Pamies et al., 2013a; Anoukou et al., 2018) that have found that the effective elastic properties for monodisperse and polydisperse spherical particles at equal volume fraction were nearly identical for the RSA microstructures. On the other hand, for $c \geq 40\%$; polydispersity is essential to achieve high values of volume fractions without interfering on the center points or characteristic sizes of generated (i.e. already accepted) inclusions by the RSA. Figure II.7 shows a rapid increase of the converged ratio D_{max}/D_{min} which reaches values as large as 45:1. This last result shows that to achieve large porosities $c \geq 75\%$, the continuous distribution of sizes imposes to build multi-scale microstructures.

It is worth noting that, for such volume fractions, the convergence in the overall elastic properties obtained with KUBC and PBC could not be reached in the numerical simulations. The deviation between the overall elastic properties obtained for both boundary conditions goes up to 8% for $c = 82\%$ and no improvment could be sought because generating these microstructures reaches the accuracy limitations of the 3D Printer. In this case, an experimental RVE obtained from averaging the experimental overall elastic properties of multiple sample realizations was chosen to remedy to that.

II.2.4 FE results for porous microstructures

Before explaining the 3D printing procedure and results of its application on our microstructures, it is worth discussing the results obtained with FEM for the effective properties of the porous RSA microstructures because these results carry intrinsic influence of the microstructure descriptions on the effective elastic properties without the effect of imperfections or specificities related to the choice

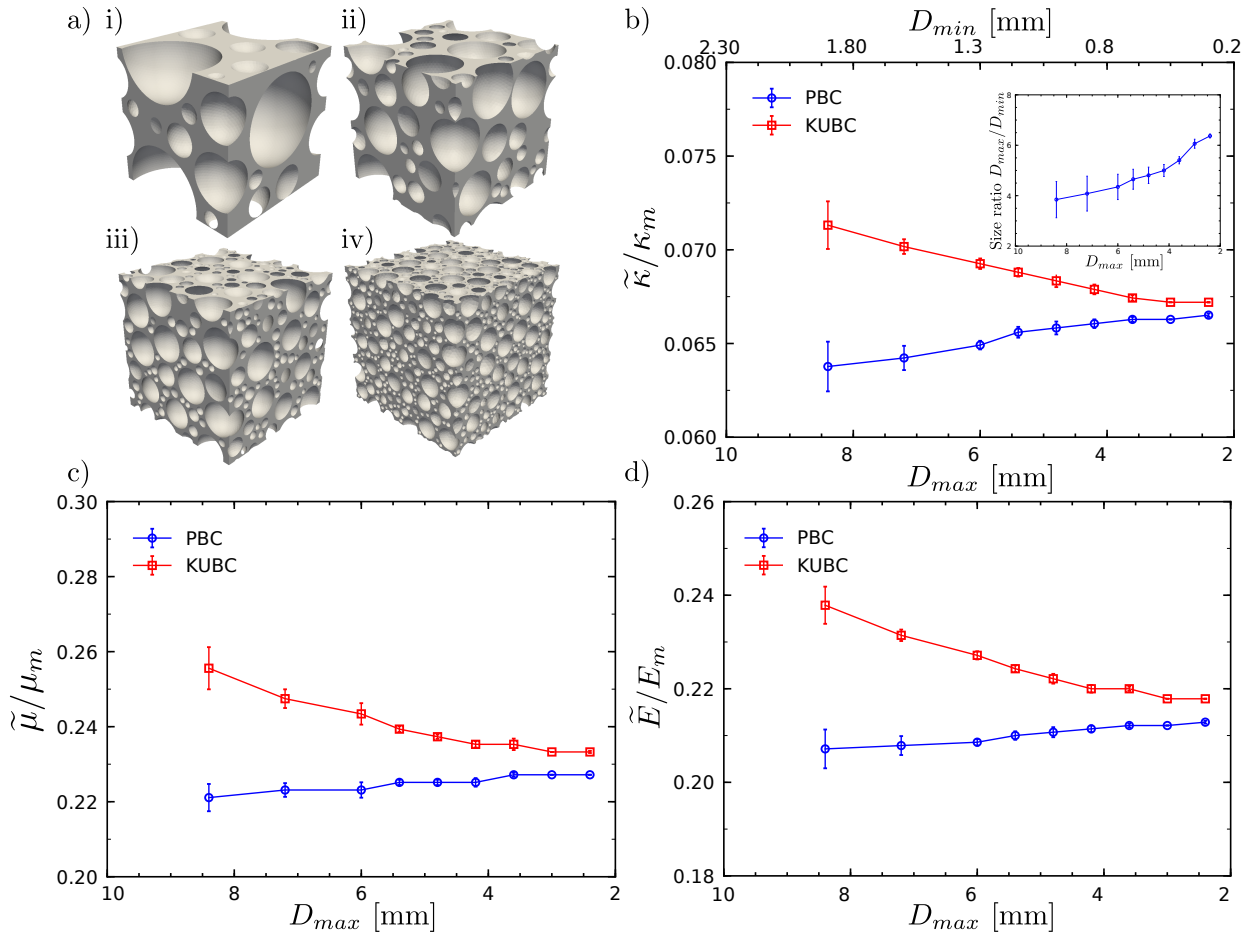

Figure II.6 – a) Realizations of microstructures containing a random distribution of polydisperse spherical voids at porosity $c = 60\%$. Geometrical paramters for these microstructures are: (i) $D_{max} = 8.4$mm and $D_{max}/D_{min} = 4$ (ii) $D_{max} = 6.0$mm and $D_{max}/D_{min} = 4.5$ (iii) $D_{max} = 4.8$mm and $D_{max}/D_{min} = 5$ (iv) $D_{max} = 2.3$mm and $D_{max}/D_{min} = 6.5$. (b-d) Results for the effective (b) bulk, (c) shear and (d) Young moduli normalized by the corresponding matrix moduli obtained from FE simulations with periodic (PBC) and kinematically uniform (KUBC) boundary conditions. data are the average of five realizations. The inset in figure (b) shows the evolution of the ratio between diameters of the biggest and smallest pores D_{max}/D_{min} for different input D_{max} values.

of 3D printing process. We explore numerically the effective elastic properties of RSA microstructures for porosities ranging from $c = 0$ to $c = 82\%$ for which no analytical solution is yet available.
The normalized effective shear $\widetilde{\mu}/\widetilde{\mu}_m$ and bulk $\widetilde{\kappa}/\widetilde{\kappa}_m$ are shown as a function of the total volume fraction c in Figure II.8. The data points, depicted by solid circles correspond to the average values of four different RVE realizations and depict very small standard deviation as shown by the error bars. Moreover, for all porosities analyzed here the deviation from isotropy is less that $\delta_{iso} < 1\%$ thereby indicating that our porous materials are fully isotropic solids.
For comparison purposes, the theoretical HS bounds defined (solid lines) for isotropic porous solids in Eq.II.A.2.b are also reported in Figure II.8.

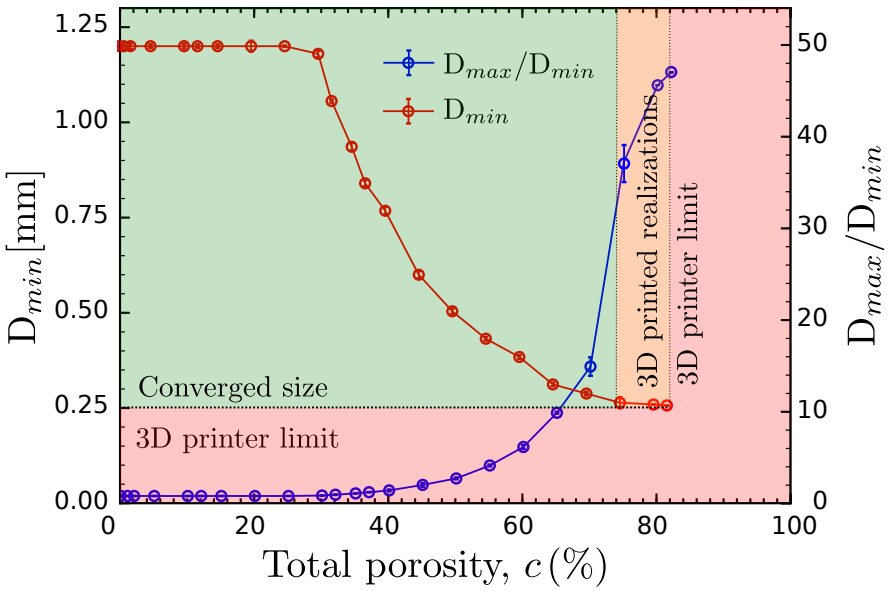

Figure II.7 – Results of the RVE convergence study for a large range of porosity, $0 \leq c \leq 82\%$ showing the ratio D_{max}/D_{min} and the D_{min} obtained as a function of the porosity.

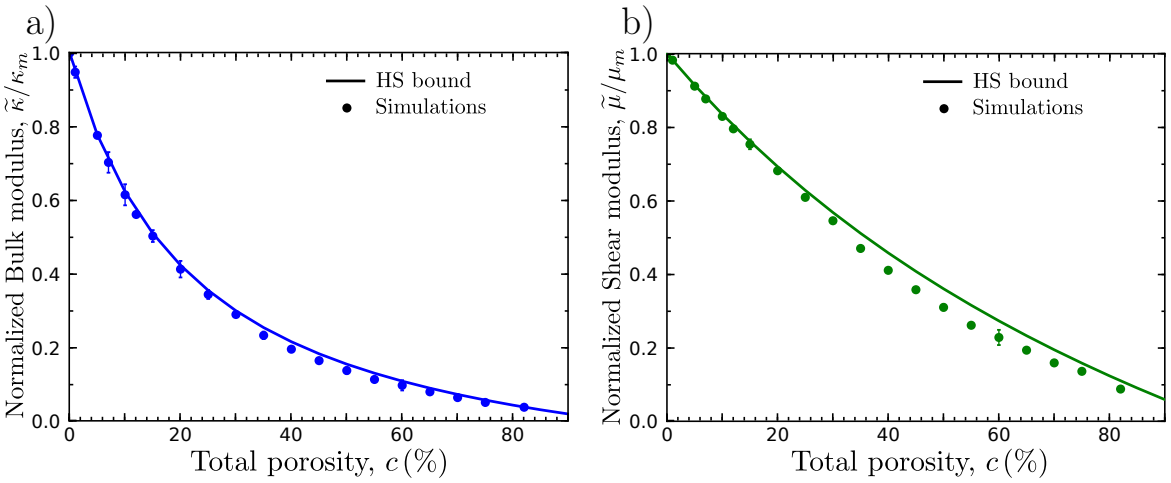

Figure II.8 – Plots of the normalized shear modulus $\widetilde{\mu}/\mu_m$ and bulk modulus $\widetilde{\kappa}/\kappa_m$ as a function of the volume fraction of inclusions c. The data points are obtained from FE periodic unit-cell simulations with periodic boundary conditions (PBC). The Hashin-Shtrikman upper bound for isotropic porous materials is also displayed for each modulus using solid lines.

$$\widetilde{\kappa}_{HS} = \frac{4(1-c)\mu_m\kappa_m}{4\mu_m + 3c\,\kappa_m} \tag{23}$$

$$\widetilde{\mu}_{HS} = \frac{(1-c)(8\mu_m + 9\kappa_m)\mu_m}{4\mu_m(2+3c) + 3\kappa_m(3+2c)} \tag{24}$$

The difference between the FE predictions and the corresponding HS bounds remains small over the entire range of porosity explored. Moreover, this difference decreases gradually for moderate to low

porosities ($0 \leq c \leq 40\%$) and for large ones ($c \geq 60\%$). Rather interestingly, this difference is found to be maximum for intermediate values of the porosity $40\% \leq c \leq 60\%$ which will be discussed with insight on the local elastic fields in the Sec.II.4.3.

II.3 3D printing and experimental protocol

This section presents the 3D polymer printing technique, the characterization of the process with optical imaging and Electronic microscopy for the determination of the resolution of printing objects. Then it presents the setup of characterization of the 3D printer materials properties and then the fabrication of porous-like materials with experimentally assessed effective properties.

II.3.1 Additive manufacturing of porous specimens

All test specimens are 3D-printed using an acrylic photopolymer available in our EDEN 260VS 3D-printer purchased by Stratasys. The photopolymeric resin employed for 3D-printing has the commercial name VeroWhitePlus and is selected for its suitability to produce parts with very fine feature details, such as our spherical void microstructures. The main aim of the experiments is then the measurement of the effective Young's modulus and Poisson's ratio of the 3D-printed random porous microstructures. Due to the viscoelastic response of the VeroWhitePlus polymer, we measure the material parameters for the basic (ground state) elasticity by means of a tensile relaxation testing. Following the experimental methodology presented in Hossain et al. (2012), we carry out two trains of experiments, namely (i) single- and (ii) multi-step relaxation tests, and we assess their suitability for obtaining the basic elasticity data from the time-dependent stress response.

II.3.1.a Fabrication of the tensile-test specimen

Specifically, our virtual test specimens have a dog-bone shape which is designed to ensure uniaxial stress conditions (on average since our porous specimens are heterogeneous) in the gage section. The ratio of the length to the width is for all samples higher than 10 (Wissler and Mazza, 2007). In order to construct the virtual geometry of the porous samples, we adopt the protocol shown in Fig. II.9. We first assemble length-wise five representative cubic RVE cells of length $L = 12$mm (see discussion in Section II.3.2) in order to build the reduced uniform section of the test specimens. The latter is enclosed between the heads of the sample which, in turn, have a solid section thus allowing us to mount the specimen onto the uniaxial machine. The physical dimensions of the test specimens can be obtained from Fig. II.9.

Next, we transform the 3D virtual model of our test specimens into a stereolitography format (i.e. STL) for 3D-printing. This is done by employing the commercial software NETGEN to mesh the 3D-models with four-node tetrahedral elements and subsequently export the latter to STL. We note in passing that more often than not the exported 3D STL models contain errors associated with the normal vectors defining the facets of the internal voids surfaces. In fact, these normal vectors define the direction towards which material should not be printed. Thus, one should correct the normal

direction so that it points towards the center of the sphere. In the present study, those normal vector directions are corrected by use of the commercial software NETFABB (presently CadVision).

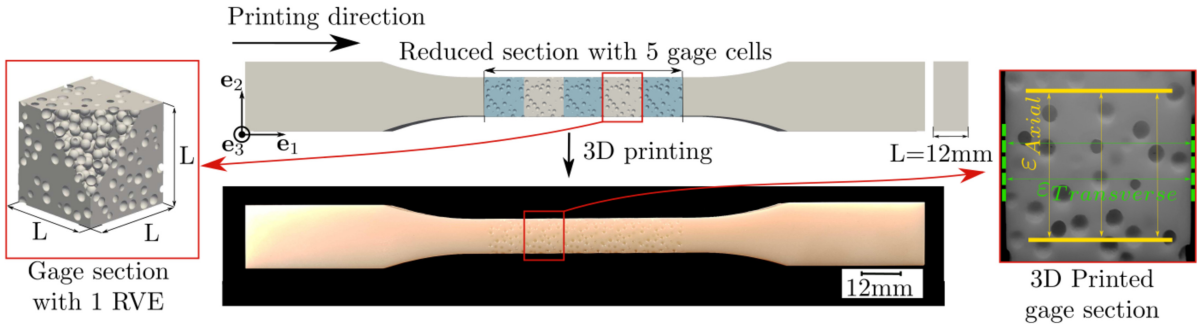

Figure II.9 – (Top) Virtual testing sample generated by assembling length-wise 5 cubic porous RVEs and by adding gripping heads of solid material. (Left) A zoom of the RVE which defines our gage section. (Bottom) 3D printed testing sample after cleaning support material from open pores and boundary surface. (Right) A zoom of the 3D printed RVE showing the size of the actual axial and transverse gage sections in the experiment.

II.3.1.b The 3D printer constraints and technical requirements

Once a correct STL model is produced, we then fabricate the specimens using the 3D-printer EDEN 260VS by Stratasys. Our printer employs a PolyJet technology that consists in building volume parts through layer deposition of liquid photopolymerizable droplets (of micrometric size) which are then cured with a UV light with no-additional post-curing. For the VeroWhitePlus resin used in this study, the layer resolution is 16µm whereas that of the jetting precision is 100µm, as specified by the manufacturer (for more information go to: http://www.stratasys.com). Furthermore, in order to overcome gravity constraints related to 3D objects such as that of a sphere, our 3D-printer uses a support gel-like material to print the spherical void volumes during layer deposition. As detailed in Section II.3.4, this support material has no influence on the effective response of the measured porous-like composites.

Another important specificity of the 3D printer related to the fabrication of the porous microstructures is the accuracy of the 3D-printing process. In order to assess the geometrical dimension that can be produced by the available 3D printer, porous microstructures are observed by mean of an optical microscope. Specifically, guided by the results of the numerical RVE calculations in Fig. II.5, we have investigated several void diameters spanning from $D = 200\mu m$ to $D = 1200\mu m$. In order to observe the microstructures under the microscope, we deliberately interrupted the 3D-printing process at arbitrary time steps and then resumed it after optical analysis. Overall, Fig. II.11 reveals that pores with circular section are finely fabricated in both cases and can be manufactured with very good dimensional accuracy within the range of size explored. Figure II.11 also shows that the spherical pores can be printed up to a diameter of about 200µm and the a thickness of ligament of about 150µm. A set of representative optical micrographs are shown in Fig. II.10, with parts (b)

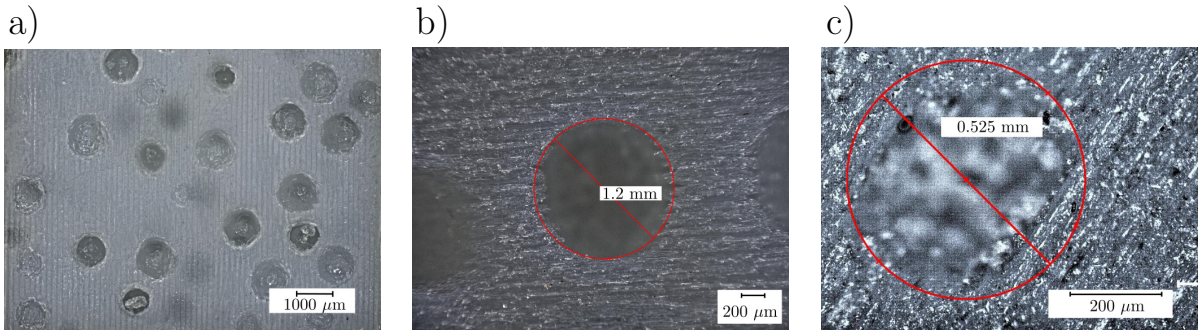

Figure II.10 – Optical image showing a cross-section of the macroscopic 3D printed specimen with the spherical pores for the assessment the printing accuracy. Observations of representative 3D printed spherical voids of diameter (b) $D \sim 1.2$mm and (c) $D \sim 0.500$mm. A fairly good printing accuracy is observed in both cases.

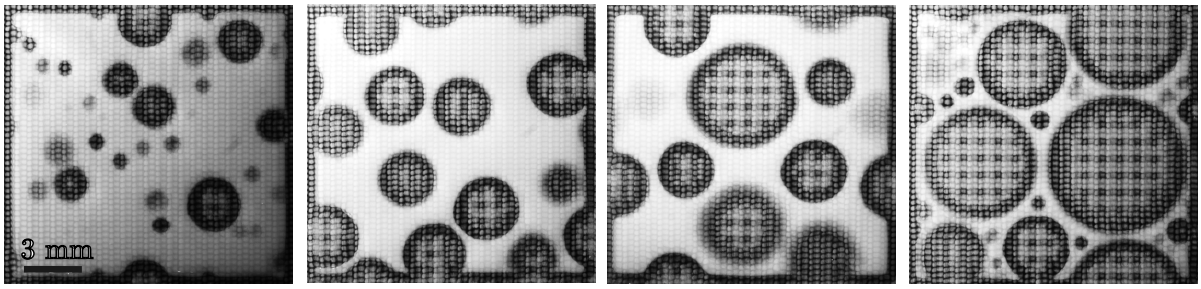

Figure II.11 – Micrographs of the 3D-printed porous microstructures obtained upon interrupting the 3D printing process at a build volume of thickness about 500 μm. The pore-like inclusions are built by the 3D-printer using a gel-like support material (i.e. nearly transparent phase). Pores through thickness are also visible (i.e. light grey phase).From left to right, the 2D micrographs represents microstructures of total volume fraction $20\%, 40\%, 60\%$ and 75%

and (c) corresponding to pore diameters of ~ 1.2mm and ~ 0.5mm, respectively. Finally, it is worth mentioning that no additional micron-size porosity has been observed in the matrix phase as a result of the printing process.

II.3.2 Experimental protocol

The tensile relaxation experiments are carried out at room-temperature using a servo-hydraulic uniaxial apparatus as shown in Fig.II.12. When increasing the volume fraction of porous-like inclusions c, the mechanical behavior of the material drops down and lowers the values of force needed to reach the monitored displacement. In order to keep accuracy of the measurements even at low force range, we measure the load history with a 10kN force transducer (accuracy $\pm$10N) for $c \leq 30\%$, and we change the setup to a 1.5kN the load transducer with accuracy of $\pm$0.1N. In turn, the measurements of the axial and transverse strains are obtained simultaneously and independently by means of two clip-on gage extensometers. Specifically, the former is measured with an MTS 632.13F-20 sensor (accuracy $\pm$0.0075mm) and the latter with an Epsilon 3475-025M-ST transducer (accuracy $\pm$0.1mm).

It is important to note here that since we are interested in measuring the effective properties of the porous materials, the gage length for each extensometer was set equal to the characteristic cubic RVE cell length, i.e. $L = 12$mm (see discussion in Section II.1.3). It is not the goal of the present study to measure the local strains in-between the voids or any other local information.
For consistency with the numerical analysis, for each test, we use four specimens to assess the degree of reproducibility of the experimental results. We also note that in order to minimize the discrepancy of the measurements, every test sample is printed individually and experiments are conducted three days after the manufacturing process (to prevent aging of the polymer matrix). As reported by Barclift and Williams (2012), the relative distance between the samples as those are set upon the building tray of the 3D-printer could be an additional source of scattering in their elastic properties.

II.3.2.a Single relaxation testing

A common approach in determining the time-independent equilibrium response, i.e., the equilibrium stress state, in viscoelastic polymers is to perform single-step relaxation tests under a constant applied displacement. Such tests typically involve the application of a constant displacement (leading to a constant overall strain) and then monitoring the force decay over time.

The value that the stress reaches asymptotically at the end of the holding time in single-step relaxation experiments corresponds to the equilibrium stress. Therefore, it is the value of interest for the estimation of the Young's modulus. We assess the suitability of this testing method by carrying out three relaxation tests at different strain rates $\overline{\dot{\varepsilon}} = \{10^{-4}, 10^{-5}, 10^{-6}\}\text{s}^{-1}$ for the pure VeroWhitePlus material (i.e. without voids) and by measuring the load history under an applied constant nominal strain of $\sim 0.5\%$. Those single-step relaxation tests, albeit useful to obtain the relaxation decay of the material and an approximate range of the linear response regime, are inappropriate to provide the pure (i.e. without viscoelastic contributions) elastic modulus of the material.

II.3.2.b Multi-step relaxation testing

In view of this, multi-step relaxation tests at various levels of deformation is an alternative to single-relaxation and can be employed to determine the basic elasticity (slopes of the stress-strain response) of the materials under study. In many practical cases, and particularly when the amount of the viscous effects in the material are unknown, the method proves more suitable and time-effective than the single-step relaxation as discussed by Hossain et al. (2012). In the present study, multi-step relaxation tests at $\overline{\dot{\varepsilon}} = 10^{-5}s^{-1}$ are conducted. At each step, a displacement corresponding to an average axial strain increment of 0.1% is applied to the test specimen and the step-wise load history is recorded except for volume fraction $c = 82\%$ for which an average axial strain increment of 0.05% is applied in order to prevent large straining of the thin matrix ligaments between neighboring pore-inclusions. Each test consists of seven relaxation steps so that the final nominal strain $\overline{\varepsilon} \leq 0.7\%$ which corresponds to the value of the nominal strain beyond which the stress-strain response of the polymer VerowhitePlus matrix starts departing from linearity.
To pilot the experiments, we use an in-built computer program where the holding time for relaxation

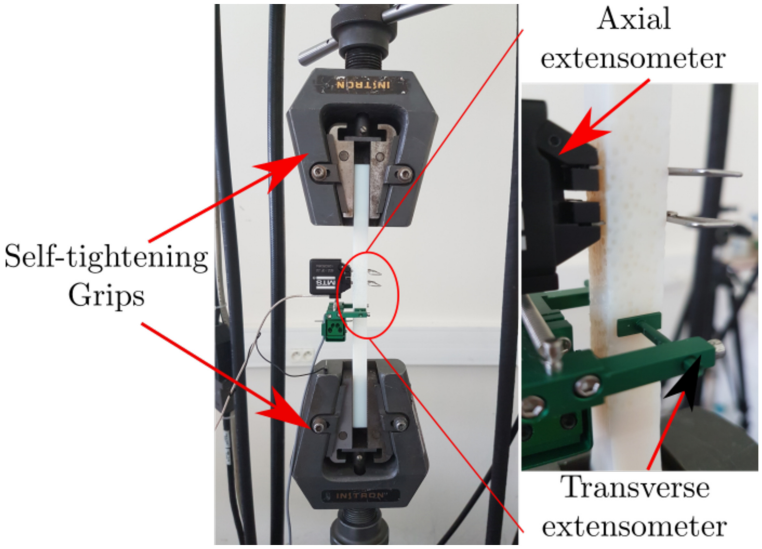

Figure II.12 – Picture of the experimental setup used in order to determine the effective elastic properties of polymeric porous microstructures.

is variable. Specifically, we consider the material to be at its equilibrium state, and therefore attaining its purely elastic response, when the difference between two consecutive force measurements is smaller than a tolerance value related to the sensitivity of the experimental setup. For volume fractions $c \leq 30\%$, this tolerance value has been set to 10N (which corresponds to the accuracy of our load cell) and the time interval between two consecutive measurements is taken to 20min following the observations of relaxation time of the matrix polymer shown in Fig.II.13. For higher volume fractions $c \geq 30\%$, the equilibrium state criterion in the relaxation phase is change from a difference smaller than 10N to a difference smaller than 4N and the time step between two consecutive force comparison measurements in the relaxation phase was also changed to 3min intervals in order to gain time on the experiment.

II.3.3 Characterization of the Matrix material

In this section, we show detailed experimental results related to the polymeric matrix material used for the 3D printing, following the procedure discussed in the previous section.

II.3.3.a Elastic moduli of the monolithic VeroWhitePlus matrix

Experimental results of the single-step relaxation tests for the monolithic VeroWhitePlus matrix at different strain rates $\bar{\dot{\varepsilon}} = \{10^{-4}, 10^{-5}, 10^{-6}\}\text{s}^{-1}$ are reported in Figs II.13a,b. Data in Fig II.13a provide quantitative measurements of the matrix strain rate sensitivity as well as of its time-dependent response. The comparison of the curves in Fig II.13a shows that the initial slope of the axial force-time response decreases with decreasing strain rate, whereas not all three curves reach to the equilibrium

state within the holding time window, although they all exhibit the tendency to reach the same asymptotic force value at large times. For completeness, we report in the inset of Fig II.13a the measured stress-strain response of the matrix at two different strain rates $\bar{\dot{\varepsilon}} = \{10^{-5}, 10^{-6}\}\text{s}^{-1}$ and observe that they depart from linearity after $\sim 0.7\%$ strain. Therefore, in order to obtain the initial Young's modulus one has to make sure that the overall applied strains remain small, which makes experimental measurements extremely sensitive. On the other hand, Fig II.13b reveals that the Poisson's ratio, obtained as the absolute value of the ratio between the transverse strain over the axial strain, is strain-rate insensitive.

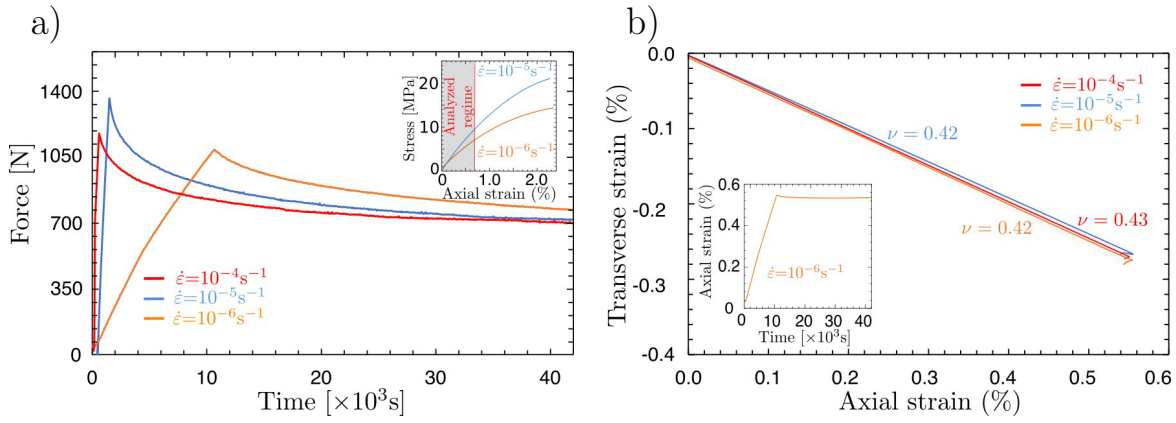

Figure II.13 – (a) Force measurements for single-step relaxation tests at different strain rates showing strong rate-dependence. Inset shows the corresponding axial stress-strain response for strain rates $\bar{\dot{\varepsilon}} = \{10^{-5}, 10^{-6}\}\,\text{s}^{-1}$. (b) Axial versus transverse strain curve obtained for different strain rates showing that the Poisson's ratio is fairly rate-independent. Inset shows the evolution of the applied strain as a function of time.

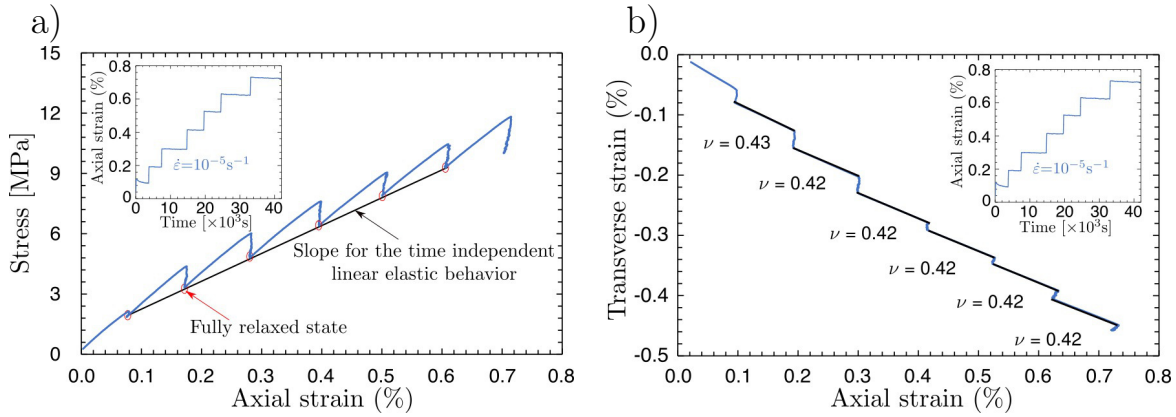

Figure II.14 – Overall applied strain rate $\bar{\dot{\varepsilon}} = 10^{-5}\text{s}^{-1}$: (a) Stress-Strain curves obtained during multi-step relaxation steps. The Young's modulus is obtained by the slope of the curve that connects the fully relaxed stress states excluding the first point. (b) Axial versus transverse strain curve during the multi-step relaxation test. Slopes during loading are found to be fairly independent of the level of the axial strain.

The results of the multi-step relaxation experiments at $\bar{\dot{\varepsilon}} = 10^{-5}$ s^{-1} for the VeroWhitePlus

matrix are reported in Fig II.14a. The effective Young's modulus, $\widetilde{E}$ (or E_m for the pure polymer), is then evaluated as the slope of the line connecting the equilibrium (fully relaxed) stress points in the nominal stress-strain curve as shown in Fig. II.13a. It is worth mentioning that in the evaluation of the slope, we use six equilibrium stress points, neglecting the one at zero strain, which can be very sensitive to initial settings of the experimental setup (e.g., gripping of the specimen, minor sliding between the heads and the machine and sensitivity of the extensometers). Moreover, in agreement with previous observations in Fig II.13b, Fig. II.14 shows that at each relaxation step the slope of transverse strain-axial strain curve is time-independent thereby making the calculation of the Poisson's ratio straightforward. Finally, a very small drop is observed for the transverse strain at each relaxation step.

II.3.3.b Isotropy of the 3D printed matrix material

Prior to testing the porous materials, we first investigate experimentally the isotropy of the mechanical response of the 3D-printed pure VeroWhitePlus matrix. This analysis is extremely important for our study since the microstructural anisotropy (if any) could be easily attributed to the intrinsic anisotropy of the polymer matrix. In order to address this issue, we print the dog-bone specimens in all three different directions with respect to the printer heads. For clarity, hereinafter $\mathbf{e}_1$ corresponds to the printing direction, i.e. the displacement direction of the printer's heads, $\mathbf{e}_2$ and $\mathbf{e}_3$ are respectively the in-plane and out-of-plane directions perpendicular to $\mathbf{e}_1$. We also note that $\mathbf{e}_3$ corresponds to the direction of deposition of the sequential layers. In Fig. II.15, we report

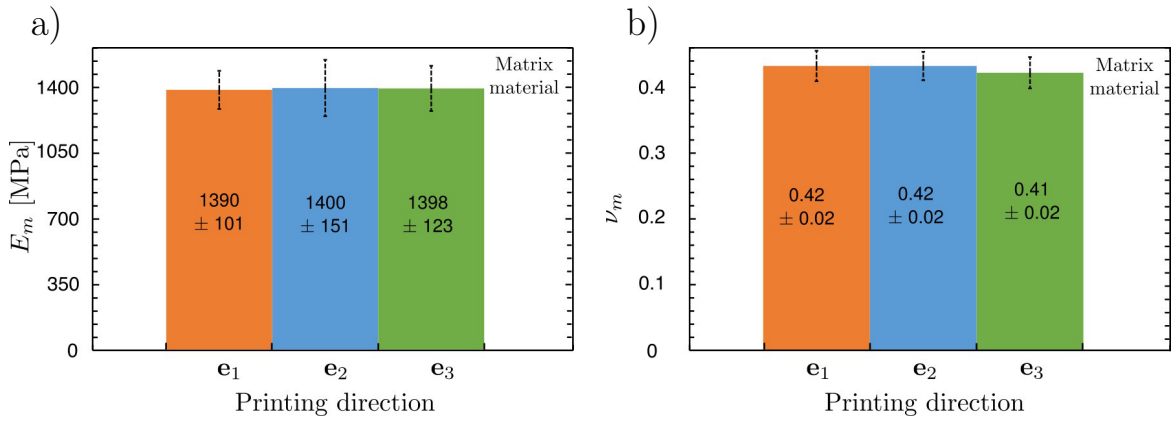

Figure II.15 – Experimental results of (a) Young's modulus E_m and (b) Poisson's ratio ν_m for the matrix phase with respect to the printing direction. The matrix is found to be isotropic.

computed values of the Young's modulus and Poisson's ratio for all three different printing directions. The elastic parameters are obtained from multi-step relaxation experiments as described in the previous section. As seen, the measured values of these moduli are within the scatter of data and are independent of the printing direction. The measured mechanical isotropy can partially be explained by observation of Fig II.10a. In our 3D printer, the liquid polymer droplets create a homogeneous solid material when coalescing and overcome any apparent laminated microstructure that would result

from the 16µm layering process. Finally, our data provided experimental evidence that the matrix material (VeroWhite) is statistically homogeneous and exhibits an elastically isotropic behavior with a Young's modulus $E_m = 1400 \pm 120$MPa and a Poisson's ratio of $\nu_m = 0.42 \pm 0.02$. These moduli correspond to a bulk modulus of $\kappa_m = 2920$MPa and a shear modulus of $\mu_m = 493$MPa.

II.3.4 Characterization of the support material

This section deals with the influence of the gel-like support material, with commercial name SUPP705 (Startasys) used to overcome gravity issues while printing the internal spherical void geometry. Similarly to the building photopolymer, this material is also an acrylic-based polymer with density $d_{SUPP705} = 1.13$ but it can be easily removed from the external surfaces of the 3D-printed parts by waterjet or chemical NaOh solution if it is inside an open (or connected with the surface) porosity. For closed-cell porosity, as is the case in the present study, this material is trapped inside the structure.

II.3.4.a Elastic moduli of SUPP705 material

As mentionned before, the 3D printer uses a gel-like support material to support the layer-by-layer building of the structure and this material is trapped inside closed space of the microstructure. It is also worth mentionning that this support material is not an option for building parts and the design of a part made of such material needs to use a shell to force the use of the support material in precise regions and to be easy to take away without damaging the support material.
Accounting for these fabrication constraints, an experimental specimen shown in Fig.II.17 has been designed to test the elastic properties of the support material. The specimen consists of a 50mm-length strips of support material with a squared gage section of 5mm-size enclosed by a U-shaped sandwich structure on both ends of its length direction and by a layer of VeroWhitePlus material of 200µm thickess on the front and in the back faces of the gage section. These two layers can be easily striped away from the support material strip and the U-shape VeroWhitePlus structure is used to mount the specimen onto the tensile testing machine without damaging the structure as shown in Fig.II.16.
To ensure appropriate characterization of the mechanical properties of the support material, four samples were tested in uniaxial testing setup. The experimental setup that was developped for VeroWhitePlus characterization cannot be applied to the support material as the weight of the transducers itself breaks the samples. For determining the Young moduli and Poisson's ratio of the material, we use optical marker tracking method that enables to measure the macroscopic longitudinal and transversal strains using a camera connected to a post-treatment software. As shown by Fig.II.16, a regular grid made of nine points is made in a central position on the gage surface of the strip of the support material in order to avoid boundary effects on the measurements. The dotted positions are manually identified in the software of the camera and are made suffisciently distant from each others to prevent the marker tracker from inverting their positions during the experiment. The tracking system is based on taking regularly pictures of the zone of interest and saving the coordinates of the central points of each identified marker. The good measurement of the displacement of the

markers is based on the hypothesis that the pictures are taken in a frequency that is higher than the one related to the variations of the actual displacement field and the dots do not overlap or switch positions so that the new position of a marker is found by tracing a high contrast gap around the previous position. The transverse and longitudinal strains are respectively computed by dividing the measured transverse and longitudinal displacement by the initial distance between the markers in the transverse and longitudinal directions. In turn, the applied force on the sample is acquired using a load cell of ±10N connected to the computer and the engineering stress is computed by dividing it by the gage section 5×5 mm^2.
The Young moduli is computed by the slope between the engineering stress and strain in the linear behavior $E_S = \dfrac{\mathrm{d}\sigma_{11}}{\mathrm{d}\varepsilon_{11}}$ while the poisson ratio is taken as the opposite of the slope between the transverse and longitudinal strains $\nu_S = -\dfrac{\mathrm{d}\varepsilon_{22}}{\mathrm{d}\varepsilon_{11}}$. The results of the tensile tests at ambient temperature and at a strain rate of $\dot{\overline{\varepsilon}} = 10^{-5}s^{-1}$, similar to the one chosen to conduct the experiments on porous material, give a tensile modulus $E_S = 1.3 \pm 0.1$MPa and a Poisson's ratio $\nu_s = 0.25$ and the stress-strain curve shows that the support material has a brittle fracture at strains around 1%.

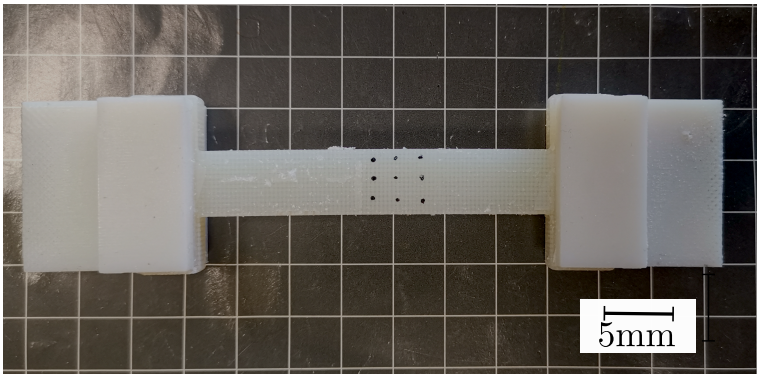

Figure II.16 – (a)Virtual design of the specimen used to enforce support material testing (b) 3D-printed specimen prepared in order to test the elastic properties of the support material.

II.3.4.b The effect of support on composite material properties

The experimental characterization of the proposed porous materials shows that the measured elastic moduli E_S and E_m have a contrast of almost thousand times. Besides that, the mechanical characterization , conducted in this study to properly account for the 3D printed material as porous-like material, needs to account for the effect of this support material and examine if it behaves closely to a voided material. To that aim, two methods were developped. An experimental assessment of the negligeable effect of the support material has been conducted by printing and chacterizing specimens with gage zone consisting of aligned cylinders in the direction of the specimen thickness (see insets in Fig.II.18) in two configurations; one where the support material has been removed from the cylinders and the other one where the support material has been retained. Results of the apparent overall

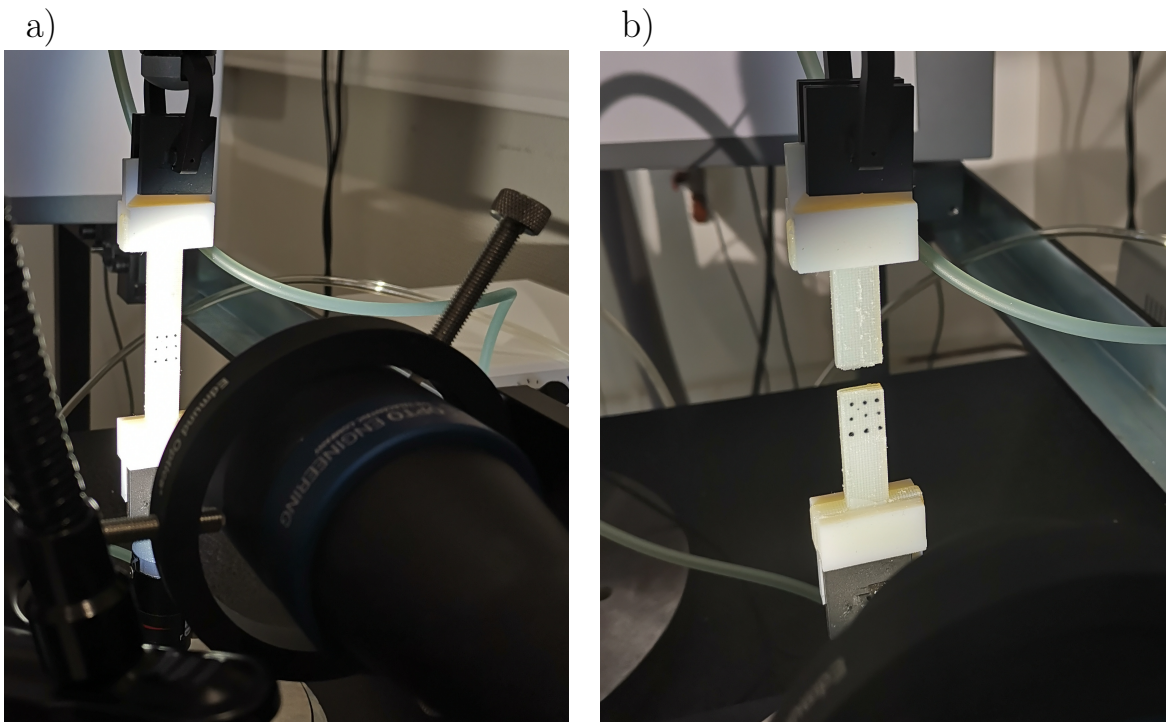

Figure II.17 – (a) Experimental setup used in order to characterize the support material of the 3D-printer (b) Illustration of the brittle fracture of the support material occuring in the central region of the gage zone.

Young's modulus [1] for these two structures are shown in Fig. II.18. No significant difference is found between the two configurations, indicating that the support material has negligible elastic properties when compared with those of the virgin matrix material (VerowhitePlus).

The second verification consists in numerical simulations using FEM conducted on the RSA microstructures at different volume fraction c at two configurations: one where the inclusions are meshed and associated to the isotropic elastic properties of the support material and another one accounting for porous inclusions. The overall elastic properties of both configurations were obtained using the same procedure as the one introduced in Sec.II.2.1 and comparison between the elastic moduli shows that a negligeable deviation is introduced by the thousand-times softer material in comparison with the fully porous material when considering a linear elastic behavior. These results are confirmed by the Hashin-Shtrikman two-phase upper bound as can be seen in the Fig.II.19.

1. Note that these structures are not representative and hence the measured elastic properties are those corresponding to a structure and not a material.

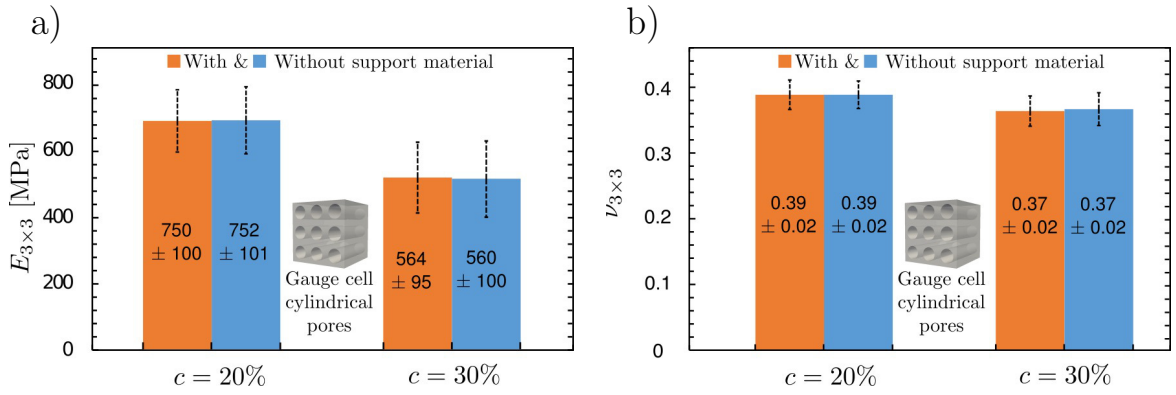

Figure II.18 – Experimental results of the apparent (a) Young's modulus and (b) Poisson's ratio for the investigation of the effect of the support material inside the voided phase. A cylindrical-void specimen is specifically fabricated in order to control the presence or not of the support material. The support material has negligible effect upon the elastic properties.

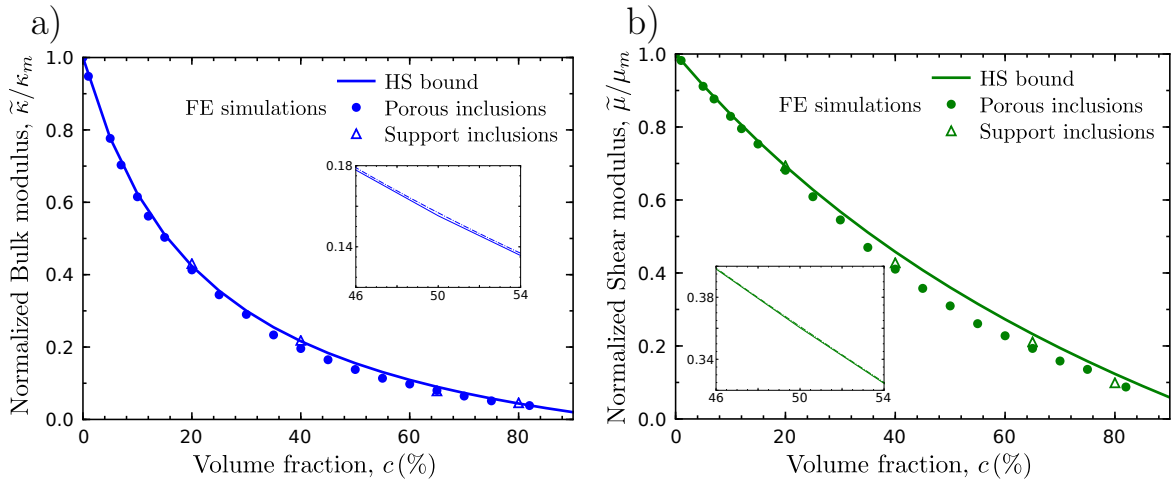

Figure II.19 – Numerical results of normalized (a) effective bulk modulus $\widetilde{\kappa}/\kappa_m$ and (b) effective shear modulus$\widetilde{\mu}/\mu m$ for microstructures with inclusions computed using either void properties for the inclusions or the support material properties. Bounds of HS in both cases are plotted along with the numerical computations to highlight the low difference in analytical estimates between the two configurations.

II.4 Experimental effective elastic properties of the 3D printed porous materials

II.4.1 Experimental isotropy assessment

An important aspect of the experimental study (similarly to the numerical one) is the isotropy of the 3D-printed RVEs. It is noted here that this is a non-trivial analysis since the RVEs under study do not exhibit any symmetry planes, as is the case in highly periodic trusses and lattices. Moreover, from the corresponding numerical study, we observe that the random dispersion of the inclusion in

such RVEs leads to similar tensile and shear moduli along the three orthogonal directions of the cube cell.

In order to probe the degree of isotropy in our 3D-printed composites, the Young's modulus along the three orthogonal axes of the cubic RVE at selected volume fractions of void-like inclusions, e.g. $c = 65\%, 70\%$ and 75%, where the RVEs comprise a very large number of void sizes. This is achieved by first rotating the generated cubic cell along its three axes and then by using each rotated cell to construct the virtual test sample. The latter is then 3D-printed and tested. Attention is here limited to the axial stiffness, since the scatter observed in the measurements of the Poisson's ratio would make it difficult to compare the values. To separate between anisotropy factors related to the process and those inherent to the microstructure, numerical simulation are conducted on the same realizations. As expected, the degree of anisotropy found on the experimental measures is small with differences between the largest and the smallest experimental moduli found to be respectively 12, 9 and 6% for $c = 75\%, 70\%, 65\%$. These deviations are in the order of the experimental scatter found for the properties of the pure matrix. In turn, differences in the numerical estimates are negligible and are consistent with the values of the deviation from isotropy $\delta_{iso} < 1\%$.

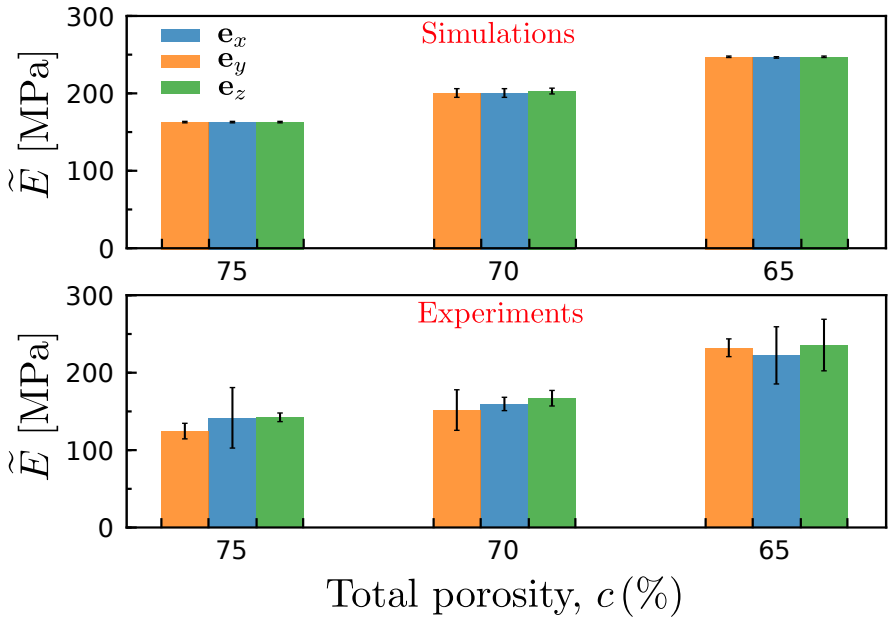

Figure II.20 – (Top) Numerical estimates of the Young's modulus along the three orthogonal directions for moderate-to-high volume fractions c. (Bottom) The experimental measurements of the Young's modulus along the three orthogonal directions conducted on the specimens built using rotation of the unit-cell microstructures

II.4.2 Evolution of the effective elastic moduli of 3D printed specimen with porosity

In this section, we compare the theoretical Hashin-Shtrikman (HS) bounds for isotropic porous materials, with numerical (FEM) calculations and the present experimental measurements. Since, the

proposed microstructures exhibit almost perfect isotropy by construction, direct comparison of their elastic effective properties with the HS isotropic bounds is meaningful in terms of moduli, such as the Young's modulus and Poisson's ratio or equivalently the bulk and shear moduli. For isotropic porous materials, the Hashin-Shtrikman bounds (Hashin and Shtrikman, 1963b; Willis, 1977) are given by the expressions in Eq.II.A.2.b. The corresponding effective Young's modulus, $\widetilde{E}$ and Poisson's ratio, $\widetilde{\nu}$, are readily obtained by Eqs. II.4.2.

It is recalled at this point that the HS homogenization bounds refer to infinitely polydisperse (i.e. infinite sizes of) voids. Nonetheless, as we will be discussed in Sec.II.4.3, for porosities up to $c = 30\%$ (see also Anoukou et al. (2018)), the monodisperse and polydisperse results are almost identical. Moreover, we recall here that both the FEM and experimental results correspond to four different realizations and samples, respectively, for each porosity. Figure II.21 shows the effective (a) Young's modulus $\widetilde{E}$, (b) Poisson's ratio $\widetilde{\nu}$, (c) bulk modulus $\widetilde{\kappa}$ and (d) shear modulus $\widetilde{\mu}$ as a function of the porosity c. The results are abtained as the average of at least four specimens and are reported together with their error bar. For comparison, the HS upper bounds fo an isotropic porous medium are plotted alongside the FE approximations. The latter are computed from values shown in Fig. II.21 using the standard linear elastic equivalence:

$$\widetilde{E} = \frac{9\widetilde{\kappa}\widetilde{\mu}}{(3\widetilde{\kappa} + \widetilde{\mu})} \quad \text{and} \quad \widetilde{\nu} = \frac{(3\widetilde{\kappa} - 2\widetilde{\mu})}{(6\widetilde{\kappa} + 2\widetilde{\mu})} \tag{25}$$

It can be observed that the experimental results for the directly measured $\widetilde{E}$ are in very good agreement with the numerical FE results and lie very close to the HS bound. The maximum deviation of the experimental Young's modulus $\widetilde{E}$ from the theoretical HS bound is observed at moderate porosity, where the error bars exhibit the highest scatter suggesting that a main factor for this dispersion is the conditioning of the polymeric material during 3D printing as well as measurement sensitivity resulting from the extensometers. In turn, the measured values of the Poisson's ratio varies a lot and more particularly when the volume fraction increases due to the sensitivity for the measurements of the transverse strain at large volume fraction of inclusions (Tarantino et al., 2016) and departs from the HS estimates for $c \geq 40\%$. It is noted that the FE results exhibit very small deviation (less than 0.1%), and thus the corresponding scatter is not shown explicitly in the plots.

II.4.3 Discussion

It is relevant at this point to make a few important comments. In particular, we recall that the Hashin-Shtrikman bounds are obtained by setting a constant stress polarization in the inclusion phase (Hashin and Shtrikman, 1963b; Willis, 1977), which implies uniform stress and strain fields therein. That allows to obtain the Eshelby (1957) exact solution for a dilute volume fraction. Nevertheless, this choice of uniform stress polarization is only approximate for spherical or ellipsoidal inclusions and moderate to high volume fractions (Willis, 1977). This has the following two implications. First, spherical voids cannot reach, even numerically, the HS bounds with increasing porosity, since the fields cannot remain uniform inside the inclusions due to strong interactions between them.

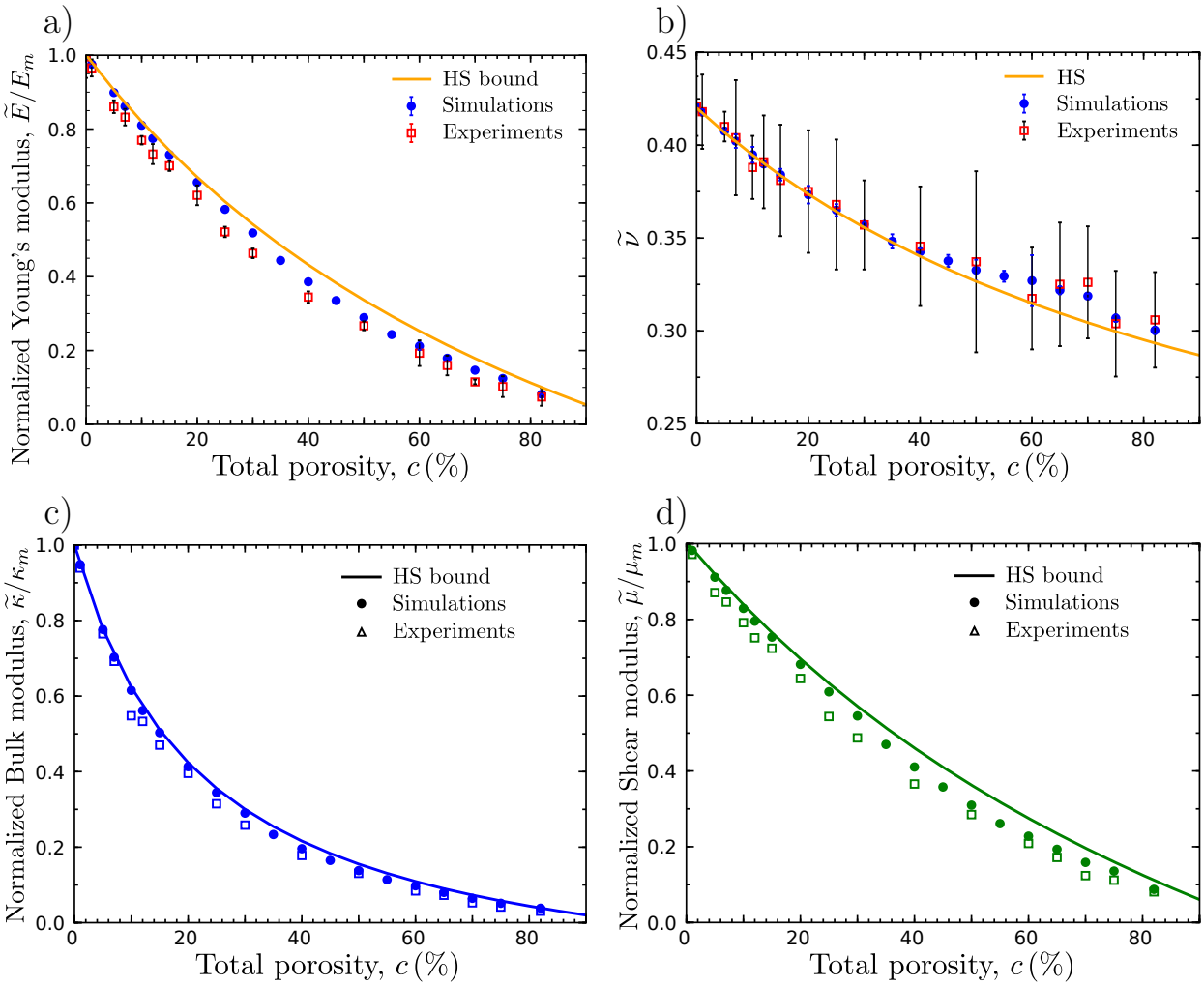

Figure II.21 – Normalized with the matrix properties effective (a) Young's modulus $\widetilde{E}/E_m$, (b) Poisson's ratio $\widetilde{\nu}$, (c) bulk modulus $\widetilde{\kappa}/\kappa_m$ and (d) shear modulus $\widetilde{\mu}/\mu_m$ as a function of the porosity c. Comparison between the analytical HS bounds, FE monodisperse numerical estimates and experimental results.

Nevertheless, it is more than interesting to observe in Fig. II.21 that both the experimental and numerical effective elastic moduli for spherical voids remain very close to the theoretical HS bounds. Second, we recall that the 6-rank laminate microstructures (Francfort and Murat, 1986) and the infinite rank-laminates (Idiart, 2008) do attain the HS bounds primarly because the fields inside each phase of the microstructure are uniform and thus are in line with the constant sress polarization assumption used in the HS bounds. It is however difficult to-date to reproduce realistically such microstructures due to the many length scales involved in their construction (but see Sigmund (2000) towards this direction). In order to explain the small differences between the FE and the experiments. two major features appears to us in relation with the experimental setup and the local fields obtained by our FE calculations. From the experimental side, the scatter can be related to the uncertainty in the elastic moduli of the matrix polymer which is in the same order with the deviation. The

second feature is related to the local nonlinear strains that are developed in the experimental material while the FE calculcation neglect because of the linear elastic assumption made on the behavior of the material. Specifically, we show in the insets of Fig. II.22 strain contours for selected porosities $c = \{5\%, 12\%, 25\%\}$. The uniform distribution of voids avoids clustering and leads to rather minimal stress and strain concentration in regions between the voids. For porosities up to 10%, the local strain fluctuations induced by the microstructural heterogeneities remain relatively small by comparison to the overall applied strain $\boldsymbol{\varepsilon}$ (see colorbars). When increasing the porosity, the denser packing of the voids creates more localized strain zones with more pronounced strain fluctuations with respect to the average strain. This implies significant interactions between voids, which, in turn, lead to the deviation observed between the numerical results and the theoretical HS bounds. Nevertheless, this deviation remains very small ($< 4\%$) (see also Böhm and Han (2001)).

In turn, Figure II.23 shows the local strain fields fo higher porosities, i.e. $c = 40, 50, 65, 75$ and

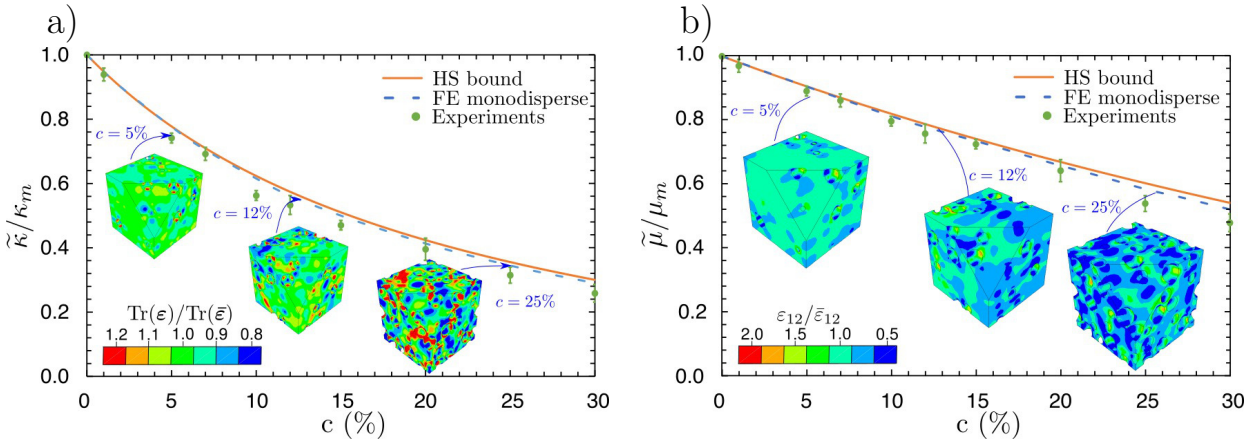

Figure II.22 – Normalized with the matrix properties effective (a) bulk modulus $\widetilde{\kappa}/\kappa_m$ and (b) shear modulus $\widetilde{\mu}/\mu_m$ for monodisperse microstructures (porosity $0 \leq c \leq 30\%$). Insets of the local strain field normalized by the overall field are shown by contour plots obtained from compressibility loading in the case (a) and of shear loading conditions for case (b).

82%, under hydrostatic and shear loadings with periodic boundary conditions. The contour plots highlights the fact that the deviation from the average value are much higher at middle range porosities $40\% \leq c \leq 60\%$, whereas the field near the internal boundaries of the voids are found to become uniform with decreasing porosity, $c \leq 30\%$ or increasing porosity (i.e. $c > 60\%$). In connection with those last observations, it is important to mention that in the FE calculations the local strains can reach values that are almost twice that of the average strain applied, see for instance $\varepsilon_{11}/\varepsilon_{11} \sim 2$ in the insets of Fig. II.22 and Fig. II.23. This, in turn, implies that in the experimental results and usually for porosities higher than 20%, the amplitude of the local strain fields could exceed the range of validity of linear elasticity in several regions of the unit-cell. For large porosities, those local strain fluctuations in random closed-cell porous solids are a direct consequence of the interaction between the closely packed spherical voids. This leads to a local nonlinear response of the matrix phase, especially in our experiments (see inset of Fig. II.13a), which constitutes an additional

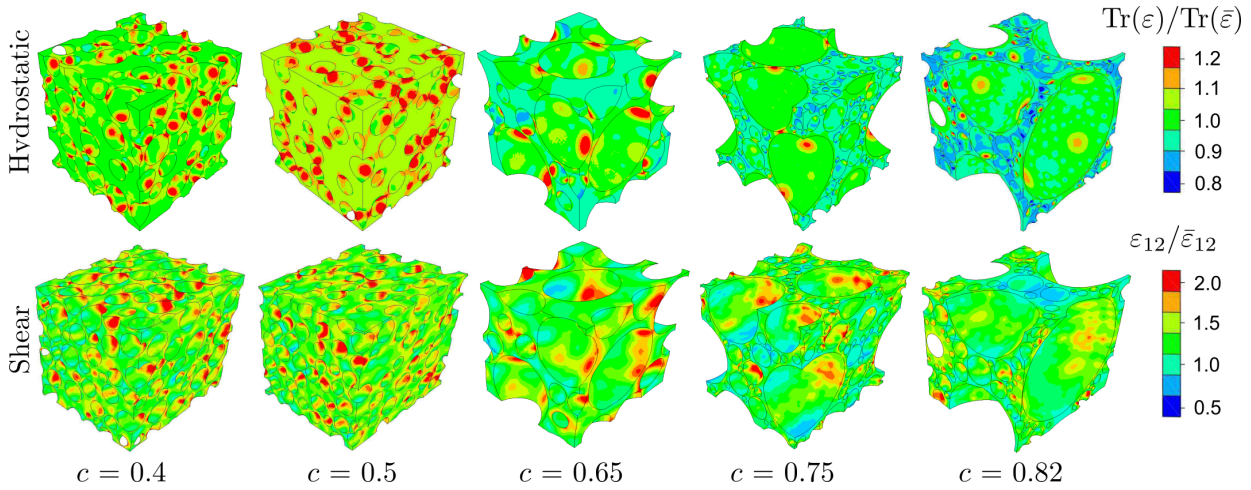

Figure II.23 – Local strain fields normalized by the overall field shown by contours plots for different volume fraction of RSA microstructures obtained from the automatic algorithm. The upper column shows the dispersion of the normalized bulk strain field obtained from compressibility simulation. The lower-one depicts the plots for normalized shear moduli.

reason for the differences observed between the HS linear bounds or the FE and the experimental measurements. However, when porosity increases to the point were the matrix ligament between the voids becomes very thin, the strain fields gradually become uniform again and that closes their gap with HS bound.

To correlate the observed local strain fields with the porous microstructures, we report in Fig.II.24 the simulated microstructures at porosity $c = \{20\%, 50\%$ and $82\%\}$ together with the numerical strain contours for hydrostatic loading. In agreement with the analysis in Fig.II.20, with increasing porosity the microstructure evolves from a random monodisperse to a finitely polydisperse distribution of spheres. As discussed earlier, the largest void diameter is observed to increase as the porosity increases from $c = 20\%$, $c = 50\%$ and $c = 82\%$(Fig.II.23). Collectively, the numerical micrographs in Fig. II.24 reveal micro- structural features similar to those reported for other random closed-cell foams produced by conventional foaming process. Prior studies on foamed polymers (Youssef et al., 2005; Dawson and Shortall, 1982; Saha et al., 2005), glass(Walsh et al., 1965) and ceramics (Meza et al., 2017) with porosity between 30% and 75%, show that the microstructure of these materials consists of a homogeneous (random) distribution of nearly spherical bubbles. These bubbles are found to be uniform both in size and shape at low porosity (Youssef et al., 2005; Dawson and Shortall, 1982), but gradually become polydisperse as the porosity increases (Dawson and Shortall, 1982; Saha et al., 2005). Interestingly, similar to random closed-cell foams (Youssef et al., 2005; Dawson and Shortall, 1982; Kim et al., 2005), the present porous composites (see the magnifications in the bottom row of Fig.II.24) clearly show that there is no unique minimal thickness for the inter-inclusion ligament t. This is a direct consequence of the void polydispersity and randomness. At high porosity, e.g. $c = 82\%$ (Fig. II.24), the matrix ligament between two neighboring large voids contains a number of smaller inclusions as is the case also for foamed polymers and ceramics at low density in

Refs. Dawson and Shortall (1982); Saha et al. (2005); Kim et al. (2005). Finally, in Fig. II.25 we

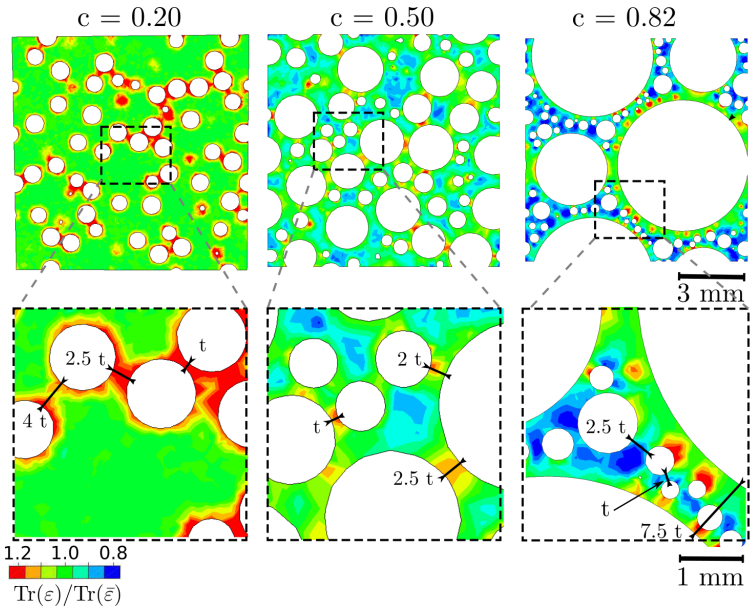

Figure II.24 – Local strain fields normalized by the overall field shown by contours plots for different volume fraction of RSA microstructures obtained from the automatic algorithm. The upper column shows the dispersion of the normalized bulk strain field obtained from compressibility simulation. The lower-one depicts the plots for normalized shear moduli.

compare, at equal matrix volume fraction $1-c$, the measured normalized axial stiffness of the present closed-cell random porous materials with recent porous materials as well as with fully-stochastic foams produced by more conventional manufacturing processes (e.g. foaming and replication). As seen, the 3D-printed porous solids of this work exhibit normalized Young modulus values that rival those of closed-cell stochastic foams. The study on the porous glass (Walsh et al., 1965) (whose moduli are reported in Ref. (Roberts and Garboczi, 2001) and in Fig.II.7 alongside experimental investigations on other foamed polymers (Youssef et al., 2005; Dawson and Shortall, 1982; Saha et al., 2005), indicate that the microstructure of these materials comprises similar geometrical features to those of the present composites. More interestingly, our materials are almost twice stiffer than most open-pore microcellular foams (Despois and Mortensen, 2005) and two to five times stiffer than two of the most performing metamaterials demonstrated today. The latter are the nano- and macroscale octet-truss lattices fabricated by 3D laser writing (Meza et al., 2017). Hence, the present random 3D-printed porous materials are promising candidates in terms of relative stiffness per unit-volume. The advantages they offer over other fully stochastic cellular solids, i.e. foams, produced by conventional processing routes (for which data in Fig. II.25 are taken from Ref.Roberts and Garboczi (2001)) are many. These notably are the precision of the size and shape of the pore-inclusions as well as the ability to reach very large and precise volume fractions in a straightforward and controlled manner. Moreover, by virtue of their fully random architecture the proposed materials offer the added benefit of being fully isotropic, whereby most of today's lightest and stiffest metamaterials of the same porosity

are not (Compton and Lewis, 2014; Bauer et al., 2014; Han et al., 2015; Meza et al., 2017). On the other hand, the present materials are not cellular in the sense of relative density (but behave as such in the mechanical sense). As explained before, the reason is that the inclusions are made of a gel-like material that, despite having low axial stiffness and behaving mechanically as a porous-like phase as shown in Sec.II.3.4, it has almost the same density of the matrix material. In order to overcome this issue, several ideas are currently being explored such as introducing a minor connectivity between the inclusions and using a chemically soluble support material. Nonetheless, this is an effort at the very early stages and is left to a future study.

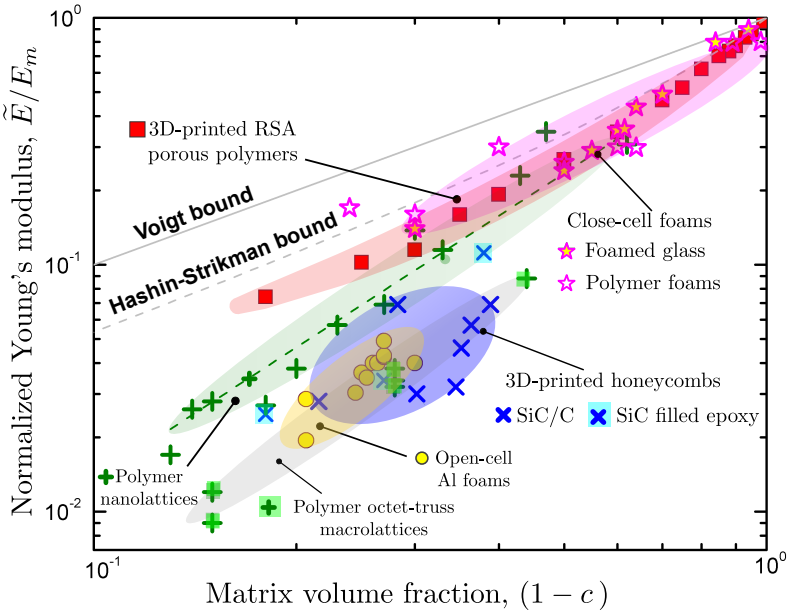

Figure II.25 – Property space map of the Young's modulus vs volume fraction of the matrix $(1-c)$, comparing the present isotropic 3D-printed porous polymers (red solid squares) with other closed-cell and open-cell foams as well as with lattice microstructures of similar volume fraction.

II.5 Concluding remarks

In this study, the elastic fields of random porous microstructures consisting of non-overlapping, finite polydisperse spherical void inclusions embedded in a homogeneous isotropic matrix have been explored in order to create polymeric (choice dictated by 3D printer) porous-like materials for volume fraction that extends from $c = 0$ up to $c = 82\%$. The microstructures are generated using RSA algorithms with different parameters to control the morphology of the inclusions and to optimize the generation of microstructure for the specific use of highly porous materials.

The chapter presented the combined numerical and experimental roadmap used to convert a computer-designed random medium into a 3D printed building material. This workflow starts from the generation of microstructures, then a numerical study has been implemented to define a cubic RVE using the convergence of the overall elastic moduli (i.e. $\widetilde{\kappa}$ and $\widetilde{\mu}$) of microstructures having the same porosity

and decreasing number of the characteristic size of heterogeneities, for the Kinematically uniform (KU-) and Periodic Boundary Conditions (PBC). The resulting cubic RVE has been subsequently assembled to form a standard dog-bone specimen for uniaxial tensile tests.
The 3D printing process and materials were analyzed in order to address the anisotropy due to the printing procedure as well as the one related to the randomness of the microstructure. The support material used by the 3D PolyJet printer to sustain voided structures has been tested and its overall elastic properties have been shown to have negligible effect on the effective properties of the composite microstructures due to the high contrast (1:1000) in the elastic properties with those of the matrix building polymer (VeroWhitePlus). The purely energetic elastic moduli of the heterogeneous materials has been obtained by an experimental procedure of multi-step relaxation at relatively small strains chosen in order to overcome the viscous effect of polymers.
An important result of the work presented in this chapter is that RSA microstructures consisting of spherical voids, for monodisperse moderate porosities (up to 30%) and polydisperse in size high porosities (up to 82%), provide effective elastic moduli that lie very close to the optimal isotropic Hashin-Shtrikman bounds. The differences between FE simulations, experimental results and Hashin-Shtrikman bounds were analyzed using the local strain fields obtained by numerical computations. The observations confirm that the deviation is related to strain localization which is found to be higher at moderate porosity whereas the elastic fields become more uniform at both ends of the volume fraction, i.e. $c \leq 30\%$ and $c \geq 70\%$. Furthermore, the normalized effective Young's modulus of the presented random microstructures exhibits stiffer properties than any experimentally tested isotropic foams and metamaterials and are promising microstructures for lightweight highly-stiff materials if 3D printing technology improves the printing of voided closed zones.
This first part of the thesis shows that the optimal effective elastic moduli of isotropic materials are almost attained by the isolated spherical pores with single-sized and polydisperse in size microstructure for a large range of porosities. However, in some cases, one would want to be able to trigger the microstructures in order to create isotropic porous microstructures with controlled effective properties. The question is therefore, which parameters of the microstroctures are significantly influencing the elastic properties of material. The next part of this thesis is devoted to this topic. The objective is to assess the infuence of some statistical descriptors of the microstructures such as the correlation function, the chord length distribution and the connectivity on the efective elastic properties.

APPENDIX

II.A Basic definitions for the effective elastic properties of heterogeneous materials

This section briefly recalls the basic assumptions on the heterogeneous materials related the determination of their effective properties. It starts by introducing, in Sec.II.A.1, the micromechanical problem of linear elasticity in heterogeneous materials and presents the different boundary conditions that are needed in order to determine the effective elastic properties in a representative volume element. Section III.1.1 introduces the n-point statistical descriptors needed in order to characterize the morphology of a random composite. In turn, Section II.A.2 recalls the classical first and second-order bounds on the effective properties of isotropic two-phase microstructures and highlights some examples of theorethical microstructures assessing the optimality of the second-order bounds of Hashin-Shtrikman (Hashin and Shtrikman, 1963b). This Hashin-Shtrikman bound is therefore the target for creating materials with high stiffness and low-density function which is the topic of the Chapter II.

II.A.1 Linear elasticity problem

Assuming statistically homogeneous and ergodic materials with no body force, the theory of homogenization relies on the scale separation between three characteristic lengths characterizing a mechanical problem in heterogeneous material. Specifically, the characteristic size d of the smallest heterogeneities is much smaller than the characteristic size L of the cell under study and the characteristic size l of variation of the applied loading. A Representative Volume Element (RVE) is defined as the cell size V in which these conditions are satisfied. Therefore, a sample constituted of such volume can be regarded as a homogeneous material with stiffness tensor corresponding to the effective elastic properties $\widetilde{\mathbb{C}}$ in V.
In order to obtain the effective stiffness tensor, one need to solve the local problem of linear elasticity

which can be formulated in the case of imposed strain boundary conditions as:

$$\begin{cases} \text{div } \boldsymbol{\sigma} &= \mathbf{0} \\ \boldsymbol{\varepsilon}(\mathbf{x}) &= \frac{1}{2}[\nabla \mathbf{u} + \nabla^{\mathrm{T}} \mathbf{u}] \\ \boldsymbol{\sigma}(\mathbf{x}) &= \mathbb{C}(\mathbf{x}) : \boldsymbol{\varepsilon}(\mathbf{x}) \\ \mathbf{u}(\mathbf{x}) &= \overline{\boldsymbol{\varepsilon}} \cdot \mathbf{x} \end{cases} \tag{26}$$

where $\boldsymbol{\sigma}(\mathbf{x})$ is the local stress field, $\boldsymbol{\varepsilon}(\mathbf{x})$ the local strain field and $\mathbb{C}(\mathbf{x})$ is the fourth-order positive definite stiffness tensor defined locally on each point $\mathbf{x}$ of the material.
The macroscopic stiffness tensor is then obtained by applying the Hooke's model between the average stress $\overline{\boldsymbol{\sigma}}$ and strain $\overline{\boldsymbol{\varepsilon}}$ fields expressed by:

$$\overline{\boldsymbol{\sigma}} = \widetilde{\mathbb{C}} : \overline{\boldsymbol{\varepsilon}} \tag{27}$$

where notation $\overline{\mathcal{X}}$ defines the volume average of quantity $\mathcal{X}$ defined as:

$$\overline{\mathcal{X}} = \frac{1}{V} \int_{\mathbf{x} \in V} \mathcal{X}(\mathbf{x}) \mathrm{d}^3\mathbf{x} \tag{28}$$

$\overline{\boldsymbol{\sigma}}$ and $\overline{\boldsymbol{\varepsilon}}$ thus denote the average stress and strain fields of the material.

II.A.2 Rigorous bounds on the elastic properties of isotropic two-phase materials

Before recalling the first and second-order bounds on the effective elastic properties for random microstructures, it should be mentioned that analytical estimates of the effective elastic properties have been derived using approximations of the elastic heterogeneous field for some particular heterogeneous microstructures. A large number of these estimates are derived from the Eshelby's solution of an inclusion of stifness tensor $\mathbb{C}_i$ embedded in a homogeneous unbounded medium with elastic tensor $\mathbb{C}_0$ and undergoing a uniform macroscopic stress-free strain field $\mathbf{E}$ (Eshelby, 1957). Following a rigorous decomposition of the inclusion problem, the Eshelby's result shows that the strain elastic field $\boldsymbol{\varepsilon}_i$ in the ellipsoidal inclusion are uniform and expressed by:

$$\boldsymbol{\varepsilon}_i = [\mathbb{I} + \mathbb{P}_i^0 : (\mathbb{C}_i - \mathbb{C}_0)]^{-1} : \mathbf{E} \tag{29}$$

where $\boldsymbol{\varepsilon}_i$ denotes the elastic field in the inclusion phase, $\mathbb{I}$ is the fourth-order identity tensor and $\mathbb{P}_i^0(\mathbb{C}_0) = \mathbb{P}_i^0$ is the Hill tensor (Hill, 1963; Willis, 1981) which depends on the stiffness tensor $\mathbb{C}_0$ of the reference medium properties and on the shape and orientation of the ellipsoidal inclusion i (see the recent review by Parnell (2016) on the expression and computation of the Hill tensor for different type of ellipsoids). In turn, the stress field in the inclusion is uniform and is computed from the stress-strain relation for the inclusion:

$$\boldsymbol{\sigma}_i = \mathbb{C}_i[\mathbb{I} + \mathbb{P}_i^0 : (\mathbb{C}_i - \mathbb{C}_0)]^{-1} : \mathbf{E} \tag{30}$$

The effective elastic properties derived from the Eqs.II.A.2 and II.A.2 depend on the choice of the stiffness tensor associated to the reference medium and on the value of the elastic field at infinity **E**. By making the hypothesis over these parameters, multiple models, usually referred to as effective medium models, have been developed, among which the Mori-Tanaka estimates (Mori and Tanaka, 1973), the self-consistent estimates (Budiansky, 1965; Hutchinson and Hill, 1976; Christensen and Lo, 1979) and the differential scheme estimates (Roscoe, 1952; McLaughlin, 1977; Norris, 1985; Nemat-Nasser and Hori, 1990).

While these homogenization estimates can be useful for fast approximation of the effective elastic properties of some heterogeneous materials, their use is constrained to verifying that the hypothesis on the elastic strain and stress fields and the internal morphology are representative of the local interactions inside the real microstructure. Based on rigorous variational principles or asymptotic expansions, bounds can be derived to obtain range of possible values for the effective elastic properties based on general information on the microstructure. Hereafter, the main bounds used for two-phase materials are recalled and specialized for porous materials.

II.A.2.a Classical Hill bounds

Using the classical variational formulation, the linear elasticity problem associated to KUBC (respectively SUBC) can be expressed as minimization problem of the potential energy (respectively the complementary energy) which leads to the Voigt bound (Voigt, 1889) (respectively Reuss bound (Reuss, 1929)) which are expressed for two-phase materials by:

$$\widetilde{\mathbb{C}} \leq \widetilde{\mathbb{C}}_V = c_1\mathbb{C}_1 + (1-c_1)\mathbb{C}_2 \tag{31}$$

$$\left[c_1\mathbb{C}_1^{-1} + (1-c_1)\mathbb{C}_2^{-1}\right]^{-1} = \widetilde{\mathbb{C}}_R \leq \widetilde{\mathbb{C}} \tag{32}$$

The Voigt bound corresponds to an isostrain condition, meaning that it is verified when the strain is the same all over the material, and the Reuss bound corresponds to an isostress condition that involves a uniform stress field in all constituents.

For isotropic linear elastic phases characterized by their bulk κ_r and shear μ_r moduli ($r = 1, 2$ denoting the phase index), these bounds lead systematically to an isotropic composite with effective bulk $\widetilde{\kappa}$ and shear $\widetilde{\mu}$ moduli:

$$\left(\frac{c_1}{\kappa_1} + \frac{1-c_1}{\kappa_2}\right) \leq \widetilde{\kappa} \leq \Big(c_1\kappa_1 + (1-c_1)\kappa_2\Big) \tag{33}$$

$$\left(\frac{c_1}{\mu 1} + \frac{1-c_1}{\mu 2}\right) \leq \widetilde{\mu} \leq \Big(c_1\mu_1 + (1-c_1)\mu_2\Big) \tag{34}$$

In the case of porous materials with homogeneous isotropic matrix with bulk κ_m and shear μ_m moduli, the results simplify:

$$0 \leq \widetilde{\kappa} \leq (1-c)\kappa_m \tag{35}$$

$$0 \leq \widetilde{\mu} \leq (1-c)\mu_m \tag{36}$$

where c denotes the porosity (or porous volume fraction). These bounds are called first-order bounds since they only include information about the elastic properties of the different constituents in the material and their volume fraction information but no information about the distribution or shape of the inclusion or more generally of higher-order microstructural statistics.

II.A.2.b Hashin-Shtrikman bounds

In the case of an isotropic elastic material with two-phase isotropic elastic constituents, improved bounds have been proposed by Hashin-Shtrikman (Hashin and Shtrikman, 1963a) using a minimization principle to the quadratic energy function obtained from the auxiliary formulation of the elasticity problem. In the case of two well-ordered phases such that $\kappa_1 \geq \kappa_2$ and $\mu_1 \geq \mu_2$, the Hashin-Shtrikman upper bounds for the effective bulk and shear moduli are written as:

$$\widetilde{\kappa}_{HS} = \kappa_1 + \frac{1-c_1}{\dfrac{1}{\kappa_2-\kappa_1} + \dfrac{c_1}{\kappa_1 + \dfrac{4}{3}\mu_1}} \tag{37}$$

$$\mu_{HS} = \mu_1 + \frac{1-c_1}{\dfrac{1}{\mu_2-\mu_1} + 2c_1\dfrac{\kappa_1+2\mu_1}{5\mu_1(\kappa_1+\dfrac{4}{3}\mu_1)}} \tag{38}$$

The lower Hashin-Shtrikman bound is obtained by inverting the indexes 1 and 2 in the previous relation (Eqs.II.A.2.b). If the constituents are not well ordered, a similar expression has been developped (Walpole, 1966) introducing an auxiliary isotropic material characterized by $\kappa_0 = \max(\kappa_1, \kappa_2)$ and $\mu_0 = \max(\mu_1, \mu_2)$ for the upper bound and $\kappa_0 = \min(\kappa_1, \kappa_2)$ and $\mu_0 = \min(\mu_1, \mu_2)$ for the lower bound such that:

$$\widetilde{\kappa}_{HS} = \kappa_1 + \frac{1-c_1}{\dfrac{1}{\kappa_2-\kappa_1} + \dfrac{c_1}{\kappa_1 + \dfrac{4}{3}\mu_0}} \tag{39}$$

$$\mu_{HS} = \mu_1 + \frac{1-c_1}{\dfrac{1}{\mu_2-\mu_1} + \dfrac{c_1}{\mu_1 + \dfrac{\mu_m}{6}\left(\dfrac{9\kappa_0+8\mu_0}{\kappa_0+2\mu_0}\right)}} \tag{40}$$

For porous materials of porosity c, the lower bound vanishes and possible values of the isotropic effective elastic moduli are limited by the upper bound of Hashin-Shtrikman:

$$\widetilde{\kappa}_{HS} = \frac{4(1-c)\mu_m\kappa_m}{4\mu_m + 3c\,\kappa_m} \tag{41}$$

$$\widetilde{\mu}_{HS} = \frac{(1-c)(8\mu_m+9\kappa_m)\mu_m}{4\mu_m(2+3c)+3\kappa_m(3+2c)} \tag{42}$$

II.B Algorithms for randomly oriented and non-overlapping ellipsoids

The generation of randomly distributed ellipsoids in a unit cell of volume V is equivalent to the problem of generating random axis uniformly distributed in the space as the ellipsoid orientation is characterized by its three principal axis $n_{i,1}$, $n_{i,2}$ and $n_{i,3}$ which are fully defined by the Euler angles of the solid. In order to build randomly oriented ellipsoid, the Euler angles have to be build such that ϕ and ψ are generated randomly $[-\pi, \pi]$ while the angle θ is generated by randomly picking $\cos(\theta) \in [-1, 1]$ and then setting $\theta = \cos^{-1}(\cos(\theta))$. The next subsections detail the procedure used to ensure the non-overlapping condition between the ellipsoids and the procedure for computing the minimum distance with the cell boundary that is important for both the numerical meshing and 3D printing workflow.

II.B.1 The minimum distance between two ellipsoids

The problem of generating non-overlapping random oriented ellipsoids that are distant by a minimum distance $\Delta_1 > s_1$ in a periodic microstructure is decomposed into two major checking processes. The first one consists in ensuring that the ellipsoid i under verification does not overlap with any of the previously added inclusions or their periodic images. Mathematically, this is equivalent to solve that the following system of equations in $\mathbb{R}^3$:

$$\begin{cases} Q_1 = (\mathbf{x} - \mathbf{v}_i)^{\mathrm{T}} \mathbb{Z}_i (\mathbf{x} - \mathbf{v}_i) - 1 \leq 0 \\ Q_2 = (\mathbf{x} - \mathbf{v}_j + \mathbf{h})^{\mathrm{T}} \mathbb{Z}_j (\mathbf{x} - \mathbf{v}_j + \mathbf{h}) - 1 \leq 0 \end{cases} \tag{43}$$

where vector $\mathbf{h} = (h_1, h_2, h_3)$ is one of the translation vectors for the periodic images of the ellipsoid. To solve the system, the algorithm uses Kurzhanski and Valyi (1997) lemma which states that a necessary and suffiscient condition to prove that two ellipsoids $\mathcal{E}(\mathbf{v}_1, \mathbb{Z}_1)$ and $\mathcal{E}(\mathbf{v}_2, \mathbb{Z}_2)$ intersect is to find for any $\alpha \in [0, 1]$, an ellipsoid $\mathcal{E}(\mathbf{v}_\alpha, \mathbb{Z}_\alpha)$ such that $\det(\mathbb{Z}_\alpha) > 0$ with:

$$\mathbf{v}_\alpha = \Big(\sum_{n=1}^{2} \alpha_n \mathbb{Z}_n \Big)^{-1} \Big(\sum_{n=1}^{2} \alpha_n \mathbb{Z}_n \cdot \mathbf{v}_n \Big) \tag{44}$$

$$\mathbb{Z}_\alpha = \frac{1}{1 - h_\alpha} \sum_{n=1}^{2} \alpha_n \mathbb{Z}_n \tag{45}$$

where $\alpha_1 = \alpha$, $\alpha_2 = 1 - \alpha$ and $h_\alpha = \sum_{n=1}^{2} \alpha_n \big(\mathbf{v}_n \cdot \mathbb{Z}_n \cdot \mathbf{v}_n \big) - \Big(\sum_{n=1}^{2} \alpha_n \mathbb{Z}_n \cdot \mathbf{v}_n \Big) \cdot \mathbf{v}_\alpha$.
In the case of non-overlapping ellipsoids, the minimal distance Δ_1 of the two ellipsoids can be formulated as an optimization problem such that:

$$\begin{cases} & \min ||\mathbf{x}_1 - \mathbf{x}_2||_2 \\ \text{such that} & (\mathbf{x}_1 - \mathbf{v}_1)^{\mathrm{T}} \mathbb{Z}_1 (\mathbf{x}_1 - \mathbf{v}_1) - 1 = 0 \\ & (\mathbf{x}_2 - \mathbf{v}_2)^{\mathrm{T}} \mathbb{Z}_2 (\mathbf{x}_2 - \mathbf{v}_2) - 1 = 0 \end{cases} \tag{46}$$

where $||.||_2$ denotes the Euclidean norm. In order to solve this problem, the algorithm uses an iterative procedure proposed by (Lin and Han, 2002) based on the local approximation of the interior ellipsoid by a ball as shown in Fig.II.B.1.

The iterative process consists in constructing two balls $\mathcal{B}_1(\mathbf{c}_1^k, r_1^k)$ and $\mathcal{B}_1(\mathbf{c}_2^k, r_2^k)$ inside the ellipsoids

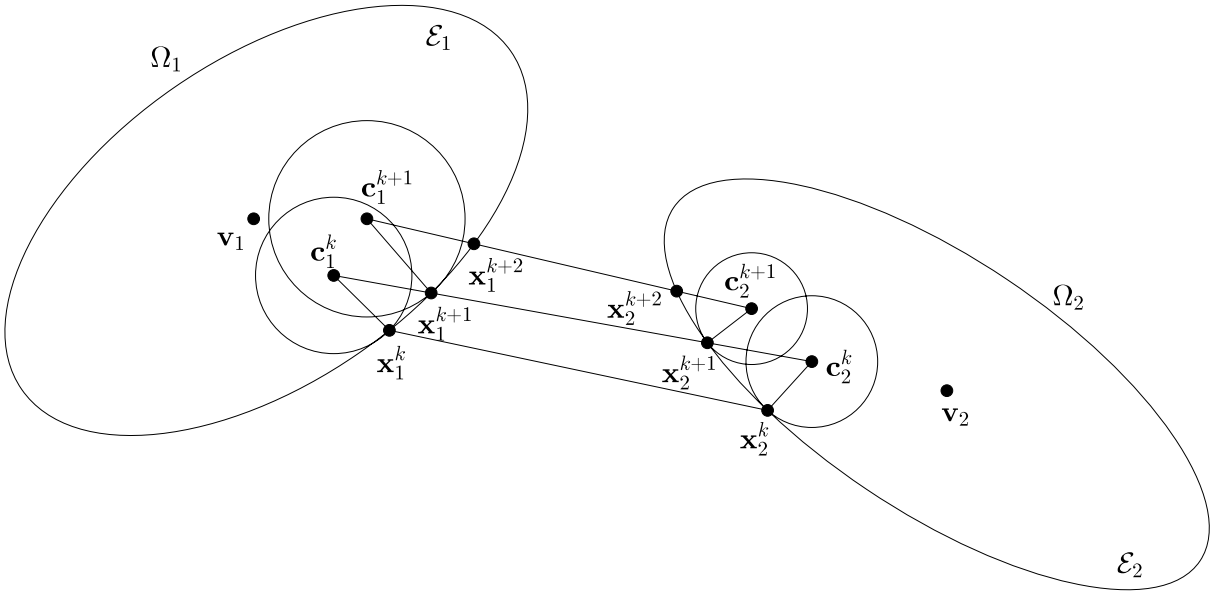

Figure II.B.1 – Geometrical representation of iterative steps to find the minimum distance between two ellipsoids.

$\mathcal{E}_1$,$\mathcal{E}_2$ and tangent to them at two points $\mathbf{x}_1^{k+1}$ and $\mathbf{x}_2^{k+1}$ such that:

$$\mathcal{B}_i(\mathbf{c}_i^k, r_i^k) = \left\{\mathbf{x} : ||\mathbf{x}_i - \mathbf{c}_i^k||_2 \leq r_i^k\right\}, \quad i = 1, 2 \tag{47}$$

where $\mathbf{c}_i^k$ is the center of the ball at the k^{th} step which are initiated at the center positions $\mathbf{v}_i$ for $i = 1, 2$. The position of points $\mathbf{x}_1^{k+1}$ and $\mathbf{x}_2^{k+1}$ are defined uniquely and in a way to verify the minimum distance between the two balls $\mathcal{B}_1(\mathbf{c}_1^k, r_1^k)$ and $\mathcal{B}_1(\mathbf{c}_2^k, r_2^k)$ by constraining them to be expressed as:

$$\mathbf{x}_i^{k+1} = \mathbf{c}_1^k + t_i(\mathbf{c}_2^k - \mathbf{c}_1^k) \quad \text{for } i = 1, 2 \tag{48}$$

where the two parameters t_1 and t_2 are defined as the solution of the system of equations:

$$t_i = \{t \in [0, 1] : A_i t^2 + B_i t + C_i = 0\} \quad \text{for } x = 1, 2 \tag{49}$$

with $A_i = (\mathbf{c}_2^k - \mathbf{c}_1^k)^{\mathrm{T}} \mathbb{Z}_i (\mathbf{c}_2^k - \mathbf{c}_1^k)$, $B_i = (\mathbf{c}_2^k - \mathbf{v}_i)^{\mathrm{T}} \mathbb{Z}_i (\mathbf{c}_2^k - \mathbf{c}_1^k)$ and $C_i = (\mathbf{c}_1^k - \mathbf{v}_n)^{\mathrm{T}} \mathbb{Z}_i (\mathbf{c}_1^k - \mathbf{v}_n)$.
In turn, these two points verify the global minimum distance between the ellipsoids $\mathcal{E}(\mathbf{v}_1, \mathbb{Z}_1)$ and $\mathcal{E}(\mathbf{v}_2, \mathbb{Z}_2)$. The normal vectors to the ellipsoids at these two points are colinear to the vector $\mathbf{x}_1^{k+1} - \mathbf{x}_2^{k+1}$ such that:

$$< \mathbf{N}_i^{k+1}, (\mathbf{x}_1^{k+1} - \mathbf{x}_2^{k+1}) >= 0 \text{ for } i = 1 \text{ and } 2 \tag{50}$$

If that is not the case, the process creates new centers $\mathbf{c}_1^{k+1}$ and $\mathbf{c}_2^{k+1}$ defined by the following expressions that enable to have fast convergence to the minimum distance:

$$\mathbf{c}_i^{k+1} = \mathbf{x}_i^{k+1} - \frac{\gamma_i}{2}\mathbf{N}_i^{k+1} \quad \text{and} \quad r_i^k = \frac{\gamma_i}{2}||\mathbf{N}_i^{k+1}||_2 \tag{51}$$

$\mathbf{N}_i^k = \nabla Q_i$ is the normal to the ellipsoid i at the point $\mathbf{x}_i^k$ and the parameter γ_i corresponds to a measure of the matrix $\mathbb{Z}_i$ related to the spectral radius of $\mathbb{Z}_i$ noted $\rho(\mathbb{Z}_i)$ as follows:

$$0 < \gamma_i < \frac{1}{\rho(\mathbb{Z}_i)} \quad \text{and} \quad \gamma_i = \frac{1}{|||\mathbb{Z}_i|||_F} \tag{52}$$

where $|||.|||_F$ is the matrix Frobenius norm.

II.B.2 Minimum distance between an ellipsoid and a plane

Any surface of the cuboidal cell can be defined by the equation of a plane $\mathcal{P}(\mathbf{n}, \mathbf{A})$ such that:

$$\mathcal{P}(\mathbf{n}, \mathbf{A}) = \Big\{\mathbf{x} : \quad \mathbf{n} \cdot (\mathbf{x} - \mathbf{A}) = 0\Big\} \tag{53}$$

where $\mathbf{n}$ is the normal vector to the plane and $\mathbf{A}$ is a known point on $\mathcal{P}$. For the cubic cell, all planes are defined by combining a normal vector $\mathbf{n} = \mathbf{e}_x, \mathbf{e}_y$ or $\mathbf{e}_z$ with a points $(0,0,0)$ or $(1,1,1)$. The problem of finding the minimum distance $d\big(\mathcal{E}, \mathcal{P}\big)$ between the ellipsoid $\mathcal{E}$ and the plane $\mathcal{P}$ is related to the problem finding the points $\mathbf{x}$ on the ellipsoid for which the normal vector $\mathbf{N}$ is parallel to the plane normal $\mathbf{n}$ such that:

$$\begin{cases} \mathbf{N} \times \mathbf{n} = \mathbf{0} \\ Q(\mathbf{x}) = 0 \end{cases} \tag{54}$$

The solutions of this system of Eqs.II.B.2 gives the closest and furthest points to the plane. To find the minimum distance, it is sufficient to compute the distance of these two points $\mathbf{x}_1$ and $\mathbf{x}_2$ to the plane $\mathcal{P}$ using the formula in Eq.II.B.2 and keep the shortest one:

$$d(\mathbf{x}_i, \mathcal{P}) = \frac{|\mathbf{n} \cdot \mathbf{x}_i + \mathbf{n} \cdot \mathbf{A}|}{||\mathbf{n}||} \tag{55}$$

CHAPTER III

A CRITICAL ASSESSMENT OF SECOND-ORDER STATISTICS

Summary of this chapter: The second part of this thesis is devoted to understanding the link between the microstructures and the effective properties of random porous materials. More specifically, we try to find which simple statistical descriptors of the microstructure, other than the porosity, have a significant effect on the effective elastic properties. In this context, the following chapter presents a quantitative analysis of the deviations on the effective elastic properties that can be obtained by accounting only for the porosity and the two-point correlation function. This assessment is conducted by comparing the effective elastic properties of two different types of microstructures having the same second-order statistical descriptors. First section III.1 gives a brief introduction to the probabilistic low-order description and presents the tools used in order to extract second-order statistical information from a 3D image. Section III.2 is devoted to thresholded Gaussian Random Fields (GRF) which enable to build two-phase random microstructures that are fully described by the porosity and the correlation function. Section III.3 presents the reconstruction methodology and results obtained from the application of these tools on isolated polydisperse pores microstructures with different sets of aspects ratios and analyzes quantitatively the differences in the effective elastic properties that can be obtained from microstructures that share the same second-order informations.

III.1 Second-order statistics of microstructures

III.1.1 Statististical description of microstructures

Predicting the properties of random porous material is an important task for a large number of industrial applications and relies on an accurate modeling of the random microstructures (Escoda et al., 2011; Azzimonti et al., 2013; Figliuzzi et al., 2016; de Francqueville et al., 2019; Cadiou et al., 2019). The microstructures of heterogeneous materials can be characterized statistically via various types of statistical descriptors. A 3D random heterogeneous material occupying a volume $V \subset \mathbb{R}^3$

can be modeled by a random field X for which the random variables $\{X(\mathbf{x}), \mathbf{x} \in \mathrm{V}\}$ takes on N discrete values corresponding to the different constituents. For a particular microstructure sample, the physical properties can be characterized through the probabilistic analysis of the underlying stochastic process.

Focusing on the statistical modeling of two-phase random composites, the material can be defined through the characteristic function $\chi^{(2)}(\mathbf{x})$ of the porous phase, named 2, such that:

$$\chi^{(2)}(\mathbf{x}) = \begin{cases} 1 & \text{if } \mathbf{x} \in \text{ heterogeneity} \\ 0 & \text{else} \end{cases} \tag{1}$$

The matrix phase characteristic function is directly related to the first one by:

$$\chi^{(1)}(\mathbf{x}) = 1 - \chi^{(2)}(\mathbf{x}) \tag{2}$$

Considering $\mathbf{t} = (t_1, t_2, ..., t_n)$ a list of n elements 1 or 2 index , the statistical measure $S_{\mathbf{t}}(\mathbf{x}_1, \mathbf{x}_2, .., \mathbf{x}_n)$ defines the probability that all points $\left(\mathbf{x}_i\right)_{i=1..n}$ lie on the assigned phases $\left(t_i\right)_{i=1..n}$. It can be expressed by the expectation of the random function $\chi^{t_1}(\mathbf{x}_1)\chi^{t_2}(\mathbf{x}_2)..\chi^{t_n}(\mathbf{x}_n)$, such that:

$$S_{\mathbf{t}}(\mathbf{x}_1, \mathbf{x}_2, .., \mathbf{x}_n) = \mathcal{P}\left\{\chi^{(t_1)}(\mathbf{x}_1) = 1, \chi^{(t_2)}(\mathbf{x}_2) = 1, .., \chi^{(t_n)}(\mathbf{x}_n) = 1\right\} \tag{3}$$

For statistically homogeneous media, the n-point distribution function is invariant by translation and thus only depends on the relative positions of the points $\left(\mathbf{x}_i\right)_{i=1..n}$ such that:

$$S_{\mathbf{t}}(\mathbf{x}_1, \mathbf{x}_2, .., \mathbf{x}_n) = S_{\mathbf{t}}(\mathbf{x}_{12}, \mathbf{x}_{13}, .., \mathbf{x}_{1n}) \tag{4}$$

where $\mathbf{x}_{ij} = \mathbf{x}_i - \mathbf{x}_j$ In the particular case when $\mathbf{t}$ is chosen such that $t_1 = t_2 = .. = t_n$, the n-point probability functions are called n-point correlation function as they define the probability that all n points $\left(\mathbf{x}_i\right)_{i=1..n}$ lie on the same phase, i.e. phase 1 or 2.

The exact expression of the effective mechanical properties are known to be dependent on an infinite set of correlation function that statistically characterize the microstructure (Torquato, 1997). In Chapter 12 of the book by Torquato (2002), the procedure in order extraction of these n-point probability functions from two-phase microstructure makes use of Monte-Carlo simulations. It is based on picking randomly n points $\left(\mathbf{x}_i\right)_{i=1..n}$ on the sample and recording the outcome of their joint characteristic function $\chi(\mathbf{x}_1)\chi(\mathbf{x}_2)..\chi(\mathbf{x}_n)$. By repeating this procedure for a large number of sets, the n-point correlation function could be determined. However, such procedure is prohibitive due to the time and computational memory needed in order to obtain statistical order, even for order higher than 3-point correlation function.

Due to this computational limitations, available statistical information for modeling of real microstructures are usually restrained to third-order correlation function obtained from 2D images (Yao et al., 1993; Roberts, 1997; Gillman et al., 2015) for microstructures assumed to be isotropic and second-order information when it comes to the study of 3D images of general materials (Øren and Bakke, 2002; Neumann et al., 2019). Because of their simple implementation (see Sec.III.1.3), a popular approach for modeling random materials consists in employing statistical models of the

microstructures based on the first and two-point stastistics (Teubner, 1991; Levitz, 1998; Roubin et al., 2015; de Francqueville et al., 2019). In this context, an important question is wether these statistics are sufficient to distinguish between microstructures in term of their effective elastic properties and the resulting uncertainties.

Studies devoted to statistical reconstruction based on the second-order information have been mostly limited to the study of morphology mimicking and the permeability properties which are known to be highly dependent on the connected porous network of the microstructures(Roberts, 1997; Roubin et al., 2015; Øren and Bakke, 2002). These studies pointed out significant differences in the morphological features of the heterogeneous phase between microstructures having similar correlation functions and have shown that these different internal geometries lead to deviations in the transport properties of the materials under comparison. In this case, a popular approach (Roberts, 1997; Roubin et al., 2015) consists in generating multiple statistical reconstructions using the same second-order statistics and then chosing a particular statistical or morphological parameter to select the right reconstruction model for the real microstructure. The physical properties investigated are then computed in order to assess the reconstruction procedure. These studies are based on approximating the correlation function of the microstructures by an analytical model which tries to match the exact correlation function of the real material by some fitting parameters. The procedure leaves therefore some uncertainties on the causes of the deviation between the effective properties of the second-order model and the investigated material. The methodology proposed by Roberts (1997) has been applied to model the effective elastic properties tungsten-silver composite and has found that the level-cut GRF reconstructed from the two-point correlation function was sufficient to retrieve the experimental elastic properties of the real material. These results showing that the second-order models can accurately predict the mechanical behavior of some specific heterogeneous materials (Roberts, 1997; Roubin et al., 2015) do not enable to conclude on the ability of the correlation function to predict the effective elastic properties of materials.

This chapter presents a quantitative analysis of the differences in the effective elastic properties that can be obtained from modeling random porous microstructures based only on the correlation function. To that aim, we consider two different types of microstructures having the same two-point statistical descriptors. The first type of microstructures consist of isolated ellipsoidal pores uniformly distributed inside the unit cell. The second type of microstructures is obtained by applying a level-cut to a Gaussian Random Field (GRF). This GRF is generated using the porosity and the correlation function measured on the first type of microstructures and thus, ensures similar two-point statistics between the two random microstructures. The chapter is organized such that the important properties related to the two-point correlation function and their practical extraction from images of the materials are briefly recalled in Sec.III.1. Section III.2 details the choice of GRFs in order to create statistically controlled random porous microstructures based only on the volume fraction and the correlation function. Section III.3 applies the GRF reconstruction procedure using the correlation function extracted from RSA microstructures with ellipsoidal inclusions of aspect ratio ω. The elastic properties of both the isolated inclusions microstructures and their associated thresholded GRF are

computed using FFT-based simulation. Comparison of the elastic properties of microstructures with the same two-point statistics highlights the insufficiency of these low-order statistics to distinguish the effective elastic properties of porous microstructures.

III.1.2 Correlation function properties

The second-order information consists of the volume fraction of phase i which can be computed using the expectation value of the indicator function of the phase $\chi(\mathbf{x})$ such that:

$$c = \mathcal{P}\Big\{\chi(\mathbf{x}) = 1\Big\} \tag{5}$$

The second statistical descriptors is the two-point correlation function of the porous phase 2, noted $S_{22}(\mathbf{x}_1, \mathbf{x}_2)$, which is simply written $S_{22}(\mathbf{r})$ for statistically homogeneous medium with $\mathbf{r} = \mathbf{x}_1 - \mathbf{x}_2$ such that:

$$S_{22}(\mathbf{r}) = \mathbb{E}[\chi(\mathbf{x})\chi(\mathbf{x}+\mathbf{r})] \tag{6}$$

The shape of the function $S_{22}(\mathbf{r})$ and its properties has been extensively studied for its use in the theory of second-order random fields (Vanmarcke, 1983; Adler and Taylor, 2007) and modeling of random phenomenon and materials (Levitz, 1998; Roberts, 1997; Roubin et al., 2015). For two-phase microstructures, the two-point correlation functions of both phases are simply related by the expression:

$$\mathbf{S}_{22}(\mathbf{r}) = \mathbf{S}_{11}(\mathbf{r}) - 2c + 1 \tag{7}$$

The cross-correlation $\mathbf{S}_{12}(\mathbf{r})$ which gives the probability that two point distant by a vector $\mathbf{r}$ lie on two different phases can be also directly related to the two-point correlation function of the porous phase such that:

$$\mathbf{S}_{21}(\mathbf{r}) = c - \mathbf{S}_{22}(\mathbf{r}) \tag{8}$$

where the total volume fraction c corresponds to phase 2. Thus, the two-point probability functions of a two-phase material can be fully expressed by the two-point correlation function of the porous phase 2 and will be simply referred to as the correlation function $S_{22}(\mathbf{r})$.
By definition, the function is bounded by the volume fraction of c such that:

$$S_{22}(\mathbf{r}) \leq S_{22}(\mathbf{0}) = c \tag{9}$$

And in the absence of long-range interaction, the random function $\chi(\mathbf{x})$ and $\chi(\mathbf{x}+\mathbf{r})$ are independent for large lag-vectors $\mathbf{r}$ and expectation of their joint function $\chi(\mathbf{x})\chi(\mathbf{x}+\mathbf{r})$ is equal to the squared value of volume fraction c^2:

$$\lim_{|\mathbf{r}|\to\infty} S_{22}(\mathbf{r}) \to c^2 \tag{10}$$

The $S_{22}(\mathbf{r})$ is an even function of $\mathbf{r}$ and is an L-periodic function when the microstructure are L-periodic. In this case, there is no convergence towards c^2 but the $S_{22}(\mathbf{r})$ remains close to the c^2 for sufficiently large values of r in the $[0, L/2]$.

In turn, using a Taylor expansion, it has been shown that the initial slope of the correlation function $S_{22}(\mathbf{r})$ is related to the specific surface s which is an important morphological descriptor of the microstructure defined as the ratio between the interface area and the volume such that for isotropic 3D materials :

$$\frac{\mathrm{d}S_{22}}{\mathrm{d}r}|_{r=0} = -\frac{s}{4} \tag{11}$$

For more details about the morphological and topological information that can extracted from the correlation function, the reader is referred to the work of Adler and Taylor (2007) and Torquato (2002).

Another parameter that is of interest in our study is the correlation length $\mathcal{L}$, the definition of which is based on the correlation function $S_{22}(\mathbf{r})$ in the present work. This parameter is a popular descriptor of the microstructure which has been defined in different ways related to some characteristic lengths in the microstructure. In some studies on reconstructed geomaterials, it is defined as the first distance at which $S_{22}(\mathbf{r})$ reaches c^2 to some uncertainty and relate that to the characteristic size of heterogeneities (Øren and Bakke, 2002). It can also be related to the integral range A of an isotropic random function when $L \to \infty$ which is known to define a reference volume for which the estimation of the volume fraction c is sufficiently precise (Lantuejoul, 2002). For isotropic L-periodic correlation microstructures, choice has been made in this study to define this parameter as:

$$\mathcal{L} = \int_0^{L/2} |S_{22}(r)|\mathrm{d}r \tag{12}$$

III.1.3 Extraction of second-order statistical descriptors from images

These two statistical descriptors can be simply extracted from a voxelized microstructure. For a two-phase material, this 3D representation of a random field $X(\mathbf{x})$ valued on a regular grid points of size $N_1 \times N_2 \times N_3$ can be considered as its characteristic function $\chi(\mathbf{x}) = X(\mathbf{x})$ such that phase 1 takes value 0 and phase 2 takes value 1.

The mean value c of the porous phase corresponds to its first-order stastical descriptor. This can be easily computed by counting the component of the image having the value 1.

In turn, since the Fourier transform of the correlation function $\hat{S}_{22}(\mathbf{k})$ is known to the equal to the power spectrum of the characteristic, the correlation function in the real space is recovered using the inverse Fourier transform:

$$S_{22}(\mathbf{r}) = \int_V |\hat{\chi}(\mathbf{k})|^2 \exp(i\mathbf{r}.\mathbf{k})\mathrm{d}\mathbf{k} \tag{13}$$

For voxelized microstructures, the Eq.III.1.3 is implemented using the direct and inverse discrete Fourier transforms.

III.2 Thresholded Gaussian Random Fields (GRF)

III.2.1 Interest of Gaussian Random Fields:

A random field is fully determined by its n-joint probability distributions $P_{\mathbf{x}_1,\mathbf{x}_2,...,\mathbf{x}_n}(\mathbf{t})$. However, a popular method to model the random heterogeneous materials is to use random fields which only accounts for simple description of the microstructure (Tran et al., 2016; Roubin et al., 2015). To that aim, Gaussian Random Fields (GRFs) are perfect candidates since they are fully controlled their correlation function. Indeed, their n-joint probability distributions can be expressed simply by the expectation m and the correlation function $\rho(\mathbf{r})$. Considering a normalized GRF such that $m = 0$ and $\sigma = 1$, the n-joint probability density function is expressed by:

$$P_{\mathbf{x}_1,\mathbf{x}_2,...,\mathbf{x}_n}(t_1, t_2, ..., t_n) = \frac{1}{(2\pi)^n \det(\mathbf{M})^{1/2}} \exp\Big(- \frac{\mathbf{t^T M^{-1} t}}{2}\Big) \tag{14}$$

where $\mathbf{t} = (t_1, t_2, ..., t_n)$ and $\mathbf{M}$ is the correlation matrix defined such that $M_{ij} = \rho(\mathbf{x}_i - \mathbf{x}_j) = \mathbb{E}[Y(\mathbf{x}_i)Y(\mathbf{x}_j)]$.

A two-phase random microstructure can be obtained by applying threshold to a continuous GRF $Y(\mathbf{x})$ with a level-cut λ such that a discrete two-valued random field $X(\mathbf{x})$ is defined:

$$\begin{cases} Y(\mathbf{x}) > \lambda \rightarrow X(\mathbf{x}) = 1 : \text{phase 1}, \\ Y(\mathbf{x}) \leq \lambda \rightarrow X(\mathbf{x}) = 0 : \text{phase 0} \end{cases} \tag{15}$$

The n-point correlation function $S_{t_1,t_2,..,t_n}(\mathbf{x}_1, \mathbf{x}_2, ..., \mathbf{x}_n)$ of such microstructure are related to the n-joint probability distribution $P_{\mathbf{x}_1,\mathbf{x}_2,...,\mathbf{x}_n}(t_1, t_2, ..., t_n)$ of the continuous GRF and the threshold level λ such that:

$$S_{\mathbf{t}}(\mathbf{x}_1, \mathbf{x}_2, ..., \mathbf{x}_n) = \int_{\lambda}^{+\infty} \int_{-\lambda}^{+\infty} ... \int_{\lambda}^{\infty} P_{\mathbf{x}_1,\mathbf{x}_2,...,\mathbf{x}_n}(\mathbf{y}) \mathrm{d}\mathbf{y} \tag{16}$$

The two-phase microstructure is therefore fully determined by the correlation function $\rho(\mathbf{r})$ and the threshold level λ.

In particular, a direct relation between the cut-off level λ and the volume fraction $c = S_2(\mathbf{x})$ of the thresholded GRF is given by:

$$c = \frac{1}{\sqrt{2\pi}} \int_{\lambda}^{+\infty} \exp\left(-\frac{t^2}{2}\right) dt \tag{17}$$

which can be computed directly using the Gauss error function denoted $erf(\mathrm{x})$:

$$c = 1 - erf(\frac{\lambda}{\sqrt{2}}) \tag{18}$$

In turn, the correlation function $\rho(\mathbf{r})$ of the continuous GRF can be related to correlation function $S_{22}(\mathbf{r})$ using the following relation (Lantuejoul, 2002)

$$S_{22}(\mathbf{r}) = c - \frac{1}{2\pi} \int_{\rho(\mathbf{r})}^{1} \exp\Big(- \frac{\lambda^2}{1+t}\Big) \frac{\mathrm{d}t}{\sqrt{1+t^2}} \tag{19}$$

By performing a derivation of Eq.III.2.1, it can be observed that this relation is independent of the vector $\mathbf{r}$ and defines a one-to-one relation between the correlation function of a continuous GRF and the two-point correlation function of a two-phase microstructure:

$$\begin{cases} \rho^{'}(S_{22}) = 2\pi\sqrt{1-\rho^2}\exp\left(\dfrac{\lambda^2}{1+\rho}\right) \\ \rho(c) = 1 \end{cases} \tag{20}$$

This differential equation enables to have an efficient implementation of the inversion of Eq.III.2.1. Therefore, a statistically controlled random porous microstructure can be generated from the only input of the target two-point correlation function and the porosity thanks to GRFs.

III.2.2 Generation of a GRF

Another interest of using GRFs relies on the central limit theorem. This theorem states that the average of independent and identically distributed random variables converges in distribution to the Gaussian distribution which makes Gaussian random variables and fields easy to generate. Therefore, multiple approaches have been developed in order to generate GRFs among which exact methods based on the matrix decomposition method (Davis, 1987; Dietrich and Newsam, 1993), spectral methods (Shinozuka and Jan, 1972) or some approximate methods such as the turning bands methods (Matheron, 1973) or the sequential simulation (Gómez-Hernández and Journel, 1993; Pebesma, 2004) (see (Liu et al., 2019) for a review on different methods of random field generation). In our work, we constructed a GRF $Y(\mathbf{x})$ in a cubic volume $V = [0, L]^3$ using the spectral method (Shinozuka and Jan, 1972; Shinozuka and Deodatis, 1991; Poirion and Soize, 1995). Such method generates the random field by manipulation in the frequency domain and makes use of the fast Fourier transform to efficiently build a continuous 3D-periodic field for any given covariance function. We generate a continuous L-periodic normalized GRF $Y(\mathbf{x})$ defined by its correlation function $\rho(\mathbf{r})$ expressed by (Poirion and Soize, 1995) (See Appendix III.A for details):

$$Y(\mathbf{x}) = \mathrm{Re}\left(\sqrt{2}\sum_{b_1=0}^{N_1-1}\sum_{b_2=0}^{N_2-1}\sum_{b_3=0}^{N_3-1}\sqrt{\tilde{\rho}_{\mathbf{b}-\mathbf{M}}}Z_{\mathbf{b}}\exp\left(\frac{2\pi}{L}(\mathbf{b}-\mathbf{M})\cdot\mathbf{x}+\Phi_{\mathbf{b}}\right)\right) \tag{21}$$

where $\Phi_{\mathbf{b}}$ are random variables uniformly distributed in $[0, 2\pi[$ and $Z_{\mathbf{b}}$ are random coefficients such that $Z_{\mathbf{b}} = \sqrt{-\ln(\Psi)}$ with Ψ uniformly distributed in $]0, 1]$. Notations $\mathbf{b}$ refers to (b_1, b_2, b_3) and $\mathbf{M}$ are chosen following the grid size $N_1 \times N_2 \times N_3$ such that $M_i = N_i/2$ for even number N_i and $M_i = (N_i - 1)/2$ for odd numbers.

In order that the correlation function of the generated field corresponds to the target correlation function, the Fourier transform of this latter should have a bounded support, i.e. its Fourier coefficients have to be zero above frequencies not accounted by the summation of Eq.III.A. The discrete values of the GRF on a grid $(\mathbf{X}_{\boldsymbol{\beta}})_{\boldsymbol{\beta}\in[0,N_1]\times[0,N_2]\times[0,N_3]}$ are then expressed as:

$$\hat{Y}(\mathbf{x}_\beta) = \mathrm{Re}\left(\sqrt{2}\sum_{b_1=0}^{N_1-1}\sum_{b_2=0}^{N_2-1}\sum_{b_3=0}^{N_3-1}\sqrt{\tilde{\rho}_{\mathbf{b}-\mathbf{M}}}Z_{\mathbf{b}}\exp\Big(-i2\pi\sum_{j=1}^{3}\frac{M_j\beta_j}{N_j}+\Phi_{\mathbf{b}}\Big)\exp\Big(i2\pi\sum_{j=1}^{3}\frac{b_j\beta_j}{N_i}\Big)\right) \tag{22}$$

where $\tilde{\rho}_b$ denotes the Fourier coefficients of the correlation function $\rho(\mathbf{r})$ defined by:

$$\tilde{\rho}_b = \frac{1}{L^3}\int_V \rho(\mathbf{r}) \exp\left(-i\frac{2\pi}{L}\sum_{i=1}^{3} b_i.r_i\right) d\mathbf{r}$$

The discrete values of the GRF expressed in Eq.III.A can be seen as the discrete inverse Fourier transform of the array $\left(\hat{Y}_{\mathbf{b}}\right)$ where $\mathbf{b} \in [0, N_1] \times [0, N_2] \times [0, N_3]$ such that:

$$\hat{Y}(\mathbf{x}_\beta) = \sqrt{2}\exp\Big(-i2\pi\sum_{j=1}^{3}\frac{M_j\beta_j}{N_j}\Big)\mathrm{DFT}^{-1}\Big[(\hat{Y}_{\mathbf{b}})\Big] \tag{23}$$

where:

$$\hat{Y}_{\mathbf{b}} = \sqrt{\tilde{\rho}_{\mathbf{b}-\mathbf{M}}}Z_{\mathbf{b}}\exp\Big(i\Phi_{\mathbf{b}}\Big) \tag{24}$$

III.2.2.a An example of GRFs microstructure

The implementation of the discrete GRF presented in Sec.III.2.2 on a grid of size $N_1 \times N_2 \times N_3$ can be outlined by the following steps:

- **Step 1:** Generation of (N_1, N_2, N_3) arrays of random numbers $Z_{\mathbf{b}}$ and phases $\phi_{\mathbf{b}}$.
- **Step 2:** Compute the square root of the Fourier coefficient of the correlation function $\sqrt{\hat{\rho}_{\mathbf{b}}}$.
- **Step 3:** Compute $Y_{\mathbf{b}}$ defined by Eq.III.A
- **Step 4:** The summation of $(Y_{\mathbf{b}})_{\mathbf{b}\in[0,N_1]\times[0,N_2]\times[0,N_3]}$ is done using FFT algorithms
- **Step 5:** Create array of numbers $\sqrt{2}\exp\Big(-\frac{2\pi}{N_i}\mathbf{M}_i\beta_i\Big)$.
- **Step 6:** The array of the GRF valued on each grid voxel is then obtained by taking the real part of the multiplication of arrays in *Step 5* and *Step 4*.

Using the FFT algorithm, this method enables to quickly generate continuous and periodic GRF in 3D independently of the grid size. To illustrate the obtained thresholded microstructures, we first take for example the periodic correlation function presented in the work of Rasmussen and Williams (2005)

$$\rho(\mathbf{x}, \alpha) = \prod_{i=1}^{3}\exp\left(-\frac{2}{\alpha^2}\sin^2\left(\frac{\pi x_i}{L}\right)\right) \tag{25}$$

The correlation length of this function is difficult to express analytically, however, it is directly linked to the input parameter α. Figure III.2.1 shows the plot of the correlation function for $\alpha = \{0.02, 0.1, 0.3, 0.5\}$. The correlation function is characterise by an initial slope up to a certain distance r characterizing the correlation length that can be interepreted as a characteristic length of heterogeneities in a unit volume. This fast decrease is linked to α and is followed by a slow asymptotic decrease to zero which highlights the no long-range interaction. In order to have an

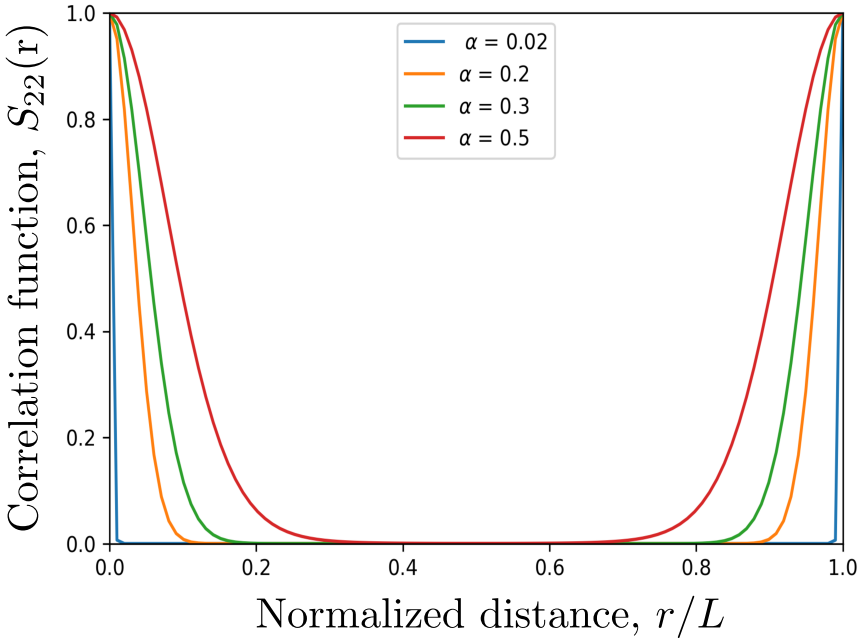

Figure III.2.1 – Periodic correlation function plotted for different values of parameter α.

efficient computation of the fast Fourier transform in the current configuration of the FFT simulation code, the grid size has to be product of powers of small prime numbers. For this example, GRFs were generated on grids of size $256 \times 256 \times 256$. Figure III.2.2 shows a realization obtained for the different input of parameter α. The importance of the correlation length is observed in the fluctuations in the desired porosity versus the porosity obtained. The microstructures with values $\alpha \leq 0.2$ have fluctuations exceeding 10% of the desired porosity. As we decrease the value of α, these fluctuations decrease and the microstructures get more complex with smaller heterogeneities.

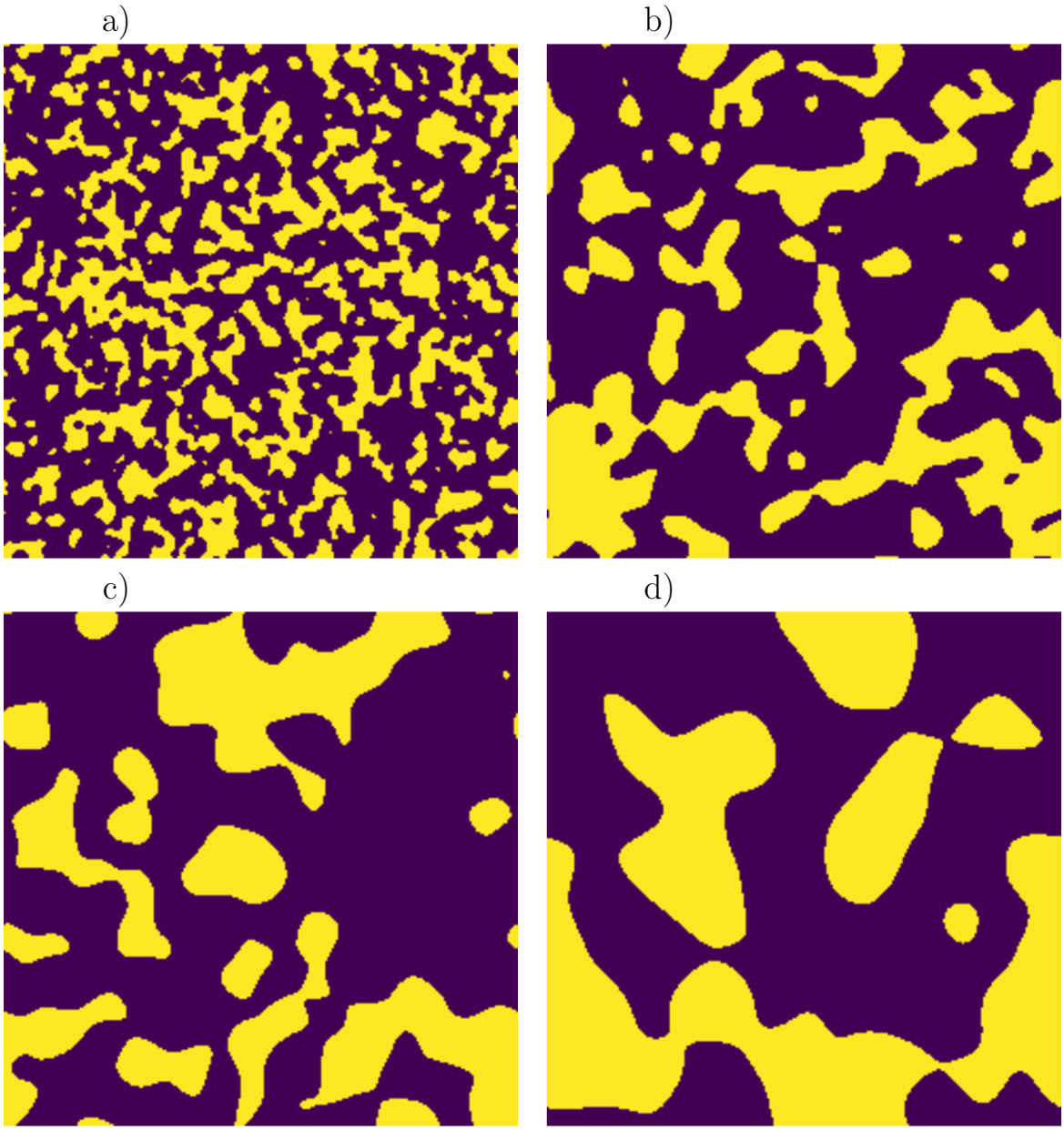

Figure III.2.2 – 2D slices of the realization of the gaussian random field with a periodic correlation function depending on the parameter α to control the integral range value expressing the size ratio between heterogeneities and the volume of the cell. Porosity threshold has been fixed to 35% and illustrations are for : a) $\alpha = 0.02$ b) $\alpha = 0.2$ c) $\alpha = 0.3$ d) $\alpha = 0.5$

III.3 Reconstruction of thresholded GRF from RSA microstructures

In this section, we apply the reconstruction procedure using the two-point correlation function obtained from random microstructures generated using the RSA algorithm presented in the Sec.II.1.2.a. Using FFT-based numerical computations, we investigate the effective elastic properties of both

isolated inclusions microstructures taken from RSA algorithm and their reconstructed thresholded GRF for a range of volume fractions. The obtained results enable to quantify numerically the errors on estimating the effective properties of a random material using the second-order information.

III.3.1 The reconstruction process

To make this study, we generate, using the RSA algorithm, microstructures consisting of uniform distribution of randomly oriented ellipsoidal inclusions of the same aspect ratio $\omega_1 = \omega_2 = \omega \in \{0.1, 0.2, 0.4, 0.6, 0.8, 1\}$ and partitionned in six sizes. The choice of polydispersity in size is motivated by the interest in achieving large range of volume factions going from 0% to 25% for all the aspect ratios and reaching up to 35% for aspect ratios $\omega \in \{0.4, 0.6, 0.8, 1\}$. In order to avoid uncertainties of results related to the multiple ways to define a polydisperse microstructure, all microstructures are build using the same set of morphological descriptors except the shape of the inclusion. These sets are fixed as:

- *Size of the biggest inclusion* is chosen such that the porous materials comprises a total number of inclusions higher than $N \geq 50$. This minimum number of inclusion represents the theoretical number of pores in the unit cell if the total porosity c comprised single-sized pores of spherical shape:
$$a_3 = \sqrt[3]{\frac{3\ c}{200\pi\omega^2}} \tag{26}$$
- *Set of size ratios:* $S_{size} = \{1, 0.85, 0.75, 0.65, 0.55, 0.45\}$
- *Set of volume fraction partition:* $S_c = \{20\%, 30\%, 10\%, 10\%, 10\%, 20\%\}$

The offset parameters defined in Sec.II.1.2.a are set to $tol_1 = tol_2 = 0.05$. Realizations obtained for such microstructures are shown in Fig.III.3.1 for different volume fractions and shape of inclusions.

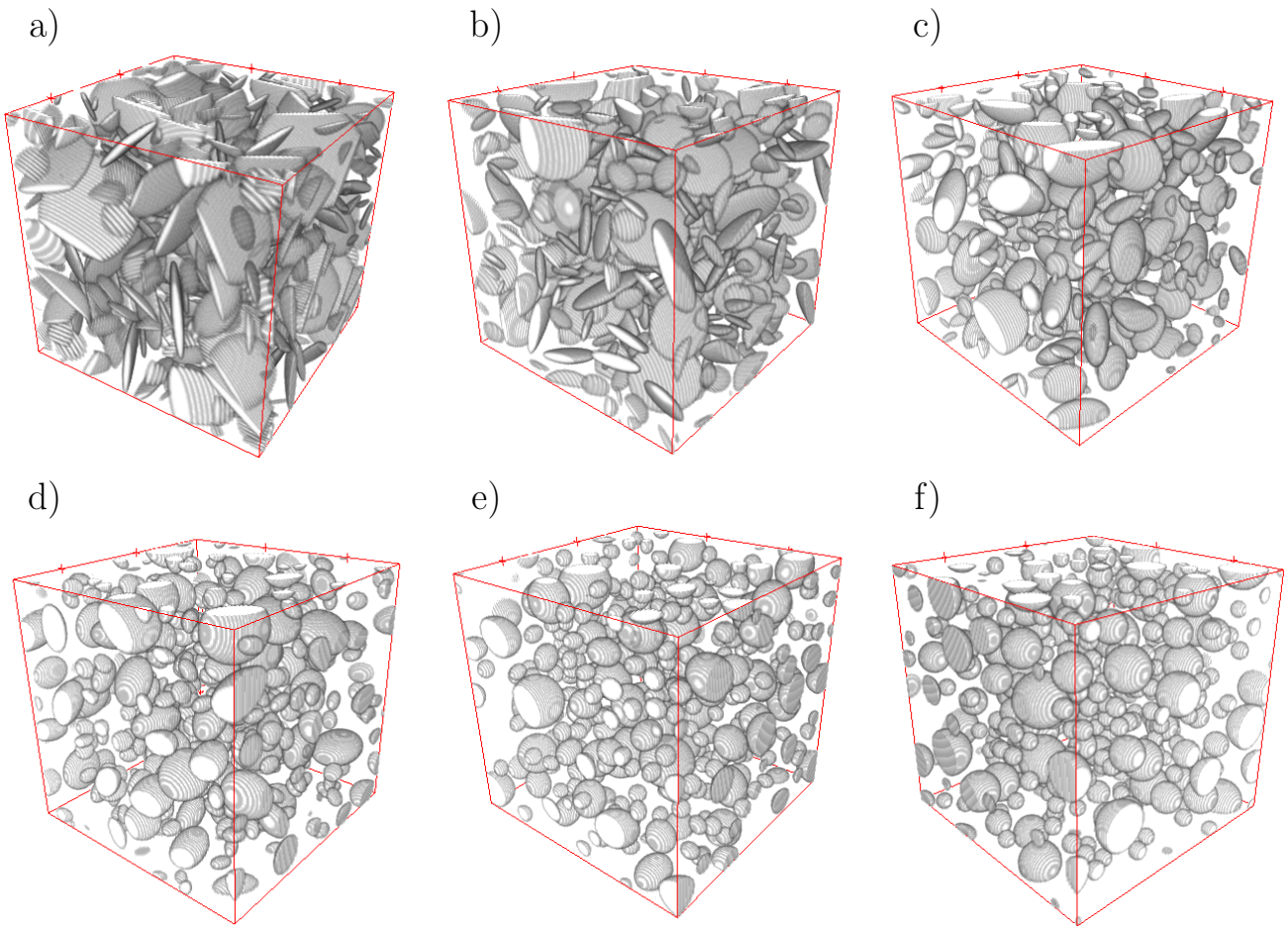

Figure III.3.1 – Realizations of microstructures generated by RSA algorithm with a total volume of $c = 15\%$ and consisting of six families of isolated pores having different sizes but the same aspect ratio ω (b) $\omega = 0.1$, (c) $\omega = 0.4$, (d) $\omega = 0.6$, (e) $\omega = 0.8$, (f) $\omega = 1.$. The 3D views are descritizations of the microstructures in regular grids of size 256^3

Following the procedure given in Sec.III.1.3, the two-point correlation function of each configuration is obtained by averaging the extracted two-point correlation function over 50 realizations discretized on a grid size of 256^3. From the plots in Fig.III.3.2, it can be observed that the correlation functions of the different configurations are almost the same on distance r measured along the three orthogonal axis. This assesses that the microstructures under investigation depict at least geometrically cubic symmetry.

The shape of the correlation function also provides information about the microstructure as we observe an initial value corresponding to the volume fraction of the microstructure and a fast decrease of the function which can be interpreted as an information of large internal surface mostly related to the smallest family of inclusions. This decrease is then smoothed when distance r increases until the function stabilizes at a value corresponding approximately to the square of the volume fraction. This smooth decrease of the correlation function witnesses the polydispersity in sizes and orientation of

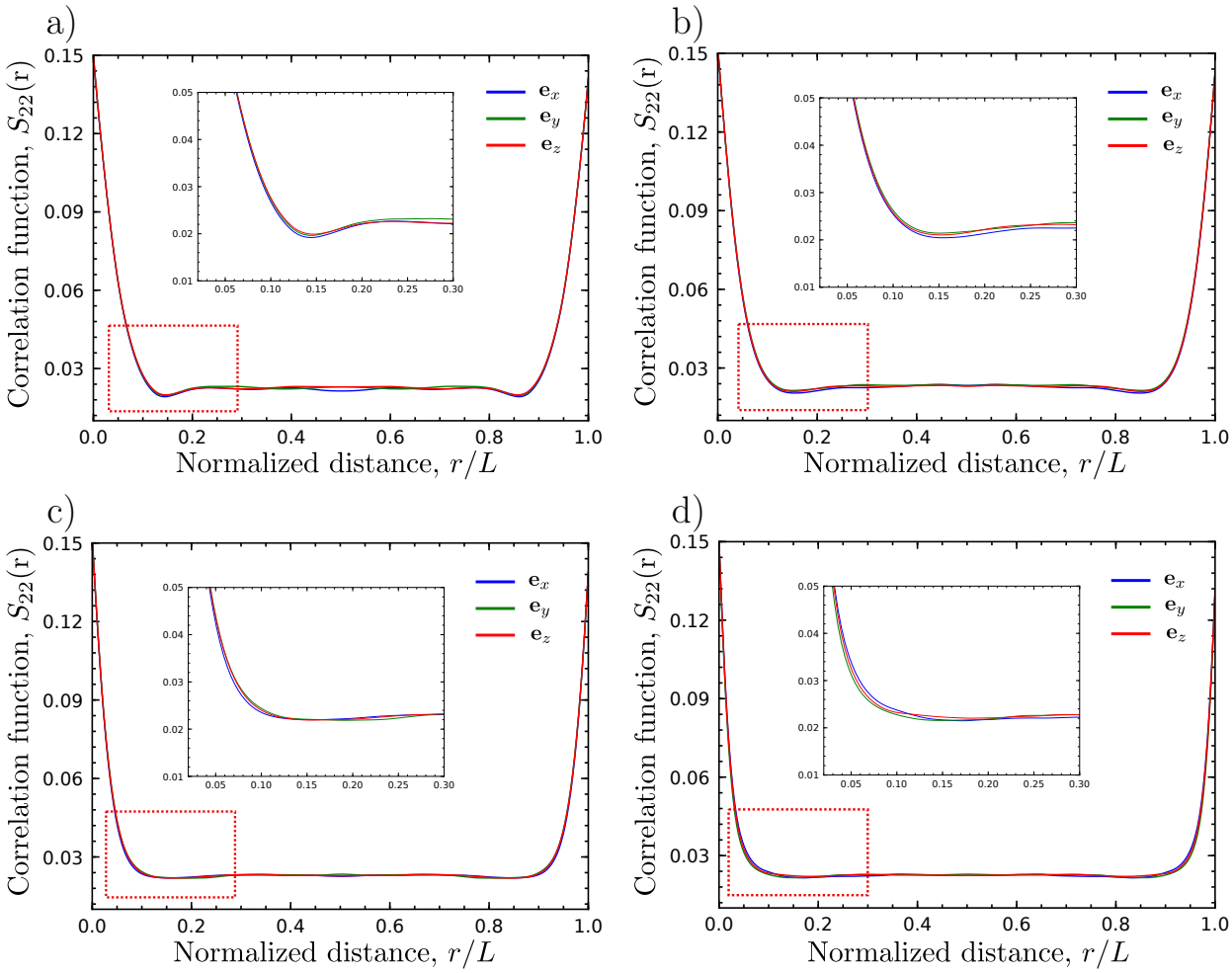

Figure III.3.2 – Correlation function plotted in the three principle directions of the cartesian grid for different aspect ratios of pores for total porosity $c = 15\%$ (a) $\omega = 1$ (b) $\omega = 0.4$ (c) $\omega = 0.2$ and (d)$\omega = 0.1$.

the inclusions as it extends a larger range of distances for small aspect ratios.

III.3.2 Numerical difficulties on reconstruction procedure

As shown in Sec.III.2.2.a, the reconstruction procedure works without any artefact when using an analytical correlation function as the Fourier coefficients can be directly computed using numerical integration of the given correlation function of the GRF. In the case of periodic microstructures with randomly oriented polydisperse and isolated ellipsoidal inclusions, no analytical expression for the correlation function can be found. This imposes the extraction of the correlation function from discretized realizations of the microstructure (as detailled in Sec.III.1.3). In turn, the Fourier coefficients of the correlation function obtained on a discrete grid are evaluated using the discrete Fourier transform of the correlation such as:

$$\hat{S}_{22}(\mathbf{k_b}) = \mathrm{DFT}[S_{22}(r_\alpha)] \tag{27}$$

Because the correlation function is evaluated on discretized microstructures, its estimation is approximated and the positive definiteness of the theoretical covariance does not necessarily hold as negative Fourier coefficients appears in the numerical procedure of reconstruction of real discretized microstructures for some cases, specifically the aspect ratios that are close to sphericity $\omega \in \{0.6, 0.8, 1.\}$. However, the condition of positive definiteness is a necessary condition to the proposed reconstruction procedure, as it uses the square root of the Fourier coefficients to build the continuous GRF. In order to avoid these negative values of Fourier coefficients, a first approach consists of increasing the grid size to obtain a better approximation of the theoretical correlation, because the correlation function on discretized microstructures is shown to converge towards the theoretical correlation function when grid size $N \to \infty$. However, memory limitations prevent from computing the extraction of the correlation function for microstructures meshed on grids larger than 1024^3 which was insufficient to reach all positive Fourier coefficients. Another approach that we have tried in order to prevent negative Fourier coefficient consists in interpolating the correlation function on each direction of the cartesian basis and compute the Fourier coefficients using numerical integration. This approximation on the correlation function was unsuccessful as negative Fourier coefficients at high order were still found. This is certainly related to the discretized description of the microstructure which induces noise on the extracted two-point correlation function (See section 2.6.4 of the book by Chiles and Delfiner (1999)). After non-concluding trials to overcome the numerical errors causing the negative Fourier coefficients, we resorted to truncating the Fourier coefficients for the reconstruction procedure. Since these negative remain small in comparison with the Fourier coefficients at small frequencies (ratio of values below 10^{-4} and an absolute intensity below 10^{-6}), we decided to apply a threshold value on the Fourier coefficients and cancel all coefficients below 10^{-6}. As shown in Fig.III.3.3, this truncation of the Fourier coefficients has no significant impact on the reconstruction of the correlation function which display very good agreement. Errors between the two correlation functions are measured using similar deviation measure than the one used for deviation from isotropy in Eq.21 such that:

$$\delta = \frac{||S_{22}^{GRF}(r) - S_{22}^{RSA}(r)||_F}{||S_{22}^{RSA}(r)||_F} \tag{28}$$

The obtained results are depicted in Fig.III.4.1 and are mostly below 5%.

3D realizations of the reconstructed microstructures obtained after cutting out the negative values of the Fourier coefficients are given as insets in Fig.III.3.3. It can be clearly observed that the morphology of the porous phase is different to the isolated inclusions microstructure it was derived from. The microstructures exhibit no clear matrix heterogeneity geometry specially for relatively high volume fractions and the heterogeneities take different sizes and morphologies in the same configuration. Furthermore, there is no clear observable distinction between the threshold GRF microstructures obtained from different correlation functions related to different aspect ratios of the RSA inclusions. The reconstruction procedure is reproduced for different volume fraction and Fig.III.3.4 shows the evolution of the thresholded GRF microstructures obtained from applying the method to RSA microstructures of aspect ratio $\omega = 0.4$ for an increasing volume fraction c.

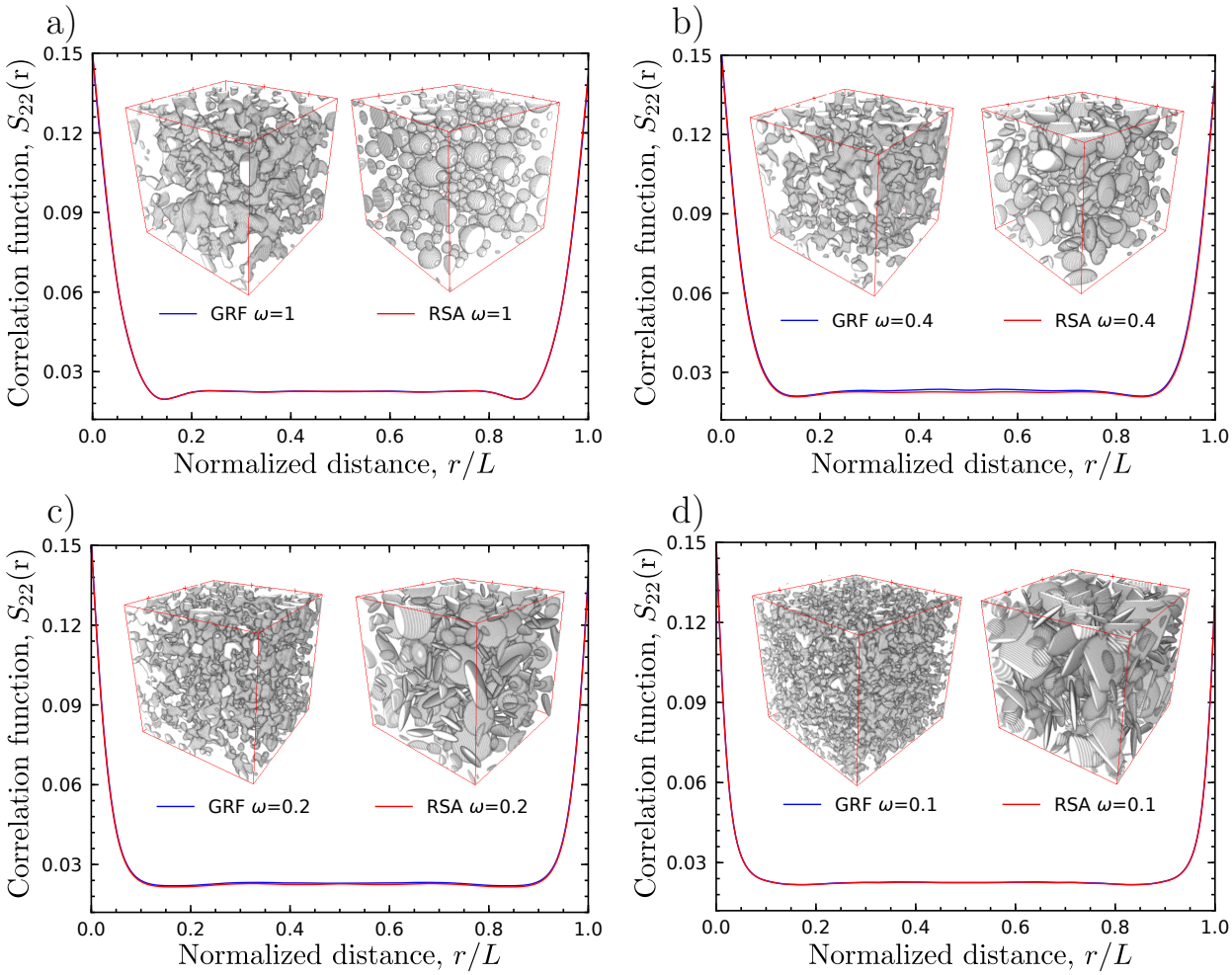

Figure III.3.3 – Comparison of the isotropic correlation function of the RSA microstructures generated and the corresponding second-order thresholded GRF for a total volume fraction $c = 5\%$ and : (a) aspect ratio $\omega = 1.$,(b) aspect ratio $\omega = 0.4$,(c) aspect ratio $\omega = 0.2$,(d) aspect ratio $\omega = 0.1$.

III.3.3 Fast-Fourier Transform (FFT) based methods

Finite element methods have been used extensively in full-field computation of mechanical behavior of heterogeneous materials. Thanks to the automated generation of conforming meshes of the microstructures with gradual sizes of elements to optimize the number of degrees of freedom to solve the discretized problem, the computations of the effective properties using such methods have been efficient in time and memory. However, such easy-meshing is more difficult when the morphology of the microstructures cannot be defined explicitly or if sharp angles are present in the microstructure as it is the case of highly elongated inclusions (higher than $\omega = 5$ or less than $\omega = 0.3$), or in case of inclusions connected by cylindrical channels (as in Sec. IV.1) or in case of images of real material. For such cases, method based on the Fast Fourier Transform (FFT) have been successfully developed in order to solve numerically the linear elastic problem and more complex behavior (Moulinec and

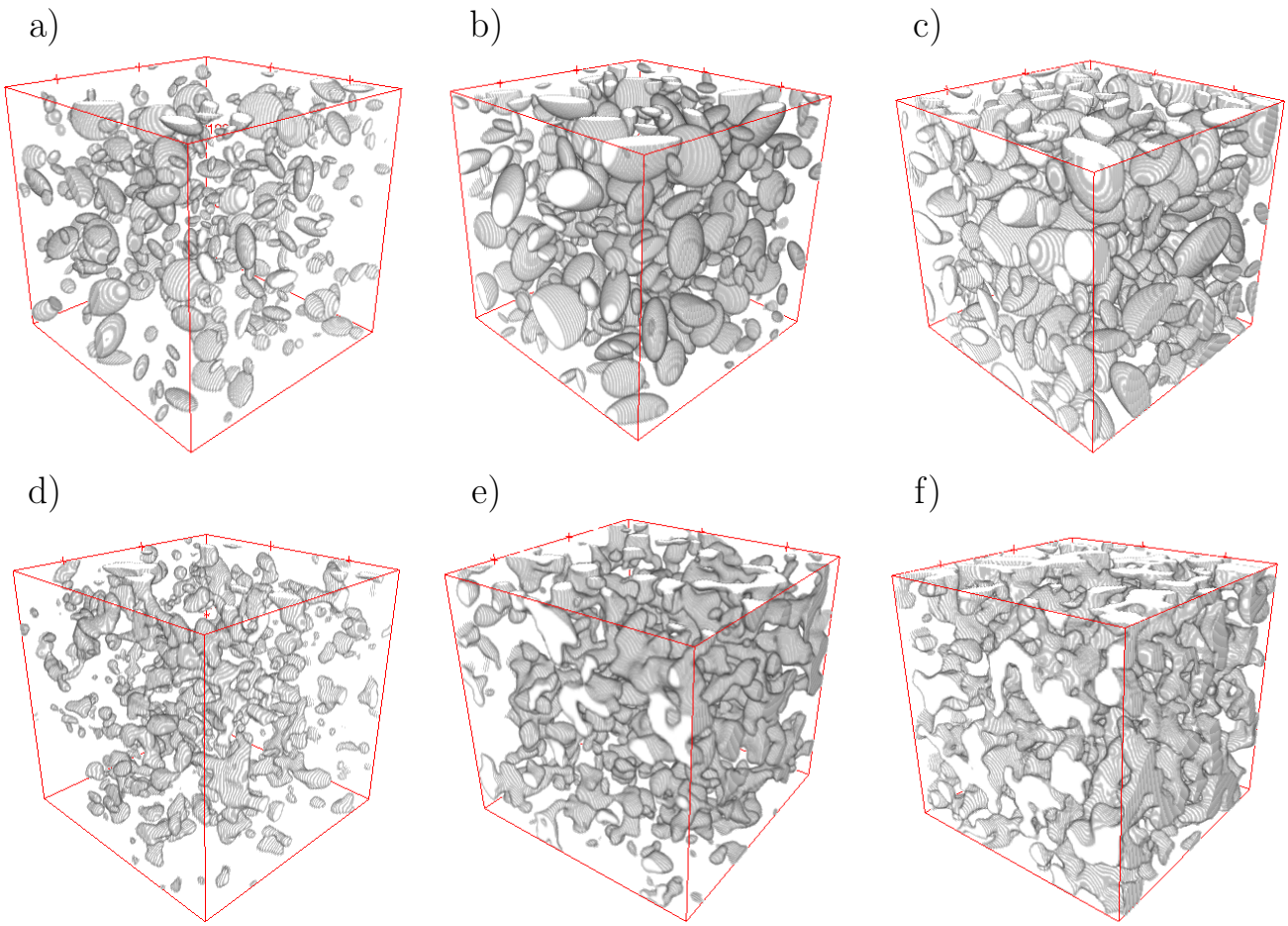

Figure III.3.4 – Realizations of the RSA microstructures generated with aspect ratio $\omega = 0.4$ for a total volume fraction (a) $c = 5\%$, (b) $c = 15\%$,(c) $c = 25\%$. Realizations of the corresponding second-order thresholded GRF (d) $c = 5\%$, (e) $c = 15\%$,(f) $c = 25\%$. The microstructures are shown by their mesh in regular grids of size 256^3

Suquet, 1998; Brenner et al., 2012; Gélébart and Mondon-Cancel, 2013; Bignonnet and Dormieux, 2014) directly on regular 3D voxel-grids (or pixel grids in 2D).

Initially proposed by Moulinec (1994)(Moulinec and Suquet, 1998), these methods are based on the Lippmann-Schwinder equation (Zeller and Dederichs, 1973) obtained by introducing a reference linear elastic homogeneous material with stiffness tensor $\mathbb{C}_0$ in the local problem of linear elasticity. This equation is an implicit equation with the strain field $\boldsymbol{\varepsilon}(\mathbf{x})$ as unknown:

$$\overline{\boldsymbol{\varepsilon}} = \boldsymbol{\varepsilon}(\mathbf{x}) + \Gamma^{(0)}[(\mathbb{C} - \mathbb{C}^0) : \boldsymbol{\varepsilon}](\mathbf{x}) \tag{29}$$

where $\Gamma^{(0)}$ is the so-called Green's operator over second-rank tensors and $\boldsymbol{\tau}(\mathbf{x})$ is the heterogeneous polarization field defined by:

$$\boldsymbol{\tau}(\mathbf{x}) = \Big(\mathbb{C} - \mathbb{C}_0\Big) : \boldsymbol{\varepsilon}(\mathbf{x}) \tag{30}$$

For our computation, we use the variational form proposed by Brisard and Dormieux (2010) with

discretized green operator proposed by Willot (2015).
The procedure for discretizing the RSA isolated pore microstructures can be time-consuming if it is conducted by loop checking if each voxel of the grid belongs to an inclusion. In order to optimize it, we use a 'bounding box' procedure which only checks center position of voxels that lie on the smallest cuboidal cell defined by each ellipsoid. The RSA microstructures are discretized on grids of size 256^3 with voxels taking values among $\{0, 0.125, 0.25, 375, 0.5, 0.625, 0.75, 0.875, 1\}$, which correspond to an approximation of the porosity contained in each voxel. This choice is motivated by the results presented in Appendix III.B.2 on the sensitivity of the effective elastic properties to the mesh size and to the elastic properties assigned to voxels sitting at the interface between the two phases. On the other hand, the thresholded GRF microstructures are generated on grids of size 256^3 with each voxel taking the value 0 or 1.
The assignement of the local elastic properties to each voxel is derived from the discretization of the method proposed in the work by Brisard and Dormieux (2012) such that:

$$(\mathbb{C}_{\boldsymbol{\alpha}} - \mathbb{C}_0)^{-1} = (1 - c_{\boldsymbol{\alpha}})(\mathbb{C}_m - \mathbb{C}_0)^{-1} + c_{\boldsymbol{\alpha}}(\mathbb{C}_i - \mathbb{C}_0)^{-1} \tag{31}$$

Where $c_{\boldsymbol{\alpha}}$ and $\mathbb{C}_{\boldsymbol{\alpha}}$ are respectively the approximate porosity and the stiffness tensor assigned to the voxel at position $\boldsymbol{\alpha} = (\alpha_1, \alpha_2, \alpha_3)$ in the cartesian grid, with $\alpha_i \in \{1, 2, .., 256\}$ for $i = 1, 2, 3$. In turn, $\mathbb{C}_0$ is the stiffness tensor of the reference material chosen as an elastic isotropic material tensor defined by its shear moduli $\mu_0 = 0.493$GPa and its Poisson ratio $\nu_0 = 0.42$ and $\mathbb{C}_m$ is the stiffness tensor of the solid phase which is an elastic isotropic material tensor defined by its shear moduli $\mu_m = 0.492$GPa and its Poisson ratio $\nu_m = 0.42$. The Stiffness tensor $\mathbb{C}_i$ corresponding to the porous phase is computed using a shear moduli $\mu_m = 0.$GPa and a Poisson's ratio $\nu_m = 0.42$.
Similarly to the FE computations presented in Sec. II.2.1, we apply six independent loading conditions in order to compute the effective stiffness tensor of the microstructures. The outcome of each step corresponds to the solution of the polarization field $\boldsymbol{\tau}_{\boldsymbol{\alpha}}$ on each voxel and the local strain field $\boldsymbol{\varepsilon}_{\boldsymbol{\alpha}}$. Using the relation III.3.3 between both fields, the components of the overall stiffness tensor are found such that:

$$\mathbb{C}_{ijkl} = \mathbb{C}_{0,ijkl} + \overline{\tau}_{ij}/\overline{\varepsilon}_{kl} \tag{32}$$

The analysis of the elastic properties is done by computing the overall bulk and shear moduli using the isotropic projectors $\mathbb{J}$ and $\mathbb{K}$ and the isotropy deviation δ_{iso} as defined in Sec.II.2.1.

III.3.4 Comparison of the effective elastic properties between GRF and RSA microstructures

The thresholded GRF are statistically controlled by their volume fractions and two-point correlation function, meaning that a realization can deviate from the targeted second-order information but the ensemble average over sufficiently large number of realizations. As shown in Fig.III.3.3, 50 realizations enable to reach accurate recontruction of the statistical information. In order to determine the effective elastic properties of the thresholded GRF in a reasonable time, FFT computations were conducted on five realizations over the fifty generated ones. The realizations were chosen to

have a volume fraction very close to the one of the associateed isolated inclusion microstructures such that the difference in the actual volume fraction and the targeted one is less than 0.1%. For all configurations of volume fractions $c = \{5\%, 10\%, 15\%, 20\%, 25\%, 30\%, 35\%\}$ and aspect ratios $\omega = \{0.1, 0.2, 0.4, 0.6, 0.8, 1\}$, the FFT computations of the thresholded GRF microstructures were conducted on grids of size 256^3 with binary voxels associated either to the pore phase or to the matrix. The local elastic properties of the matrix phase are defined by an isotropic elastic stiffness tensor defined by its shear moduli $\mu_m = 492$MPa and its Poisson ratio $\nu_m = 0.42$ corresponding to the properties found for the 3D printing material. The porous phase is modeled by an isotropic stiffness tensor with null shear moduli $\mu_p = 0$MPa. The reference material is chosen to have an isotropic elastic stiffness tensor stiffer than the matrix phase and determined by a shear moduli $\mu_0 = 493$MPa and a Poisson ratio $\nu_0 = 0.42$.

The same properties of the matrix, the porous phase and the reference material were applied to five realizations of RSA microstructures for grids of size 256^3 built with ratio $r = 2$ as explained in Sec.III.B.2. The composite voxels were assigned elastic properties following the relation III.B.2.

Figures III.3.5 depict the effective bulk and shear moduli obtained for each configuration of RSA microstructures and the second-order reconstructured thresholded GRF. The curve representing evolution of effective elastic moduli of microstructures containing isolated inclusions shows the important influence of the shape of inclusions on the elastic properties as the material is highly softened by the elongation inclusions. This behavior related to the shape of inclusions is not captured by the reconstructed microstructures for which all realizations of a given volume fraction c have similar elastic moduli. Though differences in the two-point correlation function are clearly observed, the thresholded GRFs seem only sensitive to the volume fraction.

For small volume fractions $c \leq 15\%$, the constant effective elastic moduli of the thresholded GRF microstructures are similar values with the RSA microstructure generated for aspect ratio $\omega \approx 0.4$ for the effective bulk $\widetilde{\kappa}$ and slightly smaller for the effective shear $\widetilde{\mu}$. For larger volume fraction $c \geq 15\%$, the aspect ratio corresponding to the elastic properties of the thresholded GRF microstructures drops quickly to highly elongated aspect ratio depicting change in the morphology of the microstructure. Indeed, observations of the 3D microstructure of the thresholded Gaussian random field highlight an increasing connectivity in the porous phase with increasing the total volume fraction. Studies on the conductivity and fluid flow properties on heterogeneous material using statistical modeling by thresholded GRFs (Teubner, 1991; Roubin and Colliat, 2016) have shown that the percolation of the heterogeneous phase is highly related to the roots of the Euler characteristic. This topological feature has an explicit expression in case of Gaussian distribution which leads to percolation of the porous phase at porosity $c \approx 16\%$ for sufficiently large cells(Roubin and Colliat, 2016). This morphological property explains the increasing connectivity between the heterogeneous components which lead to softening the porous GRF microstructures in comparison with the RSA microstructures (Roubin and Colliat, 2016). Due to the symmetry of random field, percolation of the matrix phase is lost when porosity reaches values higher than $c \geq 84\%$. In this case, the microstructures have a null effective stiffness tensor.

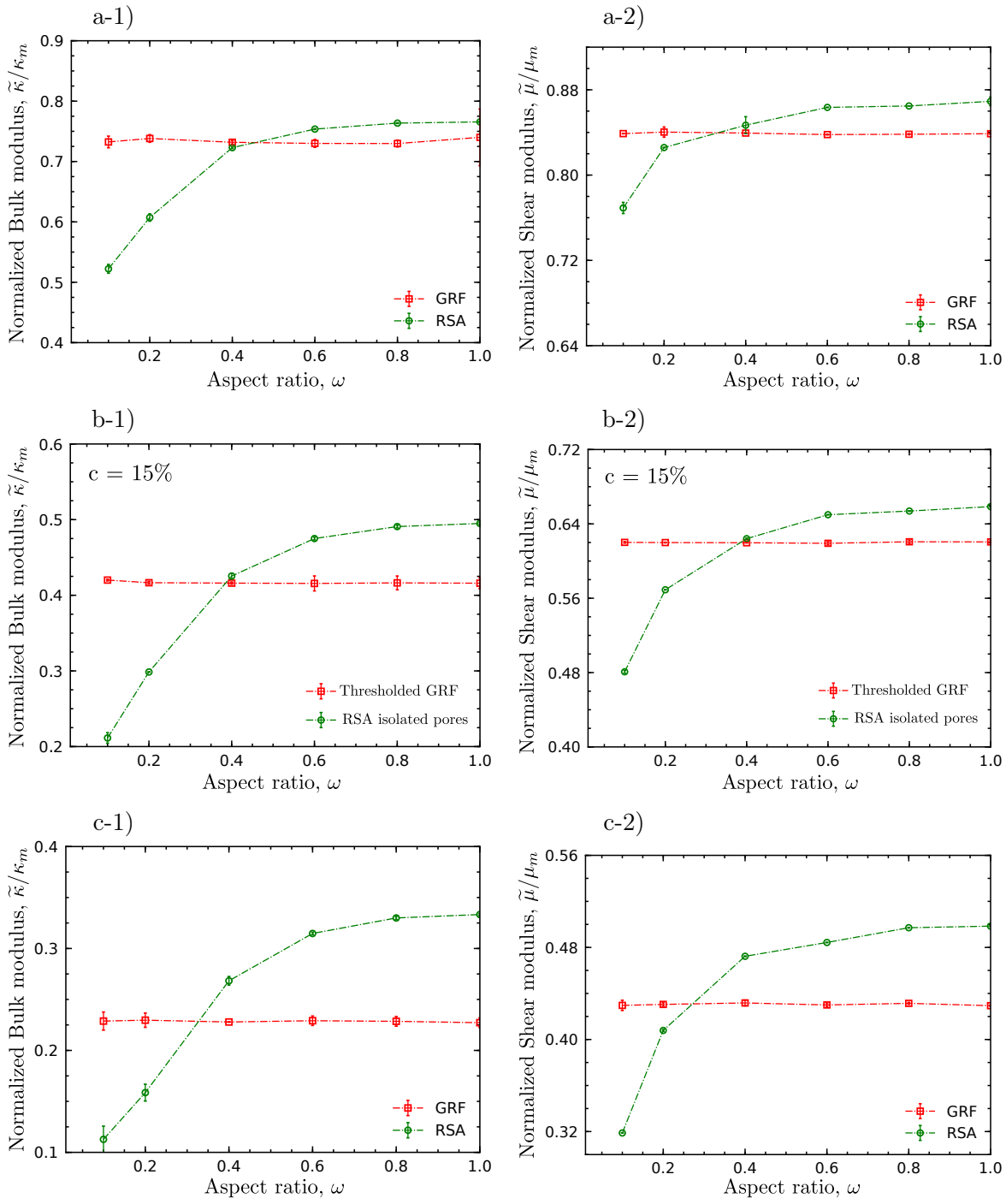

Figure III.3.5 – (1) Evolution of the effective bulk modulus normalized by the matrix modulus $\widetilde{\kappa}/\kappa_m$ as a function of the aspect ratio of for unit cell microstructures with porosity (a)$c = 5\%$ (b) $c = 15\%$ (c) $c = 25\%$ (2) Evolution of the effective shear modulus normalized by the matrix modulus $\widetilde{\mu}/\mu_m$ as a function of the aspect ratio of for unit cell microstructures with porosity (a)$c = 5\%$ (b) $c = 15\%$ (c) $c = 25\%$.

The evolution of the effective bulk modulus and shear modulus as a function of the volume fraction

c for different aspect ratios are shown in Fig.III.3.6 along with Hashin-Shtrikman estimates for the effective bulk and shear moduli of ellipsoidal microstructures (Willis, 1978; Gatt et al., 2005) (Detailed in Appendix III.C). The results show good agreement of the Hashin-Shtrikman estimates with the effective properties obtained from RSA microstructures down to aspect ratio $\omega = 0.4$. For aspect ratios below this value, the results decrease faster than predicted by the HS estimates. Besides that, the evolution of the effective bulk and shear moduli of the thresholded GRF microstructures, normalized by the moduli of the matrix phase, do not correspond to the evolution of the Willis estimates for a particular aspect ratio of inclusions. When increasing the porosity, these effective elastic moduli decrease with a higher rate due certainly to the increase in the connectivity of the porous phase. Figure III.4.1 shows a quantified error on the effective stiffness tensor in comparison

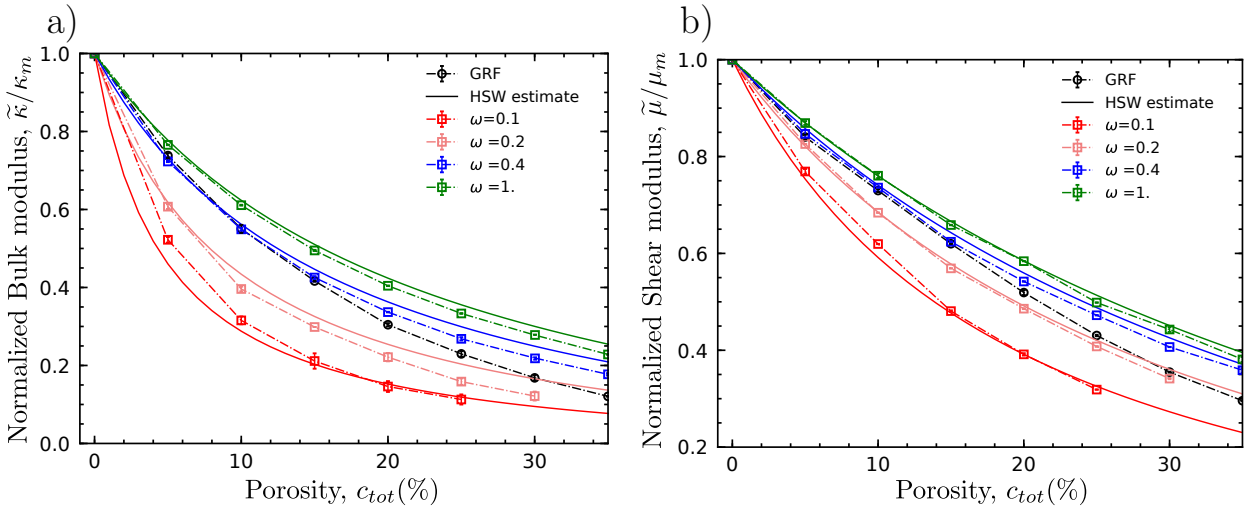

Figure III.3.6 – (a) Evolution of the effective bulk moduli $\widetilde{\kappa}/\kappa_m$ as a function of the porosity for microstructure with inclusions of aspect ratios ω and reconstructed thresholded GRF. The estimates of Hashin-Shtrikman for ellipsoids proposed by (Willis, 1978) are plotted for comparison. (b) Evolution of the effective shear moduli $\widetilde{\mu}/\mu_m$ as a function of the porosity for the same microstructures.

with the error on the reconstruction of the two-point correlation function for different volume fractions $c = 5\%, 15\%$ and 25%. The errors on the reconstruction process are contained within a relatively small range (generally below 5%), and are most certainly related to the finite number of realization used to compute the correlation function of each of the microstructures and to the numerical truncations in the Fourier coefficients to generate the GRF as mentionned in Sec.III.3.2. On the other hand, the deviations in the effective elastic properties of the material are significant and can reach more than 100% deviation. The largest differences are observed for microstructures related to elongated inclusions with $\omega = 0.1$ or 0.2 while the errors in the reconstruction as discussed in Sec.III.3.2 have been observed on aspect ratios close to sphericity $\omega = 0.8$ or 1.

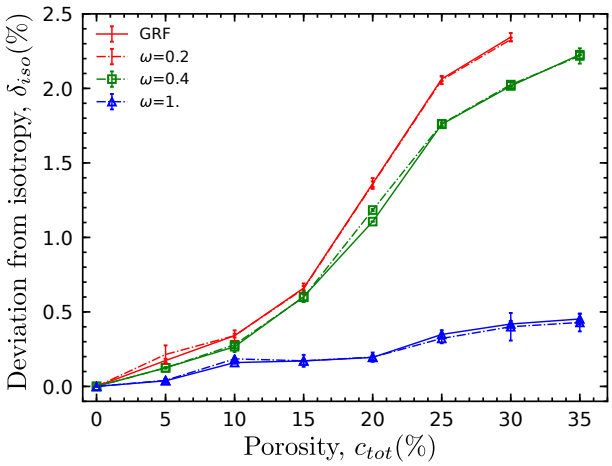

Figure III.3.7 – Evolution of the deviation from isotropy δ_{iso} plotted for a selection of RSA microstructure with aspect ratios $\omega = 0.2$ or 0.4 or 1 and their corresponding second-order reconstructed microstructures (Thresholded GRF).

III.4 Concluding remarks

In this chapter, two types of microstructures having the same second-order information (volume fraction and two-point correlation function) are generated and computed using FFT based methods. The first type of microstructures consists of isolated ellipsoidal inclusions generated using the RSA algorithm and the second type is derived from a reconstruction procedure based on the volume fraction and two-point correlation function of the latter type.
The reconstruction procedure explained in Sec.III.2, provides accurate reconstruction of the statistical information of the microstructure but the effective elastic results of the two microstructures show large differences.This assesses that the building procedure based only on the volume fraction and the correlation function of the porous phase misses important features of the microstructures which in the case of our study were related to the shape of heterogeneities and the connectivity of the pores. Though GRF reconstruction method suffers from several limitations related to the Gaussian character of the field, the results shown in this study highlight two important facts:

- The shape of the inclusions has an important effect on the effective elastic properties of the material which, in the case of isotropic microstructures, can be well captured by the effective bulk and shear moduli obtained from Hashin-Shtrikman estimates for ellipsoidal microstructures (Willis, 1978) given in Appendix III.C.
- The two-point correlation function is insufficient to deliver accurate predictions on the effective elastic properties of a random heterogeneous material. The statistical parameters captured from it are unable to distinguish the local information about the morphology of the heterogeneities such as the shape and the connectivity.

In order to quantify the differences between the two types of microstructures, we present in the next chapter the computation of statistical descriptors of the connectivity in heterogeneous microstructures.

To quantify the effect of connectivity on the elastic properties, a third type of microstructure consisting in connecting the isolated inclusions of the RSA algorithm has been developped with quantitative connectivity parameters taken from practical work on geomaterials.

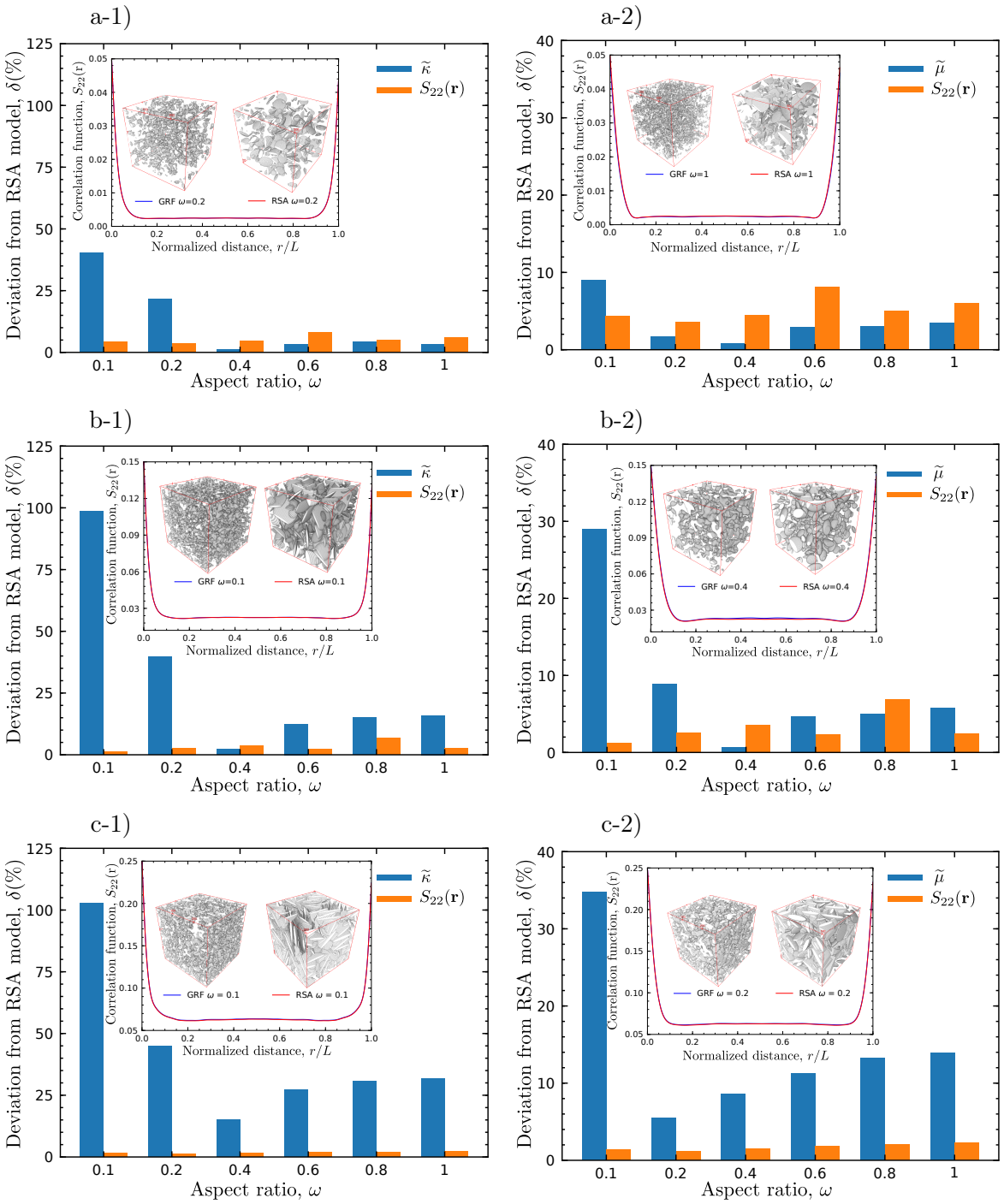

Figure III.4.1 – (1) Comparison between the deviation between the effective bulk modulus and the errors related to the 3D reconstruction of the two-point correlation function as a function of the aspect ratio ω of inclusions present in the RSA microstructure at different porosities (a) $c = 5\%$ (b) $c = 15\%$ (c) $c = 25\%$. (2) Comparison between the deviation between the effective bulk modulus and the errors related to the 3D reconstruction of the two-point correlation function as a function of the aspect ratio ω of inclusions present in the RSA microstructure at different porosities (a)$c = 5\%$ (b) $c = 15\%$ (c) $c = 25\%$.

APPENDIX

III.A Generation of the Gaussian Random Field by spectral method:

The GRF proposed in this work is defined in the continuous space by (Poirion and Soize, 1995):

$$Y(\mathbf{x}) = \alpha \sum_{b_1=0}^{N_1} \sum_{b_2=0}^{N_2} \sum_{b_3=0}^{N_3} H_{\mathbf{b}} Z_{\mathbf{b}} \cos(\mathbf{k_b}.\mathbf{x} + \Phi_{\mathbf{b}}) \tag{33}$$

where $\mathbf{b} = (b_1, b_2, b_3)$, $N_1, N_2, N_3 \in \mathbb{N}^3$. In this expression, the following variables are defined as:

— $\Phi_{\mathbf{b}}$ are random variables uniformly distributed in $[0, 2\pi[$

— $Z_{\mathbf{b}}$ are random coefficients such that $Z_{\mathbf{b}} = \sqrt{-\ln(\Psi)}$ with Ψ uniformly distributed in $]0, 1]$.

— $H_{\mathbf{b}}$ and $\mathbf{k_b}$ are deterministic coefficients chosen in order to control the correlation function of the field and make use of the Fast-Fourier Transform algorithm.

It can be seen that the two-point correlation of this normalized field $Y(\mathbf{x})$ is directly related to the Fourier coefficient of the target correlation function ρ expressed by:

$$\rho(\mathbf{r}) = \frac{\alpha^2}{2} \sum_{b_1=0}^{N_1} \sum_{b_2=0}^{N_2} \sum_{b_3=0}^{N_3} H_{\mathbf{b}}^2 \cos(\mathbf{k_b} \cdot \mathbf{r}) \tag{34}$$

Since for all $\mathbf{b} \in [0, N_1] \times [0, N_2] \times [0, N_3]$, $Z_{\mathbf{b}}$ and $\Phi_{\mathbf{b}}$ are two independent random variables:

$$\mathbb{E}[Z_{\mathbf{b}} \cos(\mathbf{k_b}.\mathbf{x} + \Phi_{\mathbf{b}})] = \mathbb{E}[Z_{\mathbf{b}}]\mathbb{E}[\cos(\mathbf{k_b}.\mathbf{x} + \Phi_{\mathbf{b}})] \tag{35}$$

Since:

$$\begin{aligned} \mathbb{E}[\cos(\mathbf{k_b}.\mathbf{x} + \Phi_{\mathbf{b}})] &= \frac{1}{2\pi} \int_0^{2\pi} \cos(\mathbf{k_b}.\mathbf{x} + \Phi_{\mathbf{b}}) \mathrm{d}\phi_{\mathbf{b}} \\ &= \frac{1}{2\pi} \big[\sin(\mathbf{k_b}.\mathbf{x} + \Phi_{\mathbf{b}}) \big]_0^{2\pi} \\ &= 0 \end{aligned} \tag{36}$$

Thus $\mathbb{E}[Y(\mathbf{x})] = 0$.

Similarly, the two-point correlation function of this field can be calculated such that:

$$\mathbb{E}[Y(\mathbf{x})Y(\mathbf{x}+\mathbf{r})] = \alpha^2 \sum_{\mathbf{b}} \sum_{\mathbf{c}} H_{\mathbf{b}} H_{\mathbf{c}} \mathbb{E}[Z_{\mathbf{b}} Z_{\mathbf{c}}] \mathbb{E}[\cos(\mathbf{k_b}.\mathbf{x} + \Phi_{\mathbf{b}}) \cos(\mathbf{k_c}.(\mathbf{x}+\mathbf{r}) + \Phi_{\mathbf{c}})] \tag{37}$$

where the notation $\sum_{\mathbf{b}}$ has been used to simplify $\sum_{b_1=1}^{N_1} \sum_{b_2=1}^{N_2} \sum_{b_3=1}^{N_3}$.

If $\mathbf{b} \neq \mathbf{c}$, the two random variables are independent and for similar calculation in Eq.III.A as it can be shown that:

$$\begin{aligned} \mathbb{E}[\cos(\mathbf{k_b}.\mathbf{x} + \Phi_{\mathbf{b}}) \cos(\mathbf{k_c}.(\mathbf{x}+\mathbf{r}) + \Phi_{\mathbf{c}})] &= \mathbb{E}[\cos((\mathbf{k_b}.\mathbf{x} + \Phi_{\mathbf{b}})] \mathbb{E}[\cos(\mathbf{k_c}.\mathbf{x}+\mathbf{r} + \Phi_{\mathbf{c}})] \\ &= 0 \end{aligned} \tag{38}$$

If $\mathbf{b} = \mathbf{c}$, then transformation of the product of cosines into a sum of cosines enables to get:

$$\begin{aligned} \mathbb{E}[\cos(\mathbf{k_b}.\mathbf{x} + \Phi_{\mathbf{b}}) \cos(\mathbf{k_b}.\mathbf{x} + \Phi_{\mathbf{b}})] &= \frac{1}{2}\mathbb{E}[\cos((\mathbf{k_b}.\mathbf{r})] + \frac{1}{2}\mathbb{E}[\cos(\mathbf{k_b}.(2\mathbf{x}+\mathbf{r}) + 2\Phi_{\mathbf{b}})] \\ &= \frac{1}{2}\mathbb{E}[\cos((\mathbf{k_b}.\mathbf{r})] \end{aligned} \tag{39}$$

In turn, for $\mathbf{b} = \mathbf{c}$:

$$\begin{aligned} \mathbb{E}[Z_{\mathbf{b}}^2] &= \mathbb{E}[\sqrt{-\log(\Psi)}^2] \\ &= -\int_0^1 \ln(\Psi) \mathrm{d}\Psi \\ &= [x\ln(x) - x]_{\lim \to 0}^1 \\ &= 1 \end{aligned} \tag{40}$$

Thus this field has a normal distribution, i.e. its mean value is $\mathbb{E}[Y(\mathbf{x})] = 0$ and its variance $\sigma^2 = 1$.

The two-point correlation of $Y(\mathbf{x})$ is also given by the expression:

$$\rho(\mathbf{r}) = \frac{\alpha^2}{2} \sum_{b_1=0}^{N_1} \sum_{b_2=0}^{N_2} \sum_{b_3=0}^{N_3} H_{\mathbf{b}}^2 \cos(\mathbf{k_b} \cdot \mathbf{r}) \tag{41}$$

It is worth mentioning that this correlation function is L-periodic as it was expected.

In order to determine the values of α, $H_{\mathbf{b}}$ and $\mathbf{k_b}$ to match the target correlation function and make use of Fast Fourier Transform, we consider a regular discretization of the spatial field by step h and a discretization of its spectral domain by step Δk and initial phase B_i in each principal direction $\mathbf{e}_i$ such that:

$$\mathbf{x_\beta} = \quad h(\beta_1\mathbf{e}_1 + \beta_2\mathbf{e}_2 + \beta_3\mathbf{e}_3) \quad , \quad k_{\mathbf{b}} = \quad \Delta k[(b_1 - B_1)\mathbf{e}_1 + (b_2 - B_2)\mathbf{e}_2 + (b_3 - B_3)\mathbf{e}_3]$$

The random field $Y(\mathbf{x})$ valued at discrete point $\mathbf{x_\beta}$ can be expressed as:

$$\begin{aligned} Y(\mathbf{x_\beta}) &= \mathrm{Re}\left(\alpha \sum_{b_1=0}^{N_1} \sum_{b_2=0}^{N_2} \sum_{b_3=0}^{N_3} H_{\mathbf{b}} Z_{\mathbf{b}} \exp(-i\mathbf{k_b}.\mathbf{x_\beta} + \Phi_{\mathbf{b}}) \right) \\ &= \mathrm{Re}\left(\alpha \sum_{b_1=0}^{N_1} \sum_{b_2=0}^{N_2} \sum_{b_3=0}^{N_3} H_{\mathbf{b}} Z_{\mathbf{b}} \exp\Big(-i\Delta k\ h \sum_{j=1}^{3} B_j\beta_j + \Phi_{\mathbf{b}} \Big) \exp\Big(-i\Delta k\ h \sum_{j=1}^{3} b_j\beta_j \Big) \right) \end{aligned} \tag{42}$$

where $\mathrm{Re}(X)$ denotes the real part of the complex X. For an efficient computation, it is interesting to write these discrete values $Y(\mathbf{x}_{\boldsymbol{\beta}})$ using discrete inverse Fourier transform $(\hat{Y}(\mathbf{b}))_{\mathbf{b}\in\mathbb{B}}$ such that:

$$Y(\mathbf{x}_{\boldsymbol{\beta}}) = \mathrm{Re}\left(\sum_{b_1=0}^{N_1}\sum_{b_2=0}^{N_2}\sum_{b_3=0}^{N_3}\hat{Y}(\mathbf{b})\exp\Big(-i2\pi\sum_{j=1}^{3}\frac{b_j\beta_j}{N_j}\Big)\right) \tag{43}$$

A natural choice to obtain equivalent expression between Eq.III.A and Eq.43 comes out by setting:

$$\Delta k = \frac{2\pi}{L} \tag{44}$$

Therefore, the correlation function $\rho(\mathbf{r})$ is expressed by:

$$\rho(\mathbf{r}) = \mathrm{Re}\left(\frac{\alpha^2}{2}\sum_{b_1=0}^{N_1-1}\sum_{b_2=0}^{N_2-1}\sum_{b_3=0}^{N_3-1}H_{\mathbf{b}}^2\exp\left(i\frac{2\pi}{L}\Big[(b_1-B_1)r_1+(b_2-B_2)r_2(b_3-B_3)r_3\Big]\right)\right) \tag{45}$$

On the one hand, using the L-periodicity of the random field in the cell of volume $V=[0,L]^3$, the correlation function is also L-periodic and can be expressed by its Fourier series as:

$$\rho(\mathbf{r}) = \sum_{\mathbf{b}\in\mathbb{Z}^3}\tilde{\rho}_b\exp(-i\mathbf{k_b}.\mathbf{r}) \tag{46}$$

where $\tilde{\rho}_b$ are the Fourier coefficients of the correlation function that are defined as:

$$\tilde{\rho}_b = \frac{1}{L^3}\int_V \rho(\mathbf{r})\exp\left(-i\frac{2\pi}{L}\sum_{i=1}^{3}b_i.r_i\right)d\mathbf{r}$$

Assuming the spectral power function is non-null only in a closed frequency domain $\Omega=[-M_1,M_1]\times[-M_2,M_2]\times[-M_3,M_3]$ centered at 0, the Fourier series of the correlation function can be written as:

$$\rho(\mathbf{r}) = \sum_{b_1=-M_1}^{M_1}\sum_{b_2=-M_2}^{M_2}\sum_{b_3=-M_3}^{M_3}\tilde{\rho}_b\exp\left(-i\frac{2\pi}{L}\mathbf{b}\cdot\mathbf{r}\right) \tag{47}$$

On the other hand, using that the correlation function of a statistically homogeneous material is an even function and translating the index of summation in the Eq.III.A, the expression of the correlation function of the GRF $Y(\mathbf{x})$ is formulated as:

$$\rho(\mathbf{r}) = \frac{\alpha^2}{2}\sum_{b_1=-N_1/2}^{N_1/2}\sum_{b_2=-N_2/2}^{N_2/2}\sum_{b_3=-N_3/2}^{N_3/2}H_{\mathbf{b}}^2\exp\left(i\frac{2\pi}{L}\Big((b_1+\frac{N_1}{2}-B_1)r_1+(b_2+\frac{N_2}{2}-B_2)r_2+(b_3+\frac{N_3}{2}-B_3)r_3\Big)\right) \tag{48}$$

From this expression, we see that the numbers N_1, N_2, N_3 have to be odd numbers and by connecting both Eq.III.A and Eq.III.A the choices of deterministic parameters of the GRF $Y(\mathbf{x})$ are defined as:

$$\begin{aligned} \alpha &= \sqrt{2} \quad , & B_i &= M_i \\ k_{b_i} &= \frac{2\pi}{L_i}(b_i - M_i) \quad , & H_{\mathbf{b}} &= \sqrt{\tilde{\rho}_{\mathbf{b}}} \end{aligned} \tag{49}$$

It is worth noting that computing the square root of the Fourier coefficients of the correlation function $\sqrt{\tilde{\rho}_{\mathbf{b}}}$ is always correct because an important property related to the realizability of two-phase correlation functions imposes that the correlation function of a GRF is positive-definite function. The positive definiteness conditions has been shown to be equivalent to Wiener-Khintchine condition which imposes the existence and non-negativity of the Fourier transform of the correlation function which is means that the Fourier coefficients of the correlation function are not negative.
To sum up, we generate a continuous L-periodic normalized GRF $Y(\mathbf{x})$ defined by its correlation function $\rho(\mathbf{r})$ expressed by:

$$Y(\mathbf{x}) = \mathrm{Re}\left(\sqrt{2}\sum_{b_1=0}^{N_1-1}\sum_{b_2=0}^{N_2-1}\sum_{b_3=0}^{N_3-1}\sqrt{\tilde{\rho}_{\mathbf{b}-\mathbf{M}}}Z_{\mathbf{b}}\exp\Big(\frac{2\pi}{L}(\mathbf{b}-\mathbf{M})\cdot\mathbf{x}+\Phi_{\mathbf{b}}\Big)\right) \tag{50}$$

with notations $\mathbf{M} = (M_1, M_2, M_3)$ and where $\Phi_{\mathbf{b}}$ are random variables uniformly distributed in $[0, 2\pi[$ and $Z_{\mathbf{b}}$ are random coefficients such that $Z_{\mathbf{b}} = \sqrt{-\ln(\Psi)}$ with Ψ uniformly distributed in $]0, 1]$.
The Fourier transform of the correlation function $\widetilde{\rho}(\mathbf{r})$ has been assumed to be fully contained within a bounded support Ω which leads to consider odd numbers N_1, N_2 and N_3. However, this condition does not restrict the generation of the GRF to only odd grid sizes as there is no loss in the expression of the field to extend the sum for wave number $\mathbf{b}$ corresponding to null values of the Fourier coefficient, i.e. $\tilde{\rho}_{\mathbf{b}} = 0$ and consider $M_i = N_i/2$ for even number N_i and $M_i = (N_i - 1)/2$ for odd numbers.
The discrete values of the GRF on a grid $(\mathbf{X}_{\boldsymbol{\beta}})_{\boldsymbol{\beta}\in[0,N_1]\times[0,N_2]\times[0,N_3]}$ are expressed as:

$$\hat{Y}(\mathbf{x}_\beta) = \mathrm{Re}\left(\sqrt{2}\sum_{b_1=0}^{N_1-1}\sum_{b_2=0}^{N_2-1}\sum_{b_3=0}^{N_3-1}\sqrt{\tilde{\rho}_{\mathbf{b}-\mathbf{M}}}Z_{\mathbf{b}}\exp\Big(-i2\pi\sum_{j=1}^{3}\frac{M_j\beta_j}{N_j}+\Phi_{\mathbf{b}}\Big)\exp\Big(i2\pi\sum_{j=1}^{3}\frac{b_j\beta_j}{N_i}\Big)\right) \tag{51}$$

Which can be seen as a discrete inverse Fourier transform of array $\left(\hat{Y}_{\mathbf{b}}\right)$ where $\mathbf{b} \in [0, N_1] \times [0, N_2] \times [0, N_3]$ such that:

$$\hat{Y}(\mathbf{x}_\beta) = \sqrt{2}\exp\Big(-i2\pi\sum_{j=1}^{3}\frac{M_j\beta_j}{N_j}\Big)\mathrm{DFT}^{-1}\Big[(\hat{Y}_{\mathbf{b}})\Big] \tag{52}$$

where:

$$\hat{Y}_{\mathbf{b}} = \sqrt{\tilde{\rho}_{\mathbf{b}-\mathbf{M}}}Z_{\mathbf{b}}\exp\Big(i\Phi_{\mathbf{b}}\Big) \tag{53}$$

III.B Fast-Fourier Transform based method

This section presents the some results related to the discretization of RSA isolated pore microstructures for Fast-Fourier Transform (FFT) based methods. First, the bounding box procedure for discretizing the microstructures in regular grids is presented and the sensitivity of the effective properties computed on these grids is conducted in order to define the grid size and parameter of the composite voxels to use in our FFT simulations.

III.B.1 Discretization of RSA microstructures using the bounding box procedure

The local attribution of voxels is conducted by defining the smallest cuboidal box containing each ellipsoidal inclusion and loop around this subset of voxels to associate each voxel with the phase lying at its center.

Consider a randomly oriented ellipsoid $\mathcal{E}_i$ characterized by its center position $\mathbf{v}_i$ and its characteristic matrix $\mathbb{Z}_i$ as defined in Sec.II.1.1.a. The determination of the smallest cuboidal box containing this quadric geometry uses the property that the tangent vector at the extremal points is colinear to the directional vector in the Cartesian basis $\mathbf{e}_1, \mathbf{e}_2$ or $\mathbf{e}_3$. The extremal points $\mathbf{x}_{ext}$ verify the boundary equation of the ellipsoid and the colinearity condition such that:

$$Q_i(\mathbf{x}_{ext}) = \big(\mathbf{x}_{ext} - \mathbf{v}_i\big)^{\mathrm{T}} \mathbb{Z}_i \big(\mathbf{x}_{ext} - \mathbf{v}_i\big) = 1 \tag{54}$$

$$\Delta Q_i(\mathbf{x}_{ext}) = \lambda_j \mathbf{e}_j \quad \text{with } j = 1, 2 \text{ or } 3 \tag{55}$$

By inserting the second equation into the first one, the six extremal points are expressed by (for $i = 1, 2$ and 3):

$$\mathbf{x}_{max,i} = \mathbf{v}_i + \frac{1}{\sqrt{\mathbb{Z}^{-1}\mathbf{e}_i \cdot \mathbf{e}_i}} \tag{56}$$

$$\mathbf{x}_{min,i} = \mathbf{v}_i - \frac{1}{\sqrt{\mathbb{Z}^{-1}\mathbf{e}_i \cdot \mathbf{e}_i}} \tag{57}$$

The smallest cuboidal box containing the ellipsoid is that defined by the two points $M_1 = (x_{min,1}, y_{min,2}, z_{min,3})$ and $M_1 = (x_{max,1}, y_{max,2}, z_{max,3})$.

To mesh a microstructure of N randomly in a grid of size $N_1 \times N_2 \times N_3$, the algorithm defines the voxel size h_1, h_2, h_3 such that $h_i = L/N_i$ and operates N loop with the following steps:

- *step 1:* Compute the extremal points of the ellipsoid $\mathbf{x}_{max,1}, \mathbf{x}_{min,1}, \mathbf{x}_{max,2}, \mathbf{x}_{min,2}, \mathbf{x}_{max,3}, \mathbf{x}_{min,3}$.
- *step 2:* Build the bounding box by discretising $[x_{min,1}, x_{max,1}]$ with a step size h_1, $[y_{min,1}, y_{max,1}]$ with a step size h_2 and $[z_{min,1}, z_{max,1}]$ with a step size h_3 and then creating the corresponding grid $G_{\boldsymbol{\alpha}}$. In order to ensure that the grid contains all points lying in that volume, the minimum numbers are taken as the ceil part and the maximum ones are taken the floor part.
- *step 3:* Compute the value of $Q_i(\mathbf{x}_{\boldsymbol{\alpha}})$ for each voxel of this grid such that:

$$Q_i(\mathbf{x}_{\boldsymbol{\alpha}}) = (\mathbf{x}_{\boldsymbol{\alpha}} - \mathbf{v}_i)^{\mathrm{T}} \mathbb{Z}_i (\mathbf{x}_{\boldsymbol{\alpha}} - \mathbf{v}_i) - 1 \tag{58}$$

- *step 4:* Apply a threshold process to the latter valued box such that:

$$G_{\boldsymbol{\alpha}} = 1 \quad \text{if } Q_i(\mathbf{x}_{\boldsymbol{\alpha}}) \leq 0 \tag{59}$$

The algorithm output the discretized ellipsoid grid and the position M_1 as the origin point of the bounding box. This latter grid is in turn inserted inside the global grid by performing a voxel by voxel addition. This includes translating the voxel when its central point lies outside the box conforming to the periodicity of the microstructure.

III.B.2 Effective properties sensitivity to the grid size and composite voxels

Prior to the use of the FFT computation for the determination of effective properties of porous materials, sensitivity analysis on the FFT results is conducted to define the size of grid that should be used for microstructures under investigation. Two parameters of the microstructures have to be defined sufficiently well to minimize the errors on the FFT computations, namely the minimum number of voxels needed to mesh a characteristic length of inclusions and the minimum number of voxels in a matrix ligament. To isolate the contribution of each of these parameters, we generate two types of microstructures for aspect ratios $\omega_1 = \omega_2 = 1$ and $\omega_1 = \omega_2 = 0.1$ to ensure a result that works for all investigated aspect ratios; the first one consists of inclusions separated by a big distance to neglect the influence of the ligament and the second type consists of large inclusions distant by the minimum size of ligament.

We compute the effective properties on grid sizes in range between 16 and 512 for all four

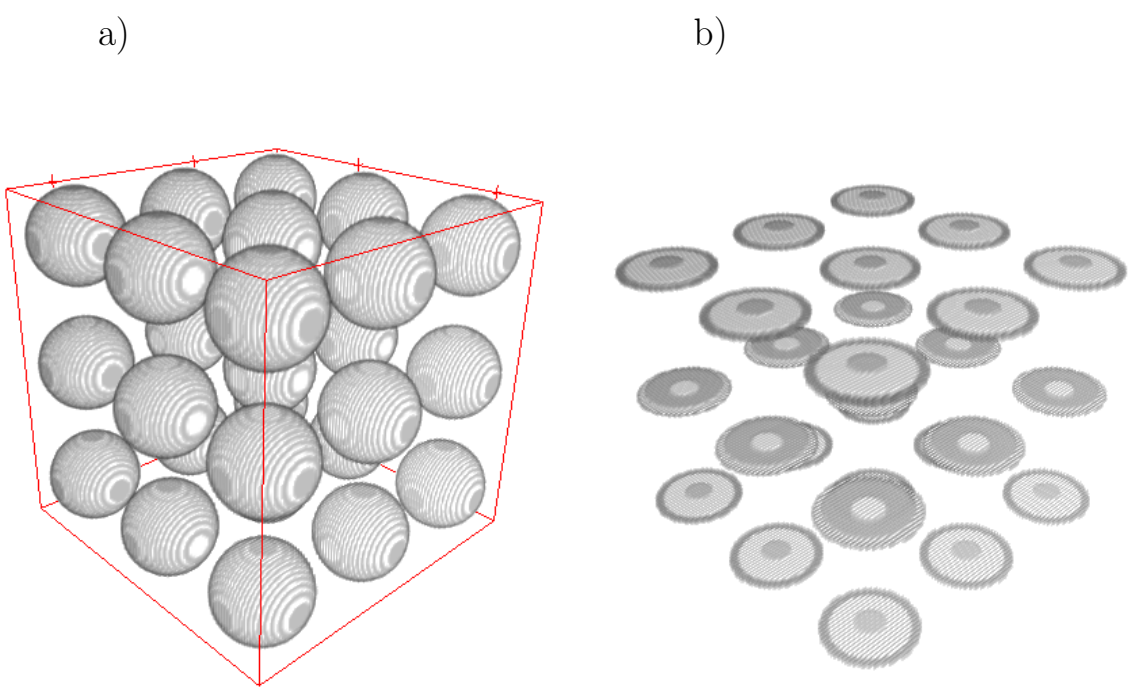

Figure III.B.1 – Illustration of the microstructures consisting of ordered distribution of ellipsoidal inclusions of aspect ratio $\omega = 1$ or $\omega = 0.1$ sufficiently distant from each other to neglect uncertainties related to inter-pores distance in order to determine the number voxel size needed to obtain accurate enough effective elastic estimates.

microstructures displayed in Fig.III.B.1 following the procedure described in Sec.III.3.3. The effective properties obtained for the finest grid (512^3) are taken as a reference to compute the error of

discretization on the effective stiffness tensor $\delta_{\mathbb{C}}$ and on the elastic moduli δ_κ and δ_μ such that:

$$\delta_{\mathbb{C}} = \frac{|\mathbb{C} - \mathbb{C}^{(512)}||_F}{||\mathbb{C}^{(512)}||_F} \tag{60}$$

$$\delta_\kappa = \frac{|\widetilde{\kappa} - \widetilde{\kappa}^{(512)}|}{\widetilde{\kappa}^{(512)}|} \tag{61}$$

$$\delta_\mu = \frac{|\widetilde{\mu} - \widetilde{\mu}^{(512)}|}{\widetilde{\mu}^{(512)}|} \tag{62}$$

The results plotted in Fig.III.B.2a) show that both aspect ratios converge to an error less than 2%

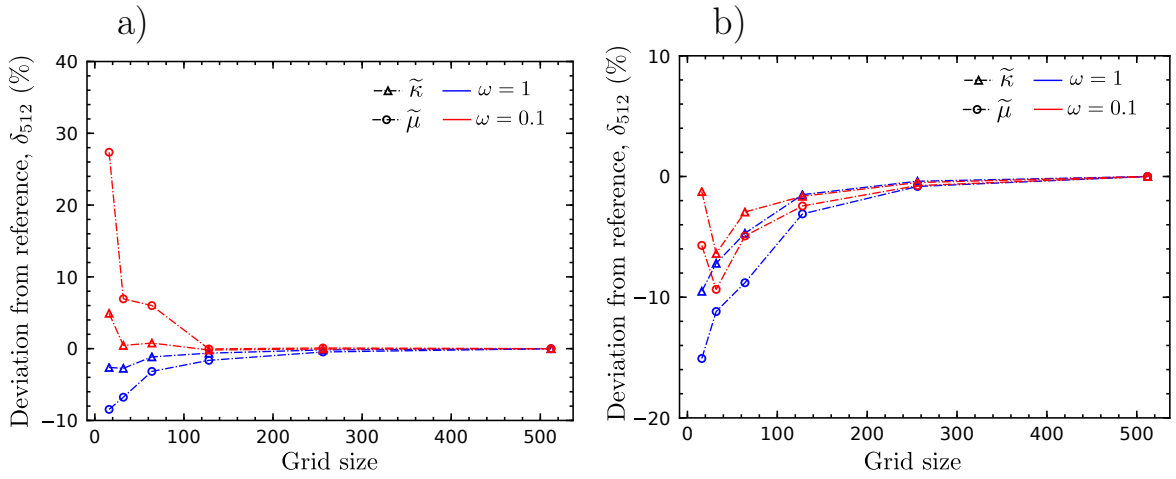

Figure III.B.2 – Evolution of the deviation in the elastic properties of the same microstructure meshed for different sizes of grid (a) Microstructures consist of ordered distribution of ellipsoidal inclusions of aspect ratio $\omega = 1$ or $\omega = 0.1$ sufficiently distant from each other to neglect uncertainties related to inter-pores distance (b) Microstructures consist of ordered densed distribution of ellipsoidal inclusions of aspect ratio $\omega = 1$ or $\omega = 0.1$ with ligament size corresponding to the minimum distance accepted by RSA algorithm.

for grid size around 128^3 which in both cases correspond to a 13 voxels on the longest semi-length of the microstructure. On the other hand, Figure III.B.2b) shows that microstructures with minimum distance between inclusions start to be insensitive to the grid size for grids beyond 256^3 for both aspect ratios which correspond to having at least three voxels between two inclusions. These results highlight the fact that in linear elasticity, the mesh sensitivity to the aspect ratio is negligible as long as we are dealing with aspect ratios in the range of the study, i.e. $0.1 \leq \omega \leq 1$, and that the number of voxels used to mesh the ligament wall between inclusions have to be carefully selected to avoid errors that can easily reach beyond 10%.

A second analysis is related to the elastic properties assigned to each voxel. Associate the elastic properties of the voxel to the elastic properties of the phase lying at its center has been the subject of discussion in the analysis of local errors related to the FFT computations, and methods have been proposed to account for the partition of volume fractions in the sub-volume corresponding to the voxel size (Gélébart and Ouaki, 2015; Kabel et al., 2015; Mareau and Robert, 2017). In the

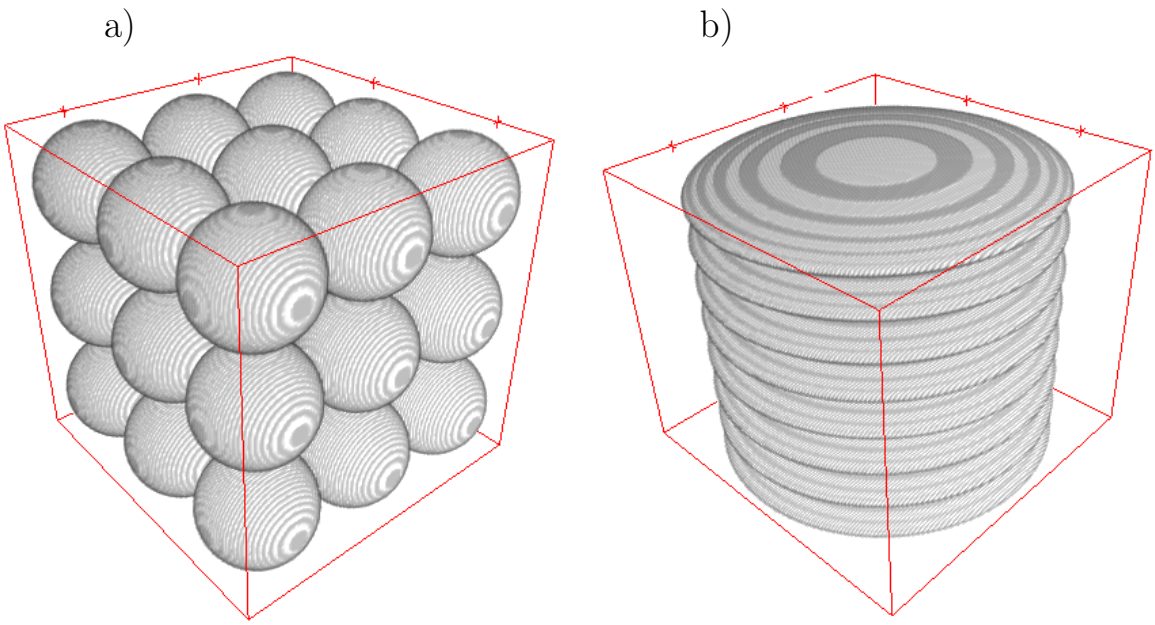

Figure III.B.3 – Illustration of the 3D microstructures consisting of ordered densed distribution of ellipsoidal inclusions of aspect ratio $\omega = 1$ or $\omega = 0.1$ with ligament size corresponding to the minimum distance accepted by RSA algorithm in order to determine the number voxel size needed to obtain accurate enough effective elastic estimates.

variational scheme used for our study, a rigorous formula for the assignation of the local elastic properties to each voxel is derived from the discretization of the method such that:

$$(\mathbb{C}_{\boldsymbol{\alpha}} - \mathbb{C}^0)^{-1} = \sum_{i=1}^{n} c_{\boldsymbol{\alpha},i} (\mathbb{C}_i - \mathbb{C}^0)^{-1} \tag{63}$$

This scheme has been applied in the work on simple microstructures by Brisard and Dormieux (2012) and highlighted the importance of voxel composites for conserving the bounding properties of the scheme and showed an improvement of the convergence of the effective elastic properties as a function of the grid size. In order to determine the procedure to use for the interface voxels, the previous microstructures are generated on binary grids from 16^3 to 2048^3 and the mesh is then compressed by a ratio $r = 1$, 2 or 4. This procedure consists of dividing the size of the array on each direction by the given ratio and associating the new voxel $[i, j, k]$ with the average of the voxels lying in the positions $\mathbf{x} \in [\![ri, r(i+1)]\!] \times [\![rj, r(j+1)]\!] \times [\![rk, r(k+1)]\!]$. For example, taking an initial discretization (grid with voxels valued 1 or 0) of size 1024^3 and a ratio $r = 2$, the final grid is 512^3 with voxels containing a value $\in \{0, 1/2^3, 2/2^3, \ldots, 1\}$.

Results depicted in Fig. III.B.4 show that results from the different strategies of voxel properties assignation all converge to the same effective properties. On one hand, these results show similarly to the observations made in the work by (Brisard and Dormieux, 2012), assignation of the voxel with the elastic properties of its central phase gives increasing effective properties and breaks the bounding property of the solution. The property of this computational scheme to produce a bound

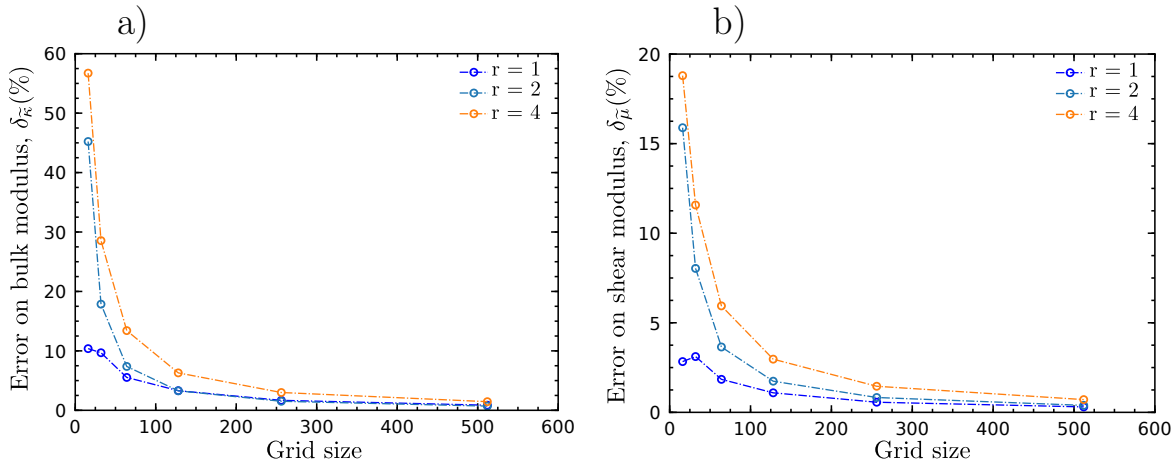

Figure III.B.4 – Evolution of the deviation in (a) the effective bulk modulus (b) the effective shear modulus of the same microstructure meshed on different grid size obtained after compression an initial grid by a ratio $r = 1, 2, 4$ to obtain voxel composites at the interface.

on the effective properties is only valid when using composite voxels with ratio $r \geq 2$ is used. On the other hand, the results shows, surprisingly, that no clear improvment of the convergence is observed by introducing information on interface voxels. On the contrary, increasing the ratio of coarsening leads to stiffer results and thus bigger deviation from the converged effective properties.

III.C Hashin-Shtrikman estimates for randomly oriented ellipsoidal inclusions

Following the celebrated work of (Willis, 1978), the Hashin and Shtrikman (1963a) bound for isotropic composites has been extended to anisotropic microstructures and more specifically to ellipsoidal microstructures. In the particular case of microstructures consisting of aligned ellipsoidal pores of the same aspect ratio ω, the effective compliance tensor $\widetilde{\mathbb{S}}_{HSW} = \widetilde{\mathbb{C}}^{-1}_{HSW}$ takes the form :

$$\widetilde{\mathbb{S}} = \mathbb{S}_m + \frac{c}{1-c}\mathbb{Q}_m^{-1} \tag{64}$$

Where $\mathbb{S}_m = \mathbb{C}_m^{-1}$ is the compliance tensor of the matrix and $\mathbb{Q}_m$ is related to the Hill tensor of the ellipsoidal pores by $\mathbb{Q}_m = \mathbb{C}_m - \mathbb{C}_m\mathbb{P}^m\mathbb{C}_m$ and is expressed by:

$$\mathbb{Q}_m = \frac{1}{4\pi\omega^2}\int_{|\boldsymbol{\zeta}|=1} [\mathbb{C}_m - \mathbb{C}_m\mathbb{H}(\boldsymbol{\zeta})\mathbb{C}_m]|\mathbb{Z}^{-1}\boldsymbol{\zeta}|^{-3}\mathrm{d}S \tag{65}$$

where $\mathbb{Z}$ is the characteristic matrix of the ellipsoidal pores which depends on their shape and orientation as expressed in Sec.II.1.1.a.

In this work, the tensor $\mathbb{Q}_m$ has been computed based on Gauss integration of the Eq.III.C as detailed in Danas (2008)(Section 2.11).

Using the equivalence between orientational averaging and projection on the isotropic basis ($\mathbb{J}$ and $\mathbb{K}$ in Sec.II.2.1) for fourth-order tensors (Gatt et al., 2005), the estimate in Eq.III.C can be used for effective properties of two phase porous materials with ellipsoidal inclusions randomly oriented and distributed in the unit cell:

$$\widetilde{\mathbb{S}} = \mathbb{S}_m + \frac{c}{1-c}\left(\mathbb{Q}_m^{iso}\right)^{-1} \tag{66}$$

where $\mathbb{Q}_m^{iso} = 3\hat{\kappa}_m\mathbb{J} + 2\hat{\mu}_m\mathbb{K}$ with :

$$\hat{\kappa}_m = \frac{\mathbb{Q}^m_{i,kkll}}{9} \tag{67}$$

$$\hat{\mu}_m = \frac{3\mathbb{Q}^m_{i,klkl} - 9\hat{\kappa}_m}{30} \tag{68}$$

Since the matrix phase is isotropic with bulk modulus κ_m and shear modulus μ_m, the effective bulk and shear estimates of Willis are expressed using $\hat{\kappa}_m$ and $\hat{\mu}_m$ such that:

$$\widetilde{\kappa}_{HSW} = \frac{\kappa_m\hat{\kappa}_m(1-c)}{\hat{\kappa}_m + c(\kappa_m - \hat{\kappa}_m)} \tag{69}$$

$$\widetilde{\mu}_{HSW} = \frac{\mu m\hat{\mu}_m(1-c)}{\hat{\kappa}_m + c(\mu m - \hat{\mu}_m)} \tag{70}$$

CHAPTER IV

A POSSIBLE EXTENSION OF RSA MICROSTRUCTURES TO THE CONNECTED NETWORKS

Summary of the chapter: This chapter aims at characterizing the effect of connectivity on both the effective elastic properties and low order statistical descriptors. To that aim, we first introduce a simple model of connected pores based on the RSA algorithm with additional cylindrical channels connecting the isolated ellispoidal pores. The influence on the effective elastic properties of the parameters used to generate the connectivity in the porous phase, namely the throat size and the number of channels per pore, are investigated using an FFT computational procedure. Next, the porous space of the three types of microstructures generated in this thesis are analyzed and compared for the same volume fraction, using the two-point correlation function, the chord-length distribution and the local strain field as a function of the Euclidean map transform. This analysis emphasizes the sensitivity of the effective elastic properties to local features of the microstructure which are lacking from the statistical descriptors investigated in this thesis.

IV.1 Generation of controlled porous network microstructures

In order to create relatively simple connected porous microstructures that enable to investigate quantitatively the effect of some parameters of the connectivity in random porous materials, we extend the RSA algorithm defined in Sec.II.1.2 to generate porous network microstructures. The porous network is a class of geometric models that can be extracted from image analysis of real rocks (Chatzis and Dullien, 1977; Dong and Blunt, 2009; Xiong et al., 2016) and that have been widely used to understand physical properties of porous media (Diaz et al., 1987; Bear et al., 1987; McCall et al., 1991; Al-Kharusi and Blunt, 2007). They are not only developed for theoretical calculations but also to generate realistic models from experimental observations as they propose more complex microstructures than the simple pore-space geometries previously used such as packing spheres or boolean models (Fatt, 1956; Blunt, 2001). A popular representation of a porous network is to fill

the void space by a regular 3D lattice of wide pores connected by narrower throats. The inclusions represent large regions of pores for which we can define an equivalent shape, size and orientation. In turn, the connecting channels represent smaller pores forming a connection path between the larger pores.

For modeling real materials, both positions of the pores and the throat can be chosen according to some deterministic or random procedure based on direct topological analysis on X-ray micro-tomography images of real materials using algorithms to determine inclusions and throats parameters. Although these models do not conform to the internal morphology of all random material, they have proven to be efficient in estimating the physical properties of porous rocks (Patzek, 2001; Oren et al., 1992). For detailed description on the pore network extraction algorithms, the reader is referred to the reviews proposed by Dong and Blunt (2009) and Xiong et al. (2016). In this work, the porous network microstructures are generated using a random distribution of the porous phase based on input parameters describing the pores (as detailed in Sec.II.1.2.a) and those describing the cylindrical channels detailed in the following section.

The objective of this section is to introduce the parameters used to build porous network microstructures and to detail their implementation in the RSA algorithm. Subsequently, a parametric study is conducted to assess the influence of the radius of the connecting cylinders and their average number per pore on the effective elastic properties. This has been carried out using numerical computations for different configurations of connected microstructures.

IV.1.1 Implementation of connectivity parameters in RSA algorithm

In this work, we propose a porous network model that extends the description of the inclusions to ellipsoids of random orientation so that the pore families are described by the discrete distribution of their sizes and shapes as it was presented in Sec.II.1.1.b. In order to introduce connectivity in the microstructures, cylindrical channels are introduced between neighboring pores using the minimum distance between the two inclusions. The parameters that are chosen in order to control the connectivity are:

- The ratio S_{th} of the diameter of the cylinder D_{th} to the smallest characteristic length of the two ellipsoidal inclusions $\mathcal{E}_i$ and $\mathcal{E}_j$ they connect expressed as:

$$S_{th} = \frac{D_{th}}{\min(a_{i,1}, a_{i,2}, a_{i,3}, a_{j,1}, a_{j,2}, a_{j,3})} \tag{1}$$

- The mean and the standard deviation of the coordination number, which represents the number of throats connected to a pore by a Gaussian distribution as it is usually observed in the image analysis of real rocks(Dong et al., 2008; Jivkov et al., 2013).
  This parameter gives an overall information on how pores are connected to each others and has been largely used in the study of its influence on the topology of the random medium and the dispersivity of materials (Vasilyev et al., 2012) as well as the transport properties such as the relative permeability in porous materials (Arns et al., 2004).

The connectivity parameters are introduced into the RSA algorithm using variables computed during the procedure for the determination of the minimum distance between two inclusions (presented in Sec.II.B.1).
For each newly generated inclusion $\mathcal{E}_i$ in the unit cell, the algorithm computes the minimum distance between $\mathcal{E}_i$ and all previously accepted inclusions $(\mathcal{E}_j)_{1\leq j\leq i-1}$ and their 26 periodic images. Besides the minimum distance, the algorithm outputs the two points $\mathbf{x}_{i,j} \in \mathcal{E}_i$ and $\mathbf{y}_{i,j} \in \mathcal{E}_j$ for which this minimum distance is obtained. Once the current inclusion verifies all constraints to be accepted in the microstructure, as stated in Sec.II.1.2, the algorithm stores the characteristic information about its distance to the other accepted inclusions (and periodic images) in a list.
When the total volume fraction of isolated inclusions is reached, the list of distance is sorted in an increasing order of the minimum distance. Subsequently, the algorithm computes the total number of connections N_{th} in the microstructure using the input parameter N_{con} and the total number of inclusions generated N_{tot} such that:

$$N_{th} = N_{con} \times N_{tot} \tag{2}$$

The N_{th} channels are built using cylinders obtained from the N_{th} first connections in the sorted distance list. For two connected inclusions $\mathcal{E}_i$ and $\mathcal{E}_j$, the cylindrical throat is directed by the vector $\mathbf{w} = \mathbf{x}_i - \mathbf{x}_j$ and has a radius defined by the input paramater S_{th}. Periodic images of the throats are ensured by the construction of the distance list that includes distances between the inclusions and the periodic images of previous inclusions.
Figure IV.1.1 shows realizations of porous network microstructures obtained for different aspect ratios of inclusions and with different setting parameters, i.e. N_{con} and S_{th}.
It is worth mentioning that this procedure enables to build a maximum number of throats equal to $N_{tot}!$ by connecting all inclusions to each others, which creates a theoretical limit to the input parameter N_{con} such that

$$N_{con} \leq (N_{tot} - 1)! \tag{3}$$

However, in order to ensure that the throats do not cross inclusions, the generated connexions are constrained to allow only those corresponding to a minimum distance below twice the radius of the smallest inclusion they are attached to. With this additional constraint, the effective number of connections N_{con} may differ from the input parameter.

IV.1.2 Effective elastic properties of porous network microstructures

Once these connected porous models are generated, the objective is to study the influence of each morphological descriptor of the connectivity on the effective elastic properties of porous materials. To that aim, different configurations of microstructures consisting of a total porosity $c = 15\%$ have been generated by changing one of the connectivity parameters (Coordination number N_{con} or throat size S_{th}) while keeping all other microstructural descriptors fixed. The microstructures are then discretized and their effective elastic properties are computed using FFT based simulations on grids of 256^3. The coming sub-section details the configurations parameters, the meshing procedure of the

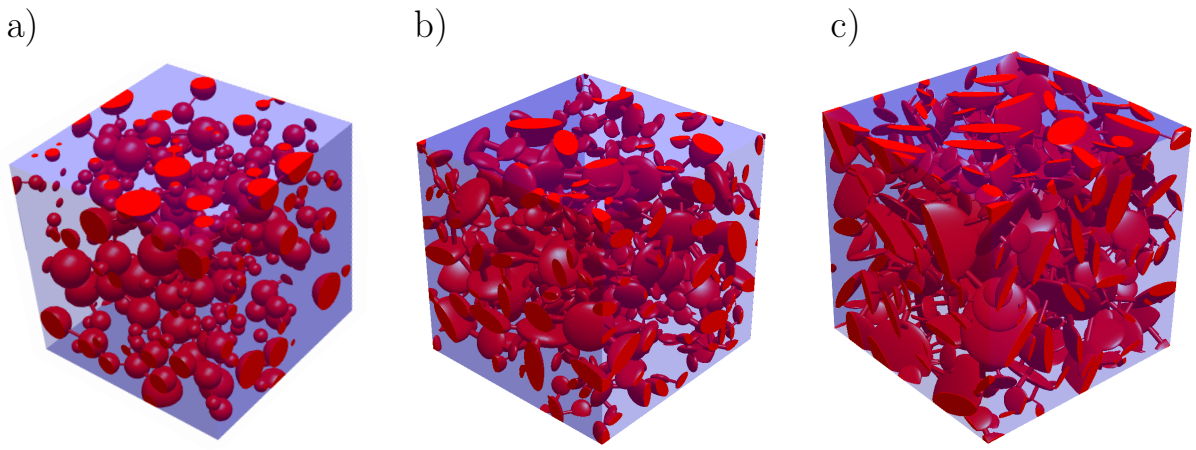

Figure IV.1.1 – RVEs of unit volume L^3 with $N = 150$ randomly distributed pores polydispersed in size for a total porosity (a) $c = 15\%$ and $\omega = 1$, (b) $c = 15\%$ and $\omega = 0.4$, (c) $c = 15\%$ and $\omega = 0.2$. The connectivity parameters for the three realizations are chosen such that the coordination number $N_{th} = 3$ and the throat size ratio $S_{th} = 0.2$.

porous network and shows the evolution of the effective elastic isotropic moduli with the change of the connectivity parameter.

IV.1.2.a Influence of the coordination number on the effective elastic properties

Firstly, the influence of the coordination number is studied by generating different realizations of microstructures having the same inclusions characteristics, in term of shape and size distribution. The cylindrical channels connecting the pores have the same throat radius (corresponding to $S_{th} = 0.3$ for spherical voids) but different coordination number $N_{con} \in \{0, 1, 2, 3, 4, 5, 7\}$, with $N_{con} = 0$ denoting the isolated inclusions microstructure type. Figure IV.1.2 shows the evolution of realizations obtained with different coordination number. Obviously, the initial volume fraction of isolated pores needed in order to reach a total volume fraction of $c = 15\%$ decreases when increasing the number of connections per pore but remains relatively higher than the additional porosity represented by the channels. Indeed, the volume fraction of throats does not exceed 2.5%.
The same study is conducted for different aspect ratios of pores, $\omega \in \{0.2, 0.4, , 1\}$ to observe the influence of connectivity along different shapes of inclusions. The throat radius is kept constant for all microstructures in order to observe only the influence of the number of connections per pore. Figure IV.1.2 shows realizations of microstructures with different aspect ratio and built with the same connectivity and pore radius.
The microstructures are meshed using a regular voxel grid for which the inclusions are meshed using the fast procedure presented in Sec.III.3.3 and the throats are meshed using the following procedure. For a channel connecting the ellipsoids $\mathcal{E}_i$ and $\mathcal{E}_j$, the axis line of the cylinder is directed by vector

$\mathbf{x}_{i,j} - \mathbf{y}_{i,j}$ and crosses the point $\mathbf{x}_{i,j}$ such that the cylinder $\mathcal{C}_{i,j}$ of radius R is defined by the equation:

$$\mathcal{C}_{i,j} = \{\mathbf{x} \quad | \quad \frac{||(\mathbf{x} - \mathbf{x}_{ij}) \wedge (\mathbf{y}_{i,j} - \mathbf{x}_{i,j})||_2}{||\mathbf{x}_2 - \mathbf{x}_1||_2} \leq R\} \tag{4}$$

where $\wedge$ denotes the cross-product and $||.||_2$ is the Euclidean norm.
For each grid voxel $\mathbf{x}_\alpha$ lying in the box comprised between the centers of the ellipsoids, the algorithm attributes the value one if the voxel center is included in the cylinder and lies outside of the ellipsoids such that $\mathcal{Q}_i(\mathbf{x}_\alpha) > 0$ and $\mathcal{Q}_j(\mathbf{x}_\alpha) > 0$. This discretization procedure is applied to all created channels and FFT computations were conducted on grids of size 256^3 with the same procedure as the one presented in Sec.III.3.3. Five realizations of each configuration were computed in order to obtain statistical mean and standard deviation on the effective elastic properties.

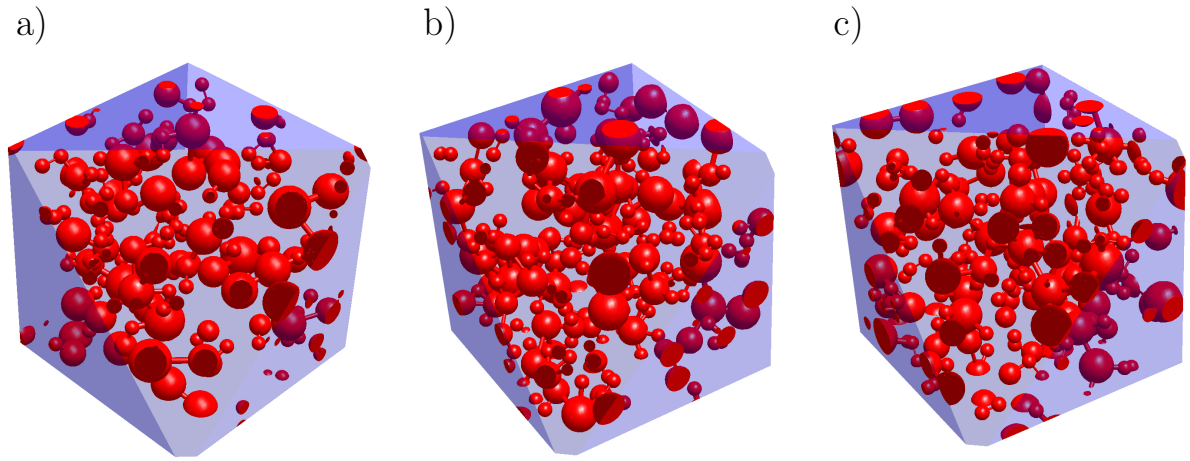

Figure IV.1.2 – Realizations of porous network microstructures of a unit volume L^3 with a total porosity $c = 15\%$ consisting of $N = 150$ randomly distributed spherical pores of different sizes. The connectivity parameters of each realization are chosen such that the throat size ratio $S_{th} = 0.3$ and the coordination number is taken (a) $N_{th} = 1$, (b) $N_{th} = 3$, (c) $N_{th} = 5$.

The results of the evolution of the effective elastic bulk and shear moduli as a function of the coordination number are shown in Fig.IV.1.3. For all aspect ratios ω, both effective moduli decrease with the increase of the connectivity in the microstructure. This decrease starts with a high rate and progressively reduces to a saturated value corresponding to a fully connected network. Depending on the aspect ratio of the isolated inclusions, the rate of decrease can vary depending on the aspect ratio of inclusions ω, as it is observed that the effective properties of microstructures with aspect ratio $\omega = 1$ drop fast as soon as a connection is generated between particules while microstructures with aspect ratio $\omega = 0.4$ have very small decrease due to connecting channels. In turn, the saturated value of effective properties with coordination number falls into very close range of values for the different aspect ratios which highlights that the aspect ratio tends to reduce the effect of connectivity.

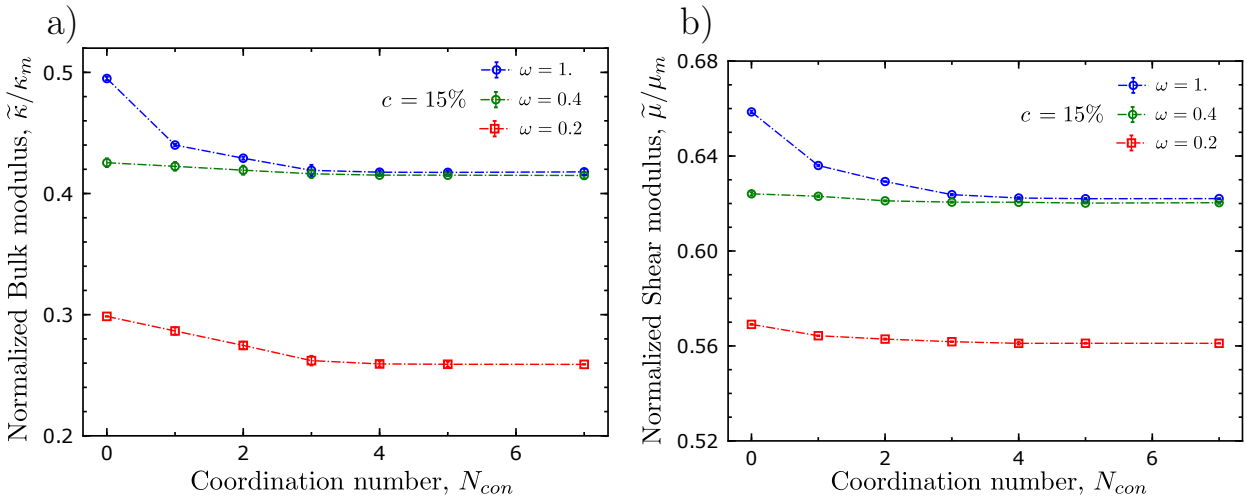

Figure IV.1.3 – Influence of the coordination number of porous networks generated with different aspects ratio on effective properties normalized by the matrix properties for the three selected aspect ratios of interest (a)the bulk modulus $\widetilde{\kappa}/\kappa_m$ and (b) shear modulus $\widetilde{\mu}/\mu_m$ as a function of the coordination number N_{con}.

IV.1.2.b Influence of the throat size on the effective elastic properties

In order to study the effect of the throat size on the effective elastic properties of porous network models, we generate microstructures with a total volume fraction $c = 15\%$ consisting of polydisperse spherical inclusions with the same aspect ratio $\omega = 1$ and connected using a coordination number $N_{con} = 3$ with various throat size ratios $S_{th} \in \{0.2, 0.3, 0.4, 0.5, 0.6\}$. Realizations of the microstructures are shown in Fig.IV.1.4, where the change in radius of channels can be observed. Similarly to the study for the influence of the number of links per pore, the study is extended to ellipsoidal inclusions with aspect ratios $\omega \in \{0.2, 0.4, 1\}$ in order to observe how the shape of inclusions influences the effect of connectivity parameters on the effective elastic properties. The throat size in that case was chosen in order to have the same initial volume fraction of isolated inclusions, before reaching total volume fraction $c = 15\%$ using connecting channels between pores with mean coordination number $N_{con} = 3$. Microstructures were meshed on 256^3 regular voxel grids and their effective elastic properties were computed using the same procedure for FFT-based method described before.

The results of this study for the effective isotropic elastic properties are plotted in Fig.IV.1.5. Similarly to the observation made for the influence of the coordination number, the effective elastic properties decrease with the size of the throats and reach a converged value at a size ratio of throat $S_{th} \approx 0.4$. In turn, the effect of the pore throat is more significant for microstructures with spherical inclusions while it reduces with the elongated inclusions. Surprisingly, the effective bulk and shear moduli obtained for different pore throat radius and the same aspect ratio of pores $\omega = 0.4$ do not vary much.

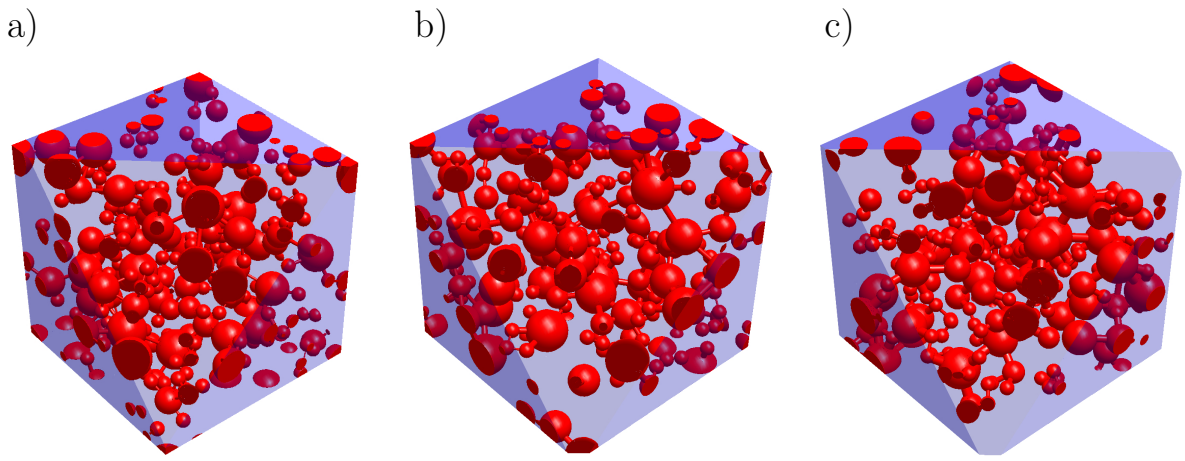

Figure IV.1.4 – Realizations of porous network microstructures of a unit volume L^3 with a total porosity $c = 15\%$ consisting of $N = 150$ randomly distributed spherical pores of different sizes. The connectivity parameters of each realization are chosen such that the coordination number $N_{th} = 3$ and the throat size ratio is taken (a) $S_{th} = 0.2$, (b) $S_{th} = 0.3$ (c) $S_{th} = 0.5$.

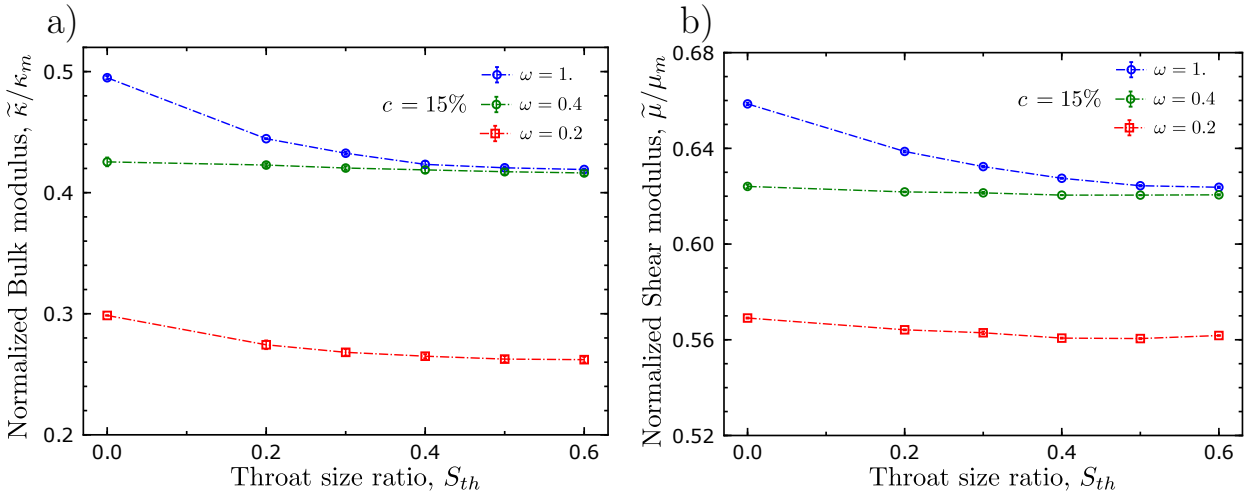

Figure IV.1.5 – Influence of the throat size of the porous networks generated with different aspects on effective properties normalized by the matrix properties for the three selected aspect ratios of interest (a)the bulk modulus $\widetilde{\kappa}/\kappa_m$ and (b)the shear modulus $\widetilde{\mu}/\mu_m$ as a function of the coordination number N_{con}.

IV.1.2.c Influence of the connectivity for different porosities

The evolution of the effective properties of porous network microstructures with $N_{con} = 3$ and $S_{th} = 0.6$ as a function of the aspect ratios ω of the ellipsoidal inclusions for $c \in \{15\%, 25\%\}$ are displayed in Figure IV.1.6 along with the RSA isolated pore microstructures and the associated thresholded GRF microstructures. For all aspect ratios of pores and porosities, the connectivity softens the effective elastic properties but the influence is more important for spherical inclusions as the channels create regions with higher stress field which involve more heterogeneous local elastic

fields. In Fig.IV.1.6 a-b) corresponding to the porosity $c = 15\%$, the effective shear moduli of all connected porous microstructures with aspect ratios $0.4 \leq \omega \leq 1$ seem to converge to the same value corresponding to the RSA microstructures with ellipsoidal shape of $\omega = 0.4$, which is also the same for the thresholded GRF microstructure of the same volume fraction. Similar results are found for the effective bulk moduli for which small differences exist between the porous network microstructures for different aspect ratios but correspond to a slightly higher aspect ratio than the shear moduli. In Fig.IV.1.6 c-d) which displays the results for $c = 25\%$ and aspect ratios of pores $0.4 \leq \omega \leq 1$, the induced connectivity in the porous network microstructures still softens the effective behavior of the material but remains larger than the values obtained with the thresholded GRF.

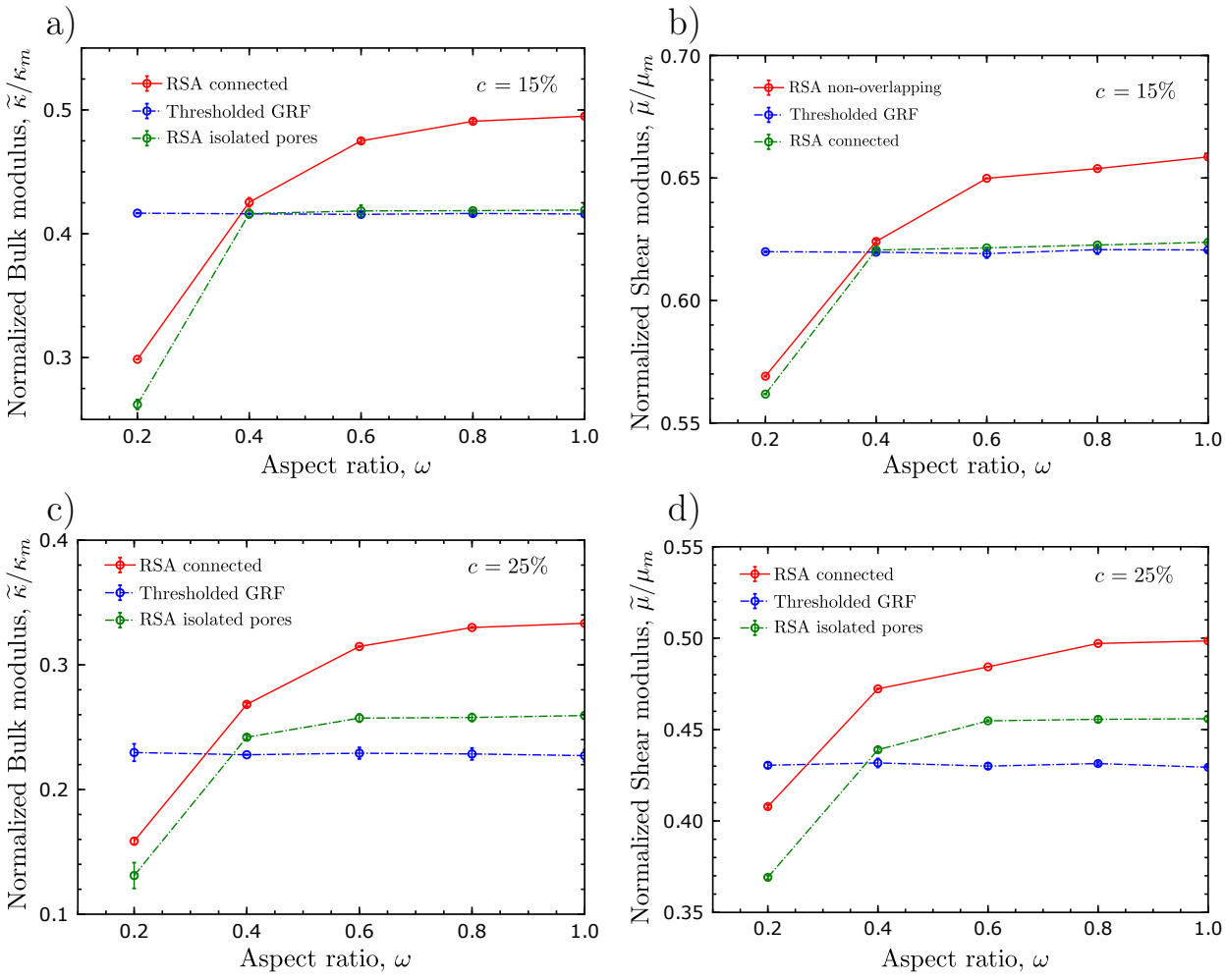

Figure IV.1.6 – (a) Evolution of the effective Bulk modulus $\widetilde{\kappa}$ obtained for the three types of microstructures (Isolated inclusion RSA, Thresholded GRF, Porous network microstructure) as a function of the aspect ratio of the inclusions for total porosity $c = 15\%$. (b)Evolution of the effective Shear modulus $\widetilde{\mu}$ obtained for the three types of microstructures (Isolated inclusion RSA, Thresholded GRF, Porous network microstructure) as a function of the aspect ratio of the inclusions for total porosity $c = 15\%$. (c) Similar to Figure (a) for total porosity $c = 25\%$. (d) Similar to Figure (b) for total porosity $c = 25\%$.

IV.2 Statistical analysis of microstructures

The objective of this section is to analyze the porous space of the different microstructures that have been presented in order to find parameters influencing the effective elastic properties. To that aim, we first extract the second-order correlation function of the porous network microstructures and compare them with those obtained for microstructures with isolated pores and their associated GRF. Next, the chord-length distribution of both porous and matrix phase is implemented in order to evaluate their ability to distinguish between microstructures with different effective elastic properties. The differences between the two-point correlation function and the chord-length distribution functions of the three types of microstructures are uncorrelated with the differences obtained in the effective elastic properties. Such observation highlights the fact that these partial statistical descriptors of the microstructure miss important geometrical features of the porous phase, which highly influence the elastic properties. In order to understand the link between the local information on the porous phase of microstructure and the elastic response, we investigate the possible connection between the Euclidean distance map of the matrix phase and the distribution of the fluctuation of the strain elastic field for each distance.

IV.2.1 Comparison of the two-point correlation functions of the three types of microstructures

In connection with the results of the observations in Sec.III.3.4, the correlation function of porous network microstructures presented in Sec.IV.1.2.c are shown in Fig.IV.2.1 along with the correlation function of RSA microstructures and its associated thresholded GRF. The porous network microstructures have the same c and descriptors of the ellipsoidal inclusions as the RSA isolated pore microstructures due to their controlled generation parameters. In turn, both types of microstructures share the same c with the thresholded GRFs as these latter are the reconstructed fields of the RSA isolated pore microstructures. For the different aspect ratios $\omega \in \{0.2, 0.4, 1\}$ and the two porosities investigated in this thesis $c \in \{15\%, 25\%\}$, the correlation functions $S_{22}(\mathbf{r})$ almost overlap and very little difference is found in the initial slope and the correlation length of the microstructures. This can be explained by the fact that the small volume fraction of cylinders added in the microstructures do not considerably change the overall measure of the specific surface fraction and the characteristic length of heterogeneities that can be captured by the correlation function. These observations assess that adding connectivity of microstructures induces large changes in the macroscopic elastic properties of the microstructures without impacting the second-order statistical descriptors. The shape of the correlation function does not highlight the added cylindrical connections and are therefore insufficient for destinguishing the internal geometry of a heterogeneous material.
In order to dig deeper onto the parameters that can influence the elastic properties of the porous materials, we turn our attention to statistical descriptors that are more related to connectivity.

IV.2.2 Stastistical descriptor of connectivity

Considering a random two-phase medium occupying a volume $V \subset \mathbb{R}^3$, a simple statistical measure of great interest in the analysis of the microstructure is the so-called lineal-path $L^{(i)}$ which correspond to the probability that a segment of size z oriented in direction $\mathbf{n}$ lies in the phase i Torquato and Lu (1993). By definition, this function contains an overall information about linear connectivity of the phase i and has characteristic values at the origin and for large values such that:

$$L^{(i)}(\mathbf{0}) = c_i \quad \text{and} \quad \lim_{|\mathbf{z}|\to\infty} L^{(i)}(\mathbf{z}) = 0 \tag{5}$$

From this probability function, the chord-length distribution function $P_i(\mathbf{z})$ can be derived. This measure represents the probability density function of finding a chord of length $|\mathbf{z}|$ and oriented by the unit vector $\mathbf{n} = \dfrac{\mathbf{z}}{|\mathbf{z}|}$ in the phase. A chord of phase i is defined as a line segment totally contained in phase i and for which both ends lie at the interface between the two phases. By definition of a probability density function, the $P_i(|\mathbf{z}|) = P_i(z)$ verifies that:

$$\int_0^\infty P_i(z)dz = 1 \tag{6}$$

This quantity has been applied in the characterization of microstructures of different materials in order to capture features of the internal geometry of heterogeneous materials such as the grain sizes in polycrystals (Latypov et al., 2018) or the lung airspace dimensions in the biological tissues (Oldmixon et al., 1994) or the analysis of the pore network of concrete (Brisard et al., 2019). For more information on the chord-length distribution, the reader is referred to Serra (1983) and Zähle (1988).

IV.2.2.a Application to the three types of generated microstructures

The chord-length distribution code has been applied to microstructures presented in sections III.3 and IV.1 in order to compare the distribution of chords in microstructures that have the same two-point correlation functions but important differences in their effective elastic properties. We chose to analyze configurations related to the pore aspect ratios $\omega = \{0.2, 0.4, 1\}$ for volume fractions $c = \{15\%, 25\%\}$. The measures were generated for both the porous and matrix phase based on 50 realizations of each configuration binarized in grids of size 256^3. Figures IV.2.2 and IV.2.3 show the probability density functions that correspond to all chords measured in the 50 realizations and their associated frequencies.

On one hand, the chord-length distributions of the matrix phase for the three microstructures display a distribution of chord lengths with small differences appearing at small lengths. The functions measured for all volume fractions are quiet similar and do not display significant deviations between the three types of microstructures neither for aspect ratio $\omega = 0.4$ where the elastic results concord nor for aspect ratios $\omega = 0.2$ and $\omega = 1$. where high differences of elastic properties were observed.

On the other hand, the chord-length distributions of the porous phase display interesting features

about the internal geometry of microstructures. The plots related to the matrix-inclusion type of microstructures display a pronounced peak for a characteristic length that is close to the characteristic size of the inclusions. For spherical pores, this size correspond to the diameter of the smallest inclusions while for the ellipsoidal inclusions, this correspond to the smallest characteristic length axis. After this peak, the chord-length distribution of microstructures with spherical inclusions $\omega = 1.$ are characterized by a sharp drop followed by a branch that decreases more gently, which acknowledges for the polydispersity in size of inclusions. For the elongated inclusions, a smoother decrease in the distribution is observed which is related to the polydispersity in size and orientation of the pores. For the thresholded GRF microstructures, the chord-length distribution is more diffuse and erases the dominant characteristic size observed in the case of RSA microstructures.
In order to compare the three types of microstructures, the deviation in the chord-length distribution of the phase i between two types of microstructure is computed using the estimator proposed in the work of Roberts (1997):

$$\delta_i^{CLD} = \sqrt{\sum_{z_l} \frac{|P_i^{M_1}(z_l) - P_i^{M_2}(z_l)|^2}{|P_i^{M_1}(z_l)|^2}} \tag{7}$$

where M_1 and M_2 refer to the two types of microstructure compared and i denotes the phase (Matrix or pores) on which chord-length distribution has been measured. Table IV.2.1 shows the result of this estimator applied on microstructures with isolated pores and their associated thresholded GRFs for the chord-length distributions of the matrix and the porous phases. Similarly, Table IV.2.3 corresponds to the result of this estimator on Isolated pore microstructures and the porous network with the same pore aspect ratio and Table IV.2.2 gives the comparison between the thresholded GRFs and the porous network.

Porous phase

c \ ω	1.	0.4	0.2
15%	37.16	13.67	11.21
25%	32.07	10.24	10.17

Matrix phase

c \ ω	1.	0.4	0.2
15%	44.26	22.89	17.92
25%	28.79	12.81	15.39

Table IV.2.1 – The deviation between the chord length distribution obtained for RSA microstructures and their reconstructed second-order thresholded GRF. (Left) shows the deviation δ_i^{CLD} (%) measured for the porous phase for different aspect ratio of pores in RSA microstructures and for porosity $c = 15\%$ and 25%. (Right) shows the deviation δ_m^{CLD} (%) measured for the matrix phase for different aspect ratio of pores in RSA microstructures and for porosity $c = 15\%$ and 25%.

From these tables, it can be noted that the smallest differences are observed for microstructures corresponding to $\omega = 0.4$. In turn, the deviations in the chord-length distribution for aspect ratios $\omega = 0.2$ and $\omega = 1.$ are in opposition with the deviation observed on the elastic properties as the differences in the effective properties of spherical inclusions are smaller than those observed for

Porous phase

c \ ω	1.	0.4	0.2
15%	35.55	16.06	14.98
25%	29.89	7.56	8.44

Matrix phase

c \ ω	1.	0.4	0.2
15%	44.41	13.35	18.98
25%	18.19	10.06	13.68

Table IV.2.2 – The deviation in the chord length distribution obtained for porous network microstructures and their reconstructed second-order thresholded GRF. (Left) shows the deviation δ_i^{CLD} (%) measured for the porous phase for different aspect ratio of pores in RSA microstructures and for porosity $c = 15\%$ and 25%. (Right) shows the deviation δ_m^{CLD} (%) measured for the matrix phase for different aspect ratio of pores in RSA microstructures and for porosity $c = 15\%$ and 25%.

Porous phase

c \ ω	1.	0.4	0.2
15%	25.41	14.18	9.40
25%	17.17	8.67	7.02

Matrix phase

c \ ω	1.	0.4	0.2
15%	38.29	21.88	16.05
25%	18.01	13.50	17.37

Table IV.2.3 – The deviation in the chord length distribution obtained for RSA microstructures and porous network with similar total porosity and aspect ratio of pores. (Left) shows the deviation δ_i^{CLD} (%) measured for the porous phase for different aspect ratio of pores in RSA microstructures and for porosity $c = 15\%$ and 25%. (Right) shows the deviation δ_m^{CLD} (%) measured for the matrix phase for different aspect ratio of pores in RSA microstructures and for porosity $c = 15\%$ and 25%.

ellipsoidal inclusions while the deviation in the chord-length distribution of spherical inclusions is more important than $\omega = 0.2$. Previous studies (Roberts, 1997; Levitz, 1998) have observed that microstructures having small differences in the chord-length had similar effective properties. The observations of this work show, on the contrary, that microstructures having different chord-length distributions (such as Thresholded GRF and porous network) can have similar effective properties and inversely microstructures with small differences in the chord-length distributions (such as RSA microstructures and porous network) can have large differences in the effective properties.

IV.2.3 Statistical analysis of the effect of the local morphology on the elastic strain field

In order to analyze the link between the local morphology of microstructures and the effective elastic properties, we use the Euclidean distance transform. This morphological measure contains information about the distribution of the pore space around a given point of the matrix phase and can only be applied to binary image. The output of such measure on a binary image is a graylevel

map representing, for each voxel, the distance to the closest interface.
The choice of the Euclidean norm is related to the fact that this metric is isotropic in the sense that the measured distance does not favour a particular direction around the point of measure.
In this study, the Euclidean distance map is obtained using the corresponding function in *scipy*. This measure is computed by finding the coordinate of the closest background point at each direction of the Cartesian system and then performing a L_2 norm distance between the point x and the point corresponding of b_i at each direction and then normalized by the characteristic size of the cubic cell L such that it is dimensionless:

$$\mathbf{D}_{||.||_2}(\mathbf{x}) = \frac{1}{L}\sqrt{\sum_{i=1}^{3}(x_i - b_i)^2} \tag{8}$$

where $\mathbf{b} = (b_i)_{i\in 1..3}$ is the boundary point with the smallest Euclidean distance along principal directions.
Figure IV.2.4 shows 2D slices of the three different types of microstructures associated to the aspect ratio $\omega = 1$ and the porosity $c = 15\%$ with the corresponding Euclidean distance map. Contrary to the indicator function representation of the microstructure which considers all matrix points as similar, the Euclidean map displays a gradient of values in the matrix phase and reflects on the 3D morphology of the porous phase. It can be already observed from the 2D slices that the range of distances measured in the thresholded GRFs is smaller than those obtained from porous networks and microstructures with isolated inclusions. Similar observations can be done from Figure IV.2.5 which displays the 2D slices and correponding Euclidean distance map for RSA isolated pore microstructures with different aspect ratios of pores $\omega = \{0.2, 0.4, 1\}$.
In turn, Figure IV.2.6 shows the probability density function of the Euclidean distance map for the three types of microstructures generated with different aspect ratio of inclusions $\omega = \{0.2, 0.4, 1\}$. These probability density functions are obtained from the histograms of the Euclidean distance map measured on four realizations of each configuration meshed on grids of size 256^3. These histograms highlight the differences in the measures obtained from thresholded GRFs and the two other types of microstructures as observed from the 2D slices. On the other hand, the porous networks and the isolated pores microstructures have similar probability density functions with those of the porous networks having lower values at small and middle range of Euclidean distances than the one of isolated pores.

IV.2.3.a Application to the three types of generated microstructures

To analyze the effect of the local distribution of the porous phase inside microstructures presented in this thesis, namely the RSA microstructures with isolated pores, the associated thresholded GRFs and the porous networks, components of the elastic strain field measured at each value found in the Euclidean distance map are recorded. For each Euclidean distance measured over four realizations of the same random microstructure, the mean value and the standard deviation of the recorded elastic strain field are computed in order to be compared for the different microstructures. The three

types of microstructures studied in this thesis, namely the RSA microstructures with isolated pores, the associated thresholded GRFs and the porous networks with similar pore aspect ratio than the isolated pores microstructures, are analyzed for the porosity $c = 15\%$ and with different values of the aspect ratio $\omega = \{0.2, 0.4, 1\}$. In this section, we investigate the hydrostatic strain field $\mathrm{Tr}(\boldsymbol{\varepsilon})$ defined by the trace of the local strain field obtained from the FFT computations of a hydrostatic loading $\overline{\boldsymbol{\varepsilon}} = (1, 1, 1, 0, 0, 0)$ and the shear strain field ε_{12} is obtained from the FFT simulations on the same microstructures with a macroscopic strain loading imposed as $\overline{\boldsymbol{\varepsilon}} = (0, 0, 0, 0, 0, \sqrt{2})$. The FFT computations are conducted on binary discretization of the microstructures on grids of size 256^3 because the Euclidean distance transform can only be computed on binary images.

As shown in Figure IV.2.7, there is no apparent correlation between the mean value of the hydrostatic and the shear strain component and the Euclidean distance. On one hand, the average value of the hydrostatic strain component is dependent on the microstructure type and morphology of inclusions embedded inside the heterogeneous microstructure. The evolution of the average hydrostatic field as a function of the Euclidean distance is similar for the different aspect ratio of inclusions and is almost constant except for short range distances where higher deviations are observed around the inclusions for similar range of distance. The differences in the mean between the three types of microstuctures are consistent with the differences in the effective bulk moduli. For microstructures that have similar effective bulk moduli such as the thresholded GRF microstructures for different associated aspect ratios ω or the three types of microstructures for $\omega = 0.4$, the hydrostatistic strain component has close values as a function of the Euclidean distance. In turn, the higher the differences in the effective bulk moduli are the larger the deviation in the mean hydrostatic strain is, as it can be observed from the comparison between isolated pore microstructures with $\omega = 0.2$ and $\omega = 1$. On the other hand, as depicted in Fig.IV.2.7 -2), the shear component of the strain field ε_{12} has a mean value close to null for all microstructures. Since the differences in the effective shear moduli are not as significant as those observed for the effective bulk moduli, the first moment of the shear strain field component is similar for all Euclidean distances and no distinction between the internal geometry of the porous materials can be drawn from it.

Subsequently, we analyze the second-moment of the strain field components obtained from the same realizations as the mean value. Figure IV.2.8 shows the evolution of the standard deviation of both hydrostatic strain and shear strain components as a function of the Euclidean distance of the point of interest. For both components, it can be observed that the standard deviation decreases towards a constant value. The amplitude of the deviation around the porous phase, the rate of this decrease and the value of the deviation at long-range Euclidean distances depend on the type of microstructures and the aspect ratio of pores ω. These differences highlight the intensity of the interactions around the heterogeneities specific to each configuration and enable to qualitatively link between the elastic field and the morphology of pore space such that:

- *At short-range distances*, the amplitude of the standard deviation is related to the local morphology of the pores. For isolated pores microstructures (red curves), the more the pores have a spherical shape, the lower the intensity of the field around the pore is. This observation is

valid for both the hydrostatic and the shear components of the local strain field and the effective elastic moduli is more reduced when the fluctuations around the pore are low. The standard deviation measured at short Euclidean distance in the connected networks with ellipsoidal pores has trends similar to the isolated pores but higher amplitude due to the cylindrical connexions. In turn, all thresholded GRF microstructures depict similar amplitude of the deviation of the strain field components around the porous phase which assesses that the morphology of the porous phase in these microstructures are similar in view of the elastic field it generates around it. Small differences are observed in the amplitude of the deviation for the shear strain component but are less significant than those observed for RSA microstructures and may be assigned to the differences in the size of heterogeneities observed in the microstructure.

- *At middle-range distances*, the rate of decrease in the standard deviation of the strain components highlights the polydispersity of the porous phase. For isolated pores, the rate is more important for spherical pores as there is no dispersion in the orientation of the inclusions. On the contrary, the more elongated the pores are, the more the rate of decrease is lower because the local orientation of the inclusions has a larger impact. When additional cylindrical channels are added between the pores to connect the porous phase, the changes in the rate depend on the aspect ratio of the ellispoidal pores. For highly elongated pores $\omega = 0.2$, the rate is unchanged when the amplitude is higher for all Euclidean distances. For $\omega = 0.4$ and $\omega = 1$, the standard deviation decreases faster with the increase of the Euclidean distance. Concerning the thresholded GRFs, the rate of decrease appears to be the same for all microstructures, as the complex morphology of the porous phase does not depict any preferential local orientation of the pores.
- *At long-range distances*, the deviation is characterized by a constant value corresponding to fluctuations of the elastic strain field at points lying relatively far from the pores. Similarly to short-range distances, the order of these constant values for the different microstructure correpond to the order of the effective elastic properties such that for the same aspect ratio ω, the higher this value is, the lower the effective properties are, which is particularly the case for microstructures containing elongated pores ($\omega = 0.2$ as depicted by Fig.IV.2.8 a-c and Fig.IV.2.8 a-c).

The qualitative differences obtained in the evolution of the second-moment of the local strain field components as a function of the Euclidean distance shows the importance of the local information of the microstructure on the local elastic fields and subsequently on the effective elastic moduli. The distribution of the porous phase in periodic microstructures acts on the amplitude of the strain field around the pore and at long-range distances. This is mostly driven by the morphology of the pores. In turn, the distribution of porous space changes the rate of decrease of the amplitude of the strain field in middle-range distances from the pores and this can be related to the local orientations of the pores. These features of the internal geometry of the porous space are not clearly distinguished by neither the two-point correlation function nor the chord-length distribution. In turn, Figures IV.2.9,IV.2.10 and IV.2.11 show the histograms of the fluctuation of the hydrostatic and shear

components of the strain field taken at different Euclidean distances for the aspect ratios of pores $\omega = 0.2, 0.4$ and 1. It can be observed that for each microstructure configuration, the shear strain component histograms have a probability distribution function which is symmetric around the mean $m \approx 0$ and the range of values obtained depends on the Euclidean distance. On the other hand, the probability distribution function of the hydrostastic strain component at different Euclidean distances has a more complex shape which is non symmetric around the mean value. Clear differences in the probability distribution functions are observed between the three types of microstructures at every Euclidean distance. The thresholded GRFs microstructures have a probability density function that is close to a Gaussian distribution for the three Euclidean distances of interest while the distribution of the porous networks and microstructures with isolated pores are non symmetric around the mean for short and middle-range distances, especially for $\omega = 0.2$ and 0.4. This may be related to the aspect ratio of pores and the relative distribution of the different sizes of pores.

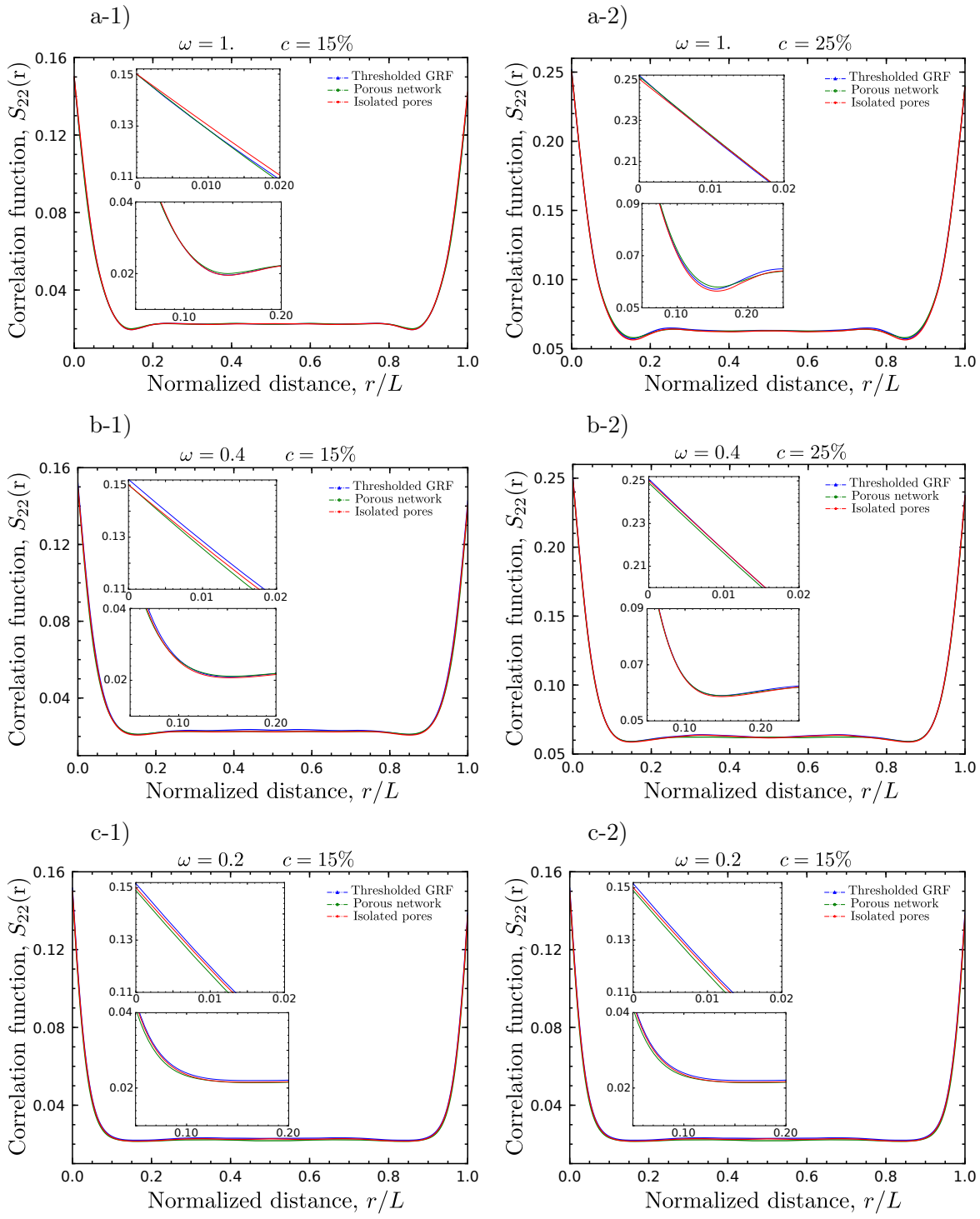

Figure IV.2.1 – (1) Comparison between the correlation functions of the three types of random porous microstructures generated in this thesis with porosity $c = 15\%$ and different aspect ratios of the ellipsoidal pores used as input parameter in the RSA algorithms (a) $\omega = 0.2$, (b) $\omega = 0.4$ (c) $\omega = 1$.
(2) Comparison between the correlation functions of the three types of random porous microstructures generated in this thesis with porosity $c = 25\%$ and different aspect ratios of the ellipsoidal pores used as input parameter in the RSA algorithms (a) $\omega = 0.2$, (b) $\omega = 0.4$ (c) $\omega = 1$.

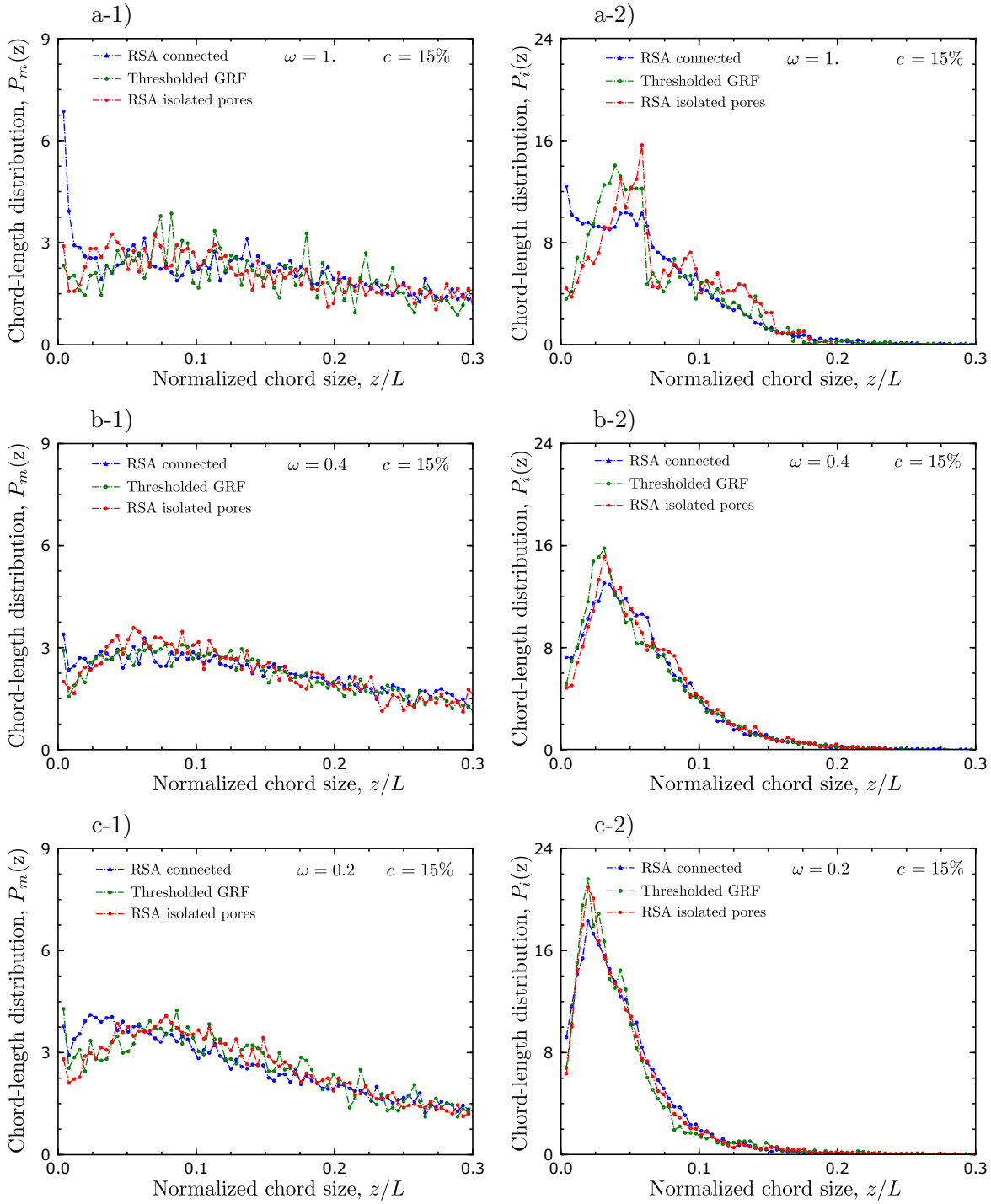

Figure IV.2.2 – (1) Comparison between the chord-length distributions of the matrix phase computed on the three types of random porous microstructures generated in this thesis with porosity $c = 15\%$ and different aspect ratios of the ellipsoidal pores used as input parameter in the RSA algorithms (a) $\omega = 0.2$, (b) $\omega = 0.4$ (c) $\omega = 1.$.

(2) Comparison between the chord-length distributions of the porous phase computed on the three types of random porous microstructures generated in this thesis with porosity $c = 15\%$ and different aspect ratios of the ellipsoidal pores used as input parameter in the RSA algorithms (a) $\omega = 0.2$, (b) $\omega = 0.4$ (c) $\omega = 1$.

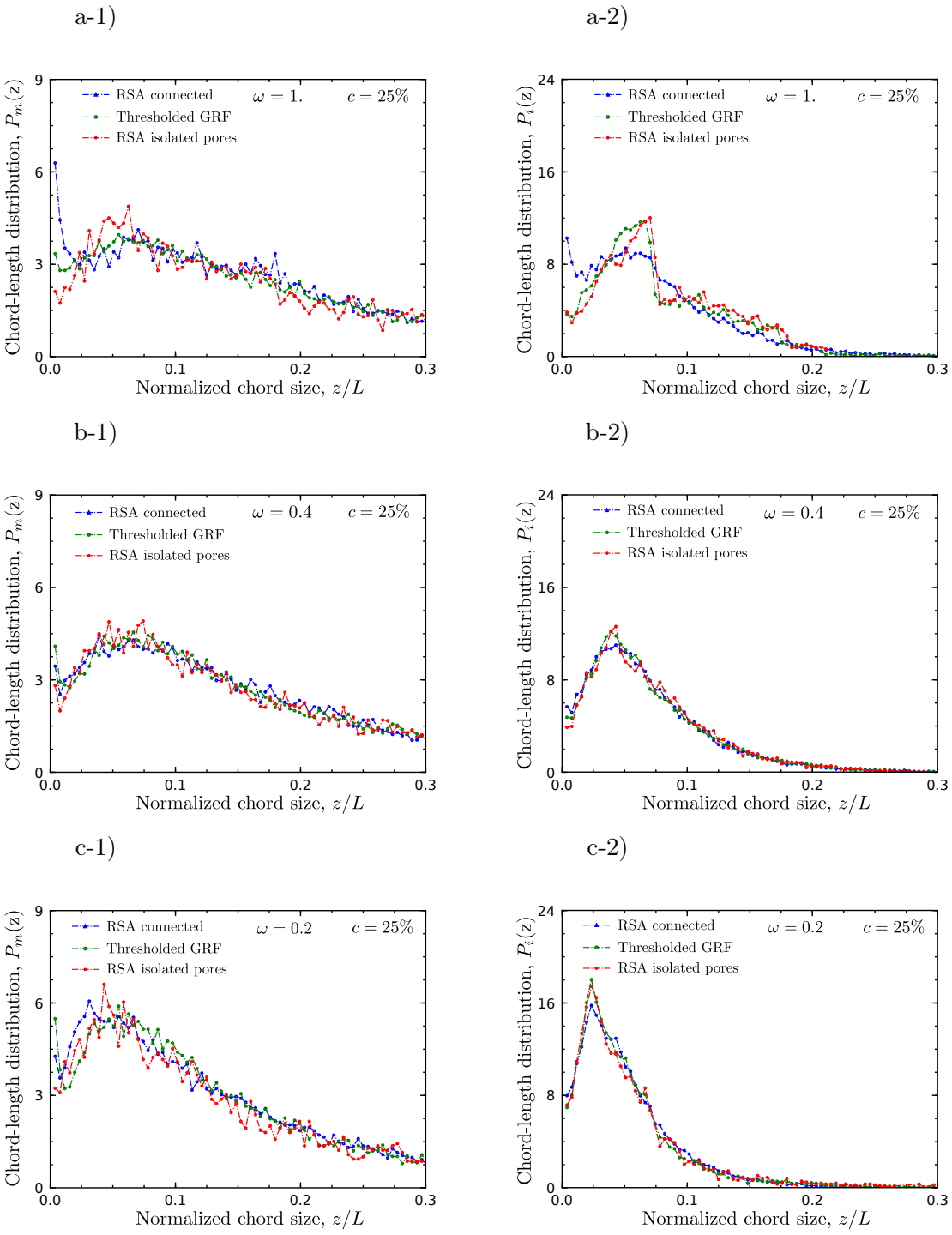

Figure IV.2.3 – ((1) Comparison between the chord-length distributions of the matrix phase computed on the three types of random porous microstructures generated in this thesis with porosity $c = 25\%$ and different aspect ratios of the ellipsoidal pores used as input parameter in the RSA algorithms (a) $\omega = 0.2$, (b) $\omega = 0.4$ (c) $\omega = 1.$.

(2) Comparison between the chord-length distributions of the porous phase computed on the three types of random porous microstructures generated in this thesis with porosity $c = 25\%$ and different aspect ratios of the ellipsoidal pores used as input parameter in the RSA algorithms (a) $\omega = 0.2$, (b) $\omega = 0.4$ (c) $\omega = 1.$

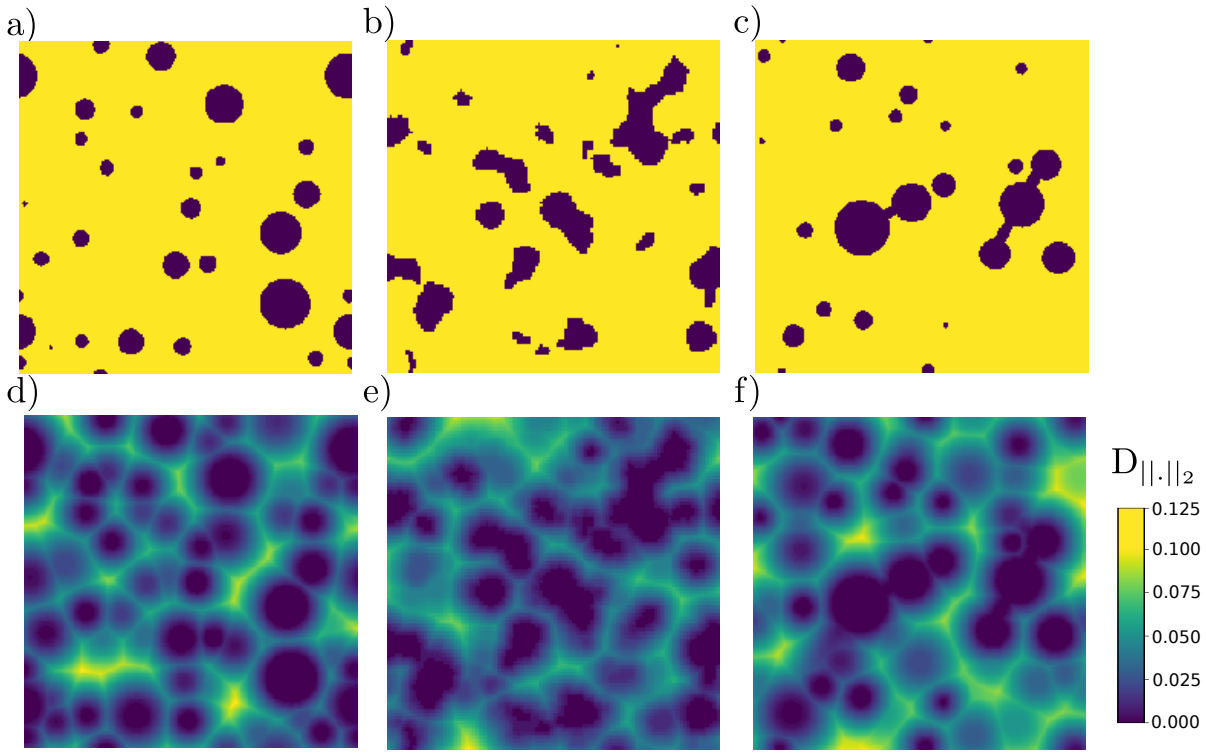

Figure IV.2.4 – (TOP) 2D slice of RVE realizations for different types of microstructures generated based on similar statistical descriptors with $\omega = 1$ and $c = 15\%$: (a) Isolated inclusion microstructure (RSA) (b) Thresholded GRF microstructures obtained using second-order information from RSA microstructures with $\omega = 1$ and $c = 15\%$ (c) Porous network microstructure with total porosity of $c = 15\%$ consisting of $c_i = 13\%$ of spherical pores $\omega = 1$ and characteristic parameters of connecting channels $S_{th} = 0.3$ and $N_{con} = 2$. (BOTTOM) The corresponding 2D slice of the Euclidean distance map of the RVE realizations (d) isolated inclusion microstructure (RSA) (e) Thresholded GRF microstructure and (f) Porous network microstructure.

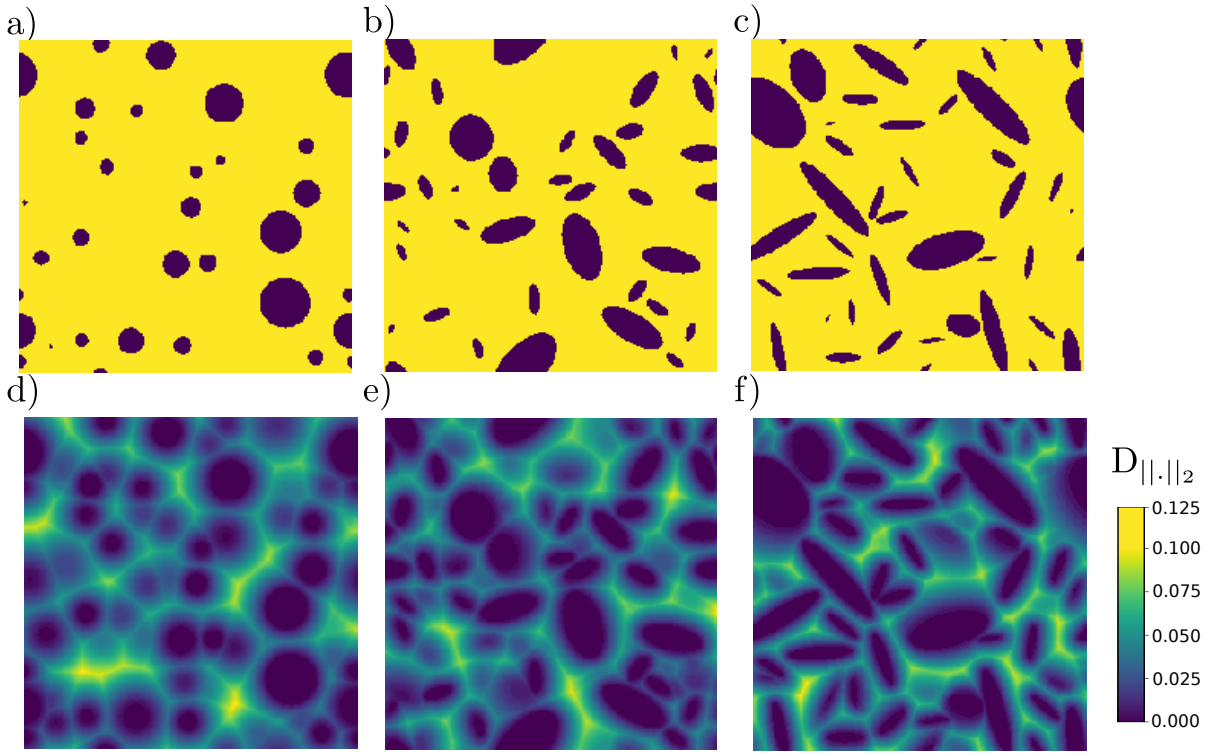

Figure IV.2.5 – (TOP) 2D slice of RVE realizations of RSA microstructures with isolated polydisperse inclusions for a total porosity of $c = 15\%$ (a) $\omega = 1$ (b) $\omega = 0.4$ and (c) $\omega = 0.2$.
(BOTTOM) The corresponding 2D slice of the Euclidean distance map of the RVE realizations for (d) $\omega = 1$ (d) $\omega = 0.4$ (d) $\omega = 0.2$.

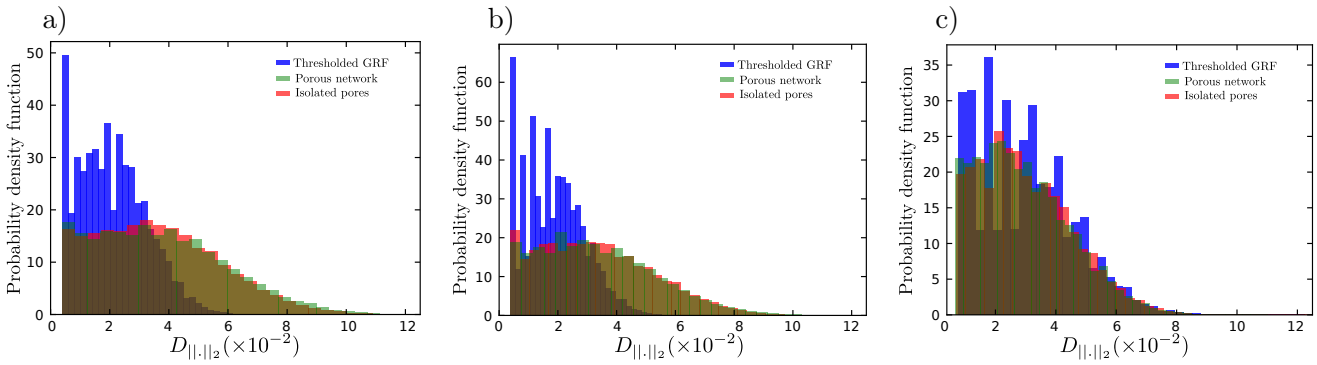

Figure IV.2.6 – The probability density function of the Euclidean distance map for the three types of microstructures, namely the isolated inclusions RSA microstructures, the associated thresholded GRF and the porous network microstructure, generated based on the similar statistical descriptors of the porous phase with porosity $c = 15\%$ (a) aspect ratio of the inclusions $\omega = 1$ (b) aspect ratio of the inclusions $\omega = 0.4$ (c) aspect ratio of the inclusions $\omega = 0.2$.

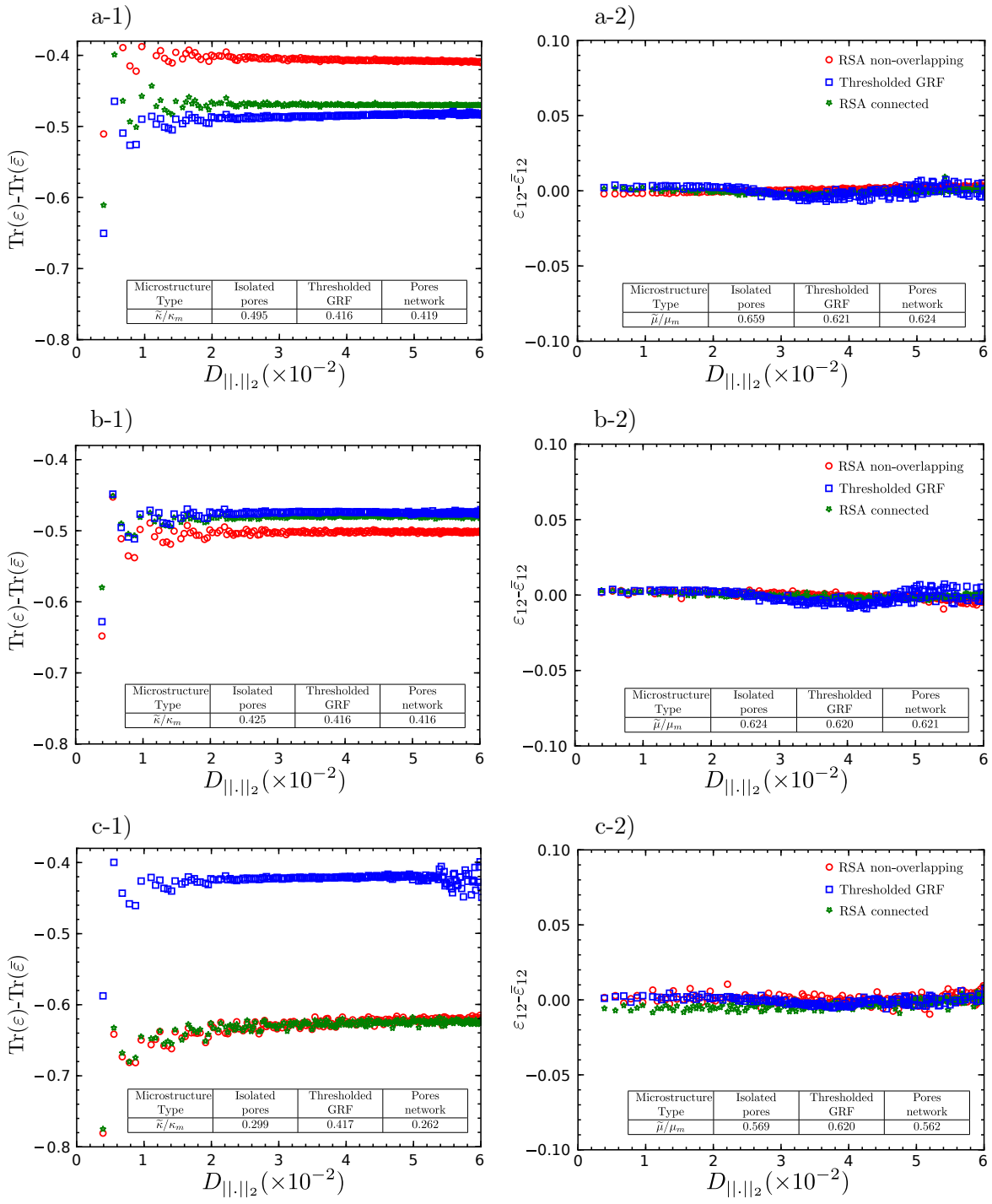

Figure IV.2.7 – (1) Evolution of the average value of the fluctuating part of the hydrostatic strain component as a function of the Euclidean distance for the three types of microstructures investigated in this thesis with porosity $c = 15\%$. The microstructures have been generated based on similar statistical descriptors of the porous phase for RSA microstructures with (a) aspect ratio of the inclusions $\omega = 1$ (b) aspect ratio of the inclusions $\omega = 0.4$ (c) aspect ratio of the inclusions $\omega = 0.2$.
(2) Evolution of the average value of the fluctuating part of the shear strain component as a function of the Euclidean distance for the three types of microstructures investigated in this thesis with porosity $c = 15\%$.

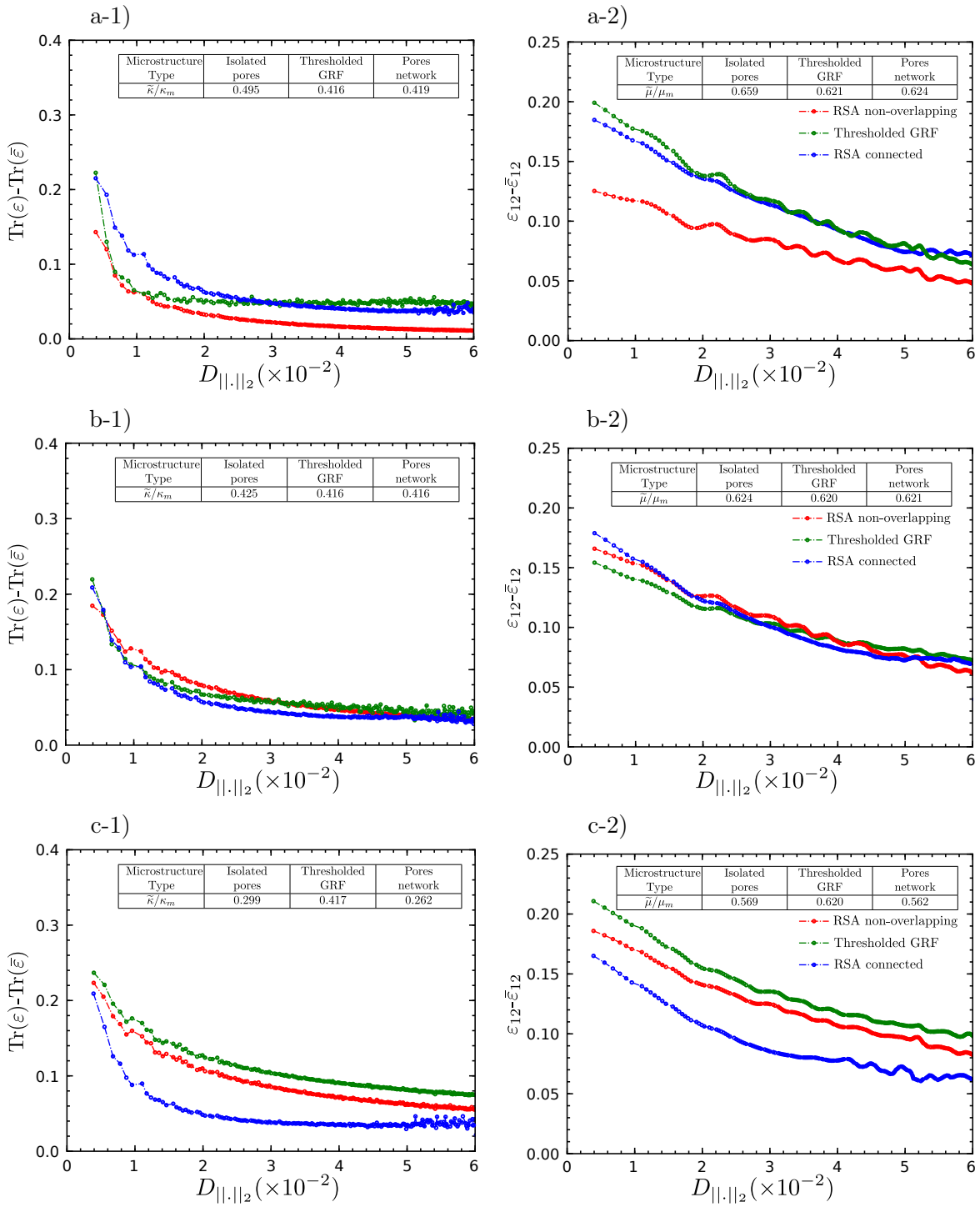

Figure IV.2.8 – (1) Evolution of the standard deviation of the fluctuating part of the hydrostatic strain component as a function of the Euclidean distance, for the three types of microstructures presented in thesis, with porosity $c = 15\%$. The microstructures have been generated based on similar statistical descriptors of the porous phase for RSA microstructures with (a) aspect ratio of the inclusions $\omega = 1$ (b) aspect ratio of the inclusions $\omega = 0.4$ (c) aspect ratio of the inclusions $\omega = 0.2$.
(2) Evolution of the standard deviation of the fluctuating part of the shear strain component as a function of the Euclidean distance for the same unit cell microstructures.

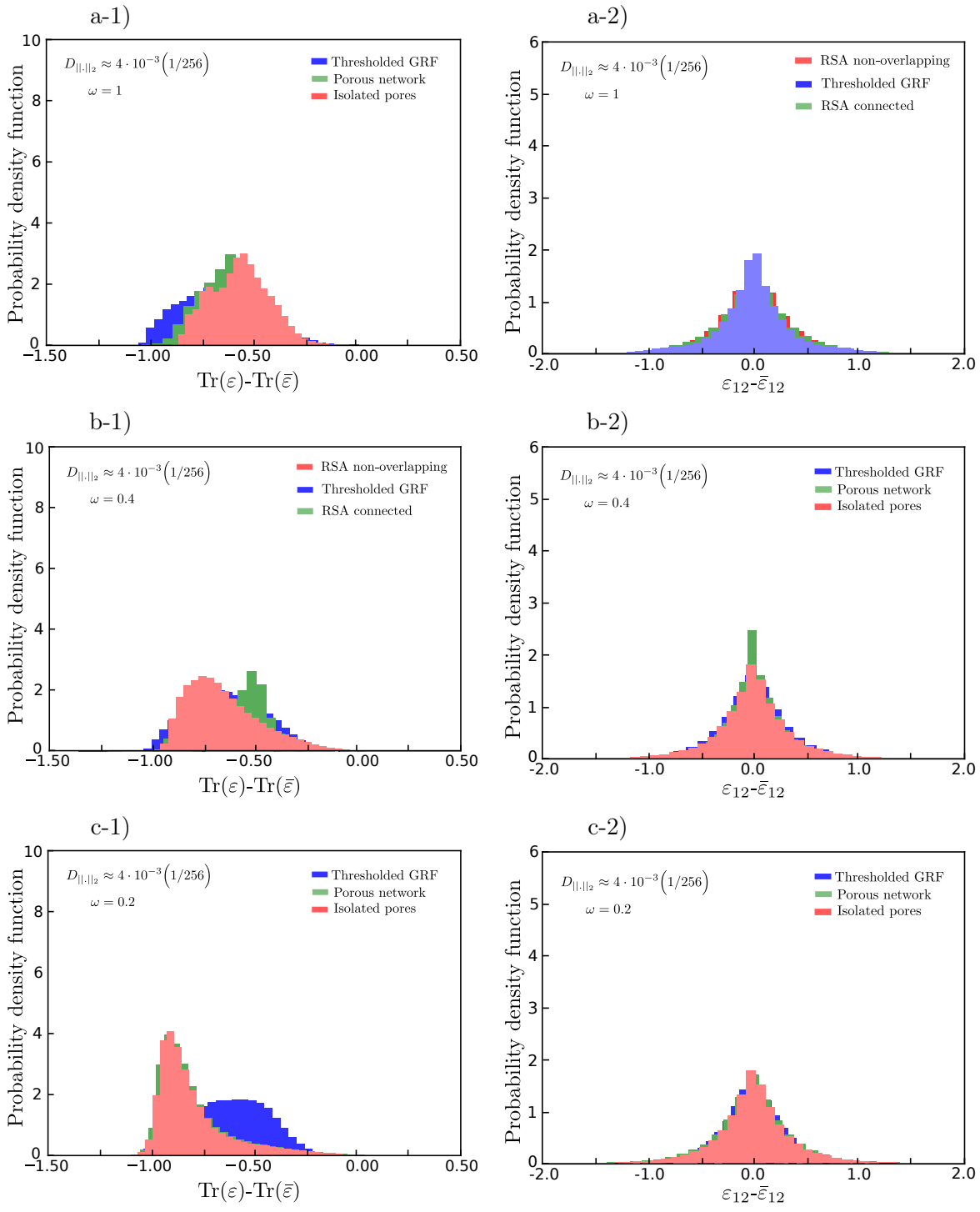

Figure IV.2.9 – (1) Histograms of the fluctuating part of the hydrostatic strain component for points lying at Euclidean distance $D_{||.||_2} = 4 \times 10^{-3}$ (which corresponds to the boundary of the pore). These histograms are obtained on the three types of microstructures presented in thesis, with porosity $c = 15\%$. The microstructures have been generated based on similar statistical descriptors of the porous phase for RSA microstructures with (a) aspect ratio of the inclusions $\omega = 1$ (b) aspect ratio of the inclusions $\omega = 0.4$ (c) aspect ratio of the inclusions $\omega = 0.2$. (2)Histograms of the fluctuating part of the shear strain component for points lying at Euclidean distance $D_{||.||_2} = 4 \times 10^{-3}$, for the same microstructures.

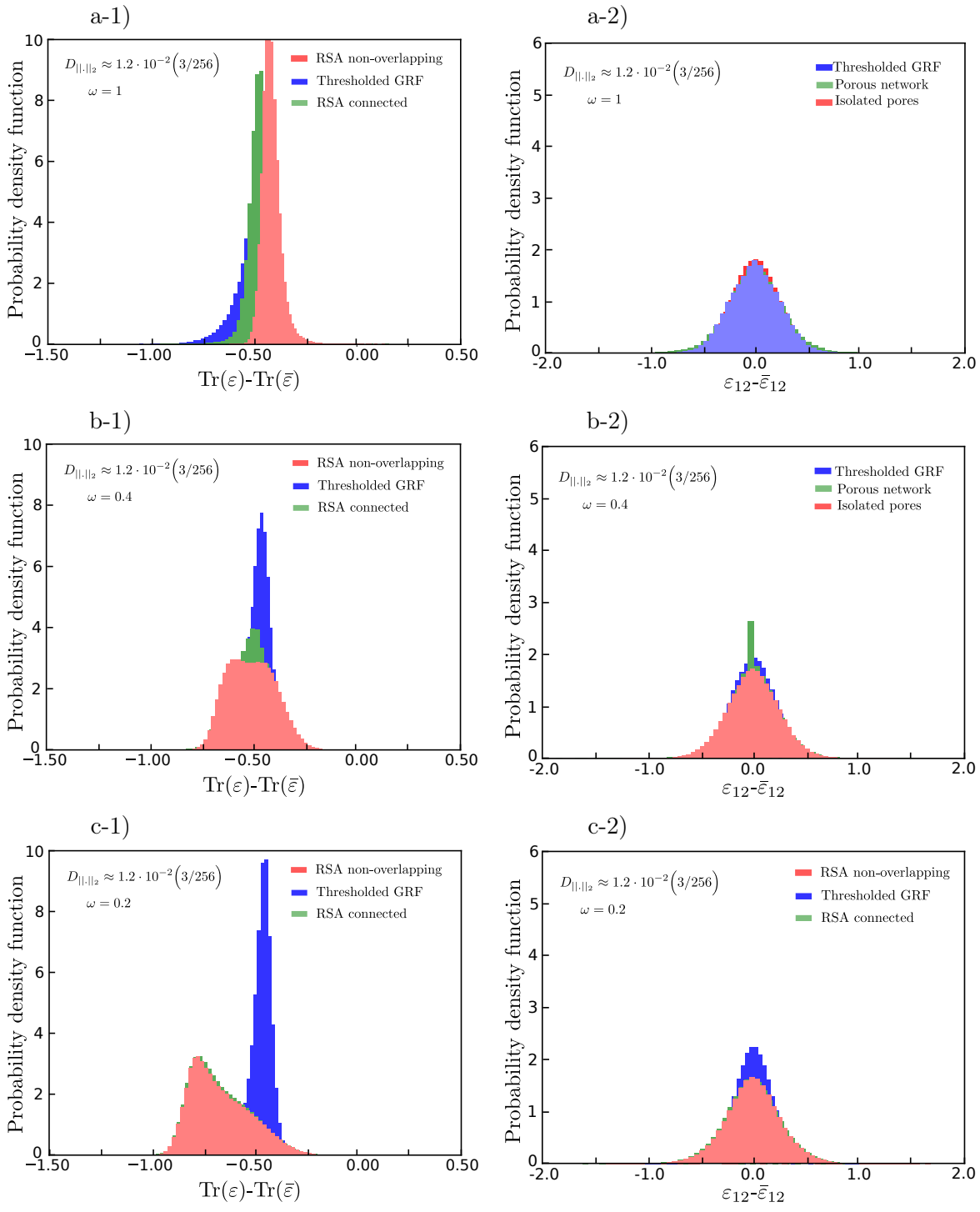

Figure IV.2.10 – (1) Histograms of the fluctuating part of the hydrostatic strain component for points lying at Euclidean distance $D_{||\cdot||_2} = 1.2 \times 10^{-2}$ (which corresponds to the boundary of the pore). These histograms are obtained on the three types of microstructures presented in thesis, with porosity $c = 15\%$. The microstructures have been generated based on similar statistical descriptors of the porous phase for RSA microstructures with (a) aspect ratio of the inclusions $\omega = 1$ (b) aspect ratio of the inclusions $\omega = 0.4$ (c) aspect ratio of the inclusions $\omega = 0.2$. (2)Histograms of the fluctuating part of the shear strain component for points lying at Euclidean distance $D_{||\cdot||_2} = 4 \times 10^{-3}$, for the same microstructures.

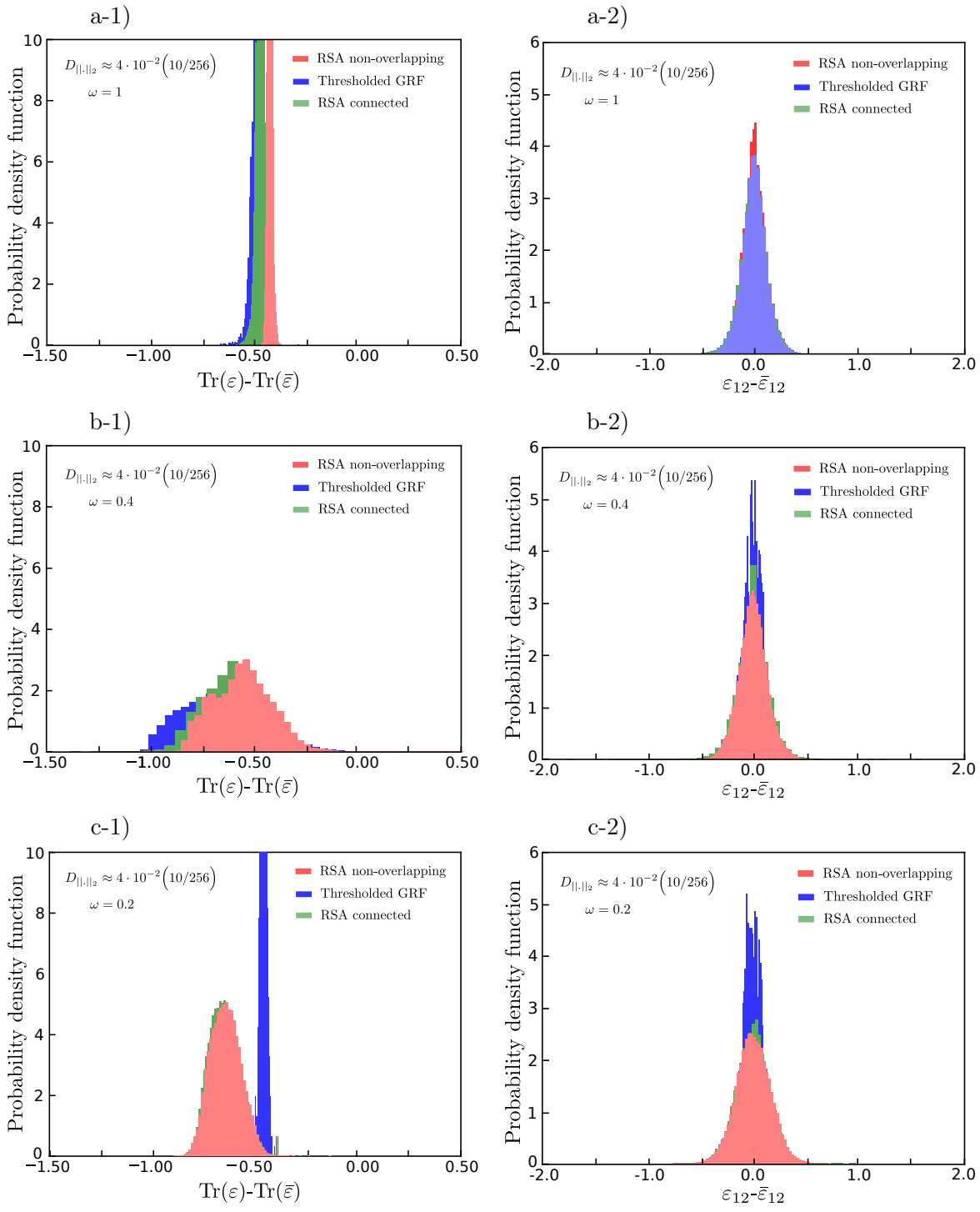

Figure IV.2.11 – (1) Histograms of the fluctuating part of the hydrostatic strain component for points lying at Euclidean distance $D_{||.||_2} = 4. \times 10^{-2}$ (which corresponds to the boundary of the pore). These histograms are obtained on the three types of microstructures presented in thesis, with porosity $c = 15\%$. The microstructures have been generated based on similar statistical descriptors of the porous phase for RSA microstructures with (a) aspect ratio of the inclusions $\omega = 1$ (b) aspect ratio of the inclusions $\omega = 0.4$ (c) aspect ratio of the inclusions $\omega = 0.2$. (2)Histograms of the fluctuating part of the shear strain component for points lying at Euclidean distance $D_{||.||_2} = 4 \times 10^{-3}$, for the same microstructures.

IV.3 Concluding remarks

In this study, the effective elastic fields of random porous microstructures consisting of non-overlapping ellipsoidal inclusions connected by cylindrical channels have been investigated for a total volume fraction of $c = 15\%$ and $c = 25\%$. The microstructures are generated using RSA algorithms presented in Sec.II.1.2.a with different aspect ratios ω of the inclusions in order to study the combined effect of the connectivity with the shape of the pores.

The chapter presents the parametric numerical study used to investigate the influence of connectivity parameters of the periodic porous networks on the effective elastic properties of these microstructures. This work starts from the extension of the RSA generation algorithm to account for cylindrical connexions between the ellipsoidal pores for which the throat radius and the average number of channels to generate for each can be triggered. Following the generation of the microstructures, an FFT numerical study has been implemented using PBC to compute the effective elastic properties of each microstructures. The results have shown a significant decrease of the effective bulk and shear moduli of the porous network microstructures in comparison with the RSA microstructures of similar volume fraction, especially for spherical inclusions for which small additional connectivity drops the effective results away from the Hashin-Shtrikman bound.

Subsequently, the chapter analyzes the low-order stastistical descriptors of the three type of microstructures generated during this work, i.e. the isolated inclusions RSA microstructure, the reconstructed thresholded GRF and the porous network with similar morphological parameters of pores. The two-point correlation function of these microstructures are almost indistinguishable assessing that this measure is unable to distinguish connectivity of microstructures precisely, which following the elastic computations result in significant changes in the effective bulk and shear moduli. In turn, the chord-length distribution analyzis of the porous and matrix phase shows large differences, which can reach up to 50% following the definition of the mean square deviation, between the RSA microstructures and the reconstructed thresholded GRFs. However, the differences found by this measure, which is often chosen to distinguish the statistical models, are not in line with the deviations in the effective elastic properties of materials. The largest deviation in the effective properties are found for highly elongated inclusions $\omega = 0.2$ while the differences in the chord-length distribution for such microstructures are of the same order as those corresponding to aspect ratio $\omega = 0.4$ for which RSA model and GRFs microstructures have almost the same effective properties.

In the second part of this work, we proposed a new measure to analyze the link between the elastic properties and the internal microstructure description. This measure is based on measuring the Euclidean distance of each point in the matrix phase of a microstructure and relating it to the local fluctuations of the strain field components. We applied this procedure on both shear and bulk strain components and found qualitative correlation between the evolution of the first and second moment of the fluctuations and the effective elastic properties of the material. Therefore, an important result out of this part is that the local elastic fields of heterogeneous materials are highly sensitive to local elongated heterogeneities (e.g. connections or isolated inclusions) which are not accurately measured

by the popular low-order statistical measures. These features, though not statistically important, have a significant effect on the mechanical fields of the material that spreads beyond their local position.

APPENDIX

IV.A Implementation of chord-length distribution in 3D microstructures:

In order to compute lineal-path function and chord-length distribution from discretized two-phase microstructures, the procedure developed by Coker and Torquato (1995) for 2D digitized samples is extended to 3D microstructures. The algorithm for the determination of the lineal-path is based on an iterative procedure of randomly throwing oriented lines and can be described by the following steps:

- **Input parameters:** The random lines are described by their unit directional vector $\mathbf{t}$ defined by the angles $\theta \in [-\pi/2, \pi/2]$ and $\phi \in [0, 2\pi]$ such that:

$$\mathbf{t} = [\cos(\theta)\cos(\phi), \cos(\theta)\sin(\phi), \sin(\theta)] \tag{9}$$

  Other input parameters are the phase i in which the chords are measured and the number of iteration of random lines thrown to generate the probability function.

- **Iterative procedure:** For the number of iterations chosen by the user, the procedure repeats the following:
  - *step 1:* Create a random line oriented by its directional vector $\mathbf{t}$ by generating a random point $A = [a_1, a_2, a_3]$ from which the line goes. A point $\mathbf{x}$ on this line is thus defined by its parameteric equation:

$$x = a_1 + \alpha t_1 \tag{10}$$
$$y = a_2 + \alpha t_2 \tag{11}$$
$$z = a_3 + \alpha t_3 \tag{12}$$
$$\alpha \in \mathbf{R} \tag{13}$$

    In order to apply the following description on a discretized grid $G_{\boldsymbol{\alpha}}$ of cubic size N^3, the line is formulated as three N-uplets $\mathbf{x}_{\boldsymbol{\alpha}}, \mathbf{y}_{\boldsymbol{\alpha}}, \mathbf{z}_{\boldsymbol{\alpha}}$ corresponding to the position of the voxels

of the grid that are crossed by the line. The positions of the voxels are found by writing the parameteric equation in a discrete way such that :

$$\alpha = \frac{(x_{\boldsymbol{\alpha}} - a_1)}{t_1} \tag{14}$$

$$y_{\boldsymbol{\alpha}} = \lfloor a_2 + \alpha t_2 \rfloor \tag{15}$$

$$z_{\boldsymbol{\alpha}} = \lfloor a_3 + \alpha t_3 \rfloor \tag{16}$$

$$x_{\boldsymbol{\alpha}} \in \{0, ..., N-1\} \tag{17}$$

where $\lfloor x \rfloor$ denotes the integer part of a number x. The following description is valid only when $t_1 \neq 0$, otherwise the positions are found using $y_{\boldsymbol{\alpha}} \in \{0, ..., N-1\}$ if $t_1 = 0$ and $t_2 \neq 0$, or $z_{\boldsymbol{\alpha}} \in \{0, ..., N-1\}$ if $t_1 = 0$ and $t_2 = 0$.
For periodic microstructures, in order to make optimal use of the line drawn in the microstructure, **To change: the final positions that are checked are the** $[x_{\boldsymbol{\alpha}}, y_{\boldsymbol{\alpha}}, z_{\boldsymbol{\alpha}}]$ **moduli the grid size** N**.**

- *step 2:* Choose a random location on the N-uplets by picking a random number β in $1, ..., N-1$. If this point is in the phase i, i.e. the value of voxel at position $[x_\beta, y_\beta, z_\beta]$ corresponds to the value associated to phase i, the procedure goes to **step 3**, otherwise a new number is picked.
- *step 3:* The algorithm moves along the list of voxels until it reaches another phase than i. The number of voxel that have been crossed, noted n_v, corresponds to a line length l_v:

$$l_v = \frac{n_v}{t_1} \quad (\text{ if } t_1 \neq 0) \tag{18}$$

$$l_v = \frac{n_v}{t_2} \quad (\text{ if } t_1 = 0, t_2 \neq 0) \tag{19}$$

$$l_v = \frac{n_v}{t_2} \quad (\text{ if } t_1 = 0, t_2 = 0, t_3 \neq 0) \tag{20}$$

- *step 4:* The algorithm increments the counter associated with lengths of line below l_v.
- *step 5:* The procedure of generating random numbers on the same oriented line is repeated multiple times.

- **Output of the algorithm:** After repeating these steps for the number of iterations defined by the user, the probability function $L_i(\mathbf{z}) = L_i(z\mathbf{t})$ is obtained by computing the frequency associated to the counter of each line segment such that:

$$L_i(z\mathbf{t}) = \frac{\text{Counter associated to } z}{\text{Total number of random location drawn}} \tag{21}$$

The implementation of the chord-length distribution function on 3D discretized and periodic microstructures follow a similar procedure than the lineal-path:

- **Input parameters:** The angles θ and ϕ defining the orientation of the random lines, the phase i value in the mesh and the number of iteration of random lines are input.
- **Iterative procedure:** The iterative procedure repeated by the algorithm consists of:
  - *step 1:* Creating a random line oriented by its directional vector $\mathbf{t}$ by generating a random point $A = [a_1, a_2, a_3]$ from which the line goes and then creating the positions of the voxels in order to move along this line.
    Hereafter, the procedure of implementation lineal-path distribution and chord-length distribution start differing:
  - *step 2:* Starting from the initial point $A = [x_0, y_0, z_0]$, move along the line until encountering the desired phase. The chord length is initiated at this position by the number of voxels $n_v = 1$.
  - *step 3:* The algorithm keeps browsing the line forward and incrementing the number of voxels while phase i is still encountered. When another phase is found, the chord length l_v is found using the relation IV.A with the number of voxels n_v. The chord length is added to list of measured chords length and the number of voxels is reset to 0.
  - *step 4:* The process is repeated while continuing to move along the line and recording the measured chord lengths.
    It should be noticed at this point that a bias in the measured chord can be introduced if recording segments that start or end at the border of the grid. Because of the bounded volume representing a periodic microstructure, these segments do not necessarely represent chord but only segment of it. In order to avoid that, a possible solution way is either to not record the boundary segments in the list of measured chord or to use periodicity of the microstructure to extend the measurement process on the line until it corresponds to an actual chord. In our algorithm, we choose to disregard boundary voxels on the recorded chords.
- **Outcome of the algorithm:** Once all iterations on random lines are done, the histogram of recorded chord lengths and frequency of appearance is outputted.

CHAPTER V

CLOSURE

In the first part of this thesis, existing homogenization results inspired the design of isotropic porous materials with nearly optimal effective elastic properties. Previous studies focused on using ordered lattice networks and 2D bio-inspired materials to obtain low-density materials with good elastic properties but usually the obtained results led to a loss in the stiffness of the material as a price to pay for isotropy or the other way around. In our work, we proposed to generate random porous materials consisting of single-size (monodisperse) and multiple-size (polydisperse) spherical inclusions in order to reach relatively high volume fractions with microstructures having morphological features similar to the coated sphere assemblage proposed by Hashin (1962) in an effort to reach the optimal isotropic bound of Hashin and Shtrikman (1963b). A combined numerical and experimental methodology has been proposed with the aim of developing computer-assisted tools that allow complex microstructures to be 3D printed and investigated. With this regard, rapid prototyping offers a promising technique for producing materials with controlled size, distribution and geometry of constituents and has so far been developed to study the mechanical and transport properties of periodic prototyped foams and controlled scaffolds. Here, we have exploited this technique to study random porous materials, and more specifically, to obtain their effective mechanical elastic properties. The proposed methodology can be summarized with the following steps:

— Periodic porous multiscale microstructures with controlled porosity consisting of non-overlapping spherical inclusions have been generated by means of a Random Sequential Addition process (RSA) that has been adapted to automatically generate high volume fractions.

— The representative volume elements (RVEs) of a porous material are generated using the converged effective properties are then calculated numerically by using both kinematic uniform (KU) and periodic boundary conditions (PBC).

— The relative size of the RVE, the voids and the specimen itself has been properly decided in order to satisfy the various technical constraints such as the minimum possible accuracy provided by the 3D-printer, as well as the maximum specimen dimension allowed by the experimental setup

and the extensometers. Thus, the representative RVEs were assembled to form a dog-bone specimen conforming to the standards for tensile tests on polymer materials.

— In order to experimentally measure the elastic properties of the 3D printed polymeric microstructures, we proposed a multi-step relaxation procedure that measures properly the linear elastic fields with the viscous one completely relaxed off. This procedure has been used to characterize the elastic properties of the matrix material (VeroWhite) and to assess the isotropy of the printing process. In turn, the elastic properties of the support material used for printing the closed porosity have been determined using experimental tensile tests on homogeneous samples. The negligible effect of the support material on the effective elastic properties of the porous material has been shown experimentally and numerically.

— The effective bulk and shear moduli of random porous samples for porosity in the range of $0 \leq c \leq 82\%$ have been experimentally measured. The comparison between the effective isotropic properties obtained from experiments, finite element (FE) computations and the upper Hashin-Shtrikman bounds showed that these microstructures are nearly optimal and reach experimentally unprecedented values of the effective properties for a wide range of porosity.

An important result of the work presented in this part is that RSA microstructures consisting of spherical voids, for monodisperse moderate porosities (up to 30%) and polydisperse in size high porosities (up to 82%), provide effective elastic moduli that lie very close to the optimal isotropic Hashin-Shtrikman bounds. The differences between FE simulations, experimental results and Hashin-Shtrikman bounds were analyzed using the local strain fields obtained by numerical computations. The observations confirm that the small deviation between the experiments and the theoretical bounds is related to the strain localization near the thinnest ligaments. Even more interestingly, this deviation is found to be higher at moderate porosity whereas the elastic fields become more uniform at low, i.e. $c \leq 30\%$ and high $c \geq 70\%$ porosities. Furthermore, the normalized effective Young's modulus of the presented random microstructures exhibits the stiffest value when compared with experimentally available results on isotropic foams and lattices or trusses. Thus, the proposed microstructures are promising candidates for lightweight highly-stiff materials provided of course that 3D printing technology improves in such a way that no support material is needed in the zones of closed-porosity.

This first part of the thesis shows that the optimal effective elastic moduli of isotropic materials are almost attained by the isolated spherical pores with single-sized and polydisperse in size microstructure for a large range of porosities. However, in some cases, one may like to be able to design microstructures with controlled effective properties that are softer than the ones with spheres and span a large range of moduli. In this regard, large number of studies have shown that microstructures with a random distribution of ellipsoidal inclusions can achieve a large range of effective elastic properties while still being isotropic. The question is therefore, which parameters and more generally statistical descriptors of the microstroctures are significantly influencing the elastic properties of material.

In view of this question, the second part of this thesis focused on the understanding of the link between the statistical description of random isotropic microstructures and the effective elastic

properties of random porous materials. Such a study provided a critical assessment of the influence of several statistical descriptors of the microstructures such as the one and two-point correlation functions, the chord length distribution and the connectivity on the effective elastic properties. To that aim, we first proposed a quantitative investigation of the two-point correlation function using a reconstruction procedure which consists in applying a level-cut process on Gaussian Random Fields (GRFs). This procedure accounts for the porosity and the correlation function extracted from 3D two-phase materials and has been applied to RVEs of porous microstructures consisting of isolated ellipsoidal pores. On one hand, the evolution of the isotropic elastic properties computed from the RSA microstructures with isolated ellipsoidal pores has shown that the local information about the shape of the pores has a large impact on the effective elastic properties even for isotropic microstructures. This influence on the bulk and shear moduli is well captured by the Willis estimates (Willis, 1977; Gatt et al., 2005) for isotropic microstructures with ellipsoidal inclusions that are not highly elongated ($0.2 \leq \omega \leq 1$)). On the other hand, the second-order modeling procedure based on level-cut GRF as explained in Sec.III.2.2, provides a very accurate reconstruction of the the first and second-order statistics of the reference RSA non-overlapping pores but the corresponding effective elastic moduli can be as low as half of that of the RSA. This is directly related to the fact that the process which generates the two-phase microstructures, i.e. the GRF and the RSA ones in this study, induces very different local geometrical features in each case. Evidently, these more complex geometrical features (such as ellipsoidal or non-canonical connected shapes) are not detected by the correlation function in a sufficient manner to yield accurate prediction of the corresponding effective elastic properties of these two types of porous materials.

In order to go deeper in the understanding of the observed differences between the non-overlapping RSA and thresholded GRF microstructures, we have introduced a third type of microstructure. The latter consists in adding cylindrical with circular cross-section porous channels to connect the ellipsoidal pores generated by the RSA algorithm. The connectivity of the original ellipsoidal voids can be fully controlled by assigning a number of connected ellipsoidal voids and a maximum distance at which this connectivity is applied. The FFT-based computations of the elasticity problem in these microstructures have shown that a relatively small number of connected regions in the closest neighborhood of a given ellipsoidal void can lead to a significant drop of the effective elastic properties as compared to the original non-overlapping RSA microstructure and for the exact same overall porosity. In turn, the two-point correlation function is completely insensitive to that connectivity thus implying the insufficiency of this statistical descriptor in this context.

In an attempt to identify a more relevant statistical descriptor that allows for the discrimination between these three microstructures, we proposed to compute the chord-length distribution of the matrix and the porous phase. The two-by-two comparison between the corresponding chord-length distributions showed that the deviations in this measure do not directly correlate to the deviations in the effective properties. Microstructures having similar effective properties such as the thresholded GRFs and the porous network with spherical pores have large deviation in the chord-length distributions of both the matrix and the porous phase. By contrast, microstructures

having smaller deviations in the chord-length distribution of the porous and the matrix phases, such as the RSA connected and the RSA non-overlapping porous microstructures with spherical pores, exhibit significant differences in the effective elastic properties. Therefore, in the present study, the chord-length distribution seems insufficient to link the statistics with the resulting effective elastic properties of the proposed microstructures.

In order to link the microstructure of the porous materials and the elastic fields, we proposed to analyze the correlation between a geometrical measure and a mechanical one. In this thesis, we chose to relate the Euclidean distance of the solid matrix phase to the fluctuating part of the hydrostatic and shear strain components. The values of the standard deviation of the fluctuating part of both the hydrostatic and shear strain components taken at a given Euclidean distance depict trends which can be linked to the local features of the different microstructures and their effective properties. At distances close to the interface, the amplitude of the standard deviation is higher for microstructures with elongated or connected pores and thus, more compliant effective properties are obtained in those cases. Similarly at longer distances, the higher the constant values of the strain field components are the lower the effective elastic properties are. The standard deviations at middle-range distances decrease with a rate that characterizes the local orientation of the pores in the microstructure. This measure highlights some important local geometrical features of the microstructures, which have an important impact on the effective elastic properties of the porous materials but unfortunately are not a all captured by more partial statistical descriptors such as the two-point correlation and the chord-length distribution functions. The extension of this work to the porous phase is left for future work.

At this point, it is important to address some of the future directions associated with the results presented in this thesis. In particular,future work related to the quest for new materials can be linked to the advances in the additive manufacturing (AM) techniques. Firstly, as it has been mentioned in Chapter II, the current AM processes are unable to print closed-cell porosity without the use of a support material or remaining powder in the case of metallic AM. The current work dodges this limitation using the mechanical contrast between the support material used in photopolymerization processes and the matrix material to obtain porous-like materials with effective properties similar to those obtained by the numerical computations using voids. However, this limits the fabrication of material to polymeric processes which are known to have low elastic moduli in comparison with metals or ceramics. A possible approach would be to use a porous network to connect internal pores to the outer surface in order to extract the support material (or unmelted powder in case of metallic processes) from the porous phase. However, adding a small fraction of cylindrical channels in the porous space has been shown in Sec.IV.1 to significantly affect the effective properties of microstructures with spherical pores. An optimization procedure over the choice of the coordination number and the cylinders radius may be used in order to minimize the drop of the effective properties due to connected porosity.

Secondly, using spherical polydisperse inclusions, 3D printed porous microstructures reached effective elastic properties close to the optimal bound of Hashin and Shtrikman (1963b) but only up

to the porosity $c = 82\%$, due to the large range of sizes of pores needed to achieve higher porosities, which cannot be printed by current 3D printers. Alternative approaches to explore in order to increase the current porosity ranges would consist in generating Voronoi cells or, starting from a configuration of spherical inclusions generated by the RSA algorithm, increasing the space occupied by a pore by evolving its shape towards a rounded polygonal inclusion. The roundness of pores corners would limit the stress concentration around them and enable to obtain relatively high isotropic stiffness properties (Berger et al., 2017).

The great versatility of the RSA algorithm combined with the generic workflow for 3D printing allows to extend the generation process to anisotropic microstructures. Those microstructures could involve ellipsoidal voids randomly (or unidirectionally) dispersed in the RVE as it is the case of the microstructures used in the chapter III. These material can also be used as test beds to a number of experimental procedures involving dynamic and static measurements of elastic moduli via wave dispersion and impact loads. Extension of the present study to the nonlinear regime (nonlinear elastic and viscoelastic (Lopez-Pamies et al., 2013b; Brenner and Suquet, 2013) as well as elasto-plastic (Mbiakop et al., 2015) is also straightforward given of course any limitations of the AM process itself. Another perspective for the use of such microstructures is to use them as a structuring element in order to optimize density and stiffness for more complex macrostructures (Allaire, 2012).

In turn, the question whether there is a simple or reduced geometrical description that is sufficient to provide quantitative estimates for the elastic properties and beyond such as non-linear elasticity, visco-elasticity and coupled problems, remains open. The results of this thesis have shown that this is not the case with the two-point correlation function and the chord-length distribution, at least in the context of the cases examined here. We have shown that two-point correlation functions coupled with the construction methodology, e.g. RSA with non-overlapping spheres, ellipsoidal inclusions, GRF with a simple threshold or RSA with connected porosity, can lead to very different effective elastic estimates. One of the perspectives is to use this coupling between the process of construction and the two-point correlation function in order to trigger the effective properties of the microstructures. Using the effect of connectivity or the size of ligament, foams and cellular material can be created in order to enhance their effective stiffness properties.

We have shown that the parameters for a porous network comprising ellipsoidal pores connected with cylindrical channels can reach various effective properties following the shape of pores, the number of connecting cylinders and their radii. A possible extension of this part might be to extract from digital image analysis of real materials the quantitative distributions of the characteristics of pores (size, shape and orientation) and those of the throats (number of connections per pore and throat radius). From this information, one can build a porous network and compute the effective elastic properties of the real image and the porous network model to assess if the approximation of local morphology does not affect the effective elastic properties of the material. Also, more complex models with control over some geometrical measures of the connectivity, such as the tortuosity map of the porous network or the local clustering of the porous phase, can be generated to create standard measures of the connectivity in the microstructure. Parametric study over these measures could lead

to empirical models of the effect of connectivity in order to predict the effective elastic properties.

BIBLIOGRAPHY

ABAQUS Version 6.11 (2011). Documentation. Dassault Systémes Simulia Corp, Providence, RI, USA. (Cited on page 21.)

Adler, R. J. and Taylor, J. E. (2007). Random Fields and Geometry. Springer-Verlag New York. (Cited on pages 58 and 59.)

Ahmadi, S., Hedayati, R., Li, Y., Lietaert, K., Tümer, N., Fatemi, A., Rans, C., Pouran, B., Weinans, H., and Zadpoor, A. (2018). Fatigue performance of additively manufactured meta-biomaterials: The effects of topology and material type. Acta Biomaterialia, 65:292 – 304. (Cited on page 2.)

Al-Kharusi, A. S. and Blunt, M. J. (2007). Network extraction from sandstone and carbonate pore space images. Journal of Petroleum Science and Engineering, 56(4):219 – 231. (Cited on page 89.)

Alderson, A., Rasburn, J., Ameer Beg, S., Mullarkey, P. G., Perrie, W., and Evans, K. E. (2000). An auxetic filter:FIXME a tuneable filter displaying enhanced size selectivity or defouling properties. Industrial Engineering Chemistry Research, 39(3):654–665. (Cited on page 2.)

Allaire, G. (2012). Shape optimization by the homogenization method. Springer Science and Business Media. (Cited on page 125.)

Anoukou, K., Danas, K., and Brenner, R. (2018). Rsa polydisperse ellipsoidal microstructures and homogenization estimates for linear elastic porous materials. unknown. (Cited on pages 11, 12, 15, 22, 25, and 40.)

Arns, J.-Y., Robins, V., Sheppard, A. P., Sok, R. M., Pinczewski, W. V., and Knackstedt, M. A. (2004). Effect of network topology on relative permeability. Transport in Porous Media, 55(1):21–46. (Cited on page 90.)

Ashby, M. (2013). Designing architectured materials. Scripta Materialia, 68(1):4 – 7. Architectured Materials. (Cited on page 3.)

Azzimonti, D., Willot, F., and Jeulin, D. (2013). Optical properties of deposit models for paints: full-fields fft computations and representative volume element. Journal of Modern Optics, 60(7):519–528. (Cited on page 55.)

Banhart, J., Baumeister, J., and Weber, M. (1996). Damping properties of aluminium foams. Materials Science and Engineering: A, 205(1):221 – 228. (Cited on page 2.)

Barclift, M. W. and Williams, C. (2012). Examining variability in the mechanical properties of parts manufactured via polyjet direct 3D printing. 23rd Annual International Solid Freeform Fabrication Symposium - An Additive Manufacturing Conference, SFF 2012. (Cited on page 31.)

Bauer, J., Hengsbach, S., Tesari, I., Schwaiger, R., and Kraft, O. (2014). High-strength cellular ceramic composites with 3d microarchitecture. Proceedings of the National Academy of Sciences, 111(7):2453–2458. (Cited on pages 2, 4, and 45.)

Bear, J., Braester, C., and Menier, P. C. (1987). Effective and relative permeabilities of anisotropie porous media. Transport in Porous Media, 2(3):301–316. (Cited on page 89.)

Bendsoe, M. P., Ben-Tal, A., and Zowe, J. (1994). Optimization methods for truss geometry and topology design. Structural optimization, 7(3):141–159. (Cited on page 3.)

Berger, J. B., Wadley, H. N. G., and McMeeking, R. M. (2017). Mechanical metamaterials at the theoretical limit of isotropic elastic stiffness. Nature, 543:533 EP –. (Cited on pages 2, 4, and 125.)

Bignonnet, F. and Dormieux, L. (2014). Fft-based bounds on the permeability of complex microstructures. International Journal for Numerical and Analytical Methods in Geomechanics, 38(16):1707–1723. (Cited on page 70.)

Blunt, M. J. (2001). Flow in porous media: pore-network models and multiphase flow. Current Opinion in Colloid & Interface Science, 6(3):197–207. (Cited on page 89.)

Böhm, H., Eckschlager, A., and Han, W. (2002). Multi-inclusion unit cell models for metal matrix composites with randomly oriented discontinuous reinforcements. Computational Materials Science, 25(1):42 – 53. (Cited on page 7.)

Böhm, H. J. and Han, W. (2001). Comparisons between three-dimensional and two-dimensional multi-particle unit cell models for particle reinforced metal matrix composites. Modelling and Simulation in Materials Science and Engineering, 9(2):47. (Cited on page 42.)

Brenner, R., Bravo-Castillero, J., and Léon, D. M. (2012). Investigation of the effective response of 2-1-2 piezoelectric composites. Procedia IUTAM, 3:292 – 300. IUTAM Symposium on Linking Scales in Computations: From Microstructure to Macro-scale Properties. (Cited on page 70.)

Brenner, R. and Suquet, P. (2013). Overall response of viscoelastic composites and polycrystals: exact asymptotic relations and approximate estimates. International Journal of Solids and Structures, 50(10):1824 – 1838. (Cited on page 125.)

Brisard, S., Davy, C. A., Michot, L., Troadec, D., and Levitz, P. (2019). Mesoscale pore structure of a high-performance concrete by coupling focused ion beam/scanning electron microscopy and small angle x-ray scattering. Journal of the American Ceramic Society, 102(5):2905–2923. (Cited on page 98.)

Brisard, S. and Dormieux, L. (2010). Fft-based methods for the mechanics of composites: A general variational framework. Computational Materials Science, 49(3):663 – 671. (Cited on page 70.)

Brisard, S. and Dormieux, L. (2012). Combining galerkin approximation techniques with the principle of hashin and shtrikman to derive a new fft-based numerical method for the homogenization of composites. Computer Methods in Applied Mechanics and Engineering, 217-220:197 – 212. (Cited on pages 71 and 86.)

Bucataru, I. and Slawinski, M. A. (2008). Invariant properties for finding distance in space of elasticity tensors. Journal of Elasticity, 94(2):97–114. (Cited on page 22.)

Budiansky, B. (1965). On the elastic moduli of some heterogeneous materials. Journal of the Mechanics and Physics of Solids, 13(4):223 – 227. (Cited on page 49.)

Cadiou, F., Etiemble, A., Douillard, T., Willot, F., Valentin, O., Badot, J.-C., Lestriez, B., and Maire, E. (2019). Numerical prediction of multiscale electronic conductivity of lithium-ion battery positive electrodes. Journal of The Electrochemical Society, 166(8):A1692–A1703. (Cited on page 55.)

Cansizoglu, O., Harrysson, O., Cormier, D., West, H., and Mahale, T. (2008). Properties of ti–6al–4v non-stochastic lattice structures fabricated via electron beam melting. Materials Science and Engineering: A, 492(1):468 – 474. (Cited on page 3.)

Chatzis, I. and Dullien, F. A. L. (1977). Modelling pore structure by 2-d and 3-d networks with applicationto sandstones. Journal of Canadian Petroleum Technology, 16(01):12. (Cited on page 89.)

Chen, H. and Chan, C. T. (2007). Acoustic cloaking in three dimensions using acoustic metamaterials. Applied Physics Letters, 91(18):183518. (Cited on page 2.)

Chen, Z., Wang, X., Giuliani, F., and Atkinson, A. (2015). Microstructural characteristics and elastic modulus of porous solids. Acta Materialia, 89:268 – 277. (Cited on page 1.)

Chiles, J.-P. and Delfiner, P. (1999). Geostatistics: modeling spatial uncertainty. Wiley, New York. (Cited on page 68.)

Christensen, R. M. and Lo, K. H. (1979). Solution for effective shear properties in three-phase sphere and cylinder models. Journal of the Mechanics and Physics of Solids, (27):315–330. (Cited on page 49.)

Coker, D. and Torquato, S. (1995). Extraction of morphological quantities from a digitized medium. Journal of Applied Physics, 77(12):6087–6099. (Cited on page 117.)

Compton, B. G. and Lewis, J. A. (2014). 3d-printing of lightweight cellular composites. Advanced Materials, 26(34):5930–5935. (Cited on pages 4 and 45.)

Conde, Y., Despois, J.-F., Goodall, R., Marmottant, A., Salvo, L., SanFIXMEMarchi, C., and Mortensen, A. (2006). Replication processing of highly porous materials. Advanced Engineering Materials, 8(9):795–803. (Cited on page 2.)

Danas, K. (2008). Heterogeneous materials with evolving microstructure : constitutive modeling, numerical implementation and applications. Theses, Ecole Polytechnique X. (Cited on page 87.)

Danas, K. (2017). Effective response of classical, auxetic and chiral magnetoelastic materials by use of a new variational principle. Journal of the Mechanics and Physics of Solids, 105:25 – 53. (Cited on page 20.)

Davies, G. J. and Zhen, S. (1983). Metallic foams: their production, properties and applications. Journal of Materials Science, 18(7):1899–1911. (Cited on page 2.)

Davis, M. W. (1987). Production of conditional simulations via the lu triangular decomposition of the covariance matrix. Mathematical Geology, 19(2):91–98. (Cited on page 61.)

Dawson, J. R. and Shortall, J. B. (1982). The microstructure of rigid polyurethane foams. Journal of Materials Science, 17(1):220–224. (Cited on pages 43 and 44.)

de Francqueville, F., Gilormini, P., and Diani, J. (2019). Representative volume elements for the simulation of isotropic composites highly filled with monosized spheres. International Journal of Solids and Structures, 158:277 – 286. (Cited on pages 55 and 57.)

Dean, E. A. and Lopez, J. A. (1983). Empirical dependence of elastic moduli on porosity for ceramic materials. Journal of the American Ceramic Society, 66(5):366–370. (Cited on page 1.)

Deshpande, V. and Fleck, N. (2000). Isotropic constitutive models for metallic foams. Journal of the Mechanics and Physics of Solids, 48(6):1253 – 1283. (Cited on page 2.)

Deshpande, V., Fleck, N., and Ashby, M. (2001). Effective properties of the octet-truss lattice material. Journal of the Mechanics and Physics of Solids, 49(8):1747 – 1769. (Cited on page 2.)

Despois, J.-F. and Mortensen, A. (2005). Permeability of open-pore microcellular materials. Acta Materialia, 53(5):1381 – 1388. (Cited on page 44.)

Diaz, C. E., Chatzis, I., and Dullien, F. A. L. (1987). Simulation of capillary pressure curves using bond correlated site percolation on a simple cubic network. Transport in Porous Media, 2(3):215–240. (Cited on page 89.)

Dietrich, C. R. and Newsam, G. N. (1993). A fast and exact method for multidimensional gaussian stochastic simulations. Water Resources Research, 29(8):2861–2869. (Cited on page 61.)

Dirrenberger, J., Forest, S., and Jeulin, D. (2013). Effective elastic properties of auxetic microstructures: anisotropy and structural applications. International Journal of Mechanics and Materials in Design, 9(1):21–33. (Cited on page 4.)

Dong, H. and Blunt, M. J. (2009). Pore-network extraction from micro-computerized-tomography images. Phys. Rev. E, 80:036307. (Cited on pages 89 and 90.)

Dong, H., Fjeldstad, S., Alberts, L., Roth, S., Bakke, S., and Oeren, P.-E. (2008). Pore network modelling on carbonate: A comparative study of different micro-ct network extraction methods. (Cited on page 90.)

Escoda, J., Willot, F., Jeulin, D., Sanahuja, J., and Toulemonde, C. (2011). Estimation of local stresses and elastic properties of a mortar sample by fft computation of fields on a 3d image. Cement and Concrete Research, 41(5):542 – 556. (Cited on page 55.)

Eshelby, J. (1957). The determination of elastic field of an ellipsoidal inclusion and related problems. Proceedings of the Royal Society of London, (421):379–396. (Cited on pages 40 and 48.)

Fatt, I. (1956). The network model of porous media. (Cited on page 89.)

Figliuzzi, B., Jeulin, D., Faessel, M., Willot, F., Koishi, M., and Kowatari, N. (2016). Modelling the microstructure and the viscoelastic behaviour of carbon black filled rubber materials from 3D simulations. Technische Mechanik, 32(1-2):22–46. (Cited on page 55.)

Fleck, N., Deshpande, V., and Ashby, M. (2010). Micro-architectured materials: past, present and future. Proceedings of the Royal Society of London A: Mathematical, Physical and Engineering Sciences, 466(2121):2495–2516. (Cited on page 2.)

Francfort, G. A. and Murat, F. (1986). Homogenization and optimal bounds in linear elasticity. Archive for Rational Mechanics and Analysis, 94:307–334. (Cited on pages 5, 6, and 41.)

Fritzen, F., Forest, S., Bohlke, T., Kondo, D., and Kanit, T. (2012). Computational homogenization of elasto-plastic porous metals. International Journal of Plasticity, 29:102 – 119. (Cited on page 12.)

Fryxell, R. E. and Chandler, B. A. (1964). Creep, strength, expansion, and elastic moduli of sintered beo as a function of grain size, porosity, and grain orientation. Journal of the American Ceramic Society, 47(6):283–291. (Cited on page 1.)

Garboczi, E. and Day, A. (1995). An algorithm for computing the effective linear elastic properties of heterogeneous materials: Three-dimensional results for composites with equal phase poisson ratios. Journal of the Mechanics and Physics of Solids, 43(9):1349 – 1362. (Cited on page 7.)

Gatt, J.-M., Monerie, Y., Laux, D., and Baron, D. (2005). Elastic behavior of porous ceramics: application to nuclear fuel materials. Journal of Nuclear Materials, 336(2):145 – 155. (Cited on pages 74, 88, and 123.)

Gélébart, L. and Ouaki, F. (2015). Filtering material properties to improve fft-based methods for numerical homogenization. Journal of Computational Physics, 294:90 – 95. (Cited on page 85.)

Gerke, K. M., Karsanina, M. V., and Mallants, D. (2015). Universal stochastic multiscale image fusion: An example application for shale rock. Scientific Reports, 5:15880 EP –. (Cited on page 8.)

Ghossein, E. and Lévesque, M. (2014). A comprehensive validation of analytical homogenization models: The case of ellipsoidal particles reinforced composites. Mechanics of Materials, 75:135 – 150. (Cited on page 22.)

Gibson, L. J. and Ashby, M. F. (1988). Cellular solids: structure and properties. Pergamon Press, Oxford, Orlando, FL, USA. (Cited on page 8.)

Gibson, L. J. and Ashby, M. F. (1997). Cellular Solids: Structure and Properties. Cambridge Solid State Science Series. Cambridge University Press, 2 edition. (Cited on page 2.)

Gillman, A., Amadio, G., Matouš, K., and Jackson, T. L. (2015). Third-order thermo-mechanical properties for packs of platonic solids using statistical micromechanics. Proceedings of the Royal Society A: Mathematical, Physical and Engineering Sciences, 471(2177):20150060. (Cited on page 56.)

Gómez-Hernández, J. J. and Journel, A. G. (1993). Joint Sequential Simulation of MultiGaussian Fields, pages 85–94. Springer Netherlands, Dordrecht. (Cited on page 61.)

Göransson, P. (2006). Acoustic and vibrational damping in porous solids. Philosophical Transactions of the Royal Society of London A: Mathematical, Physical and Engineering Sciences, 364(1838):89–108. (Cited on page 2.)

Gorny, B., Niendorf, T., Lackmann, J., Thoene, M., Troester, T., and Maier, H. (2011). In situ characterization of the deformation and failure behavior of non-stochastic porous structures processed by selective laser melting. Materials Science and Engineering: A, 528(27):7962 – 7967. (Cited on page 3.)

Gosselin, C., Duballet, R., Roux, P., Gaudillière, N., Dirrenberger, J., and Morel, P. (2016). Large-scale 3d printing of ultra-high performance concrete – a new processing route for architects and builders. Materials & Design, 100:102 – 109. (Cited on page 3.)

Gélébart, L. and Mondon-Cancel, R. (2013). Non-linear extension of fft-based methods accelerated by conjugate gradients to evaluate the mechanical behavior of composite materials. Computational Materials Science, 77:430–439. (Cited on page 70.)

Han, S. C., Lee, J. W., and Kang, K. (2015). A new type of low density material: Shellular. Advanced Materials, 27(37):5506–5511. (Cited on pages 2 and 45.)

Hashin, Z. (1962). The elastic moduli of heterogeneous materials. Journal of Applied Mechanics, (29):481–505. (Cited on pages 5, 6, and 121.)

Hashin, Z. and Shtrikman, S. (1963a). A variational approach to the theory of the elastic behaviour of multiphase materials. Journal of the Mechanics and Physics of Solids, 11(2):127 – 140. (Cited on pages 5, 50, and 87.)

Hashin, Z. and Shtrikman, S. (1963b). A variational approach to the theory of the elastic behaviour of multiphase materials. Journal of the Mechanics and Physics of Solids, (11):127–140. (Cited on pages 40, 47, 121, and 124.)

Head, D. and Vanorio, T. (2016). Effects of changes in rock microstructures on permeability: 3-d printing investigation. Geophysical Research Letters, 43(14):7494–7502. 2016GL069334. (Cited on page 8.)

Heinl, P., Rottmair, A., Körner, C., and F. Singer, R. (2007). Cellular titanium by selective electron beam melting. Advanced Engineering Materials, 9:360 – 364. (Cited on page 3.)

Hengsbach, S. and Lantada, A. D. (2014). Direct laser writing of auxetic structures: present capabilities and challenges. Smart Materials and Structures, 23(8):085033. (Cited on page 3.)

Hill, R. (1952). The elastic behaviour of a crystalline aggregate. Proceedings of the Physical Society. Section A, 65(5):349. (Cited on page 5.)

Hill, R. (1963). Elastic properties of reinforced solids: Some theoretical principles. Journal of the Mechanics and Physics of Solids, 11(5):357 – 372. (Cited on pages 21 and 48.)

Hossain, M., Vu, D., and Steinmann, P. (2012). Experimental study and numerical modelling of vhb 4910 polymer. Computational Materials Science, 59:65–74. (Cited on pages 7, 28, and 31.)

Huet, C. (1990). Application of variational concepts to size effects in elastic heterogeneous bodies. Journal of the Mechanics and Physics of Solids, 38(6):813 – 841. (Cited on page 20.)

Hutchinson, J. W. and Hill, R. (1976). Bounds and self-consistent estimates for creep of polycrystalline materials. Proceedings of the Royal Society of London. A. Mathematical and Physical Sciences, 348(1652):101–127. (Cited on page 49.)

Idiart, M. I. (2008). Modeling the macroscopic behavior of two-phase nonlinear composites by infinite-rank laminates. Journal of the Mechanics and Physics of Solids, 56(8):2599 – 2617. (Cited on page 41.)

Ishutov, S., Hasiuk, F. J., Fullmer, S. M., Buono, A. S., Gray, J. N., and Harding, C. (2017). Resurrection of a reservoir sandstone from tomographic data using three-dimensional printing. AAPG Bulletin, 101(9):1425–1443. (Cited on page 8.)

Jang, D., Meza, L. R., Greer, F., and Greer, J. R. (2013). Fabrication and deformation of three-dimensional hollow ceramic nanostructures. Nature Materials, 12:893 EP –. (Cited on page 2.)

Jeulin, D. (2001). Random structure models for homogenization and fracture statistics. D. Jeulin, M. Ostoja-Starzewski (Eds.), Mechanics of Random and Multiscale Microstructures, Springer-Verlag. (Cited on pages 5 and 6.)

Jivkov, A., Hollis, C., Etiese, F., Mcdonald, S., and Withers, P. (2013). A novel architecture for pore network modelling with applications to permeability of porous media. Journal of Hydrology, 486:246–258. (Cited on page 90.)

Kabel, M., Merkert, D., and Schneider, M. (2015). Use of composite voxels in fft-based homogenization. Computer Methods in Applied Mechanics and Engineering, 294:168 – 188. (Cited on page 85.)

Kanit, T., Forest, S., Galliet, I., Mounoury, V., and Jeulin, D. (2003). Determination of the size of the representative volume element for random composites: statistical and numerical approach. International Journal of Solids and Structures, 40(13):3647 – 3679. (Cited on pages 20 and 21.)

Kim, Y.-W., Jin, Y.-J., Chun, Y.-S., Song, I.-H., and Kim, H.-D. (2005). A simple pressing route to closed-cell microcellular ceramics. Scripta Materialia, 53(8):921 – 925. (Cited on pages 43 and 44.)

Kurzhanski, A. B. and Valyi, Istvan, . (1997). Ellipsoidal calculus for estimation and control. Laxenburg, Austria : IIASA ; Boston : Birkhauser Boston. Includes bibliographical references (p. [291]-318) and index. (Cited on page 51.)

Landy, N. I., Sajuyigbe, S., Mock, J. J., Smith, D. R., and Padilla, W. J. (2008). Perfect metamaterial absorber. Phys. Rev. Lett., 100:207402. (Cited on page 2.)

Lantuejoul, C. (2002). Geostatistical Simulations: Models and Algorithms. Springer, Berlin/Heidelberg, Germany/New York. (Cited on pages 59 and 60.)

Latypov, M. I., Kühbach, M., Beyerlein, I. J., Stinville, J.-C., Toth, L. S., Pollock, T. M., and Kalidindi, S. R. (2018). Application of chord length distributions and principal component analysis for quantification and representation of diverse polycrystalline microstructures. Materials Characterization, 145:671 – 685. (Cited on page 98.)

Lee, J.-H., Singer, J. P., and Thomas, E. L. (2012). Micro-/nanostructured mechanical metamaterials. Advanced Materials, 24(36):4782–4810. (Cited on page 2.)

Levitz, P. (1998). Off-lattice reconstruction of porous media: critical evaluation, geometrical confinement and molecular transport. Advances in Colloid and Interface Science, 76-77:71 – 106. (Cited on pages 9, 57, 58, and 100.)

Lin, A. and Han, S. (2002). On the distance between two ellipsoids. SIAM Journal on Optimization, 13(1):298–308. (Cited on pages 12 and 52.)

Liu, Y., Li, J., Sun, S., and Yu, B. (2019). Advances in gaussian random field generation: a review. Computational Geosciences. (Cited on page 61.)

Lopez-Pamies, O., Goudarzi, T., and Danas, K. (2013a). The nonlinear elastic response of suspensions of rigid inclusions in rubber: Ii—a simple explicit approximation for finite-concentration suspensions. Journal of the Mechanics and Physics of Solids, 61(1):19 – 37. (Cited on pages 5, 7, 12, 14, and 25.)

Lopez-Pamies, O., Goudarzi, T., and Danas, K. (2013b). The nonlinear elastic response of suspensions of rigid inclusions in rubber: Ii—a simple explicit approximation for finite-concentration suspensions. Journal of the Mechanics and Physics of Solids, 61(1):19 – 37. (Cited on page 125.)

Ma, Y., Scarpa, F., Zhang, D., Zhu, B., Chen, L., and Hong, J. (2013). A nonlinear auxetic structural vibration damper with metal rubber particles. Smart Materials and Structures, 22(8):084012. (Cited on page 2.)

Mareau, C. and Robert, C. (2017). Different composite voxel methods for the numerical homogenization of heterogeneous inelastic materials with fft-based techniques. Mechanics of Materials, 105:157 – 165. (Cited on page 85.)

Matheron, G. (1973). The intrinsic random functions and their applications. Advances in Applied Probability, 5(3):439–468. (Cited on page 61.)

Mbiakop, A., Constantinescu, A., and Danas, K. (2015). An analytical model for porous single crystals with ellipsoidal voids. Journal of the Mechanics and Physics of Solids, 84:436 – 467. (Cited on pages 20 and 125.)

McCall, K. R., Johnson, D. L., and Guyer, R. A. (1991). Magnetization evolution in connected pore systems. Phys. Rev. B, 44:7344–7355. (Cited on page 89.)

McLaughlin, R. (1977). A study of the differential scheme for composite materials. International Journal of Engineering Science, 15(4):237 – 244. (Cited on page 49.)

Messner, M. (2016). Optimal lattice-structured materials. Journal of Mechanics Physics of Solids, 96:162–183. (Cited on page 4.)

Meza, L., Das, S., and Greer, J. (2014). Strong, lightweight, and recoverable three-dimensional ceramic nanolattices. Science, 345(6202):1322–1326. (Cited on pages 2 and 3.)

Meza, L. R., Phlipot, G. P., Portela, C. M., Maggi, A., Montemayor, L. C., Comella, A., Kochmann, D. M., and Greer, J. R. (2017). Reexamining the mechanical property space of three-dimensional lattice architectures. Acta Materialia, 140:424 – 432. (Cited on pages 4, 43, 44, and 45.)

Moakher, M. and Norris, A. N. (2006). The closest elastic tensor of arbitrary symmetry to an elasticity tensor of lower symmetry. Journal of Elasticity, 85(3):215–263. (Cited on page 22.)

Mori, T. and Tanaka, K. (1973). Average stress in matrix and average elastic energy of materials with misfitting inclusions. Acta Metallurgica et Materiallia, (21):571–574. (Cited on page 49.)

Moulinec, H. and Suquet, P. (1998). A numerical method for computing the overall response of nonlinear composites with complex microstructure. Computer Methods in Applied Mechanics and Engineering, 157(1-2):69–94. (Cited on pages 7, 69, and 70.)

Moulinec, H; Suquet, P. (1994). A fast numerical method for computing the linear and nonlinear mechanical properties of composites. Comptes rendus de l'Académie des sciences. Série II, Mécanique, physique, chimie, astronomie. (Cited on page 70.)

Moussaddy, H., Therriault, D., and Lévesque, M. (2013). Assessment of existing and introduction of a new and robust efficient definition of the representative volume element. International Journal of Solids and Structures, 50(24):3817 – 3828. (Cited on page 22.)

Nemat-Nasser, S. and Hori, M. (1990). Elastic Solids with Microdefects, pages 297–320. Springer New York, New York, NY. (Cited on page 49.)

Neumann, M., Osenberg, M., Hilger, A., Franzen, D., Turek, T., Manke, I., and Schmidt, V. (2019). On a pluri-gaussian model for three-phase microstructures, with applications to 3d image data of gas-diffusion electrodes. Computational Materials Science, 156:325 – 331. (Cited on page 56.)

Norris, A. (1985). A differential scheme for the effective moduli of composites. Mechanics of Materials, 4(1):1 – 16. (Cited on page 49.)

Oldmixon, E. H., Butler, J. P., and Hoppin, F. G. (1994). Semi-automated measurement of true chord length distributions and moments by video microscopy and image analysis. Journal of Microscopy, 175(1):60–69. (Cited on page 98.)

Øren, P.-E. and Bakke, S. (2002). Process based reconstruction of sandstones and prediction of transport properties. Transport in Porous Media, 46(2):311–343. (Cited on pages 9, 56, 57, and 59.)

Oren, P. E., Billiotte, J., and Pinczewski, W. V. (1992). Mobilization of waterflood residual oil by gas injection for water-wet conditions. SPE Formation Evaluation, 7(01):70–78. (Cited on page 90.)

Parnell, W. J. (2016). The eshelby, hill, moment and concentration tensors for ellipsoidal inhomogeneities in the newtonian potential problem and linear elastostatics. Journal of Elasticity, 125(2):231–294. (Cited on page 48.)

Patzek, T. W. (2001). Verification of a complete pore network simulator of drainage and imbibition. SPE Journal, 6(02):144–156. (Cited on page 90.)

Pebesma, E. J. (2004). Multivariable geostatistics in s: the gstat package. Computers & Geosciences, 30(7):683 – 691. (Cited on page 61.)

Phani, K. K. and Niyogi, S. K. (1987). Young's modulus of porous brittle solids. Journal of Materials Science, 22(1):257–263. (Cited on page 1.)

Pierard, O., Gonzalez, C., Segurado, J., LLorca, J., and Doghri, I. (2007). Micromechanics of elasto-plastic materials reinforced with ellipsoidal inclusions. International Journal of Solids and Structures, 44(21):6945 – 6962. (Cited on page 12.)

Poirion, F. and Soize, C. (1995). Numerical methods and mathematical aspects for simulation of homogeneous and non homogeneous gaussian vector fields. In Krée, P. and Wedig, W., editors, Probabilistic Methods in Applied Physics, volume 451 of Lecture Notes in Physics, pages 17–53. Springer Berlin Heidelberg. (Cited on pages 61 and 79.)

Rasmussen, C. E. and Williams, C. K. I. (2005). Gaussian Processes for Machine Learning (Adaptive Computation and Machine Learning). The MIT Press. (Cited on page 62.)

Reuss, A. (1929). Berechnung der fliessgrenze von mischkristallen auf grund der plastizitätsbedingung für einkristalle. Journal of Apllied Mathematics and Mechanics, (9):49–58. (Cited on pages 5 and 49.)

Rintoul, M. and Torquato, S. (1997). Reconstruction of the structure of dispersions. Journal of Colloid and Interface Science, 186(2):467 – 476. (Cited on pages 6 and 12.)

Roberts, A. and Garboczi, E. (2001). Elastic moduli of model random three-dimensional closed-cell cellular solids. Acta Materialia, 49(2):189 – 197. (Cited on pages 8, 9, and 44.)

Roberts, A. P. (1997). Statistical reconstruction of three-dimensional porous media from two-dimensional images. Phys. Rev. E, 56:3203–3212. (Cited on pages 9, 56, 57, 58, 99, and 100.)

Roberts, A. P. and Teubner, M. (1995). Transport properties of heterogeneous materials derived from gaussian random fields: Bounds and simulation. Physical Review E, 51(5):4141–4154. (Cited on page 9.)

Roscoe, R. (1952). The viscosity of suspensions of rigid spheres. British Journal of Applied Physics, 3(8):267–269. (Cited on page 49.)

Roubin, E. and Colliat, J.-B. (2016). Critical probability of percolation over bounded region in n-dimensional euclidean space. Journal of Statistical Mechanics: Theory and Experiment, 2016(3):033306. (Cited on page 72.)

Roubin, E., Colliat, J.-B., and Benkemoun, N. (2015). Meso-scale modeling of concrete: A morphological description based on excursion sets of random fields. Computational Materials Science, 102:183 – 195. (Cited on pages 9, 57, 58, and 60.)

Saha, M., Mahfuz, H., Chakravarty, U., Uddin, M., Kabir, M. E., and Jeelani, S. (2005). Effect of density, microstructure, and strain rate on compression behavior of polymeric foams. Materials Science and Engineering: A, 406(1):328 – 336. (Cited on pages 43 and 44.)

Schaedler, T. A., Jacobsen, A. J., Torrents, A., Sorensen, A. E., Lian, J., Greer, J. R., Valdevit, L., and Carter, W. B. (2011). Ultralight metallic microlattices. Science, 334(6058):962–965. (Cited on pages 2 and 3.)

Schöberl, J. (1997). Netgen an advancing front 2d/3d-mesh generator based on abstract rules. Computing and Visualization in Science, 1(1):41–52. (Cited on page 21.)

Schurig, D. (2006). Off-normal incidence simulations of metamaterials using fdtd. International Journal of Numerical Modelling: Electronic Networks, Devices and Fields, 19(2):215–228. (Cited on page 2.)

Segurado, J. and Llorca, J. (2002). A numerical approximation to the elastic properties of sphere-reinforced composites. Journal of the Mechanics and Physics of Solids, 50. (Cited on pages 7 and 12.)

Serra, J. (1983). Image Analysis and Mathematical Morphology. Pergamon Press, Orlando, FL, USA. (Cited on page 98.)

Shinozuka, M. and Deodatis, G. (1991). Simulation of Stochastic Processes by Spectral Representation. Applied Mechanics Reviews, 44(4):191–204. (Cited on page 61.)

Shinozuka, M. and Jan, C.-M. (1972). Digital simulation of random processes and its applications. Journal of Sound and Vibration, 25(1):111 – 128. (Cited on page 61.)

Sigmund, O. (2000). New class of extremal composites. Journal of the Mechanics and Physics of Solids, 48:397–428. (Cited on pages 4, 6, and 41.)

Smith, D. R., Pendry, J. B., and Wiltshire, M. C. K. (2004). Metamaterials and negative refractive index. Science, 305(5685):788–792. (Cited on page 2.)

Spoor, P. S., Maynard, J. D., and Kortan, A. R. (1995). Elastic isotropy and anisotropy in quasicrystalline and cubic alculi. Phys. Rev. Lett., 75:3462–3465. (Cited on page 22.)

Suquet, P. (1987). Homogenization Techniques for Composite Media: Lectures Delivered at the CISM International Center for Mechanical Sciences Udine, Italy, July 1–5, 1985, pages 193–230. Springer Berlin Heidelberg, Berlin, Heidelberg. (Cited on page 20.)

Suzuki, A., Li, K., and Horne, R. (2014). fracture network, flow experiment, 3d printer, ct scan images. Stanford Geothermal Workshop, pages n/a–n/a. (Cited on page 9.)

Tancogne-Dejean, T. and Mohr, D. (2017). Elastically-isotropic truss lattice materials of reduced plastic anisotropy. International Journal of Solids and Structures. (Cited on page 4.)

Tarantino, M., Weber, L., and Mortensen, A. (2016). Effect of hydrostatic pressure on flow and deformation in highly reinforced particulate composites. Acta Materialia, 117:345 – 355. (Cited on page 40.)

Tarantino, M., Zerhouni, O., and Danas, K. (2019). Random 3d-printed isotropic composites with high volume fraction of pore-like polydisperse inclusions and near-optimal elastic stiffness. Acta Materialia, 175:331 – 340. (Cited on pages 6 and 11.)

Teubner, M. (1991). Level surfaces of gaussian random fields and microemulsions. Europhysics Letters (EPL), 14(5):403–408. (Cited on pages 9, 57, and 72.)

Torquato, S. (1997). Effective stiffness tensor of composite media—i. exact series expansions. Journal of the Mechanics and Physics of Solids, 45(9):1421 – 1448. (Cited on page 56.)

Torquato, S. (2002). Random Heterogeneous Materials: Microstructure and Macroscopic Properties. Springer, New York. (Cited on pages 56 and 59.)

Torquato, S. and Lu, B. (1993). Chord-length distribution function for two-phase random media. Phys. Rev. E, 47:2950–2953. (Cited on page 98.)

Tran, V.-P., Guilleminot, J., Brisard, S., and Sab, K. (2016). Stochastic modeling of mesoscopic elasticity random field. Mechanics of Materials, 93:1 – 12. (Cited on page 60.)

Vanmarcke, E. (1983). Random Fields. (Cited on page 58.)

Vasilyev, L., Raoof, A., and Nordbotten, J. M. (2012). Effect of mean network coordination number on dispersivity characteristics. Transport in Porous Media, 95(2):447–463. (Cited on page 90.)

Voigt, W. (1889). Über die beziehung zwischen den beiden elastizitätskonstanten isotroper körper. Wiedmanns Annalen der Physic and Chemie, (38):573–587. (Cited on pages 5 and 49.)

Walpole, L. J. (1966). On bounds for the overall elastic moduli of inhomogeneous systems–i/. Journal of the Mechanics and Physics of Solids, 14(3):151–162. (Cited on page 50.)

Walsh, J. B., BRACE, W. F., and ENGLAND, A. W. (1965). Effect of porosity on compressibility of glass. Journal of the American Ceramic Society, 48(12):605–608. (Cited on pages 43 and 44.)

Wang, D. W., Li, F., Liu, M., Lu, G., and Cheng, H. M. (2008). 3d aperiodic hierarchical porous graphitic carbon material for high rate electrochemical capacitive energy storage. Angewandte Chemie International Edition, 47(2):373–376. (Cited on page 2.)

Wang, L., Lau, J., Thomas, E. L., and Boyce, M. C. (2011). Co-continuous composite materials for stiffness, strength, and energy dissipation. Advanced Materials, 23(13):1524–1529. (Cited on page 4.)

Willis, J. (1977). Bounds and self-consistent estimates for the overall properties of anisotropic composites. Journal of the Mechanics and Physics of Solids, 25(3):185 – 202. (Cited on pages 5, 40, and 123.)

Willis, J. (1978). Variational principles and bounds for the overall properties of composites. In Provan, J., editor, Continuum Models and Discrete Systems, volume 2, pages 185–212. University of Waterloo Press. (Cited on pages 74, 75, and 87.)

Willis, J. (1981). Variational and related methods for the overall properties of composites. volume 21 of Advances in Applied Mechanics, pages 1 – 78. Elsevier. (Cited on page 48.)

Willot, F. (2015). Fourier-based schemes for computing the mechanical response of composites with accurate local fields. Comptes Rendus Mécanique, 343(3):232 – 245. (Cited on page 71.)

Wissler, M. and Mazza, E. (2007). Mechanical behavior of an acrylic elastomer used in dielectric elastomer actuators. Sensors and Actuators A: Physical, 134(2):494 – 504. (Cited on page 28.)

Xiong, Q., Baychev, T. G., and Jivkov, A. P. (2016). Review of pore network modelling of porous media: Experimental characterisations, network constructions and applications to reactive transport. Journal of Contaminant Hydrology, 192:101 – 117. (Cited on pages 89 and 90.)

Yao, J., Frykman, P., Kalaydjian, F., Thovert, J., and Adler, P. (1993). High-order moments of the phase function for real and reconstructed model porous media: A comparison. Journal of Colloid and Interface Science, 156(2):478 – 490. (Cited on page 56.)

Youssef, S., Maire, E., and Gaertner, R. (2005). Finite element modelling of the actual structure of cellular materials determined by x-ray tomography. Acta Materialia, 53(3):719 – 730. (Cited on pages 43 and 44.)

Zadpoor, A. A. (2016). Mechanical meta-materials. Mater. Horiz., 3:371–381. (Cited on page 2.)

Zähle, M. (1988). Stoyan, d., w. kendall, j. mecke: Stochastic geometry and its applications. j. wiley & sons/akademie-verlag, berlin 1987, 345 pp. Biometrical Journal, 30(6):758–758. (Cited on page 98.)

Zeller, R. and Dederichs, P. H. (1973). Elastic constants of polycrystals. physica status solidi (b), 55(2):831–842. (Cited on page 70.)

Zener, C. M. and Siegel, S. (1949). Elasticity and anelasticity of metals. The Journal of Physical and Colloid Chemistry, 53(9):1468–1468. (Cited on page 22.)

Zerhouni, O., Tarantino, M., and Danas, K. (2019). Numerically-aided 3d printed random isotropic porous materials approaching the hashin-shtrikman bounds. Composites Part B: Engineering, 156:344 – 354. (Cited on pages 6 and 11.)

Zheng, X., Lee, H., Weisgraber, T. H., Shusteff, M., DeOtte, J., Duoss, E. B., Kuntz, J. D., Biener, M. M., Ge, Q., Jackson, J. A., Kucheyev, S. O., Fang, N. X., and Spadaccini, C. M. (2014). Ultralight, ultrastiff mechanical metamaterials. Science, 344(6190):1373–1377. (Cited on page 2.)

Zok, F., Waltner, S., Wei, Z., Rathbun, H., McMeeking, R., and Evans, A. (2004). A protocol for characterizing the structural performance of metallic sandwich panels: application to pyramidal truss cores. International Journal of Solids and Structures, 41(22):6249 – 6271. (Cited on page 2.)

Titre : Étude des propriétés élastiques effectives de matériaux avec microstructure : Impression 3D, caractérisation expérimentale et numérique.

Mots clés : Elasticité linéaire, Matériaux poreux aléatoires, propriétés effectives, Microstructures imprimées, Modélisation statistique, Réseaux poreux

Résumé : Dans le cadre de cette thèse, la combinaison de plusieurs outils numériques et expérimentaux a permis la génération de différents modèles de microstructures aléatoires afin d'étudier l'influence des descripteurs statistiques sur les propriétés élastiques effectives des matériaux poreux. Dans la première partie de cette thèse, nous avons développé une procédure qui associe impression 3D, caractérisation expérimentale et numérique ainsi que les résultats théoriques sur les propriétés effectives de matériaux poreux désordonnés. Cette méthodologie est appliquée à la fabrication de microstructures constituées de pores sphériques, de taille unique ou avec une distribution de plusieurs tailles dont les propriétés élastiques effectives sont proches de la borne supérieure de Hashin-Shtrikman pour les matériaux isotropes pour une large gamme de porosité. Dans la seconde partie de cette thèse, on cherche à évaluer l'influence de certains descripteurs statistiques de la microstructure sur les propriétés élastiques macroscopiques pour les relier à l'espace poreux aléatoire et multiéchelle dans les carbonates. Pour cela, nous évaluons la pertinence des fonctions de corrélation à deux points et nous proposons une manière d'évaluer l'influence de la connectivité sur les propriétés élastiques en considérant un réseau connecté de pores ellipsoïdaux reliés par des canaux cylindriques. Les résultats montrent que la fonction de corrélation et la fonction de distribution de cordes ne permet pas de capturer l'effet de la connectivité et de l'élancement des pores sur les modules élastiques effectifs. Pour mieux comprendre l'influence de ces paramètres de la microstructure sur les propriétés effectives, on propose une analyse du lien entre la géométrie locale dans l'espace poreux et les champs élastiques du matériaux. Cela consiste à étudier la distribution des fluctuations locales du champ de déformation par rapport à la distance euclidienne séparant un point de la phase solide de l'interface avec la phase poreuse. La moyenne et l'écart type des fluctuations de la composante hydrostatique du champ de déformation pour un chargement hydrostatique concordent qualitativement avec les modules de compressibilité effectives obtenus. Compte tenu de ces résultats, il semble que les propriétés élastiques effectives des différentes microstructures étudiées sont fortement sensibles à l'information géométrique locale contenus dans la forme des pores et leur connectivité.

Title : A study on the effective elastic properties of materials with microstructure: 3D Printing, Experiments and Numerics.

Keywords : Linear elasticity, Porous materials, Effective properties, 3D printed microstructures, Statistical modeling, Porous network.

Abstract : In this thesis, we combine numerical and experimental tools to generate models for internal geometry of porous materials and to assess the effect of controlled statistical descriptors of the microstructures on their effective elastic properties. The first part of this work is devoted to a methodology that allows for the combination of 3D-printing, experimental testing, numerical and analytical analysis of random porous materials with controlled homogenized elastic properties. We applied this methodology to fabricate porous material containing single-sized (monodisperse) or polydisperse spherical voids that have been numerically and experimentally found to reach effective elastic properties that are close to the optimal Hashin-Shtrikman upper bound for isotropic porous material.
In the second part of this thesis, the objective is to assess the influence of some statistical descriptors of the microstructure on the effective elastic properties in order to link them with the distribution of the porous space in the multiscale structure of carbonate rocks. To that aim, we investigate the ability of the two-point correlation function to characterize the effective elastic properties of random porous microstructures. Furthermore, we propose a porous network model to capture the influence of connectivity on the effective elastic properties. The effective elastic properties, computed using a Fast Fourier Transform (FFT) based method, show that the correlation function and chord-length distribution functions are insufficient to predict the effective elastic properties of random porous materials as they do not capture accurately the effect of the local shape of pores and the degree of connectivity of the porous phase. These latter are found to be important parameters on the effective elastic properties as a small additional fraction of porosity to connect pores lead to important decrease in the effective properties.
Subsequently, we propose to analyze the link between the local geometry of the porous space and the elastic fields in the microstructure. We study, the distribution of the fluctuating part of the strain field as a function of the Euclidean distance between a point in the solid phase and the interface of the two-phase material. The average value and the standard deviation of the fluctuations in the hydrostatic strain component are qualitatively consistent with the effective bulk modulus obtained in the microstructure. Similar observa- tions are found for the shear strain component with the effective shear moduli. Following these results, it appears that the effective elastic properties of the three types of microstructures investigated are highly related to the local information on the porous phase which defines the shape and the connectivity of the pores.

Institut Polytechnique de Paris
91120 Palaiseau, France